工學博士學位論文

Conducting Polymer Thin Films via Solution Process as Electrode Materials for Chemical Sensor, Supercapacitor and Solar Cell Applications

용액 공정법에 의해 제조된 전도성 고분자 박막의 화학 센서, 초고용량 커패시터 및 태양전지 분야의 전극 물질에의 응용

2015年 2月

서울大學校 大學院

化學生物工學部

曺 城 熏

Conducting Polymer Thin Films via Solution Process as Electrode Materials for Chemical Sensor, Supercapacitor and Solar Cell Applications

용액 공정법에 의해 제조된 전도성 고분자 박막의 화학 센서, 초고용량 커패시터 및 태양전지 분야의 전극 물질에의 응용

指導敎授: 張 正 植

이 論文을 工學博士 學位論文으로 提出함

2014年 11月

서울大學校 大學院

化學生物工學部

曺 城 熏

曺城熏의 工學博士 學位論文을 認准함

2014年 11月

委 員 長 _____ (인)

副委員長 _____ (인)

委 員 _____ (인)

委 員 _____ (인)

委 員 _____ (인)

Conducting Polymer Thin Films via Solution Process as Electrode Materials for Chemical Sensor, Supercapacitor and Solar Cell Applications

by

Sunghun Cho

Submitted to the Graduate School of Seoul National University

in Partial Fulfillment of the Requirements

for the Degree of Doctor of Philosophy

February, 2015

Thesis Adviser: Jyongsik Jang

ABSTRACT

Thin films consisting of conducting polymer nanostructures provide a larger surface-to-volume ratio for charge-carrier transport as compared to their bulky counterparts. Thus, a facile and inexpensive fabrication technique for conducting polymers on the basis of solution processing, which offer a reproducible control of thickness and morphological homogenity, is an attractive option for various applications including solar cells, sensors, and capacitors.

This dissertation describes various ways in the synthetic methodology of high-performance conducting polymer thin films using solution processes in the viewpoint of shape-controlled nanomaterials, organic solvent-dispersible, and water-dispersible conducting polymer nanostructures. Firstly, the shaped-controlled PANI nanomaterials, such as nanofibers (NFs), nanorods (NRs), and nanoparticles (NPs), could be prepared by adjusting the amount of the oxidizing agent and the monomer during chemical oxidation polymerization to identify the optimal shape of PANI to detect dimethyl methylphosphonate (DMMP). Porous polyaniline/camphorsulfonic acid (PANI/CSA) nanostructures were fabricated by introducing thermally decomposing

compounds into a solution of PANI/CSA dissolved in a *m*-cresol/chloroform co-solvent. The porous PANI/CSA thin films were employed as electrode materials in both supercapacitor and dye-sensitized solar cell (DSSC). In order to create water-dispersible conducting polymer nanostructures, poly(4-styrenesulfonic acid) (PSS) has been used a binding agent and a charge-balancing counterion for polyaniline (PANI) and poly(3,4-ethylenedioxythiophene) (PEDOT). The PSS allowed homogeneous dispersion and successful incorporation of various materials, such as palladium (II) chloride ($PdCl_2$), ruthenium (IV) oxide (RuO_2), and graphene sheets, into the conducting polymers. Pd NPs-decorated porous P(ANI-*co*-ASA):PSS nanostructure was prepared in aqueous solution, and exhibited high H_2 sensitivity. PSS-doped PANI/graphene nanocomposite was fabricated by incorporating PSS-coated graphenes into the PANI doped with PSS having different molecular weight (M_w), and as-prepared nanocomposites successfully detected hydrogen sulfide (H_2S) even at low gas concentration. A ternary nanostructure composed of RuO_2 NPs-decorated PEDOT:PSS/graphene was highly dispered in water, and the nanostructure could be formed as a patterned electrode with high conductivity and electrochemical properties for use a

supercapacitor via a screen-printing method.

The procedure described herein provides a facile, cost-effective, and new means for producing high-performance thin films with improved electrical and electrochemical properties via solution processes, and these novel approaches can be used for fabricating electrode materials in sensors, supercapacitors, and solar cells.

KEYWORDS: conducting polymers; thin film; solution process; electrode material; polyaniline; poly (3,4-ethylenedioxythiophene) ; poly(4-styrenesulfonic acid)

STUDENT NUMBER: 2010–22823

List of Abbreviations

AAPH : 2,2´-Azobis(2-amidinopropane) dihydrochloride

AB : ammonium bicarbonate

AFM : atomic force micrograph

AIBN : azoisobutyronitrile

ANI : aniline

APS : ammonium persulfate

ASA : aniline-2-sulfonic acid

BET : Brunauer–Emmett–Teller

BPO : benzoyl peroxide

CB : conduction band

CCl_4 : carbon tetrachloride

CE : counter electrode

$CHCl_3$: chloroform

CH_3OH : methanol

C_2H_5OH : ethanol

$C_4H_{10}O$: diethyl ether

CNT : carbon nanotube

CO_2 : carbon dioxide

CPNT : carboxylated polypyrrole nanotube

CSA : camphorsulfonic acid

CV : cyclic voltammogram

Da : Dalton

DBSA : dodecylbenzenesulfonic acid

DLS : dynamic light scattering

DMF : *N*,*N*-dimethyl formamide

DMSO : dimethyl sulfoxide

DMMP : dimethyl methylphosphonate

DP : degree of polymerization

DSSC : dye-sensitized solar cell

EB : emeraldine base

EDOT : 3,4-ethylenedioxythiophene

EDLC : electric double layer capacitor

EIS : electrochemical impedance spectra

EG : ethylene glycol

ES : emeraldine salt

$FeCl_3$: ferric (III) chloride

$Fe(OTs)_3$: iron(III) toluenesulfonate

FE-SEM : field emission scanning electron micrograph

FF : fill factor

FT-IR : Fourier-transform infrared

FTO : fluorine-doped tin oxide

GO : graphene oxide

GPC : gel permeation chromatography

H_2 : hydrogen

H_2O : water

H_2O_2 : hydrogen peroxide

H_2S : hydrogen sulfide

H_2SO_4 : sulfuric acid

HCl : hydrogen chloride

IPA : isopropanol

IPCE : incident photon-to-electron conversion efficiency

ITO : indium tin oxide

I–*V* : current–voltage

J_{sc} : short-circuit photocurrent density

$K_2S_2O_8$: potassium persulfate

$KMnO_4$: potassium permanganate (99.3%)

LB : leucomeraldine base

$m_{APS}/m_{aniline}$: molar ratio of ammonium persulfate to aniline

MDL : minimum detection limit

MFC : mass flow controller

MnO_2 : manganese (IV) oxide

M_n : number-average molecular weight

M_w : weight-average molecular weight

N_2 : nitrogen

N_2H_4 : hydrazine

NaCl : sodium chloride

$NaNO_3$: sodium nitrate

NC : nanocrystal

NCS : nanocrystalline semiconductor

NH_3 :ammonia

NH_4OH : ammonium hydroxide

NF : nanofiber

NMP : *N*-methylpyrrolidone

NP : nanoparticle

NR : nanorod

NT : nanotube

NW : nanowire

O_2 : oxygen

OLED : organic light-emitting diodes

OPV : organic photovoltaic

P_2O_5 : phosphorus pentoxide

PA : polyacetylene

PADPA : *p*-amino diphenylamine

PANI : polyaniline

PB : pernigraniline base

PC : polycarbonate

PCE : power conversion efficiency

Pd : palladium

$PdCl_2$: palladium (II) chloride

PEDOT : poly(3,4-ethylenedioxythiophene)

PET : poly(ethylene terephthalate)

PI : polyimide

PMMA : poly(methyl methacrylate)

ppb : parts per billion

ppm : parts per million

PPP : poly(*p*-phenylene)

PS : pernigraniline salt

PSS : poly(4-styrenesulfonic acid)

PT : polythiophene

Pt : platinum

PPV : poly(*p*-phenylene vinylene)

PPy : polypyrrole

QD : quantum dot

RGO : reduced graphene oxide

$RuCl_3$: Ruthenium (III) chloride

RuO_2 : ruthenium (IV) oxide

sccm : standard cubic centimeters per minute

slm : standard liters per minute

SSDP : self-stabilized dispersion polymerization

TCO : transparent conductive oxide

TEM : transmission electron micrograph

THF : tetrahydrofuran

TiO_2 : titanium dioxide

Torr : 1⁄760 of a standard atmosphere

UV/VIS/NIR : ultraviolet/visible/near-Infrared

VB : valance band

V_2O_5 : vanadium (V) oxide

VOC : volatile organic compound

V_{oc} : open-circuit voltage

w_{PSS}/w_{ANI} : weight ratio of aniline to PSS

XPS: X-ray photoelectron spectroscopy

XRD : X-ray diffractogram

δ_h : hydrogen bonding interaction parameter

δ_p : polarity interaction parameter

$\Delta R/R_0$: normalized resistance change

工學博士學位論文

Conducting Polymer Thin Films via Solution Process as Electrode Materials for Chemical Sensor, Supercapacitor and Solar Cell Applications

용액 공정법에 의해 제조된 전도성 고분자 박막의 화학 센서, 초고용량 커패시터 및 태양전지 분야의 전극 물질에의 응용

2015年 2月

서울大學校 大學院

化學生物工學部

曺 城 熏

Table of Contents

1. INTRODUCTION

1.1. Background

1.1.1. Conducting polymers

Since the discovery of polyacetylene (PA) and its high electrical conductivity upon doping in 1977, a variety of conducting polymers, such as polyaniline (PANI), poly(3,4-ethylenedioxythiophene) (PEDOT), polypyrrole (PPy), polythiophene (PT), poly(*p*-phenylene) (PPP), and poly(*p*-phenylene vinylene) (PPV) have attracted considerable attention as important electronic materials due to low cost, ease of synthesis, high electrical conductivity, and good environmental stability (Figure 1) [1–5]. In general, the common feature of conducting polymers is the π-conjugated systems consisting of carbon p_z orbitals and alternating single (σ bond) and double (π bond) bonds, and these polyconjugated systems provide the electric conductivity after doping with appropriate dopants. The doping refers to the process of producing charge carriers in order to achieve electrical conductivity by removing electrons from valance band (VB) (*p*-type doping) or adding electrons into the conduction band (CB) (*n*-type doping) (Figure 2a and b, respectively) [4,6]. Most conducting polymers discussed above are synthesized from chemical oxidative polymerization, which is referred to as the *p*-type doping (Figure 2c). In the doping process, a radical cation is partially delocalized over polymer segment,

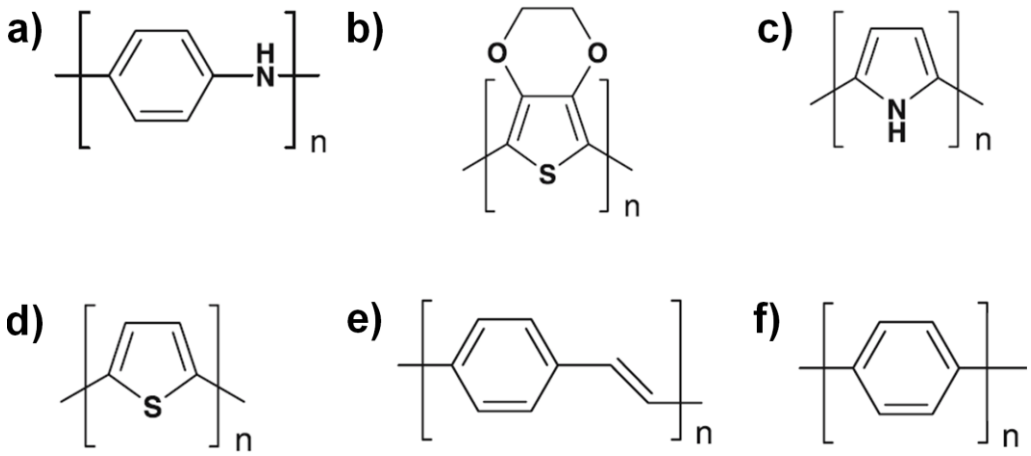

Figure 1. Several typical conducting polymers: (a) polyaniline (PANI), (b) poly(3,4-dioxythiophene) (PEDOT), (c) polypyrrole (PPy), (d) polythiophene (PT), (e) poly(phenylene vinylene) (PPV), and (f) poly(*p*-phenylene) (PPP) [4].

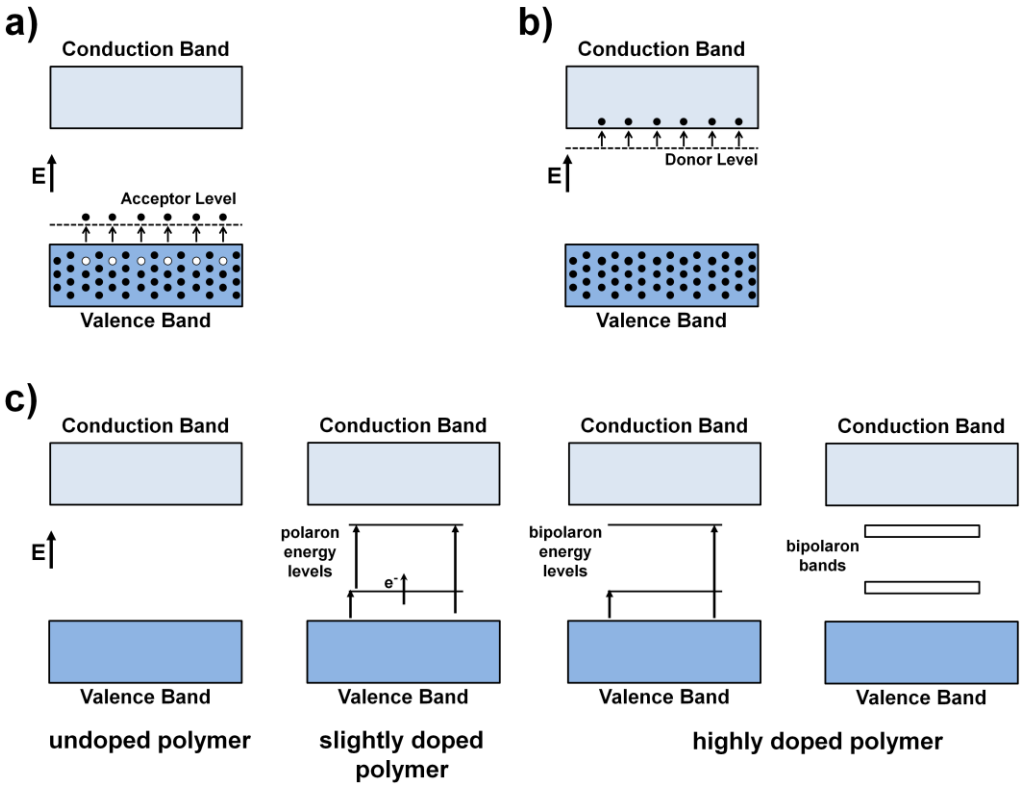

Figure 2. Illustration of energy levels of (a) *p*-type doping and (b) *n*-type doping. (c) Illustration of energy levels and allowed transitions of polarons and bipolarons during doping process.

which is called a polaron. The polaron represents a destabilized bonding orbital having higher energy than the energies in the VB. The next step is followed by the formation of a dication (bipolaron), which is related to a strong local lattice distortion and presence of two localized energy states in the gap. The overlap between the bipolaron states results in the formation of two wide bipolaron bands in the gap. These polaron and bipolaron became mobile and they can move along the polymer chain, resulting in the electron delocalization of π-conjugated structure [4]. As a consequence, the doping and dedoping processes in conducting polymers are reversible by the addition and removal of dopants, respectively. The unique conduction mechanism of conducting polymers has led to substantial efforts to prepare conducting polymers for various practical applications, such as sensors, supercapacitors, solar cells, organic light-emitting diodes (OLEDs), electrostatic coatings, and electrochromic devices [1,3,7−11]. However, many of the potential uses for conducting polymers are still unexplored due to a number of limitations, including poor solubility, low processability, mechanical properties, and crystallinity, which need to be overcome.

1.1.1.1. PANI

Since the conductive states of polyaniline (PANI) have been demonstrated by Macdiarmid and co-workers, PANI has attracted a great deal of interest due to its unique redox behavior, simple doping/dedoping, good environmental stability, facile synthesis, and lower synthetic cost compared to other conducting polymers [1−3,7,8,12]. Chemical oxidation polymerization of PANI has usually been conducted in an acidic condition (Figure 3) [2,3]. In the first step, aniline monomers are protonated by the addition of protonic acids and change into radical cations (Figure 3a). In the next step, a *para*-radical cation is coupled with a *N*-radical cation to form a *p*-amino diphenylamine (PADPA) unit (Figure 3b). The PADPA unit is oxidized after the addition of oxidizing agents, and usually forms the fully oxidized pernigraniline salt (PS) structure because of the high oxidizing power of the oxidant including ammonium persulfate (APS) (Figure 3c). During the oxidation of PANI, the predominant head-to-tail coupling and the minor tail-to-tail coupling occur in the *para*- and *ortho*-positions, respectively, which lead to conjugation defects in the final product. After all the oxidants are consumed, the unreacted aniline monomers reduce the PS form to produce the half-oxidized emeraldine salt (ES) form as the final product. In the final step of PANI synthesis, the PANI ES is formed and the ES form can be converted to the emeraldine base (EB)

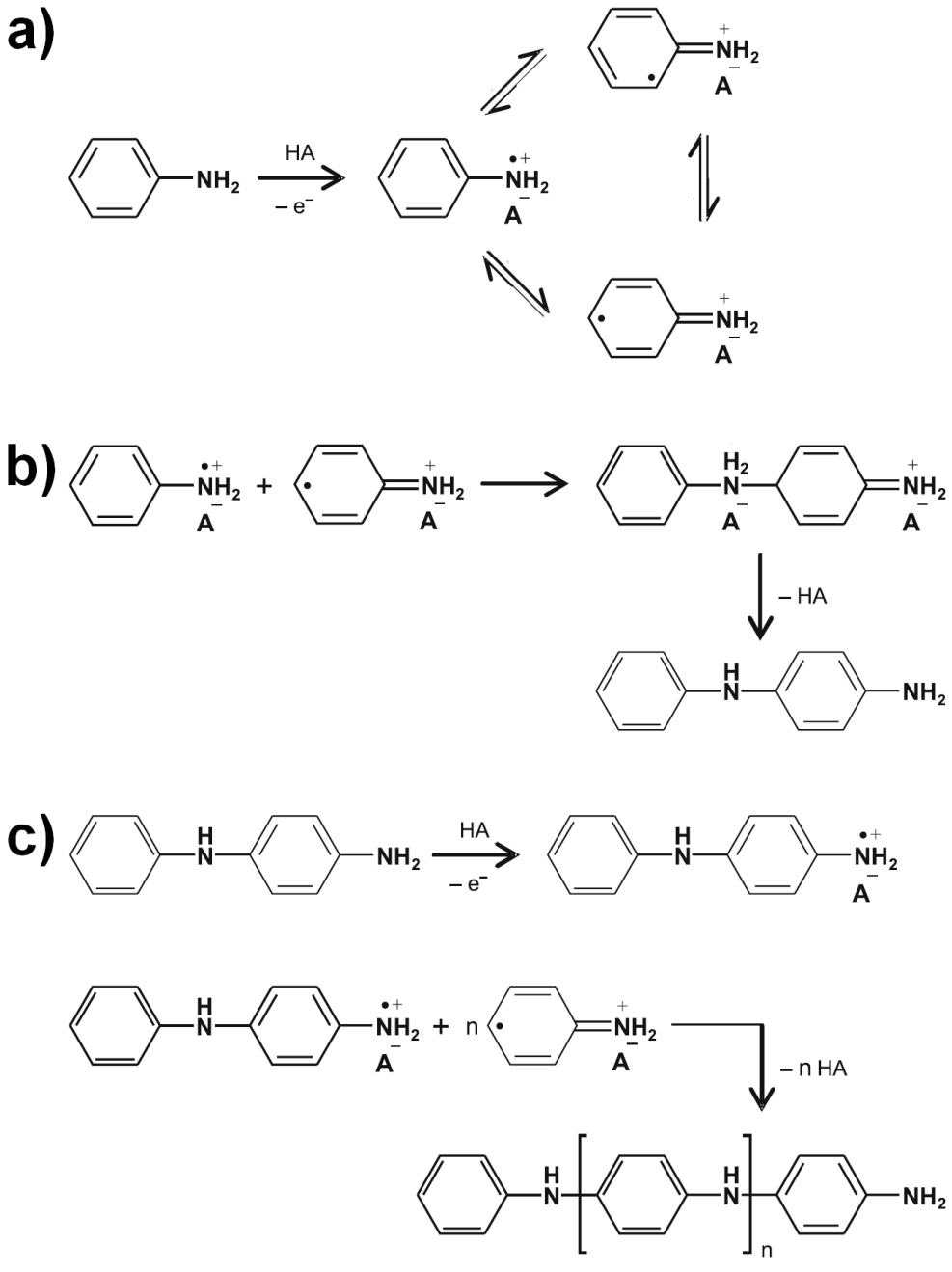

Figure 3. Polymerization mechanism of aniline: (a) oxidation of aniline, (b) radical coupling, and (c) chain propagation [2,3].

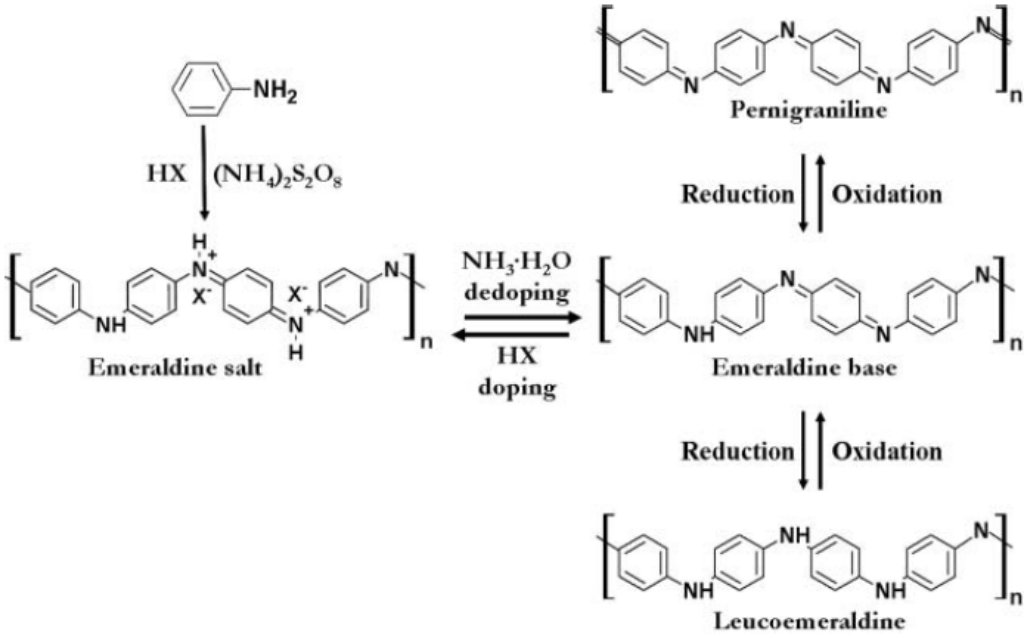

Figure 4. The reversible acid/base doping/dedoping and different oxidation states of PANI [12].

form by the addition of reducing agents such as ammonium hydroxide (NH_4OH). The PANI EB can change into two insulating forms of PANI with different colors such as the completely reduced lecomeraldine base (LB) and completely oxidized pernigraniline base (PB) depending on the oxidation states (Figure 4) [12]. These unique molecular structures and redox behaviors of PANI can be useful for numerous practical applications in bio/chemical sensors, supercapacitors, lithium-ion (Li^+) batteries, antistatic/conductive coatings, and electrochromic devices [1,3,7,8,11,12].

1.1.1.2. PEDOT

Poly(3,4-ethylenedioxythiophene) (PEDOT), which is a polythiophene (PT) derivative, has received great attention as one of the most outstainding conducting polymers for practical fields due to its numerous advantages including a small bandgap, good optical properties, and better electrical conductivity compared to other conducting polymers [1,3,9,10]. PEDOT can be prepared by using both electrochemical and chemical oxidation polymerization methods. However, PEDOT obtained by the electrochemical polymerization usually suffers from poor optical transparency and small sample sizes despite the enhanced electrical conductivity. Therefore, the chemical oxidation polymerization is regarded as the most promising approach

for preparing high quality PEDOT. The chemical oxidation polymerization of EDOT monomers into a PEDOT is shown in Figure 5 [9,10]. In the first step, oxidants, such as ferric (III) chloride ($FeCl_3$) or iron(III) toluenesulfonate ($Fe(OTs)_3$), react with the EDOT monomers to produce radical cations (Figure 5a). After pairs of the radical cations dimerize, the anions of oxidant scavenge two protons to stabilize the dimer (Figure 5b and c). The oxidant further oxidizes the dimers, and chain growth proceeds as a step polymerization (Figure 5d). The stepwise reactions are repeated continuously to form PEDOT with doped state (Figure 5e). Some of the positively charged thiophene rings can be stabilized by the anions in a PEDOT structure, which have orginated from the oxidants (Figure 5f). Among the various forms of PEDOT, poly(3,4-ethylenedioxythiophene):poly(4-styrenesulfonic acid) (PEDOT:PSS) has shown significant promise to meet the needs of competing properties, such as low surface resistances and high optical transparency. Thus, the PEDOT:PSS has been widely applied for a variety of applications in OLEDs, electrostatic coatings, solar cells, electrochromic devices, chemical sensors, and thermoelectric devices [3,9,13−28].

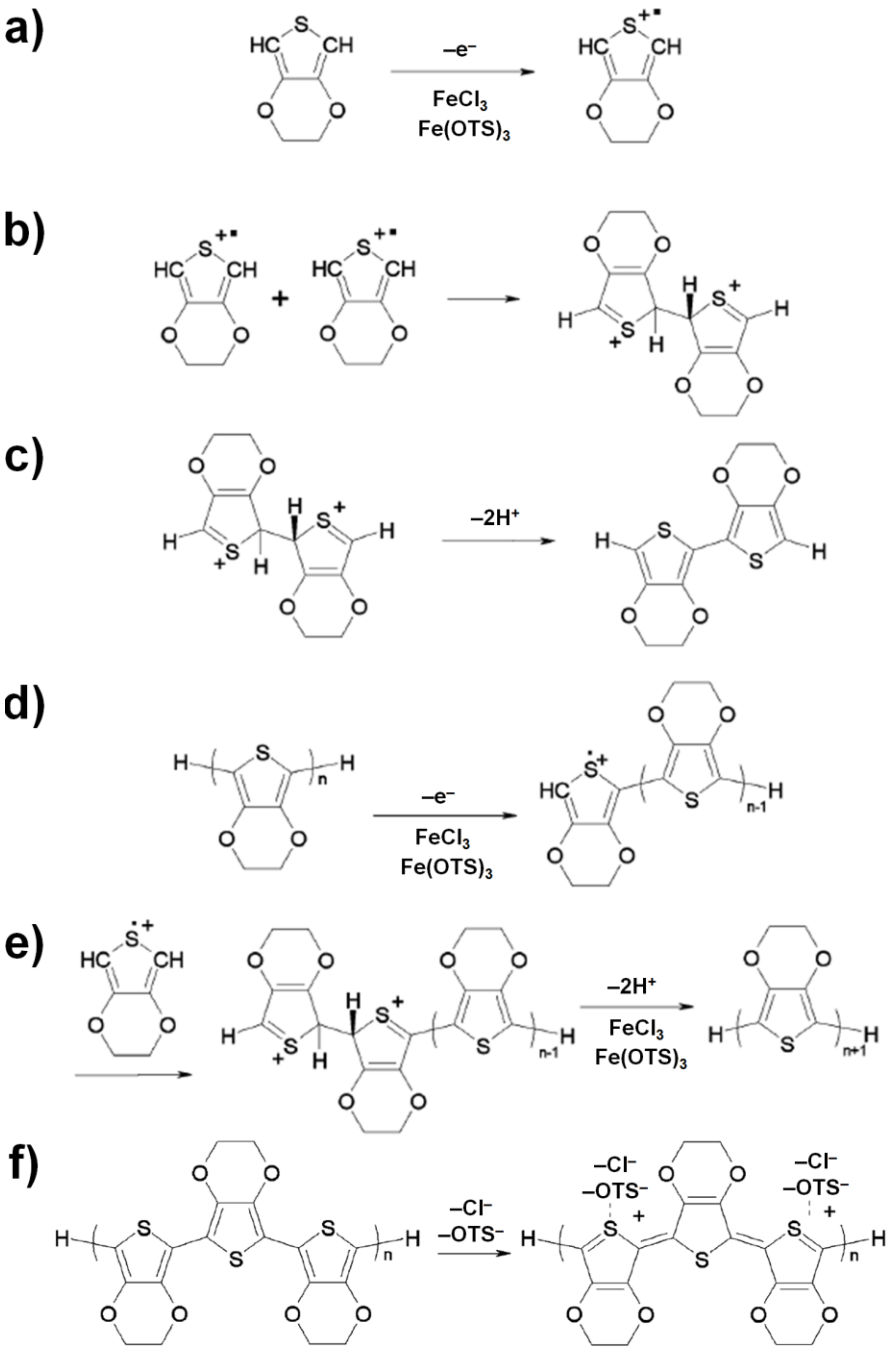

Figure 5. Polymerization mechanism of EDOT [10].

1.1.1.3. Conducting polymer nanomaterials

With the advancement of science and technology, there has been a growing interest in nanostructured materials in the range of 1 to 100 nm due to their unusual properties of nanomaterials, such as optical, electrical, mechanical, and chemical performances [3,11]. These properties of nanomaterials arose from the quantum-confinement effect owing to their discrete or quantized electronic levels. In the last decades, a variety of nanomaterials, including carbon nanotubes (CNTs), inorganic semiconductor nanocrystals (NCs), catalysts/magnetic nanoparticles (NPs), and quantum dots (QDs) have been intensively studied by a number of groups. However, the preparation of conducting polymer nanomaterials has been unexploited relatively. In comparison with their larger-scale counterparts, conducting polymer nanomaterials have superior chemical and physical properties derived from higher surface areas and smaller dimensions. Such advantages of conducting polymer nanomaterials have intrigued chemists and physicists for decades. The charge-transport properties of conducting polymer nanomaterials, including doping level, oxidation level, and conjugation length, are highly influenced by their shapes, e.g., nanofibers (NFs), nanorods (NRs), nanotubes (NTs), or nanoparticles (NPs) (Figure 6) [3,11,12,29−34]. Much work, such as hard template, soft template, and template-free methods, has been done to establish

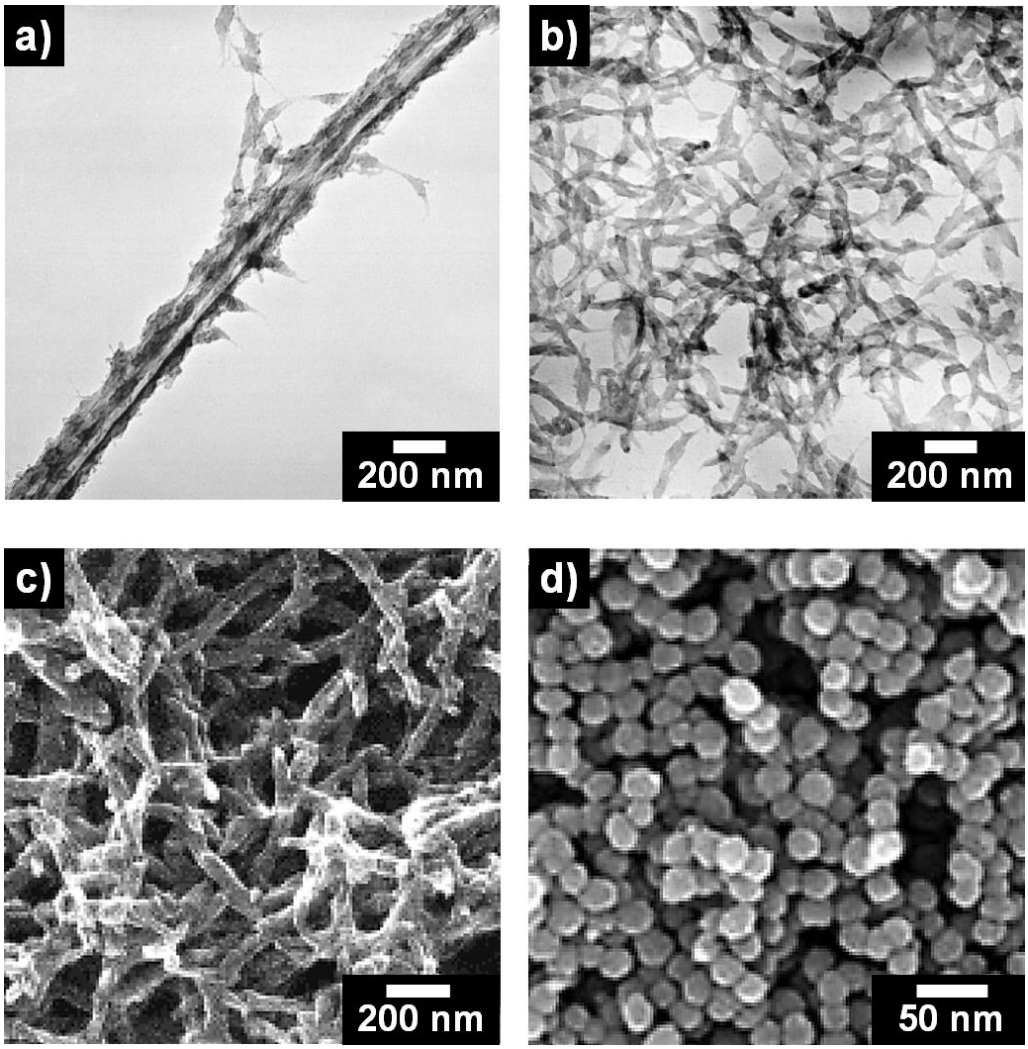

Figure 6. Conducting polymer nanomaterials with different shapes: (a) PEDOT NTs and (b) PEDOT NRs [29]. (c) PANI NFs [30] and (d) PPy NPs [34].

synthetic routes for controlling the shape of conducting polymer nanomaterials. Although various shapes of conducting polymers could be achieved by using the template-assisted methods, there are several problems associated with their use as electrode materials in energy and environmental applications. Firstly, it is difficult to remove either hard or soft templates completely from the reaction medium. Furthermore, the remnant templates may also reduce the electric properties of conducting polymers [35,36]. According to the template-free system, the formation of conducting polymers is highly affected by the amounts of monomers, doping agents, and oxidizing agents used. Although the effects of the oxidizing agent/monomer ratio on the conductivity of polymers have been reported, optimizing synthetic conditions for specifically shaped conducting polymer nanomaterials is still a challenge [37]. Thus, the optimized amounts of monomers, doping agents, and oxidizing agents are important factors to obtain high-quality conducting polymer nanomaterials with high conductivity and desirable shapes.

1.1.2. Conducting polymer solutions

Solution processable, conductive polymers, have been widely investigated as electrode materials because they provide a facile and inexpensive way to form thin-film electrodes [15,38]. These conducting polymer solutions can be

categorized into two different types: organic solvent-dispersible and water-dispersible conducting polymers. Polyaniline-camphorsulfonic acid (PANI/CSA) [39−42] can be readily cast as high conductive thin-films from the *m*-cresol/chloroform *co*-solvent system through the strong hydrogen bonds between the CSA, *m*-cresol, and chloroform ($CHCl_3$). PSS-based conducting polymers, such as polyethylene(3,4-dioxythiophene):poly(4-styrenesulfonate) (PEDOT:PSS) [13−28], and polyaniline:poly(4-styrenesulfonate) (PANI:PSS) [33,43−46] form as dimensionally stable and free-standing thin-films from the aqueous solutions through the electrostatic interactions between the positively charged PEDOT, PANI, and negatively charged PSS anions. With these advantages of conducting polymer solutions, various kinds of functional materials, such as graphene, carbon nanotubes (CNTs), and metal oxides, have been incorporated into solution-processed conducting polymers to integrate the useful properties of conducting polymers and their derivatives in nanocomposites [8].

1.1.2.1. Fabrication of conducting polymer thin-films

Several deposition methods of the conducting polymer solutions, such as drop casting, spin-coating, dip-coating, inkjet-printing, screen-printing, and electrospray deposition, have been utilized to realize high-performance

conducting polymer thin-films [5,33,45−48]. Drop casting is the simplest method for preparing conducting polymer thin films by dropping and drying conducting polymer solutions on a substrate. However, the resulting thin-film prepared by using this process is not usually uniform. In comparison to the drop casting method, the spin coating method ensures more accurate thickness control and uniform coating of the samples, which is closely associated with stable and reliable properties of the resulting thin-films. Spin-coating is a simple method for preparing thin-films by spreading the conducting polymer solution a rotating substrate. In this process, the thickness of the conducting polymer thin films can be adjusted by varying concentration of the solution and rotating rate of the substrate. Recently, printing processes, such as inkjet-printing and screen-printing, provide a simple, effective way to obtain desired patterns of conducting materials having various shapes and sizes. The inkjet-printing method is a type of computer printing, and creates specific patterns by propelling droplets of the conducting polymer solutions in the ink catridge onto paper or flexible plastic substrate. Jang *et* al. reported the water-dispersible PANI:PSS nanoparticles with a diameter of *ca.* 28 nm for inkjet-printed sensors [33]. In the screen-printing method, the conducting polymer solutions can be transferred onto both rigid and flexible substrates, such as poly(ethylene terephthalate) (PET), polycarbonate (PC), poly(methyl methacrylate) (PMMA),

polyimide (PI), and glass, through a screen mask which contains the desired patterns [45−48]. The PEDOT:PSS has been manufactured by Kodak and Heraeus as a conducting ink for the screen-printing process. Despite such significant improvements in conducting polymers for the printing processes, both inkjet- and screen-printing methods require sophisticated synthetic procedures for preparing conducting inks satisfying specific conditions in terms of solubility, viscosity, and chemical compatibility with substrate materials.

1.1.2.2. Interfacial polymerization method

Conventional PANI has been synthesized according to the MacDiarmid et al., which includes the chemical oxidation of aniline in an acidic medium [1–3,5,7]. In the conventional method, the polymerization of aniline randomly occurs at the interfaces of growing PANI, swollen PANI, and aqueous medium, which making the obtaibned PANI to be vurnerable to the *ortho*-coupling and Michael reductive reactions. To prepare high-performance PANI without the undesirable reactions, an attempt to polymerize aniline in a biphasic solvent system composed of aqueous and organic phases (distilled water/chloroform phase) (Figure 7) [30,40,41]. According to Kaner et al., the PANI preferentially forms as nanofibers in a distilled water/chloroform interface system and the

secondary growth of PANI leading to agglomerated PANI nanorods and nanoparticles could be minimized (Figure 7a) [30]. Therefore, the aqueous/organic interface system has become one of the effective ways to suppress the undesirable side reactions during the polymerization of aniline. Lee *et* al. reported that the protonated anilinium ions serve as self-stabilizers to form charge-stabilized colloidal particles spontaneously in an aqueous phase, while the organic phases effectively separate insoluble oligomers and grown PANI chains in the aqueous phase (Figure 7b) [40,41]. Furthermore, Lee and *co*-workers conducted the polymerization of aniline at lower temperature (−40 °C) than the conventional methods, allowing the lower defects and higher conductivity than the samples prepared using conventional interfacial polymerization methods. Thus, the modified aqueous/organic system is called the "self-stabilized dispersion polymerization (SSDP)." The PANI samples prepared by using the SSDP method are grown radially, promoting the successive couplings of *para*-mode on benzene rings of aniline monomers. This enhanced *para*-directed polymerization is related to the high quality PANI nanostructures with lower defects and improved charge transports compared to the PANI samples obtained by using the conventional methods. Thus, the SSDP method has been combined with the secondary doping process to form highly conductive thin-films having conductivity up to 1000 S cm^{-1} [40].

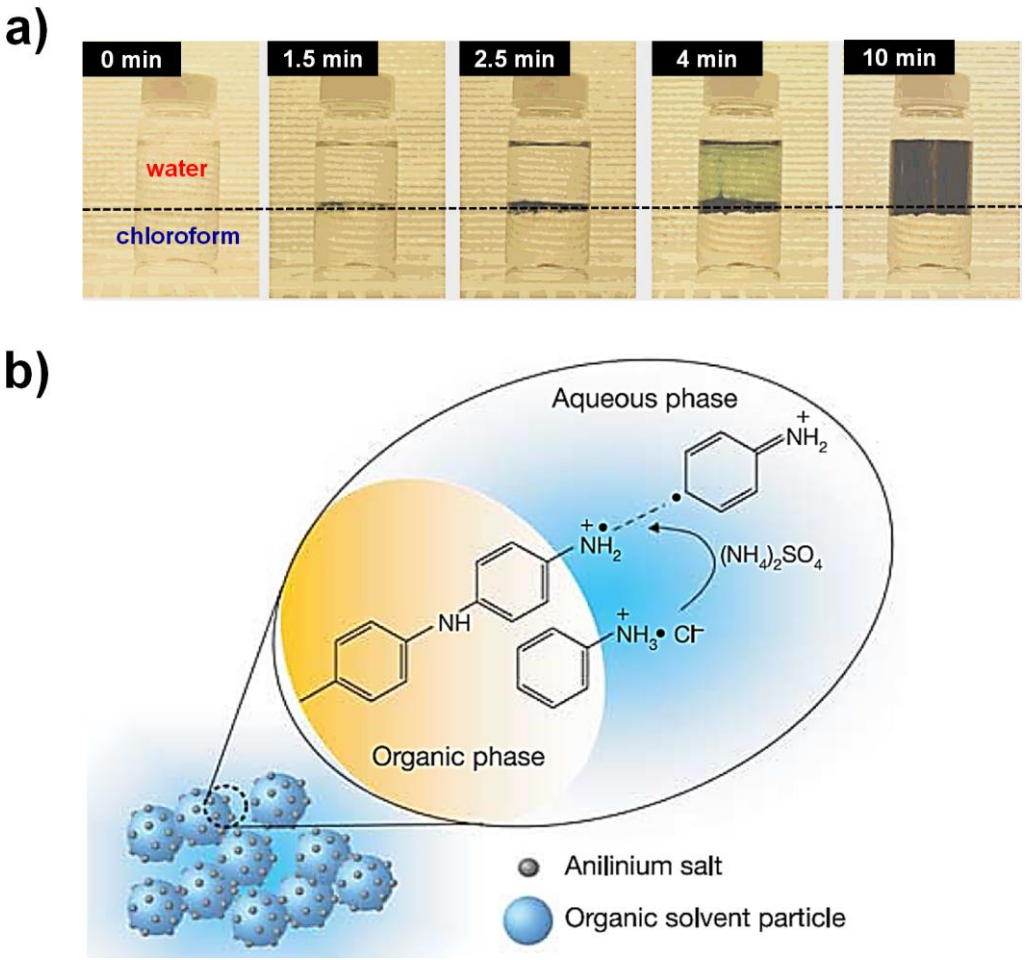

Figure 7. (a) Snapshots showing interfacial polymerization of aniline in a water/chloroform system with different reaction times from 0 to 10 min. The top layer is an aqueous solution of 1.0 M perchloric acid and ammonium peroxydisulfate; the bottom layer is aniline dissolved in the organic solvent chloroform [30]. (b) Diagram of the self-stabilized dispersion polymerization of PANI [41].

1.1.2.3. Secondary doping method

Since the mechanism of secondary doping using organic acids with big counter ions, such as dodecylbenzenesulfonic acid (DBSA) and camphorsulfonic acid (CSA), has been proposed by MacDiarmid and co-workers in 1994, various work on improving conductivity of the secondarily doped PANI have been discussed [39−42]. In general, these DBSA and CSA are known to change the structure of PANI from a compact coil structure to an expanded coil structure, resulting in the increased linear conformation of PANI chains and reduced π-conjugation defects in the PANI backbone (Figure 8a). Accordingly, the secondary doping of aniline has become an effective way to the increase the intra- and inter-molecular components of the conductivity of PANI [39]. Furthermore, these secondarily doped aniline monomers are known to have good compatibility with the *m*-cresol/chloroform *co*-solvent system because of strong hydrogen interactions between the sulfonic acid group (−SO_3H) of CSA, hydroxyl group (−OH) of *m*-cresol, and the hydrogen (−H) of chloroform (Figure 8b) [39−41]. Accordingly, the polymerization of CSA-doped aniline has usually been carried out in the *m*-cresol/chloroform biphasic solvent system to achieve highly conductive PANI thin-films. Compared to conventional PANI electrodes, electrodes generated from PANI/CSA solution boast two or three orders of magnitude greater conductivity. In addition, PANI/

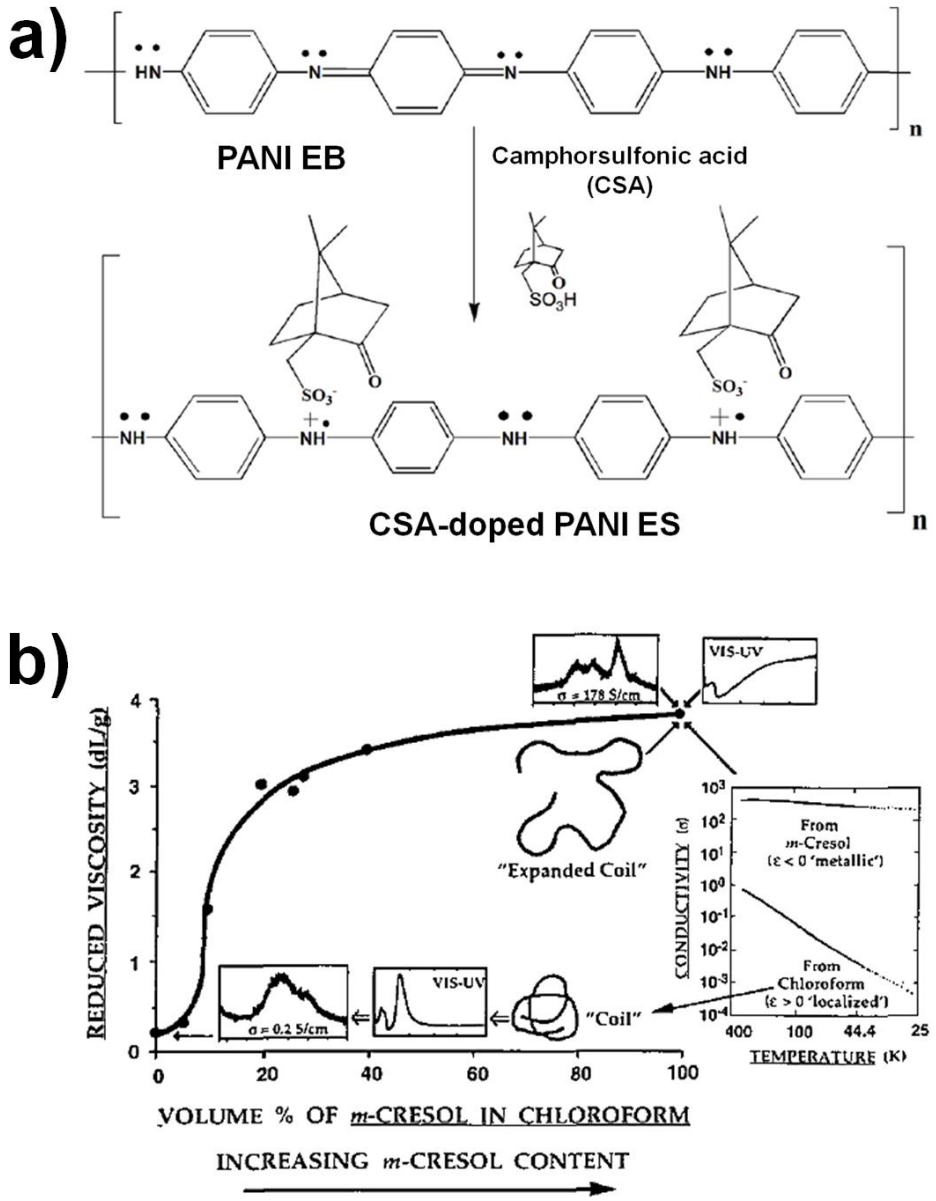

Figure 8. (a) Chemical structure of PANI/CSA [42]. (b) Inter-relationships between viscosity of PANI doped with CSA in solutions of $CHCl_3$ and *m*-cresol of increasing *m*-cresol content, and electronic spectra, conductivity, dielectric constant and X-ray diffraction spectra of free-standing films [39].

CSA films deposited from solution adhere well to various substrates, including glass, metal, flexible plastic, and silicon, without any further treatment to ease their formation. While PANI/CSA appears to overcome the limitations of conventional PANI, the low surface area of PANI/CSA films limits their applicability in supercapacitors, solar cells, and Li-ion batteries. Electro-catalytic activity depends on the degree of contact between the electrode and electrolyte, and increases with increasing surface area of the electrode in most energy and environmental devices [49,50]. Thus, new approaches for enlarging the contact surface areas of the solution-processable PANI/CSA electrodes are highly desirable.

1.1.2.4. PSS-based conducting polymers

Poly(4-styrenesulfonic acid) (PSS), a water-soluble and polymeric acid, has been widely used to obtain the water-dispersible and free-standing conducting polymer thin films due to its excellent ion exchange properties [9,13−28,41,43−46]. The PSS, which consists of hydrophilic sulfonate groups ($-SO_3^-$) and insulating matrices, act as both a binding agent and a charge-balancing counterion for conducting polymers, facilitating the dispersion of conducting polymer segments. As a water-dispersible polymeric binder, PSS possesses a high viscosity; this viscosity can be tuned by controlling the

molecular weight (M_w) or monomer concentration of PSS [45]. Moreover, PSS possesses sufficient $-SO_3^-$ groups, which enable uniform anchoring and good dispersion of various materials through electrostatic repulsion interactions [27,51]. The PSS preferentially aligns the EDOT and ANI monomers during the polymerization reactions, resulting in the head-to-tail polymerizations of the corresponding EDOT and ANI monomers. For these reasons, the PSS has become one of the most effective ionomers for the preparation of highly conductive, ductile, and dimensionally stable thin-film electrodes.

1.1.2.4.1. PANI:PSS

PANI:PSS, which is highly dispersible with water, has become an attractive PEDOT:PSS replacement due to its relatively lower synthetic cost, facile synthesis, tunable oxidation states with different colors, and simple doping/dedoping processes. Such properties made the PANI:PSS an attractive electrode material for chemical sensors, electrochromics, and OLEDs [33,43−46]. In the conventional synthetic procedure of water-dispersible PANI:PSS, the protonated aniline monomers electrostatically interact with the negatively charged $-SO_3^-$ groups of PSS, and the polymerization of the aniline monomers is carried out by the addition of ammonium persulfate (APS) used as an oxidizing agent (Figure 9) [33]. In addition, the PSS provides both

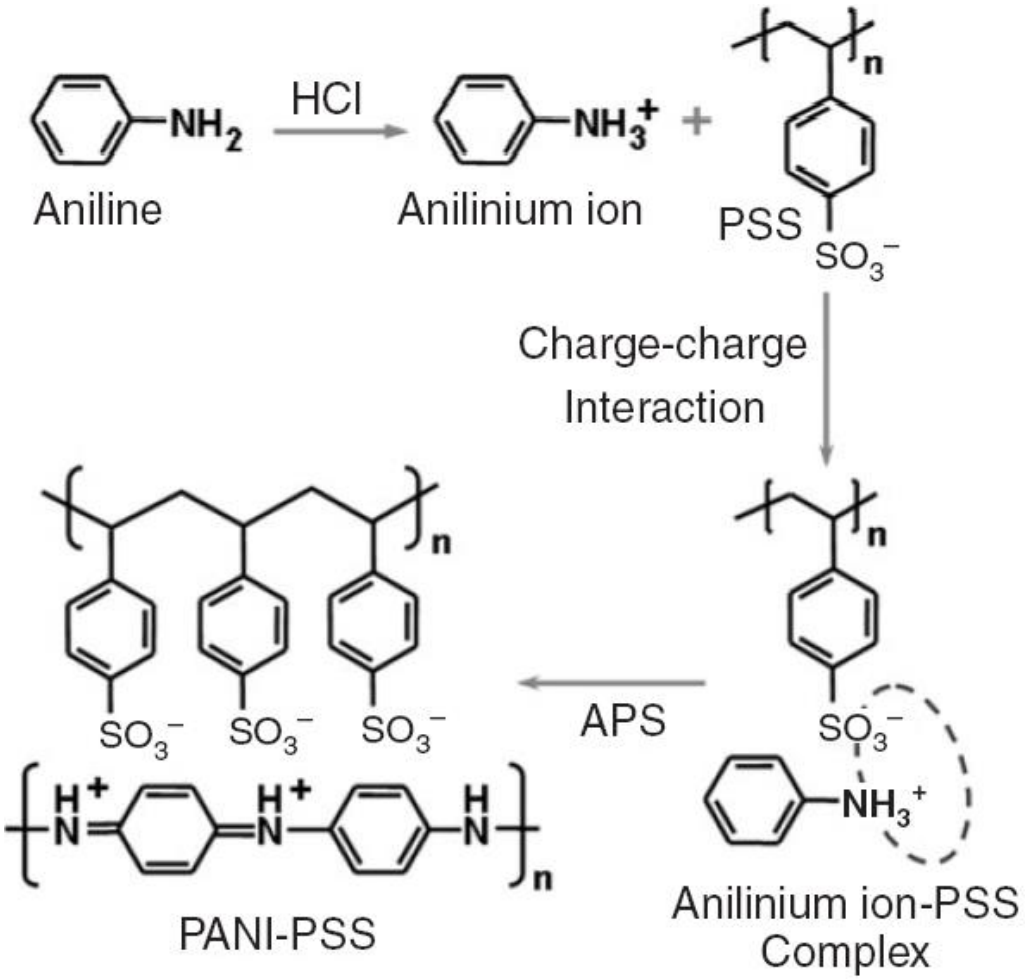

Figure 9. Synthetic procedure for production of water-dispersible PANI:PSS [33].

protons for doping aniline monomers and counter ions that compensate the protonated PANI structure. Therefore, the PSS has been also suggested as an efficient replacement for hydrogen chloride (HCl) as a dopant. However, the ability of a polymeric acid to donate protons is much lower than that of HCl due to their polymeric counter ions [46,52−54]. As a result, charge transport in PANI that has been doped with PSS typically insufficient for most practical applications as electrode materials. Hence, more effective synthetic approaches of the PANI:PSS are needed to improve the electrical and electrochemical properties of the electrode materials.

1.1.2.4.2. PEDOT:PSS

PEDOT:PSS, which consists of cationic PEDOT segments and PSS counter anions, has been proposed to improve the processability of conventional PEDOT powders from aqueous solution (Figure 10). The PEDOT:PSS has become the most commercially available conducting polymer due to its relatively higher conductivity and better optical properties than other conducting polymers [9,13−28]. Various organic compounds with high dielectric constants, such as dimethyl sulfoxide (DMSO), ethylene glycol (EG), tetrahydrofuran (THF), sorbitol, *N*-methylpyrrolidone (NMP), isopropanol (IPA), and *N*,*N*-dimethyl formamide (DMF), increase the conductivity of

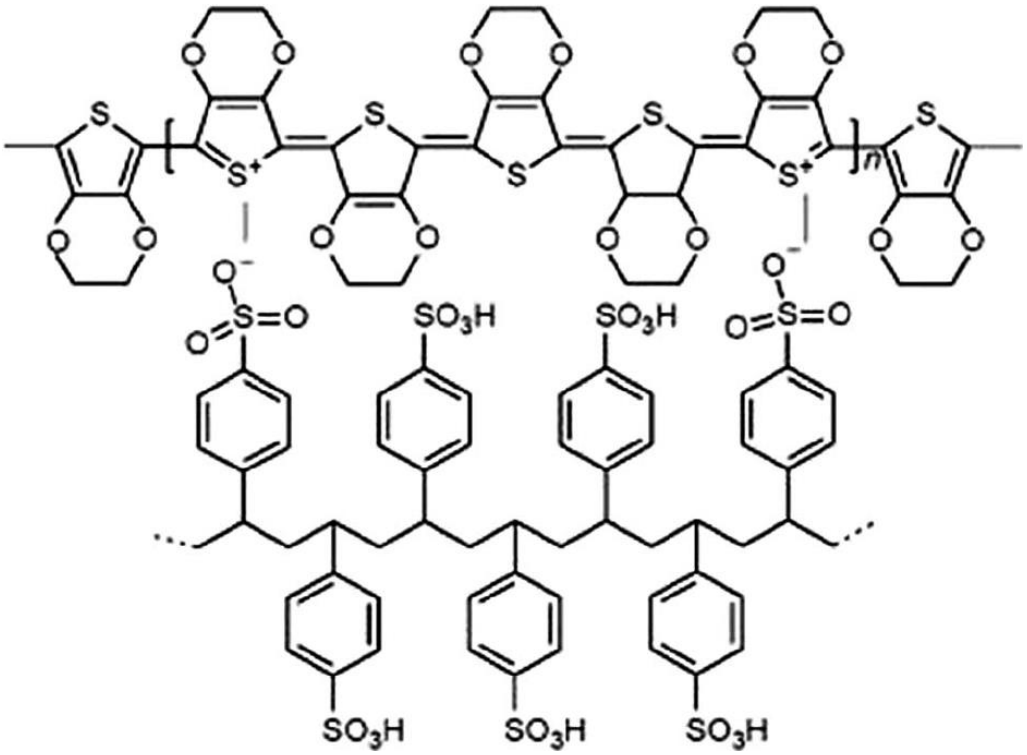

Figure 10. Chemical structure of PEDOT:PSS [28].

PEDOT:PSS by several orders of magnitude (up to ~10^3 S cm^{-1}) by reducing the ionic interactions between positively charged PEDOT and negatively charged PSS [14−16,18−20,25,26]. Due to their high conductivity, PEDOT:PSS thin films have been considered for use as the cathode material in supercapacitors [55−57]. But despite their high conductivity, conducting polymers, including PEDOT:PSS, usually suffer from a low capacitance because only a fractional number of electrons are obtainable from the monomer units of the polymer [58]. Recently, screen-printing has provided a simple, effective way to obtain defined patterns of conducting materials having various shapes and sizes [45,47,48]. In general, conducting inks for screen-printing require a relatively high viscosity (~10^3 centipoise, cp) to achieve good adhesion between the patterns and the substrate. Despite the high conductivity of PEDOT:PSS, most PEDOT:PSS solutions usually have viscosities of less than 10^2 cp to facilitate transparent thin-film formation [48]. Although the PSS is a promising material for optimizing the viscosity of PEDOT:PSS solutions for screen-printing, an excess of polymeric binders significantly lowers the conductivity of PEDOT:PSS-based electrodes due to their insulating properties [59]. Hence, the preparation of PEDOT:PSS inks for fabricating screen-printed electrodes having both high conductivity (>10^3 S cm^{-1}) and optimized viscosity (>10^3 cp) still poses a challenge.

1.1.2.5. Conducting polymer/graphene nanocomposites

Graphene, consisting of sp^2-hybrid carbon atoms with a honeycomb crystal structure, is a promising candidate as a next generation electrode material due to its high charge transfer ability, thermal conductivity, mechanical strength, and flexibility [60,61]. Graphene oxide (GO) that can be readily produced by simple oxidation and exfoliation of graphite is dispersible in water and electrically insulating due to the loss of electronic conjugation brought about during the oxidation, while reduced graphene oxide (RGO) deoxygenated by chemical, thermal, electrochemical, electromagnetic flash, and laser-scribe techniques, is electrically conductive and intensively explored in various applications (Figure 11). However, the reduction of water-dispersible GO results in a gradual decrease in its hydrophilic characteristics, and thus RGO becomes irreversible agglomerated and precipitated [51]. Recently, a number of researchers are focusing on chemical and physical combination of conducting polymers and graphene in order to integrate the redox behaviors of conducting polymers and electron-conduction of graphene [8,21,27,45,47,57, 63−68]. However, the drawback of the conducting polymer/graphene binary electrode system is the relatively high interfacial resistance between the graphene and conducting polymers, which leads to a low charge-transfer kinetics. Thus, a homogeneous dispersion of RGO in both aqueous and organic

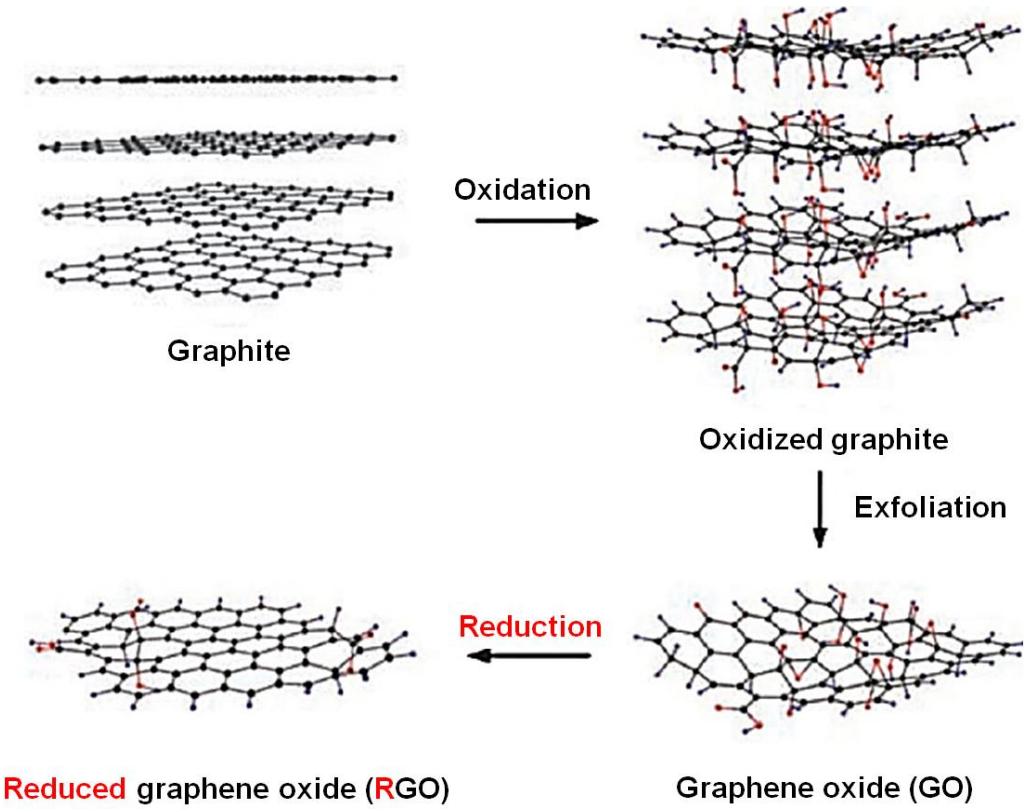

Figure 11. Overall procedures for production of GO and RGO [61].

phases is essential for incorporating graphene into conducting polymers. Ruoff et al. demonstrated that the homogeneous suspensions of RGO could be readily produced in optimized co-solvent systems, which are made of *N*,*N*-dimethyl formamide (DMF), dimethyl sulfoxide (DMSO), and water (H_2O) [62]. According to Hansen's equation, the DMF/H_2O co-solvent system further mixed with DMSO provide appropriate hydrogen bonding (δ_h) and polarity interaction (δ_p) parameters, which are related to good colloidal dispersion of the RGO in the co-solvent systems [69]. Furthermore, several papers have reported the formation of a stable dispersion of RGO in aqueous solutions through electrostatic repulsion interactions between the $-SO_3^-$ groups of PSS and RGO [27,51]. The improved dispersion of graphene sheets in the conducting polymer solution may induce strong π–π stacking interactions between the conducting polymers and the basal planes of the graphene sheets, thereby resulting in extended π-conjugation within the conducting polymer structure (Figure 12) [21,63−66]. As a consequence, these synergetic effects significantly enhance the charge-transport properties, such as redox behavior and charge-transfer ability, of conducting polymer/graphene nanocomposites.

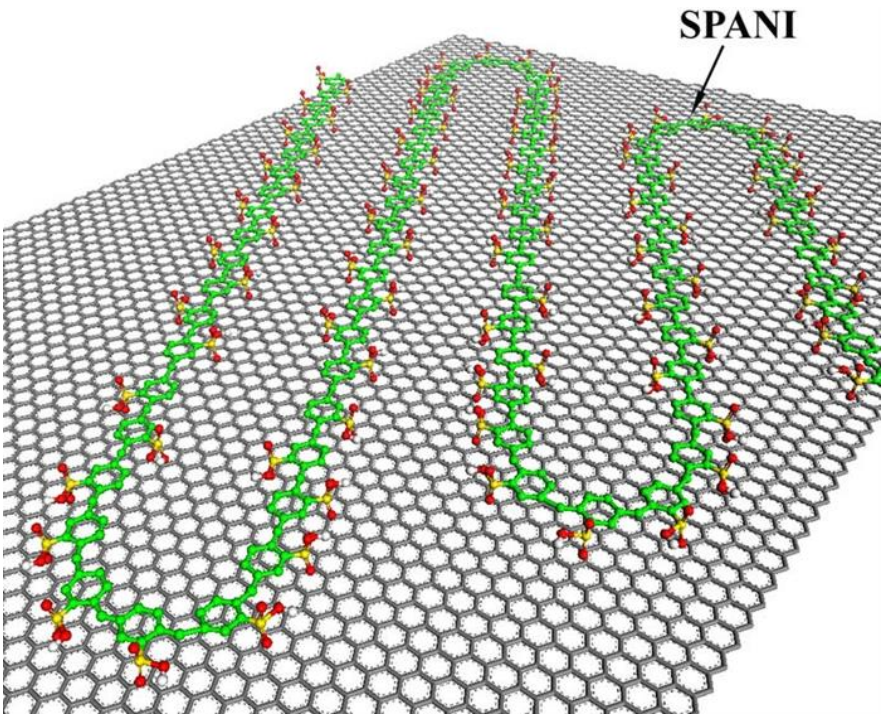

Figure 12. Illustration of π–π stacking interactions between PANI and graphene sheets.

1.1.3. Applicaion Fields

Conductive polymer thin-films have shown several beneficial characteristics including tunable film thicknesses, flexibility, and high processability from solution [3,9−28,33,39−46]. The thin films of conducting polymers provides a large ratio of charge carriers to volume of active layer and morphological homogeneity at the nanoscale, which leads to enhanced charge transports in the π-conjugated system of conducting polymers [3,11]. These advantages have opened up many possibilities for energy and environmental applications of conducting polymer thin-films in the fields of dye-sensitized solar cells (DSSCs), organic photovoltaics (OPVs), OLEDs, antistatic/conductive coatings, and sensors [3,5,7−11,67,68,70−73] Furthermore, they have been studied as potential replacements for metals and transparent conductive oxide (TCO) films such as indium tin oxide (ITO) and fluorine-doped tin oxide (FTO) [15,19]. While TCO films may crack after repeated bending, thin films of solution-processed, conductive polymers are seldom affected by repeated bending.

1.1.3.1. Sensors

Conducting polymers thin-films have offered great possibility as attractive sensing elements for detection of various analytes due to their special

conduction mechanism, reversible doping/dedoping process, tunable chemical and electrochemical properties [3,5,11,29−33,74]. Most of all, the oxidation states of conducting polymers is readily adjusted by simple doping/dedoping processes, which allow a sensitive and rapid response to specific chemical species (Figure 13). Furthermore, conducting polymer sensors can achieve low minimum detection limit (MDL) level, rapid response, and short recovery times for some analytes, while the sensors made of metal oxides and carbon materials usually suffer from relatively high operation temperature in order to achieve high sensing performance [3,5,11]. Especially, the conducting polymers of nanometer sizes offer greater surface areas and smaller dimensions than their conventional bulky counterparts, which permit enhanced interactions of chemical species with the conducting polymers [3,11]. Thus, extensive studies on the conducting polymer thin-films based on PANI, PEDOT, and PPy nanomaterials have been perform to fabricate sensing elements for the highly sensitive and selective recognition of both chemical and biological species [3,5,11,29−33,74]. Numerous groups have employed PANI nanofibers as the chemical sensor for the detection of hydrogen (H_2), hydrogen chloride (HCl), hydrogen peroxide (H_2O_2), carbon dioxide (CO_2), ammonia (NH_3), and hydrazine (N_2H_4) [5,30−32]. Jang et al. fabricated the PEDOT nanotubes via chemical oxidation polymerization in reverse (water-in-oil) microemulsions

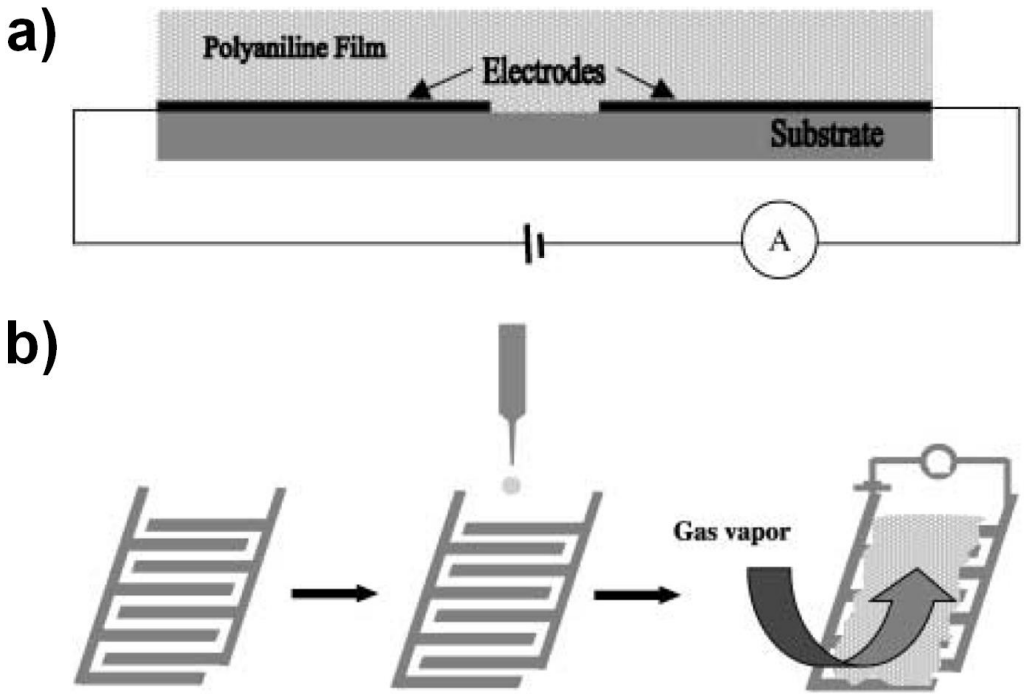

Figure 13. (a) A schematic diagram of a polyaniline chemiresistor consisting of a PANI film, electrodes, substrate and the electronic components needed to monitor current flowing through the resistor. (b) Schematic diagram showing a typical sensor experiment: gold interdigitated electrodes (left) are coated with a PANI film by drop-casting (middle), and the resistance of the film is monitored as the sensor is exposed to vapor (right) [31].

and investigated its sensitivity to various volatile organic compounds (VOCs) including ethanol (C_2H_5OH), methanol (CH_3OH), diethyl ether ($C_4H_{10}O$), triethylamine, acetonitrile, carbon tetrachloride (CCl_4), and chloroform ($CHCl_3$) [29]. Moreover, carboxylated PPy nanotubes (CPNTs) exhibited amplified sensitivity and real time response upon exposure to anti-cancer agents, ordants, and proteins [11,74]. Nevertherless, it is still challenging to fabricate the high-performance thin-film sensors based on the conducting polymer nanomaterials because of the following difficulties that need to be overcome: 1) Larger surface areas of the conducting polymers are required to permit sufficient interactions between the analytes and conducting polymers ; 2) In general, the conducting polymer thin-films have relatively lower conductivity compared with the carbon materials and metal oxides, indicating that only limited electric currents can be conducted at the sensor electrode.

1.1.3.2. Supercapacitors

Supercapacitor is an energy device that store and release energy through electrostatic separation between electrolyte ions and electrodes. The Supercapacitors can be divided into two categories: electric double layer capacitor (EDLCs) and pseudocapacitors. The EDLCs, such as graphene and CNTs, store the energy through ion adsorption, while the psuedocapacitors,

including conducting polymers and metal oxides, store the energy through fast redox reactions between the electrolyte and the electrode materials [70−72] (Figure 14). The psedocapacitors can store a greater amount of capacitance per gram than the EDLC because of the fast redox reactions. On the other hand, the EDLC provides higher power capabilities than the pseudocapacitor due to its rapid sorption and desorption of ions at the surface layer of the carbon. From the view point of electrode materials, the conducting polymers are generally attractive candidates for the electrode materials owing to their high conductivity, reversible and fast redox reactions, and relatively lower cost compared with the metal oxides. Moreover, the conducting polymer thin-films made of nanomaterials are expected to exhibit enhanced capacitance in comparison to bulky conducting polymers because of their advantages arising from their nanoscale size: 1) larger specific surface area ; 2) shorter path lengths for the transport of ions ; 3) light weight and large ratio of specific discharge power to weight [70]. However, the conducting polymers often start to degrade under less than a thousand cycles because of the changes in their physical structures that are caused by the doping/dedoping process of ions [71]. Therefore, the conducting polymer nanomaterials, including PANI, PEDOT, PPy, and PT, have usually been incorporated into metal oxides and carbon materials to realize the high-performance supercapacitors [8,55,63,

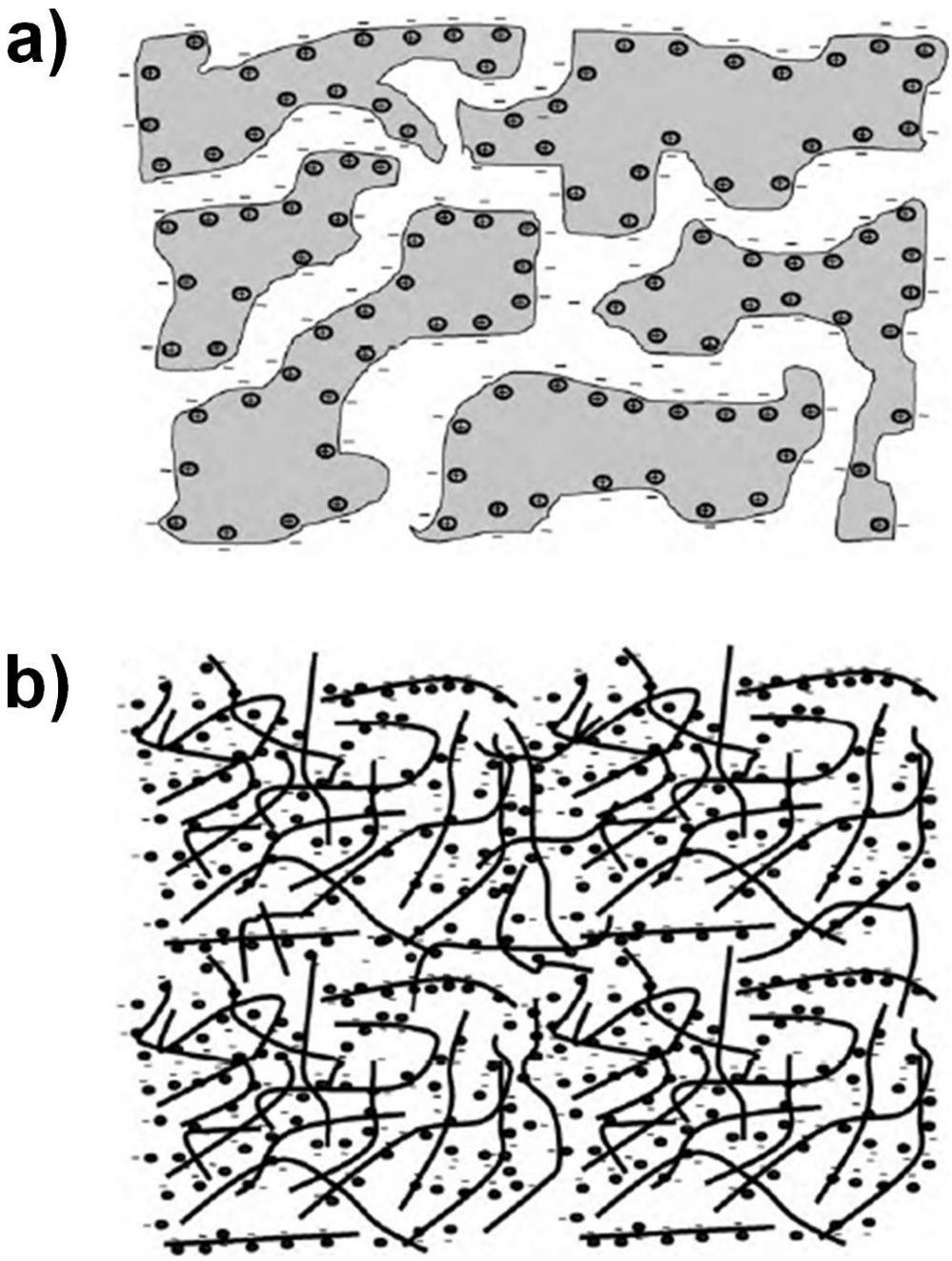

Figure 14. Comparison of charging of (a) EDLC (carbon) and (b) pseudocapacitor (conducting polymer) [71].

65,66,70−72,75]. In these hybrid materials, the conducting polymer nanomaterials can interact synergetically with other components to form an electrode better than either material alone. The metal oxides, such as ruthenium (IV) oxide (RuO_2), manganese (IV) oxide (MnO_2), and vanadium (V) oxide (V_2O_5) enhance the energy storage capacity of conducting polymers, while the conducting polymers facilitate fast charge/discharge of the metal oxides and prevents them from agglomerating, collapsing, and breaking. Lee and co-workers fabricated the MnO_2 nanoparticles (NPs) enriched PEDOT nanowires (NWs) via the redox exchange of $KMnO_4$ with the sulfur sites on the PEDOT structures, and the resulting capacity of PEDOT NWs increased 4 times after loading of MnO_2 NPs [75]. In conducting polymer/graphene hybrid nanocomposites, the graphene sheets form strong π–π stacking interactions with the conducting polymers; this significantly enhances the charge-transport properties and capacitances of the electrode materials. Furthermore, graphene sheets possess better thermal and chemical stability than the conducting polymers, which eventually lead to improvement in the cycling stability of electrode materials [21,63−66].

1.1.3.3. DSSC

Dye-sensitized solar cells (DSSCs) have attracted interest over the past two decades due to their low cost, simple fabrication, and eco-friendliness [68,73,76−78]. In a conventional DSSC system, the device includes a nanocrystalline semiconductor (NCS) electrode, dye-sensitizer, redox electrolyte, and counter-electrode (CE) (Figure 15) [77]. To date, the best power conversion efficiency (PCE) of 12.3% has been obtained with liquid electrolyte-based DSSC [78] and various efforts have been made to enhance the overall performance of DSSCs, such as modifying the morphology of NCS [79,80] and the molecular structures of organic sensitizers [81,82] as well as using low-volatility electrolytes [78,83−85] and new CE materials [20,68,73,86−108]. One of the important issues for realizing the high-performance DSSCs is the development of CEs with high electro-catalytic activity and electrical conductivity to facilitate the reduction of triiodide ions (I_3^-) from iodide ions (I^-) in the redox electrolytes. Platinum (Pt)-coated transparent conductive oxides (TCOs), such as indium doped tin oxide (ITO) or fluorine-doped tin oxide (FTO), have generally been used as CEs in DSSCs due to the high electro-catalytic activity for triiodide reduction of Pt and high conductivity of TCOs. However, Pt-coated TCOs are expensive to produce and are incompatible with the I^-/I_3^- redox electrolyte [85,95]. Various CEs based

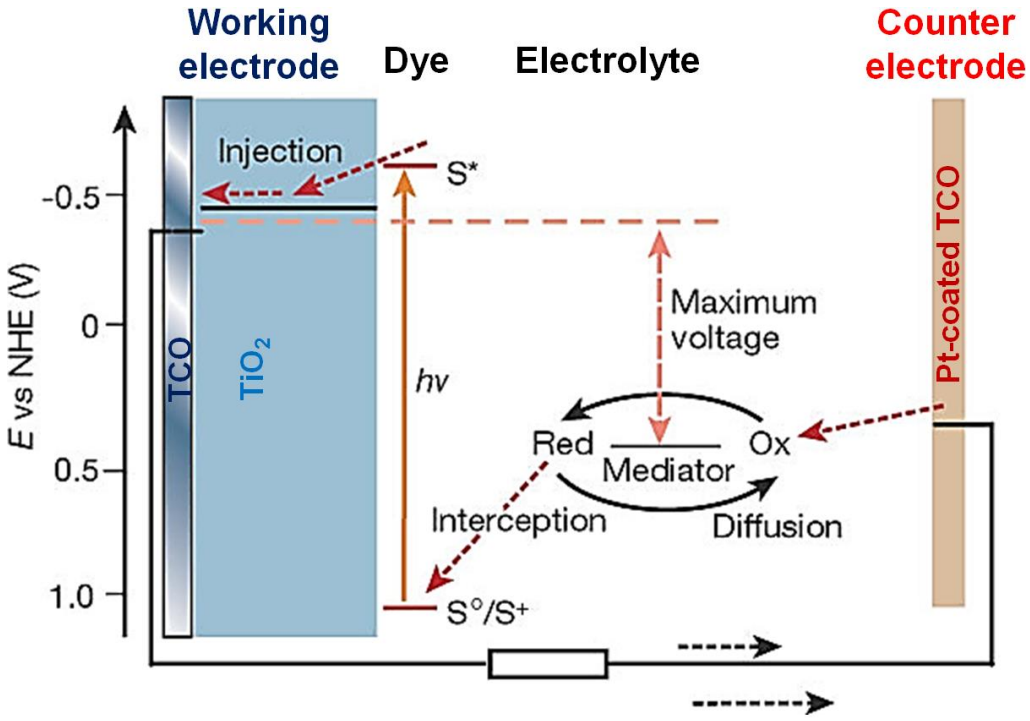

Figure 15. A schematic diagram of DSSC system [77].

on carbon materials [73,86−91], metals [73,92−94], conducting polymers [20,68,73,95−104], and hybrid-structured materials [68,73,105−108] have been made to substitute the Pt and TCO. Among these alternatives to Pt-coated TCOs, conducting polymers with excellent electrochemical activity and high electric conductivity have great potential to produce high-performance CEs because of their ease of thin-film formation from solution. Conducting polymers, such as poly(3,4-ethylenedioxythiphene) (PEDOT) [73,96−100], polyaniline (PANI) [68,101,102], and polypyrrole (PPy) [103,104], have been investigated as alternative materials for Pt CEs. However, the lower surface area of film-type conducting polymers compared to their carbon and inorganic counterparts has limited the performance of DSSCs. Thus, increasing the surface areas of thin-film type conducting polymers is desired to improve their electro-catalytic activity for used as the CEs in DSSCs.

1.2. Objectives and Outlines

1.2.1. Objectives

In the preceding section, the importance of solution-processed conducting polymer thin films as electrode materials for chemical sensor, supercapacitor, and solar cell applications was introduced from the viewpoint of academic research and practical applications. The aim of this dissertation is to present synthetic methodologies of high-performance conducting polymer thin films using solution processes in the viewpoint of shape-controlled nanomaterials, organic solvent-dispersible, and water-dispersible conducting polymer nanostructures. Furthermore, the morphological, spectroscopic, crystalline, electrical, and electrochemical properties of the conducting polymer thin films are systematically investigated, and their application fields are also explored, including chemical sensors, supercapacitors, and DSSCs.

1.2.2. Outlines

This dissertation involves the following subtopics:

I. Fabrication of shape-controlled PANI nanomaterials with different monomer-to-oxidant ratio for DMMP sensors
   1. Fabrication of shape-controlled PANI nanomaterials
   2. DMMP sensors based on PANI nanomaterials

II. Fabrication of organic solvent-dispersible porous PANI/CSA nanostructures and their applications

1. Fabrication of porous PANI/CSA nanostructures
2. Supercapacitors based on porous PANI/CSA as electrode materials
3. DSSCs based on porous PANI/CSA CEs

III. Fabrication of water-dispersible PSS-based conducing polymer nanocomposites and their applications

1. Fabrication of Pd NPs-decorated porous P(ANI-*co*-ASA):PSS for H_2 sensors
2. Fabrication of PSS-doped PANI/graphene for H_2S sensors
3. Fabrication of RuO_2 NPs-decorated PEDOT:PSS/graphene for screen-printable and flexible electrodes in supercapacitors

A detailed outline of the study is as follows:

1.1 Shape-designed PANI nanomaterials (NPs, NRs, and NFs) are prepared by adjusting the amount of the oxidizing agent and the monomer during chemical oxidation polymerization. The charge-transport properties of the precisely controlled PANI geometries at the nanometer scale were systematically investigated to identify the optimal sensing conditions to detect the nerve gas agent dimethyl methylphosphonate (DMMP). Intrinsically, the aspect ratio of PANI nanomaterials can change with the oxidation state, which is closely related to the doping level and conjugation length. Our results suggest that the transport behavior of the nanomaterials is highly dependent on their aspect ratios. Extrinsically, PANI nanomaterials deposited onto gold-interdigitated microelectrodes are able to form stable conductive channels by minimizing the contact resistance between the microelectrodes and the nanomaterials. High-performance chemiresistive sensors based on PANI nanomaterials were successfully fabricated and their sensing properties were demonstrated. The real-time response of a DMMP-sensor based on PANI NFs was better than that of sensors based on PANI NPs or NRs. High-performance chemiresistive sensors with a low minimum detection limit (MDL, 5 ppb) could be designed through comparative studies of charge-transport

properties.

2.1 Highly porous PANI/CSA thin films have been successfully fabricated by introducing thermally decomposing compounds such as benzoyl peroxide (BPO), azoisobutyronitrile (AIBN), and ammonium bicarbonate (AB) into a solution of PANI/CSA dissolved in a *m*-cresol/chloroform co-solvent. Such thin films have contained pores of 30−150 nm. The pore-forming reactions within the thin films only resulted in a small increase in the surface roughness of the samples, and thus provided higher electro-catalytic activity and sustainable conductivity relative to that of a pristine PANI thin film. These improvements were attributed to faster redox reactions at the PANI electrode/electrolyte interface. The PANI/CSA thin films were employed as electrode materials in a supercapacitor, with a maximum specific capacitance of 361 F g^{-1} at 0.25 A g−1, which is more than twice that of an equivalent electrode made with pristine PANI.

2.2 Porous PANI/CSA CEs for DSSCs were fabricated by secondary doping-based polymerization with different porogen decomposition. Porous nanostructures of PANI/CSA CEs were readily obtained *via* decomposition of embedded porogens, such as BPO and AIBN. The porous PANI/CSA CEs provided higher electro-catalytic performance than that of Pt-coated indium-doped tin oxide (ITO) CE due to the facilitated facile electron

exchange between the CEs and the redox electrolyte. They were successfully used as Pt- and TCO-free CEs in DSSCs, resulting in a power-conversion efficiency (PCE) of η = 6.23% and excellent efficiency of 101.0% compared to a DSSC with aonventional Pt-coated ITO CE (η_{Pt} = 6.17%).

3.1 Pd NPs-decorated porous P(ANI-*co*-ASA):PSS nanostructure was designed for the construction of high-performance H_2 gas sensors, and all the fabrication procedures used in the preparation of the Pd-decorated porous P(ANI-*co*-ASA):PSS nanostructure are water-based, providing a facile and inexpensive method to create thin-film H_2 sensors. Both co-monomers and PSS provide sufficient–SO_3H groups to effectively anchor palladium nanoparticles and lead to enhanced interactions with H_2 gas, while retaining the charge transport properties of the P(ANI-*co*-ASA):PSS. The pores were 10–30 nm in diameter and were readily formed on the Pd-decorated P(ANI-*co*-ASA):PSS surfaces by introducing AB as water-soluble porogen agents. The pores enlarged the surface area available for interaction with the H_2 gas molecules, resulting in much higher sensitivity compared with both the non-porous Pd-decorated P(ANI-*co*-ASA):PSS and the pristine P(ANI-*co*-ASA):PSS. A detection limit of 5 ppm for H_2 gas was achieved using the Pd-decorated porous P(ANI-*co*-ASA):PSS at room temperature.

3.2 PSS-doped PANI/graphene-based H_2S sensors were designed for obtaining the high-performance and mass-producible H_2S sensors from less acidic and aqueous solutions. PSS with a weight average molecular weight (M_w) of 1.96×10^6 was synthesized using low-temperature free-radical polymerization. The PSS was used as both a doping agent and a binding agent for the polymerization of aniline monomers in a biphasic system (water/chloroform) at −50℃. The high M_w of PSS resulted in relatively large particle sizes and smooth surfaces of the PSS-doped PANI. These physical characteristics, in turn, resulted in low interparticle resistance and high conductivity. In addition, the PSS allowed homogeneous dispersion of reduced graphene sheets through electrostatic repulsion. The prepared PSS-doped PANI/graphene solutions showed good compatibility with flexible PET substrates, making them suitable for flexible sensor electrodes. Changes in the charge-transport properties, such as protonation level, conjugation length, crystalline structure, and charge-transfer resistance, of the electrode materials were the main factors influencing the electrical and sensor performance of the PSS-doped PANI-based electrodes. PSS-doped PANI/graphene composites containing 30-wt% graphene showed the highest conductivity (168.4 S cm^{-1}) and the lowest minimum detection limit (MDL) for H_2S gas (1 ppm).

3.3 Ternary electrode system, composed of aqueous PEDOT:PSS, graphene, and hydrous RuO_2 NPs, has been fabricated using screen-printing method, and the screen-printed RuO_2 NPs-decorated PEDOT:PSS/graphene nanocomposites were employed as electrode materials in high-performance supercapacitors. As a polymeric binder, PSS allows stable dispersion of graphene and hydrous RuO_2 NPs in an aqueous PEDOT:PSS system through electrostatic stabilization, ensuring better utilization of the three components. Additional PSS molecules were added to optimize the solution viscosity to obtain screen-printed electrodes. The effects of graphene and hydrous RuO_2 NPs on the electrical and electrochemical properties of PEDOT:PSS were systematically investigated. The graphene sheets greatly enhanced the charge-transport properties, such as the doping level and conjugation length, through strong π–π stacking interactions with the PEDOT structure. The hydrous RuO_2 NPs anchored to the PEDOT:PSS/graphene surfaces facilitated redox reactions with the surrounding electrolyte, and significantly enhanced the specific capacitance of the electrode materials. The resulting RuO_2/PEDOT:PSS/graphene electrode with a thickness of ~5 μm exhibited high conductivity (1570 S cm^{-1}), large specific capacitance (820 F g^{-1}), high energy density (73 Wh kg^{-1}) and good cycling stability (81.5% after 1000 cycles).

2. EXPERIMENTAL DETAILS

2.1. Fabrication of shape-controlled PANI nanomaterials with different monomer-to-oxidant ratio for DMMP sensors

2.1.1. Fabrication of shape-controlled PANI nanomaterials

Materials: Aniline (99.0%) and ammonium persulfate (APS, 98.0%) were purchased from Sigma-Aldrich (St. Louis, MO, USA). Hydrochloric acid (HCl, 35.0–37.0%) was obtained from Samchun (Seoul, Korea). Distilled water was us−ed as the solvent for the polymerization of aniline.

Fabrication of shape-controlled PANI nanomaterials: PANI nanomaterials of three different shapes were synthesized by chemical oxidation polymerization. HCl (49 mmol), a dopant for aniline monomer, was added to distilled water (30 mL). Then, aniline (10 mmol) was added dropwise to the acidic solution and the solution vigorously stirred for 10 min. APS, an oxidizing agent, was chosen as the key variable to control the aspect ratio and charge-transport behavior of PANI nanomaterials. The amount of APS dissolved in the distilled water (10 mL) was adjusted from 1.2 to 20 mmol. Polymerization of aniline was initiated by pouring an APS solution into the aqueous anilinium ion solution at 25^{o}C for 1.5 h with vigorous stirring. PANI powders were isolated by filtration and washed with water, ethanol, and acetone.

Instrumentation: FE-SEM images of the PANI nanomaterials were obtained with a JSM-6701F microscope (JEOL, Tokyo, Japan). XPS traces of the PANI nanomaterials were recorded on an AXIS-HIs spectrometer (Kratos/Shimadzu, Kyoto, Japan). Electrical conductivity (defined as σ (S cm^{-1}) $= \frac{1}{\rho} = \frac{\ln 2}{\pi t}\left(\frac{1}{R}\right)$, where ρ is the static resistivity, R is the sheet resistivity, and t is the thickness of a pelletized PANI) of the PANI nanomaterials was measured using a four-point probe system (Mode systems Co, Korea) equipped with a current-source meter (Keithley 2400; Keithley Co., Cleveland, OH, USA) [111,112]. The CVs and *I–V* characteristics of the PANI nanomaterials were determined using a WBCS 3000 potentiostat (WonATech, Seoul, Korea). BET surface areas of the PANI nanomaterials were measured using a Micromeritics analyzer (ASAP 2000; Micromeritics Co., Norcross, GA, USA). UV/VIS/NIR and FT-IR spectra of the PANI nanomaterials were measured on Lambda 35 and Frontier FT-IR spectrometers (Perkin Elmer Inc., Waltham, MA, USA), respectively.

2.1.2. DMMP sensors based on PANI nanomaterials

Fabrication of PANI-based sensor devices: The photolithographic process was used to pattern a microarray consisting of 25 pairs of fingers onto a glass substrate. Each finger was 2 µm × 1 mm × 0.030 µm (width × length × height) with a 2 µm interfinger gap (Figure 16). Gold 20-nm-thick was deposited using

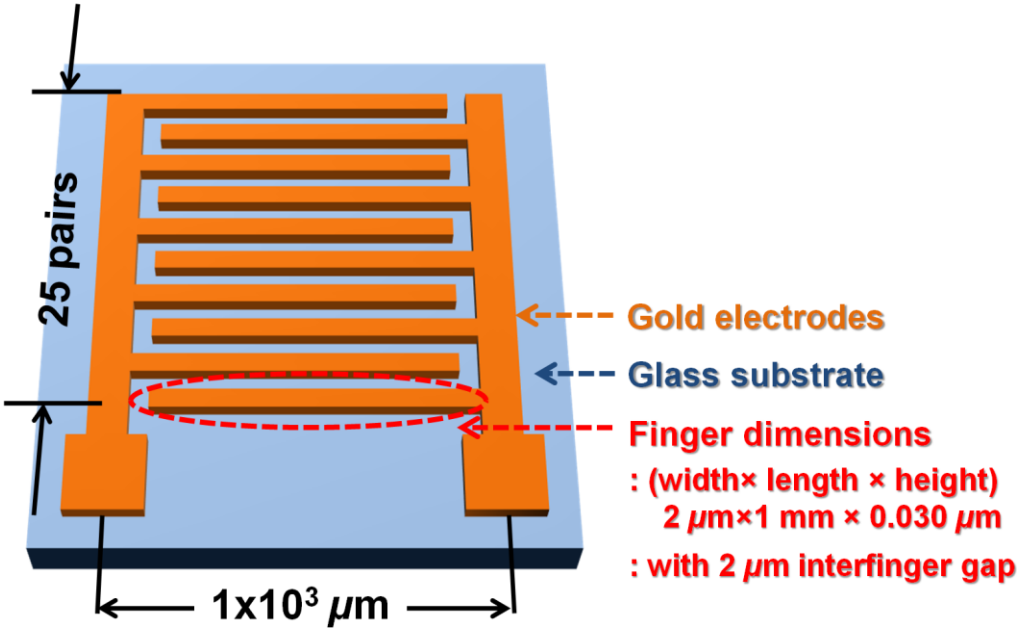

Figure 16. Schematic illustration of the interdigitated microelectrode used.

sputtering onto a 10-nm-thick Ti adhesion layer. PANI solutions (0.05 wt% in ethanol) were prepared by ultrasonication for deposition on the gold-interdigitated microelectrodes. Good dispersion of the PANI nanomaterials in the solution was necessary to reduce inter-material contact resistances. The ultrasonication treatment was carried out using an ultrasonic homogenizer (Autotune 750 W; Cole-Parmer Instruments, Vernon Hills, IL, USA) over 50 min at an ultrasonic intensity of 15 W cm^{-2}. The microelectrode substrates were cleaned using distilled water and ethanol, and subsequently 1 mL of the PANI solutions was dropped on the interdigitated microelectrodes. The microelectrodes were then dried at 25 ^{o}C in an inert atmosphere to remove ethanol. The PANI-based sensor devices were mounted in a 350 mL vacuum chamber with an electrical feed-through and a gas inlet and outlet; pressure was held at *ca.* 10 Torr. A N_2 stream passed through an external bubbler in a vessel containing the DMMP and then flowed into the vacuum chamber at a flow rate of 2000 sccm. DMMP vapor concentration was varied from 5 to 50,000 ppb by adjusting the ratio of N_2 gas to DMMP vapor. Cyclic DMMP/N_2 exposures were conducted using a MFC (KNH Instruments, Pucheon, Korea). The PANI nanomaterials were exposed to the DMMP vapor for 2 minutes, after which time the DMMP vapor was replaced by compressed N_2 for 2 minutes; this process was repeated several times. The resistance changes of the sensor

devices were monitored at room temperature using a current-source meter (Keithley 2400; Keithley Co., Cleveland, OH, USA).

Measurements of sensing performances: The normalized resistance change $\Delta R/R_0$ (defined as $\frac{\Delta R}{R} = \frac{R\text{-}R_0}{R_0}$, where R_0 is the initial resistance and R is the measured real-time resistance) was examined in real time at a constant applied current of 10^{-6} A to evaluate the sensitivity of the PANI nanomaterials upon exposure to the DMMP vapor [74]. The response time indicates the time required for the conductance to reach 90% of the equilibrium value after a test gas was injected. The recovery time is defined as the time necessary for a sensor to attain a conductance 10% above its original value in air [29].

2.2. Fabrication of organic solvent-dispersible porous PANI/CSA nanostructures and their applications

2.2.1. Fabrication of porous PANI/CSA nanostructures

Materials: Aniline (99.0%), ammonium persulfate (APS, 98.0%), camphorsulfonic acid (CSA, 98.0%), benzoyl peroxide (BPO), azoisobutyronitrile (AIBN), and ammonium bicarbonate (AB) were purchased from Sigma-Aldrich (St. Louis, MO, U.S.A.). Hydrochloric acid (HCl, 35.0−37.0%), chloroform ($CHCl_3$), and ammonia solution (NH_3) were acquired

from Samchun (Seoul, Korea). *m*-cresol was obtained from Tokyo Chemical Industry (Tokyo, Japan). Distilled water was used as the solvent for the polymerization of aniline.

Synthesis of porous PANI thin films for use as electrode materials: PANI ES powders were synthesized using a self-stabilized dispersion polymerization (SSDP) method based on chemical oxidation polymerization at −30 °C. HCl (0.1 mol) was introduced as a primary dopant into distilled water (30 mL) [40.41]. The aqueous anilinium ion solution was mixed with $CHCl_3$ (60 mL). Aniline monomer (21 mmol) was added drop-wise to the as-prepared solution. The polymerization of aniline was performed using APS (2.4 g) as an oxidizing agent for 8 h at −30°C. The overall reaction progressed at the interface between the aqueous phase and chloroform. After washing with water, ethanol, and acetone, precipitates of greenish PANI ES were obtained. The primary dopant of PANI ES was removed by adding 0.5 M NH_3 solution as a reducing agent. The products were washed with ethanol and acetone to obtain brownish PANI EB powders. Secondary doping of the PANI EB powders was conducted with CSA. PANI/CSA solutions, each containing a different porogen agent, were prepared by mixing secondary-doped PANI/CSA powders (0.04 g mL^{-1}) with either BPO (2–10 mg mL^{-1}), AIBN (2–10mg L^{-1}), or AB (2–10 mg mL^{-1}) in *m*-cresol/$CHCl_3$ (4:1, v/v) co-solvent. The *m*-cresol/$CHCl_3$ co-solvent solutions

were sonicated for 24 h to increase the solubility of PANI/CSA powders within the solutions. The resulting PANI/CSA solutions were fabricated as 10 μm thin films onto an area (1.5 cm^2) of non-conducting glass substrate using a spin-coater (PWM32, Headway Research Inc., USA) at 500 rpm for 10 s. Two drying steps were used to obtain porous PANI thin-film electrodes. The first drying step (40 ℃ for 12 h) was designed to evaporate the *m*-cresol solvent. The second drying step (100 ℃ for 3 h) was used to induce thermal decomposition of BPO, AIBN, or AB within the PANI thin-film electrode.

Instrumentation: Surface images of the PANI/CSA thin films were acquired using FE-SEM (JSM-6701F, JEOL, Japan) and AFM (Innova SPM, Vecco, U.S.A.). Electrical conductivity (defined as σ (S cm^{-1}) $= \frac{1}{\rho} = \frac{\ln 2}{\pi t}\left(\frac{1}{R}\right)$, where ρ is the static resistivity, R is the sheet resistivity, and t is the thickness of a thin film) of the PANI/CSA thin films were measured using a four-point probe system (Mode systems Co, Korea) equipped with a current-source meter (Keithley 2400; Keithley Co., Cleveland, OH, USA). XRDs of the PANI/CSA thin films were measured with a powder X-ray diffractometer (M18XHF-SRA, MAC Science Co., U.S.A.). UV/VIS/NIR and FT-IR spectra of the PANI/CSA thin films were measured on Lambda 35 and Frontier FT-IR spectrometers (Perkin Elmer Inc., Waltham, MA, USA), respectively.

2.2.2. Supercapacitors based on porous PANI/CSA nanostructures as electrode materials

Electrochemical measurements: The electrochemical characteristics of PANI/CSA thin-film electrodes were observed using a WBCS 3000 potentiostat/galvanostat (WonATech, Seoul, Korea) under a 0.5 M H_2SO_4 electrolyte solution. The PANI/CSA thin films served as working electrodes, and a Pt wire (CH Instruments, Inc., USA) was used as the counter electrode. The reference electrode was Ag/AgCl in saturated KCl solution. CVs of porous electrodes were measured from 0 and 1.0 V at 20 mV s^{-1}. Galvanostatic charge/discharge experiments were performed by cycling the potential from 0 to 0.8 V at a current density of 0.25 A g^{-1}. Mass specific capacitances (C_m) of electrochemical cells based on the PANI/CSA thin films were calculated by using the equation C_m (F g^{-1}) $= \frac{I\Delta t}{m\Delta V}$, where I, Δt, m, and ΔV denote the constant discharge current, discharge time, mass of a thin film, and voltage drop upon discharge, respectively [66,115].

2.2.3. DSSCs based on porous PANI/CSA nanostructures CEs

Assembly of DSSCs with CEs: To compare the overall performance to conventional DSSCs, a Pt-coated ITO was prepared by adding 0.25 mL of 5 mM chloroplatinic acid hexahydrate to an area (1.5 cm^2) of the ITO substrate

followed by heating treatment at 400℃ for 30 min. Two steps of preparing TiO_2 paste were conducted to obtain highly viscous TiO_2 paste. Firstly, terpineol (2.25 mL), ethyl cellulose (0.1 g), and lauric acid (0.18 g) were mixed followed by sonication for 24 h. Then, the as-prepared solution was mixed with the TiO_2 NPs by vigorous stirring. FTO glasses were immersed into an aqueous TTIP solution at 60℃ for 30 min before depositing the TiO_2 paste onto the FTO glasses. TiO_2 thin films were deposited onto active areas (0.25 cm^2) of FTO glasses. Sintering of the TiO_2-coated FTO glasses were conducted at 450℃ for 30 min. The FTO glasses with TiO_2 thin films were immersed in the dye solution (0.5mM N719 dye in acetonitrile and *t*-butanol (volume ratio of 1 : 1)) for 36 h at 25℃. As-prepared working electrodes were assembled with the PANI/CSA thin-film CEs into sandwich-type cells using thermal adhesive films (Surlyn: 60 mm, Dupont). A drop of the redox electrolyte (50mM triiodide, 0.1M LiI, and 0.5M 1,2-dimethyl-3-propylimidazolium iodide in acetonitrile) was injected into the cell.

Measurements of DSSC performances: The electro-catalytic activities of porous PANI/CSA CEs were evaluated using CVs (WBCS 3000, Korea) with 10 mM acetonitrile, 1 mM I_2, and 0.1 M $LiClO_4$ as an electrolyte. The *J*–*V* characteristics of the assembled DSSCs were evaluated using a 500 W xenon lamp (XIL model 05A50KS source units). Incident photon-to-electron

conversion efficiency (IPCE) was measured using a Solar Cell Spectral Response QE/IPCE Measurement System (QEX7, PV Measurements, Inc. Boulder, USA) from 300 nm to 800 nm under the global AM 1.5 solar emission spectrum.

2.3. Fabrication of water-dispersible PSS-based conducing polymer nanostructures and their applications

2.3.1. Fabication of Pd NPs-decorated porous P(ANI-*co*-ASA):PSS nanostructures for H_2 sensors

2.3.1.1. Fabrication of Pd NPs-decorated porous P(ANI-*co*-ASA):PSS nanostructures

Fabrication of Pd NPs-decorated porous P(ANI-co-ASA):PSS: Aniline (99.0%), aniline-2-sulfonic acid (ASA), ammonium bicarbonate (AB), ammonium persulfate (APS, 98.0%), and palladium (II) chloride ($PdCl_2$) (99.0%) were purchased from Sigma-Aldrich (St. Louis, MO, USA). Hydrochloric acid (HCl, 35.0–37.0%) was obtained from Samchun (Seoul, Korea). P(ANI-*co*-ASA):PSS solution was synthesized *via* chemical oxidation polymerization. ASA (20 mg) was added to 0.22 g of the aniline monomer in a 20 mL volumetric flask. Then, ASA was melted in the monomer liquid by vigorous stirring for 1 h at 50℃. The as-prepared aniline/ASA co-monomer

liquid was used to fabricate the Pd-decorated P(ANI-*co*-ASA):PSS. HCl (10 mmol), a dopant for the co-monomer, was added to the co-monomer liquid. PSS (2.4 mL) was then added to 30 mL of distilled water in a 100 mL beaker, and the solution was vigorously stirred for 10 min. The anilinium aqueous solution in the 20 mL volumetric flask was then poured into the PSS solution under vigorous stirring for 20 min. $PdCl_2$ (20 mg), a catalyst for H_2 detection, was added to the reaction medium. Sonication was carried out for 30 min at 3℃ to increase the dispersion of the $PdCl_2$ powder in the solution. Polymerization was initiated by adding 0.3 mmol APS to the reaction medium at 25℃ for 1.5 h with vigorous stirring. As a result of the polymerization, green Pd-decorated P(ANI-*co*-ASA):PSS solution was obtained. The water-soluble porogen agent AB (10 mg) was introduced into the as-prepared P(ANI-*co*-ASA) solution, and subsequently the solution was sonicated to prepare the Pd-decorated porous P(ANI-*co*-ASA):PSS.

Instrumentation: Morphological images of the Pd NPs, pristine P(ANI-*co*-ASA):PSS, and Pd NPs-decorated P(ANI-*co*-ASA):PSS nanostructures were obtained using a TEM (LIBRA 120, Carl Zeiss, Germany), a FE-SEM (JSM-6701F, JEOL, Japan), and an AFM (Innova SPM, Vecco, USA). An optical image of the sensor electrode was obtained using a Nikon LV100 microscope (Nikon, Japan). The particle-

size distribution of the Pd NPs-decorated P(ANI-*co*-ASA):PSS nanostructures was measured using a DLS (DLS-7000, Otsuka Electronics Co., Inc., Japan). XPS spectra of the pristine P(ANI-*co*-ASA):PSS and Pd NPs-decorated P(ANI-*co*-ASA):PSS nanostructures were recorded on an AXIS-HIs spectrometer (Kratos/Shimadzu, Kyoto, Japan). Electrical conductivity (σ) (defined as σ (S cm^{-1}) $= \frac{1}{\rho} = \frac{\ln 2}{\pi t}\left(\frac{1}{R}\right)$, where ρ is the static resistivity, R is the sheet resistivity, and t is the thickness of a thin film) of the pristine P(ANI-*co*-ASA):PSS and Pd NPs-decorated P(ANI-*co*-ASA):PSS nanostructures was measured using a four-point probe system (Mode systems Co, Korea) equipped with a current-source meter (Keithley 2400; Keithley Co., Cleveland, OH, USA). The CVs and *I–V* characteristics of the pristine P(ANI-*co*-ASA):PSS and Pd NPs-decorated P(ANI-*co*-ASA):PSS nanostructures were determined using a WBCS 3000 potentiostat (WonATech, Seoul, Korea). UV/VIS/NIR and FT-IR spectra of the pristine P(ANI-*co*-ASA):PSS and Pd NPs-decorated P(ANI-*co*-ASA):PSS nanostructures were measured using a Lambda 35 and a Frontier FT-IR spectrometer (Perkin Elmer Inc., Waltham, MA, USA), respectively.

2.3.1.2. H_2 Sensors based on Pd NPs-decorated porous P(ANI-*co*-ASA):PSS nanostructures

Fabrication of sensor devices: A photolithographic process was used to pattern a microarray of 25 pairs of fingers onto a glass substrate. Each finger on the electrode was 1.5 µm × 1 mm × 0.030 µm (width × length × height) with a 2 µm interfinger gap (Figure 17). As shown in the optical image, the used electrode consists of each finger with a length of 1 mm (Figure 17a). In the FE-SEM image of the sensor electrode, we could confirm that the width of each finger and interfinger gap on the sensor electrode was 1.5 µm and 2 µm, respectively (Figure 17b). A 10 nm-thick Ti adhesion layer followed by a 20 nm-thick layer of gold was deposited using sputtering. The microelectrode substrates were cleaned using distilled water and ethanol, and subsequently 0.025 mL of the pristine P(ANI-*co*-ASA):PSS and Pd NPs-decorated P(ANI-*co*-ASA):PSS solutions were dropped onto the gold-interdigitated microelectrodes. The solutions were spread over the microelectrodes using a spin-coater (EC101D, Headway Research, Garland, TX, USA) at 1000 rpm for 10 s, resulting in a nanostructure thickness of approximately 5 mm. The microelectrode was dried at 60 ℃ for 5 h in an inert atmosphere to evaporate the solvent and to induce thermal decomposition of AB within the Pd NPs-decorated P(ANI-*co*-ASA):PSS nanostructure.

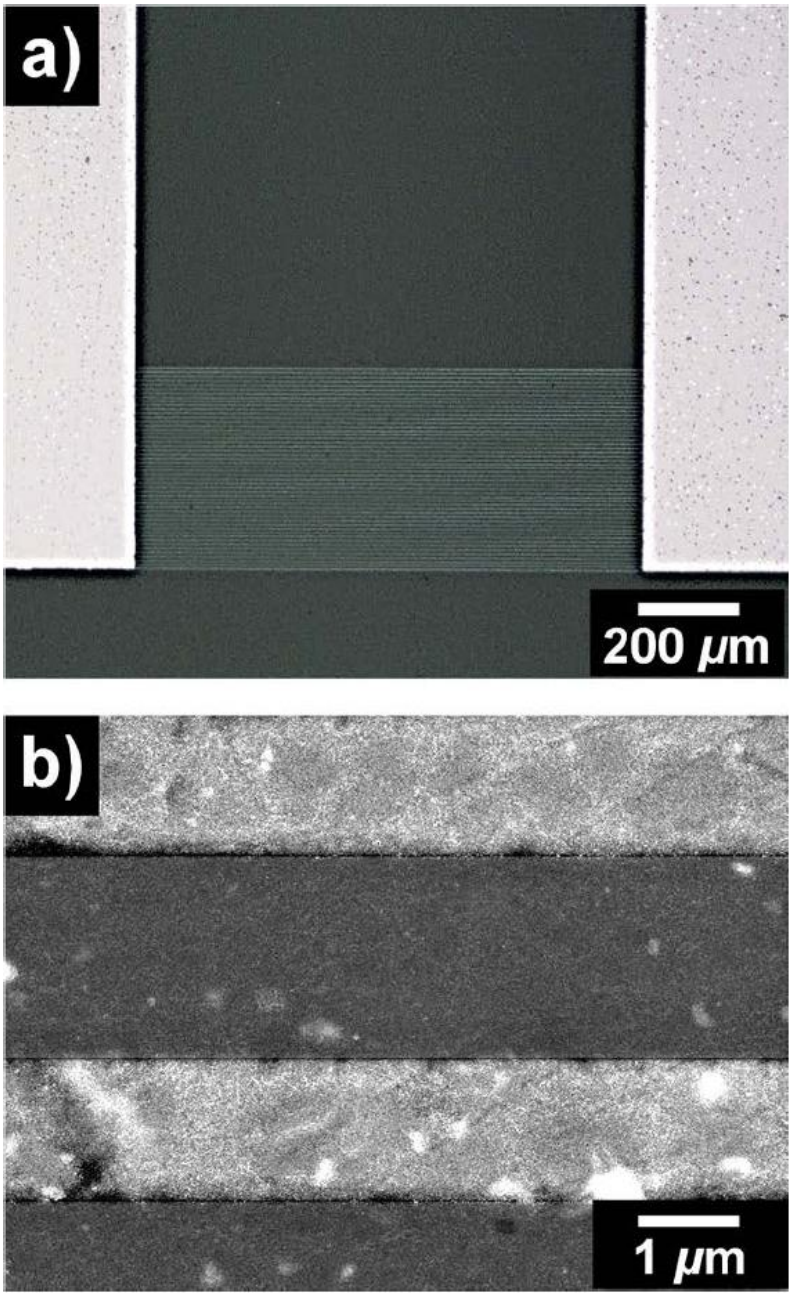

Figure 17. (a) Optical microscopy and (b) FE-SEM images of interdigitated microelectrode used.

Measurements of sensing performances: The Pd NPs-decorated porous P(ANI-*co*-ASA):PSS sensor devices were mounted in a vacuum chamber with an electrical feed-through and a gas inlet and outlet, and the pressure was maintained at 10 Torr. A stream of synthetic air, which consisted of 79% N_2 and 21% O_2, passed through an external bubbler in a vessel containing H_2 and then flowed into the small vacuum chamber at a flow rate of 2000 sccm. The concentration of H_2 gas was varied from 5 to 100 ppm by adjusting the ratio of synthetic air to H_2 gas. Cyclic H_2/synthetic air exposures were conducted using a MFC (KNH Instruments, Pucheon, Korea). The pristine P(ANI-*co*-ASA):PSS and Pd NPs-decorated P(ANI-*co*-ASA):PSS were exposed to H_2 gas at a given concentration, and then the H_2 gas was removed by owing compressed synthetic air; this process was repeated several times. The change in the resistance of the sensors was monitored at room temperature using a current-source meter (Keithley 2400; Keithley Co., Cleveland, OH, USA). The normalized resistance change, $\Delta R/R_0$ (defined as $\frac{\Delta R}{R} = \frac{R\text{-}R_0}{R_0}$, where R_0 is the initial resistance and R is the measured real-time resistance), was measured in real time at a constant applied current of 10^{-6} A to evaluate the sensitivity of pristine P(ANI-*co*-ASA):PSS and Pd NPs-decorated P(ANI-*co*-ASA):PSS nanostructures upon exposure to H_2 gas. The response time refers to the time required for the conductance to reach 90% of the response signal, whereas the

recovery time refers to the time necessary for a sensor to attain a conductance 10% above its original value in air [28].

2.3.2. Fabrication of PSS-doped PANI/graphene nanocomposites for H_2S sensors

2.3.2.1. Fabrication of PSS-doped PANI/graphene nanocomposites

Fabrication and characterization of high-molecular weight PSS solution: 4-styrenesulfonic acid and AAPH were obtained from Sigma-Aldrich (St. Louis, MO, USA). 14.4 g of 4-styrenesulfonic acid monomer was added into 33.6 mL of distilled water with vigorous stirring at 45℃ for 1 h. Polymerization of 4-styrenesulfonic acid was carried out by adding different amounts of AAPH (1.5, 3.0, 7.5, and 15 mg) at 45℃ for 12 h in a N_2 atmosphere. M_w values of the samples were determined by EcoSEC gel permeation chromatography (GPC) System (HLC-8320; Tosoh. Co., Tokyo, Japan) using a commercially available narrow molecular PSS samples as standards. Each PSS sample (3 mg mL^{-1}) was eluted at 1.0 mL min^{-1} with 0.1 M $NaNO_3$+0.02 M NaH_2PO_4 (pH=9) as an eluent at 35℃.

Fabrication of PSS-coated graphene powders: Natural flake graphite, sodium nitrate ($NaNO_3$, 99%), and hydrazine monohydrate ($N_2H_4 \cdot H_2O$, 98%) were obtained from Sigma-Aldrich (St. Louis, MO, USA). Potassium permanganate ($KMnO_4$, 99.3%) and phosphorus pentoxide (P_2O_5, extra pure)

were purchased from Junsei Chemical Co (Tokyo, Japan). Potassium persulfate ($K_2S_2O_8$, 99%) was purchased from Kanto Chemical Co (Tokyo, Japan). Sulfuric acid (H_2SO_4, 95%), hydrogen peroxide (H_2O_2, 30~35.5%), and hydrochloric acid (HCl, 35~37%) were purchased from Samchun (Seoul, Korea). Graphene sheets were synthesized by combining Hummers and Ruoff methods [51]. 5 g of graphite powder, 2.5 g of P_2O_5, and 2.5 g of $K_2S_2O_8$ were dissolved in 30 mL of H_2SO_4 solution to pre-oxidize natural graphite powders and the mixed solution was heated at 80℃ for 6 h. The solution was filtered using a cellulose acetate filter (Whatmann Inc., USA) with excess distilled water. The pre-oxidized graphite powders were dried in a vacuum oven at 25℃ for 24h. 2.5 g of $NaNO_3$ was dissolved in 120 mL of H_2SO_4 solution, and the pre-oxidized graphite was added into the solution with vigorously stirring for 0.5 h in an ice bath. 15.0 g of $KMnO_4$ was slowly added into the system at the temperature lower than 20 ℃ and brownish gray paste was obtained after heating the solution at 35℃ for 4 h. 600 mL of distilled water was slowly poured into the brownish gray paste, followed by addition of 25 mL of H_2O_2 solution, which resulted in the brightly yellow paste. The solution was washed with 5 wt% HCl and distilled water to adjust the pH of solution to 7, and sonochemically treated to exfoliate graphitic oxide into GO. Then the solution was centrifuged at 6000 rpm for 40 min to exclude residue. As-prepared GO

solution was dried in a vacuum oven at 40℃ for 24 h. The dried GO was poured into the diluted PSS solution (1 mg mL^{-1} in distilled water, 3/1 w/w *vs.* GO) with vigorous stirring. The PSS-coated GO was reduced by adding $N_2H_4 \cdot H_2O$ (1/1000 v/v *vs.* distilled water) with vigorous stirring at 95 ℃ for 1 h. The PSS-coated RGO solution was filtered using excess distilled water. Powders of PSS-coated graphene were dried in a vacuum oven at 25℃ for 24 h.

Fabrication of PSS-doped PANI/graphene: Aniline (99%), Ammonium persulface (APS, 98%), and PSS solutions with different M_w (7.0×10^4, 2.0×10^5, and 2.0×10^4) were obtained from Sigma-Aldrich (St. Louis, MO, USA). Chloroform ($CHCl_3$, 99%) was purchased from Samchun (Seoul, Korea). PSS-doped PANI solutions were synthesized using a modified self-stabilized dispersion polymerization (SSDP) method based on electrostatic polymerization at –50℃ [33,39,40,44]. 15.8 mL of PSS solution (0.3 g mL^{-1} in distilled water) was introduced into distilled water (14.2 mL) in a 250-mL volumetric flask. Aniline monomer (5 mmol) was added drop-wise to the PSS solution. 60 mL of chloroform was poured into the aqueous anilinium ion solution. Polymerization was carried out by adding 2.4-mmol APS to the reaction medium at –50℃ for 12 h with vigorous stirring. As a result of polymerization, greenish PSS-doped PANI solutions were obtained, and

chloroform solvents in the solutions were removed by using a 250-mL separatory funnel and centrifugation treatment. PSS-coated RGO (PSS-coated RGO : PSS-doped PANI = 30 : 70 by weight) powders were added into the PSS-doped PANI solution with vigorous stirring and sonochemical treatment. Afterwards, the PSS-doped PANI/graphene solutions were spreaded onto 2 cm-square poly(ethylene terephthalate) (PET) substrates by a spin-coater (EC101D, Headway Research, Garland, TX, USA), and the samples were dried at 60℃ for 3 h in an inert atmosphere to evaporate the solvent. The resultant samples were prepared as films of *ca.* 1 μm thickness.

Instrumentation: Surface images of the pristine PSS-doped PANI, graphene, and PSS-doped PANI/graphene nanocomposites were acquired with a TEM (LIBRA 120, Carl Zeiss, Germany), a FE-SEM (JSM-6701F, JEOL, Japan), an AFM (Innova SPM, Vecco, USA). XPS spectra of the pristine PSS-doped PANI, graphene, and PSS-doped PANI/graphene nanocomposites were recorded on an AXIS-HIs spectrometer (Kratos/Shimadzu, Kyoto, Japan). Electrical conductivity (σ) of the pristine PSS-doped PANI, graphene, and PSS-doped PANI/graphene nanocomposites was calculated using the equation σ (S cm^{-1}) $= \frac{1}{\rho} = \frac{\ln 2}{\pi t}\left(\frac{1}{R}\right)$, where ρ is the static resistivity, R is the sheet

resistivity, and t is the thickness of a thin film [111,112]. The conductivity values of the samples were measured using a four-point probe system (Mode systems Co, Korea) equipped with a current-source meter (Keithley 2400; Keithley Co., Cleveland, OH, USA). XRDs of the pristine PSS-doped PANI, graphene, and PSS-doped PANI/graphene nanocomposites were recorded on a SmartLab X-ray diffractometer (Rigaku Co., Tokyo, Japan). UV/VIS/NIR and Raman spectra of the pristine PSS-doped PANI, graphene, and PSS-doped PANI/graphene nanocomposites were measured on Lambda 35 (Perkin Elmer Inc., Waltham, MA, USA) and T6 (Horiba-Jobin Yvon Co., Tokyo, Japan) spectrometers, respectively. FT-IR spectra of the pristine PSS-doped PANI, graphene, and PSS-doped PANI/graphene nanocomposites were obtained using a Frontier FT-IR spectrometer (Perkin Elmer Inc., Waltham, MA, USA). CVs and $I-V$ characteristics of the pristine PSS-doped PANI, graphene, and PSS-doped PANI/graphene nanocomposites were observed using a WBCS 3000 potentiostat (WonATech, Seoul, Korea). EIS of electrochemical cells based on of the pristine PSS-doped PANI, graphene, and PSS-doped PANI/graphene nanocomposites were acquired in the frequency range of 100 kHz to 0.01 Hz using a ZIVE SP2 impedance analyzer (WonATech, Seoul, Korea).

2.3.2.2. H_2S Sensors based on PSS-doped PANI/graphene nanocomposites

Measurements of sensing performances: The PSS-doped PANI/graphene nanocomposites were placed in a vacuum chamber with an electrical feed-through and a gas inlet and outlet, and the pressure was maintained at 10^0 Torr. Cyclic H_2S/synthetic air exposures were carried out using a MFC (KNH Instruments, Pucheon, Korea). For analyte vapor exposures, a stream of synthetic air, which is composed of 79% N_2 and 21% O_2, passed through an external bubbler in a vessel containing H_2S and then flowed into the small vacuum chamber at a flow rate of 1−5 slm. The concentration of H_2S gas was regulated from 1 to 50 ppm by adjusting the ratio of synthetic air to H_2 gas. The PSS-doped PANI/graphene nanocomposites were exposed to H_2S gas at various flow rates of 0.3−5 sccm, and then the H_2S gas was removed by flowing compressed synthetic air; this process was repeated several times. The change in the resistance of the sensors was monitored at room temperature using a current-source meter (Keithley 2400; Keithley Co., Cleveland, OH, USA). For the evaluation of sensing performances of the PSS-doped PANI/graphene nanocomposites upon exposure to H_2S gas, the normalized resistance change, $\Delta R/R_0$, was measured in real time at a constant applied current of 10^{-6} A. The response time means the time

required for the conductance to reach 90% of the response signal, whereas the recovery time denotes the time necessary for a sensor to attain a conductance 10% above its original value in air [29].

2.3.3. Fabrication of RuO_2 NPs-decorated PEDOT:PSS/graphene nanocomposites for screen-printable and flexible electrodes in electrochemical capacitors

2.3.3.1. Fabrication of RuO_2 NPs-decorated PEDOT:PSS/graphene nanocomposites

Fabrication of RuO_2 NPs: Ruthenium (III) chloride hydrate ($RuCl_3 \cdot nH_2O$, reagent plus) was obtained from Sigma-Aldrich (St. Louis, MO, USA). Sodium hydroxide (NaOH, 99%), and sodium chloride (NaCl, 99%) were purchased from Samchun (Seoul, Korea). Hydrous RuO_2 NPs were synthesized according to sol-gel method given as; $RuCl_3 + 3NaOH \rightarrow 3Ru(OH)_3 + 3NaCl$ [109,110]. To balance the Ph to 7, 1M NaOH solution was added into 100 mL of 0.1M $RuCl_3$ with vigorous stirring for 1h at 25℃. The mixed solution was continuously stirred for 12 h, and then washed and centrifuged with distilled water several times to remove residual NaCl salts. The washed sample was dried at 150℃ for 12 h. The dried RuO_2 NPs were re-dispersed in distilled water by using an ultrasonicator (VCX 500, Sonics & Materials. Inc. USA) for 3 h in an ice bath. In the sample, the density of RuO_2 NPs in the distilled water was about 5 mg mL^{-1}.

Fabrication of RuO_2 NPs-decorated PEDOT:PSS/graphene patterns: PEDOT:PSS solution (Clevios PH1000) was obtained from Heraeus Precious Metals GmbH & Co. (Leverkusen, Germany). The solid content and PEDOT to PSS ratio of the PH 1000 solution was 1–1.3% and 1:2.5 by weight, respectively. Ruthenium (III) chloride hydrate ($RuCl_3 \cdot nH_2O$, reagent plus) was obtained from Sigma-Aldrich (St. Louis, MO, USA). Dimethyl sulfoxide (DMSO, 98%) was purchased from Samchun (Seoul, Korea). DMSO (DMSO : PEDOT:PSS = 5 : 95 by weight) was added into PEDOT:PSS solution, and followed by addition of the PSS-coated RGO (PSS-coated RGO : DMSO-PEDOT:PSS = 30 : 70 by weight) with vigorous stirring and sonochemical treatment. The synthesized PSS (30 wt% with respect to distilled water, 1/5 v/v *vs.* PEDOT:PSS) was further introduced into the DMSO-PEDOT:PSS solution with vigorous stirring and sonochemical treatment. For comparison, screen-printable ink based on the PEDOT:PSS and graphene sheets were also prepared by the same procedure without the other components. In the next step, the hydrous RuO_2 NPs (5 mg mL^{-1} in distilled water, 1/10 w/w *vs.* PEDOT:PSS/graphene) was added into the PEDOT:PSS/graphene solution with vigorous stirring and sonochemical treatment. RuO_2/PEDOT:PSS/graphene electrodes with 1 cm-square pattern were deposited on flexible poly(ethylene terephthalate) (PET) substrates by a screen-

printing machine (SM-S320, Sun Mechanix Co., Seoul, Korea) using as-prepared RuO_2/PEDOT:PSS/graphene solutions. The electrode thicknesses were adjusted by the number of screen-printings, which also adjust the mass of screen-printed electrode. 10 times of screen-printing were conducted to form a pattern having a thickness of about 5 μm and an electrode mass of 3 mg. To obtain a 20 μm-thick pattern and with electrode mass of 12 mg, 40 times of screen-printing were carried out. As-prepared screen-printed patterns were placed on the hot plate and dried at 100℃ on for 10 min.

Instrumentation: Surface images of pristine PEDOT:PSS, graphene, PEDOT:PSS/graphene, and RuO_2/PEDOT:PSS nanocomposites were acquired with a FE-SEM (JSM-6701F, JEOL, Japan) and an AFM (Innova SPM, Vecco, USA). Microscopic images of the graphene sheets and RuO_2 NPs were obtained with a TEM (LIBRA 120, Carl Zeiss, Germany). XPS spectra of the pristine PEDOT:PSS, graphene, PEDOT:PSS/graphene, and RuO_2/PEDOT:PSS nanocomposites were recorded on an AXIS-HIs spectrometer (Kratos/Shimadzu, Kyoto, Japan). Surface resistances and conductivities of the pristine PEDOT:PSS, graphene, PEDOT:PSS/graphene, and RuO_2/PEDOT:PSS nanocomposites were measured using a four-point probe system (Mode systems Co, Korea) equipped with a current-source meter (Keithley 2400, Keithley Co., USA). Electrical conductivity (σ) of the pristine

PEDOT:PSS, graphene, PEDOT:PSS/graphene, and RuO_2/PEDOT:PSS nanocomposites was calculated using the equation σ (S cm^{-1}) $= \frac{1}{\rho} = \frac{\ln 2}{\pi t}\left(\frac{1}{R}\right)$, where ρ is the static resistivity, R is the sheet resistivity, and t is the thickness of a thin film [111,112]. XRDs of the pristine PEDOT:PSS, graphene, PEDOT:PSS/graphene, and RuO_2/PEDOT:PSS nanocomposites were measured with a SmartLab X-ray diffractometer (Rigaku Co., Tokyo, Japan). Raman spectra of the pristine PEDOT:PSS, graphene, PEDOT:PSS/graphene, and RuO_2/PEDOT:PSS nanocomposites were measured on T6 (Horiba-Jobin Yvon Co., Tokyo, Japan) spectrometers, respectively.

2.3.3.2. Supercapacitors based on RuO_2 NPs-decorated PEDOT:PSS/graphene nanocomposites as electrode materials

Electrochemical measurements: For the evaluation of electrochemical characteristics on the pristine PEDOT:PSS, graphene, PEDOT:PSS/graphene, and RuO_2/PEDOT:PSS nanocomposites, CV and galvanostatic charge/discharge measurements were observed in 1M H_2SO_4 electrolyte solution using a WBCS 3000 potentiostat/galvanostat (WonATech, Seoul, Korea). Screen-printed electrodes, 1-cm square patterns deposited on PET substrates, served as working electrodes and a platinum wire (CH Instruments, Inc., USA) was utilized as a counter electrode. Ag/AgCl in saturated KCl

solution was used as a reference electrode. CVs of the pristine PEDOT:PSS, graphene, PEDOT:PSS/graphene, and RuO_2/PEDOT:PSS nanocomposites were measured from 0 and 0.8 V at various scan rates (10, 20, and 50 mV s^{-1}). Galvanostatic charge/discharge experiments performed by cycling the potential from 0 to 0.8 V at various current densities (0.5 to 8.0 A g^{-1}). Mass specific capacitances (C_m) of electrochemical cells were calculated by using the equation C_m (F g^{-1}) $= \frac{I\Delta t}{m\Delta V}$, where I, Δt, m, and ΔV denote the constant discharge current, discharge time, mass of a thin film, and voltage drop upon discharge, respectively [66,115]. Energy density of each sample was calculated by using the equation E (Wh kg^{-1}) $= \frac{C_m(\Delta V)^2}{2}$, where C_m and ΔV denote the mass capacitance of each sample and voltage drop upon discharge, respectively [190]. Power density of each sample was estimated using the equation P (W kg^{-1}) $= \frac{E}{t}$, where E and t denote the energy density and discharge time of each sample, respectively [190]. EIS of the electrochemical cells based on the pristine PEDOT:PSS, graphene, PEDOT:PSS/graphene, and RuO_2/PEDOT:PSS nanocomposites were acquired in the frequency range of 100 kHz to 0.01 Hz using a ZIVE SP2 impedance analyzer (WonATech, Seoul, Korea).

3.1. Fabrication of shape-controlled PANI nanomaterials with different monomer-to-oxidant ratio for DMMP sensors

3.1.1. Fabrication of shape-controlled PANI nanomaterials

Shape-designed PANI nanomaterials, such as NPs, NRs, and NFs, were prepared by chemical oxidation polymerization using different amounts of oxidizing agent (APS) (Figure 18). Assuming that the concentration of anilinium ions (NH_3^+) within the reaction medium remained constant, the charge-transport properties and morphologies of the PANI nanomaterials were mainly dependent on the amount of APS. Synthesized NFs, NRs, and NPs were deposited onto separate gold-interdigitated microelectrodes.

Figure 19 shows FE-SEM images of the PANI nanomaterials prepared with different $m_{APS}/m_{aniline}$ ratios. When this ratio was between 0.1 and 0.25, NFs 40–60 nm in diameter and 1000–2000 nm long were obtained (Figure 19a and b). When the ratio was 0.5, NFs 40–60 nm in diameter and 600–1000 nm long were obtained, which is similar to the previous reports (Figure 19c). According to the previous work, the $m_{APS}/m_{aniline}$ ratio was fixed at 0.5 to obtain PANI NFs, indicating that further increase in the aspect ratio of the PANI has been limited. Conventional methods only focused on reducing the size of PANI with increasing amounts of polyvinyl alcohol (PVA) or polyvinylpyrrolidone (PVP) [115,116], whereas our approach either increases or decreases the size of PANI

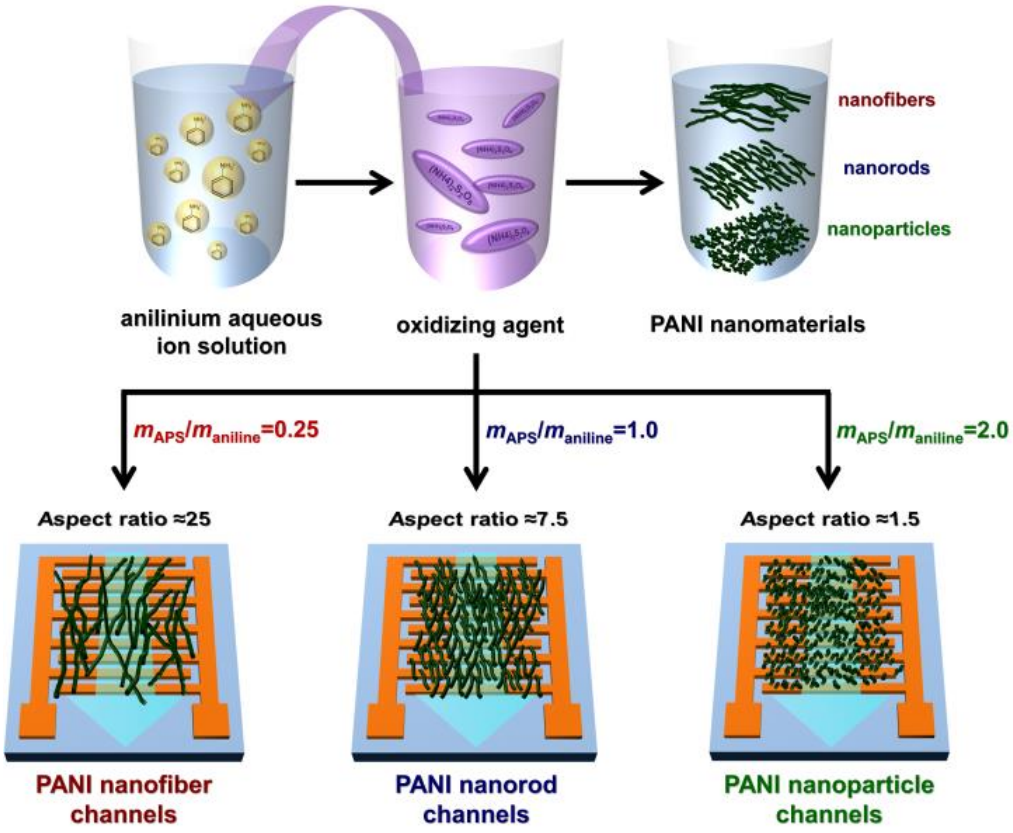

Figure 18. Overall procedure for the fabrication of shape-controlled PANI nanomaterials in DMMP sensor application.

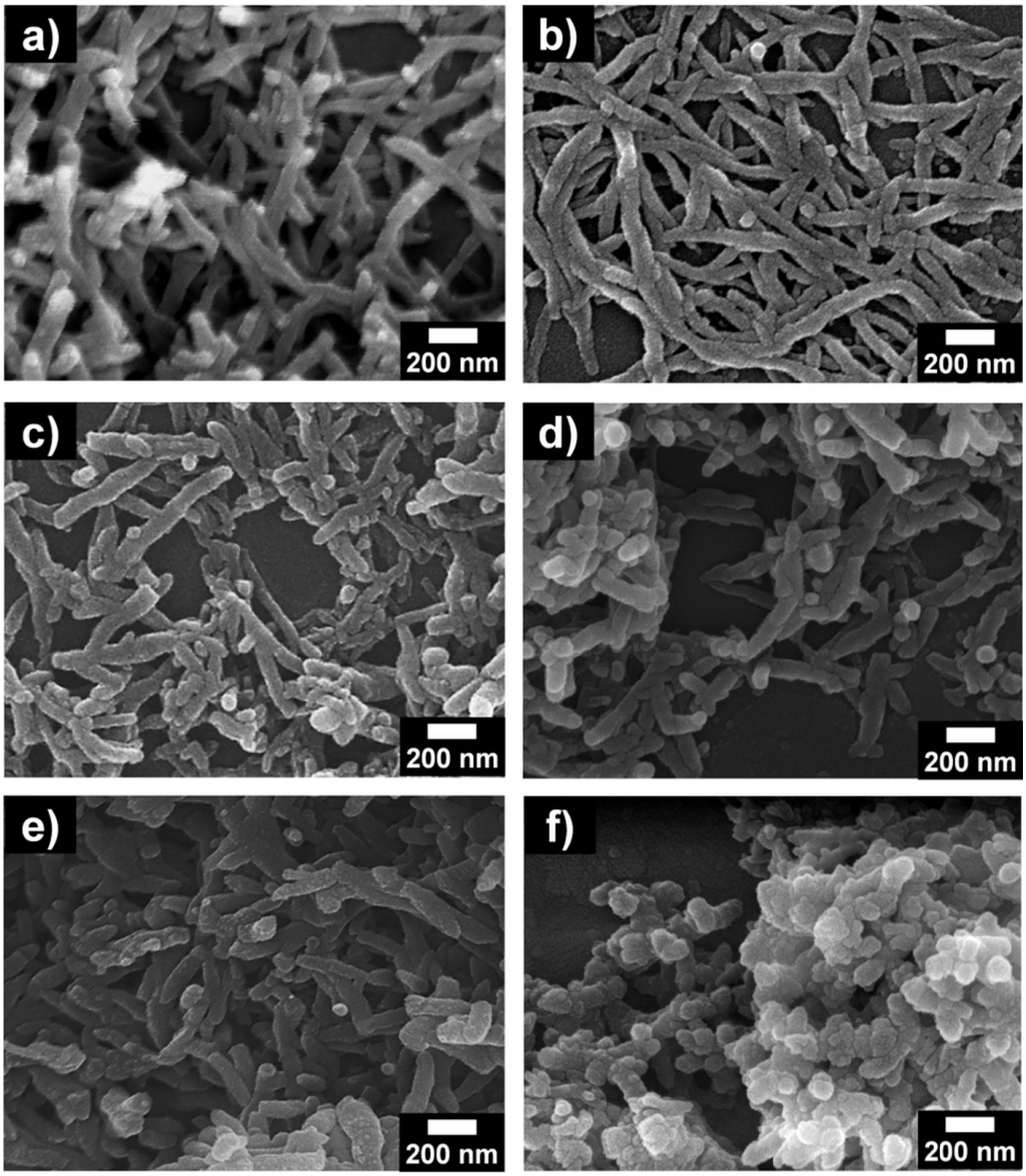

Figure 19. FE-SEM images of PANI nanomaterials synthesized at various $m_{APS}/m_{aniline}$ ratios: (a) 0.12, (b) 0.25 and (c) 0.5, (d) 1.0, (e) 1.5, and (f) 2.0.

by changing the aniline/oxidant ratio because the oxidizing agent is consumed for each act of addition of the monomer unit [2]. Accordingly, the difference in these synthetic approaches induced a much higher aspect ratio than the conventional method. The higher aspect ratio of PANI is associated with the enhanced conjugation length and doping level as will be discussed in detail. NRs were generated using a ratio of 0.5–1.5, and their diameters and lengths were 40–60 nm and 200–500 nm, respectively (Figure 19d and e). When a ratio between 1.5 and 2.0 was employed, NPs 50–100 nm in diameter and 50–150 nm long were obtained (Figure 19f). The higher ratio resulted in a higher oxidation state of the PANI structure; using excess APS can degrade the polymer chain by hydrolysis to form quinone end groups [37]. Accordingly, PANI nanomaterials with shorter lengths and smaller sizes were prepared at higher $m_{APS}/m_{aniline}$ ratios.

To provide a better understanding of the electrical properties of the PANI nanomaterials, conductivities of the pelletized PANI NFs, NRs, and NPs were measured using the four-line probe method (Figure 20) [111,112]. PANI powders were compressed into pellets with *ca.* 300 mm thickness. When the samples were pressed into pellets for measuring the conductivity, the inter-material charge transport could be improved through a kind of sintering effect [117]. Every conductivity measurement was conducted at a low RH of 25%,

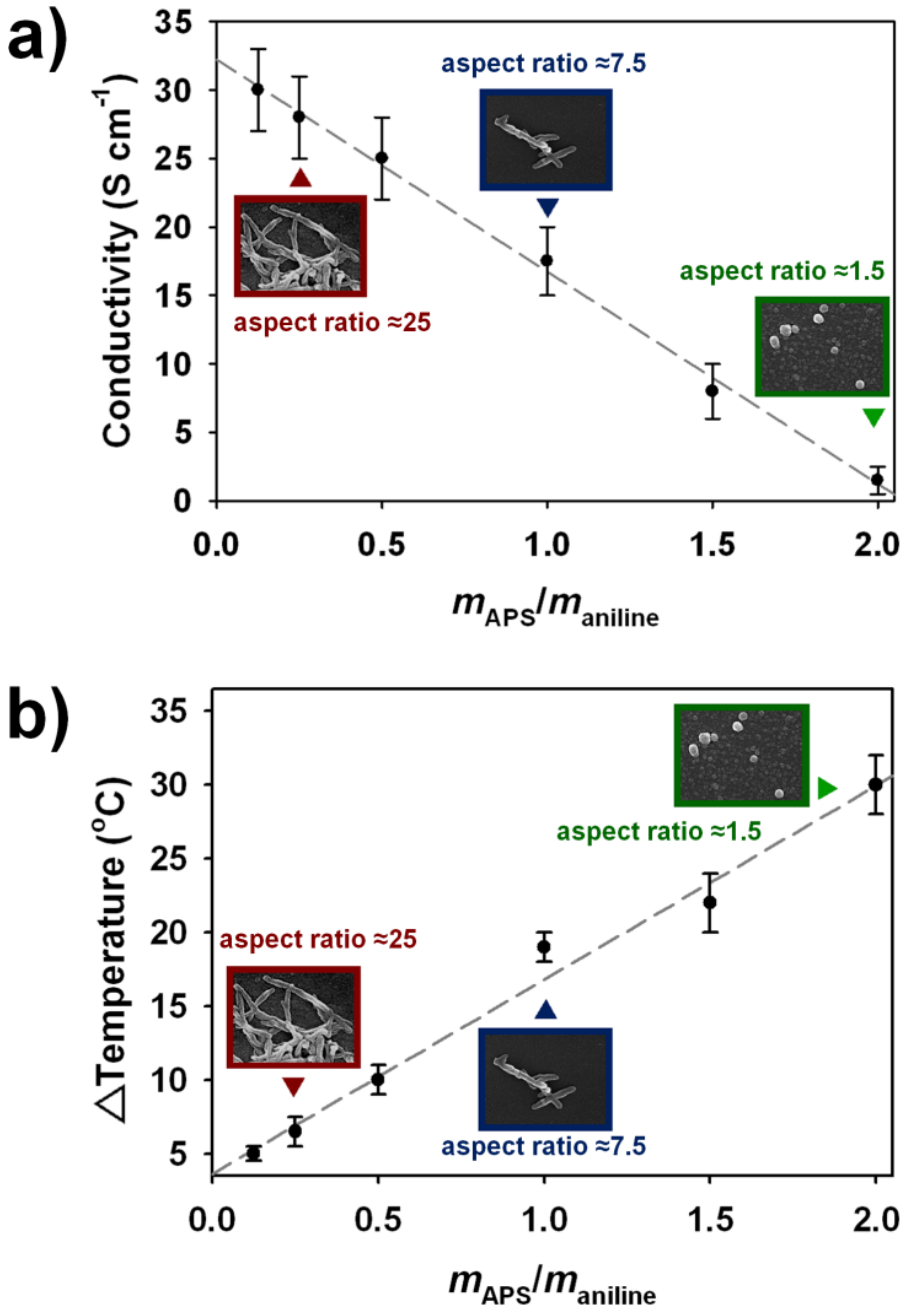

Figure 20. (a) Conductivity and (b) temperature increment of PANI nanomaterials synthesized at different $m_{APS}/m_{aniline}$ ratios.

which does not seriously affect the surface resistance of PANI [118]. Conductivity refers to the ability of the sensor device microelectrode to conduct electric current. If there is much loss of conductivity at the microelectrode, then the normalized resistance change ($\Delta R/R_0$) of the PANI sensor would be dramatically reduced. The high conductivity of the PANI nanomaterials is important for enhanced sensing performance. Figure 20a and Table 1 indicate that PANI nanomaterial conductivities are inversely proportional to the $m_{APS}/m_{aniline}$ ratio used for their syntheses. Furthermore, comparison of this ratio with the temperature change (ΔT) revealed an approximately linear relationship between them. Varying the $m_{APS}/m_{aniline}$ ratio affected the ΔT because the polymerization of aniline is highly exothermic (Figure 20b and Table 1) [37]. Assuming that the acid concentration within the reaction medium remains unchanged, the oxidation state of the reaction medium depends mainly on the $m_{APS}/m_{aniline}$ ratio. A decrease in conductivity was observed at higher temperatures because of the increase in temperature from the formation of PANI having a higher oxidation state. This lower conductivity at higher temperatures is attributable to a large number of structural defects in the PANI chain [119]. The conductivities of the PANI NFs, NRs, and NPs were strongly dependent on their aspect ratios. PANI NFs possess the highest aspect ratio among the PANI nanomaterials, and the NFs

Table 1. The relationship between $m_{APS}/m_{aniline}$, aspect ratio, conductivity (σ), and temperature increment (ΔT) from polymerization of aniline.

$m_{APS}/m_{aniline}$	aspect ratio[a]	σ (S cm^{-1})	ΔT(°C)[b]
0.12	25±5	30.0±3.0	5.0±0.5
0.25	25±5	28.0±3.0	6.5±1.0
0.50	15±5	25.0±3.0	10.0±1.0
1.00	7.5±2.5	17.5±2.5	19.0±2.0
1.50	5±1	8.0±2.0	22.0±3.0
2.00	1.5±0.5	1.5±1.0	30.0±3.0

[a] Aspect ratio of the PANI nanomaterials is defined as the ratio of length to diameter of the nanomaterial.

[b] Temperature increment (ΔT) during polymerization was measured from initial temperature (25 °C).

deposited on the microelectrodes appeared to be less aggregated than the NRs and NPs. Accordingly, the contact resistance between the individual PANI NFs was minimized, making them more conductive than the NRs and NPs. PANI NPs, the most aggregated species, were particularly poor at minimizing the contact resistance at the microelectrode. The difference between the contact resistances of the PANI nanomaterials was a crucial factor that affected the sensitivity of the PANI-based sensor device, as will be discussed in detail. The conductivities of the PANI nanomaterials increased in the order of NPs < NRs < NFs, i.e., according to the $m_{APS}/m_{aniline}$ ratio (Table 1). The values were almost within the same range as mentioned in the previous work (10^0 to 10^1 S cm^{-1}) [120–124].

X-Ray photoelectron spectroscopy (XPS) was used to monitor changes in the elemental compositions and doping states of the PANI nanomaterials (Figure 21 and 22). Elemental compositions were determined from the full-scan XPS patterns (Figure 21). The PANI NFs ($m_{APS}/m_{aniline}$ = 0.25) and NRs ($m_{APS}/m_{aniline}$ = 1.0) had very similar elemental compositions, whereas the PANI NPs prepared at the $m_{APS}/m_{aniline}$ ratio of 2.0 had significantly higher oxygen content. Elsenbaumer et al. reported that the increasing reaction enthalpy rate is considerably lower for $m_{APS}/m_{aniline}$ < 1.25 than for $m_{APS}/m_{aniline}$ > 1.25, and is an indication that the reaction stoichiometry has changed [37].

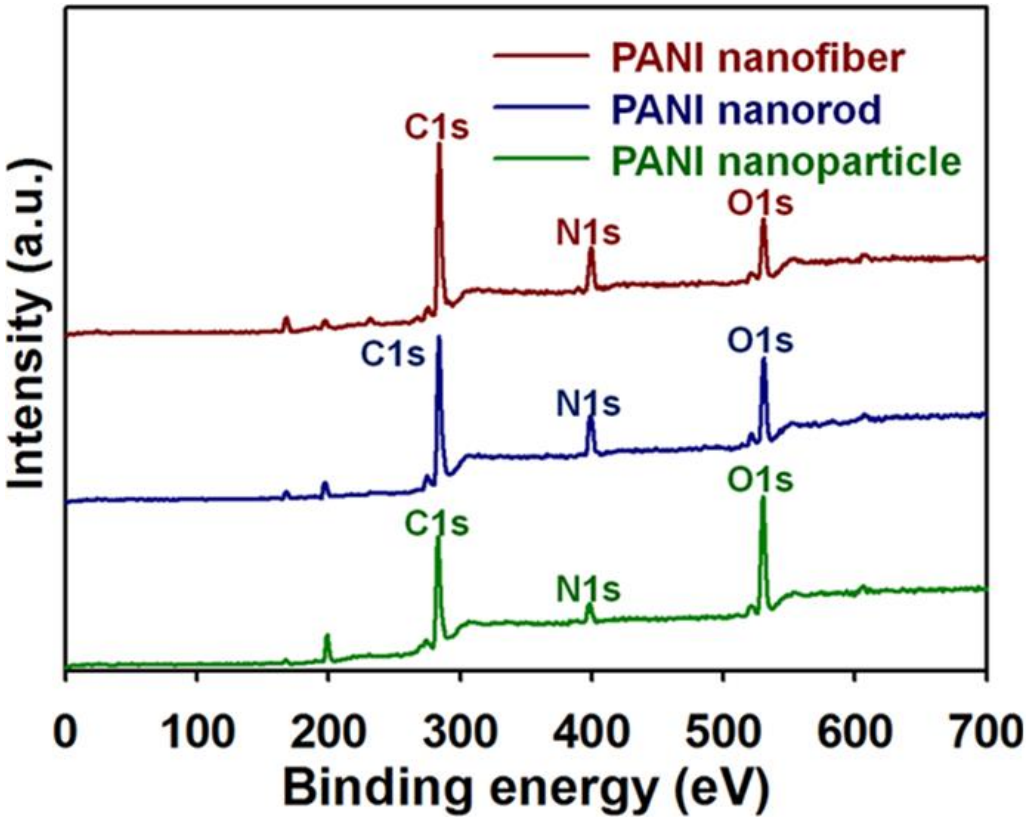

Figure 21. (a) Fully scanned XPS spectra of PANI nanomaterials.

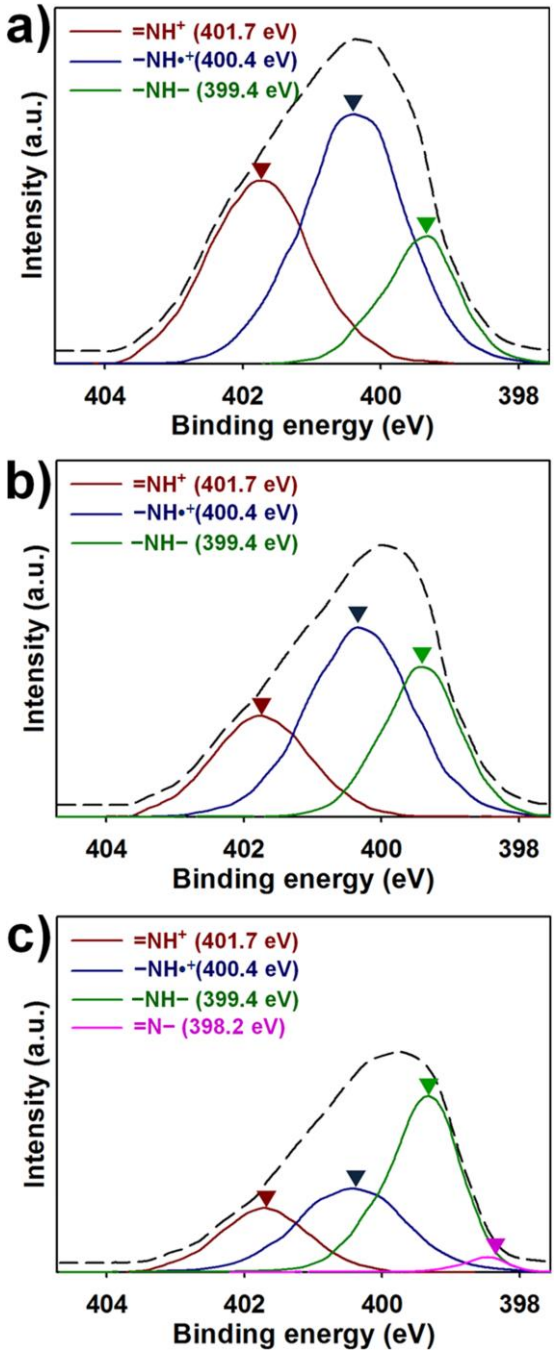

Figure 22. XPS core spectra of N1s in (a) PANI NFs, (b) PANI NRs, and (c) PANI NPs.

Table 2. XPS atomic ratios of PANI nanomaterials with different shapes.

morphologies	XPS atomic ratio				
	$=NH^{+a}$	$–NH•^{+a}$	$–NH–^{a}$	$=N–^{a}$	N^{+}/N ratio^{a}
NFs	0.32	0.45	0.23	·	0.77
NRs	0.22	0.43	0.34	·	0.65
NPs	0.19	0.24	0.52	0.05	0.43

[a] The values were calculated using the N1s core spectra of the samples.

The $m_{APS}/m_{aniline}$ ratios greater than 1.25 may overoxidize the PANI structure, resulting in smaller aspect ratios and larger temperature increases. Carbon contents of the PANI nanomaterials increased in the order of NPs < NRs < NFs. The results may suggest that NFs have a larger portion of π-conjugation extent than the NRs and NPs, offering longer conjugation length to delocalize electrons within the PANI structure. Figure 22 show the N(1s) core spectra of the PANI NFs ($m_{APS}/m_{aniline}$ = 0.25), NRs ($m_{APS}/m_{aniline}$ = 1.0), and NPs ($m_{APS}/m_{aniline}$ = 2.0), respectively. The N(1s) spectra of the PANI NFs and NRs were deconvoluted into three peaks at 399.4, 400.4, and 401.7 eV, corresponding to –NH– (benzenoid amine nitrogen), $–NH•^+$ (radical cation), and $=NH^+$ (imine cation) functionalities, respectively [125–128]. The spectra of the PANI NPs were resolved into four peaks with the additional peak at a binding energy of 398.2 eV corresponding to –N= (imine nitrogen). The proportion of positively charged nitrogen of the $–NH•^+$ and $=NH^+$ groups decreased with the increasing $m_{APS}/m_{aniline}$ ratio, whereas the proportion of –NH– and –N= groups increased with the increasing $m_{APS}/m_{aniline}$ ratio. These results indicate that the decrease in doping level is because of overoxidation of the PANI structure. The doping levels of the PANI nanomaterials were estimated by calculating the ratio of N^+ species (sum of $–NH•^+$ and $=NH^+$) to N species (sum of –N=, –NH–, $–NH•^+$, and $=NH^+$) (N^+/N ratio) [126]. This ratio

was 0.77, 0.65, and 0.43 for the PANI NFs, NRs, and NPs, respectively (Table 2). The N^+/N ratio exceeded 50% for both the NFs and NRs, indicating that the H^+ of the HCl dopant not only protonated the –NH– but also the –N= in the PANI structure [125]. For this reason, the peak for –N= was absent from the spectra of PANI NFs and NRs. Moreover, the increased N^+ species of the PANI structure not only suggests the higher doping level but also the increased ability to interact with the DMMP vapor. As PANI is acknowledged to behave in accordance with *p*-type conducting materials, it is reasonable to expect that a highly protonated structure will cause an increase in the electron transport upon exposure to the DMMP vapor due to the increased carrier mobility along the PANI structure.

UV/VIS/NIR and FT-IR spectroscopy studies were used to further clarify the charge-transport properties of the PANI nanomaterials (Figure 23). Two characteristic bands for emeraldine salts were found in every PANI UV/VIS/NIR spectrum (Figure S1a) [37,129–131]. The absorption bands at 371 and 798 nm in the UV/VIS/NIR spectrum of the NF were assigned to π–π excitation of the *para*-substituted benzenoid segment (–B–NH–B–) and the quinone diamine structure (–N=Q=N–), respectively (Figure 23a) [129]. These two bands appeared at 365 and 790 nm, respectively, for the NRs. Therefore, the doping levels in the NFs and NRs are likely similar. These two bands appeared at

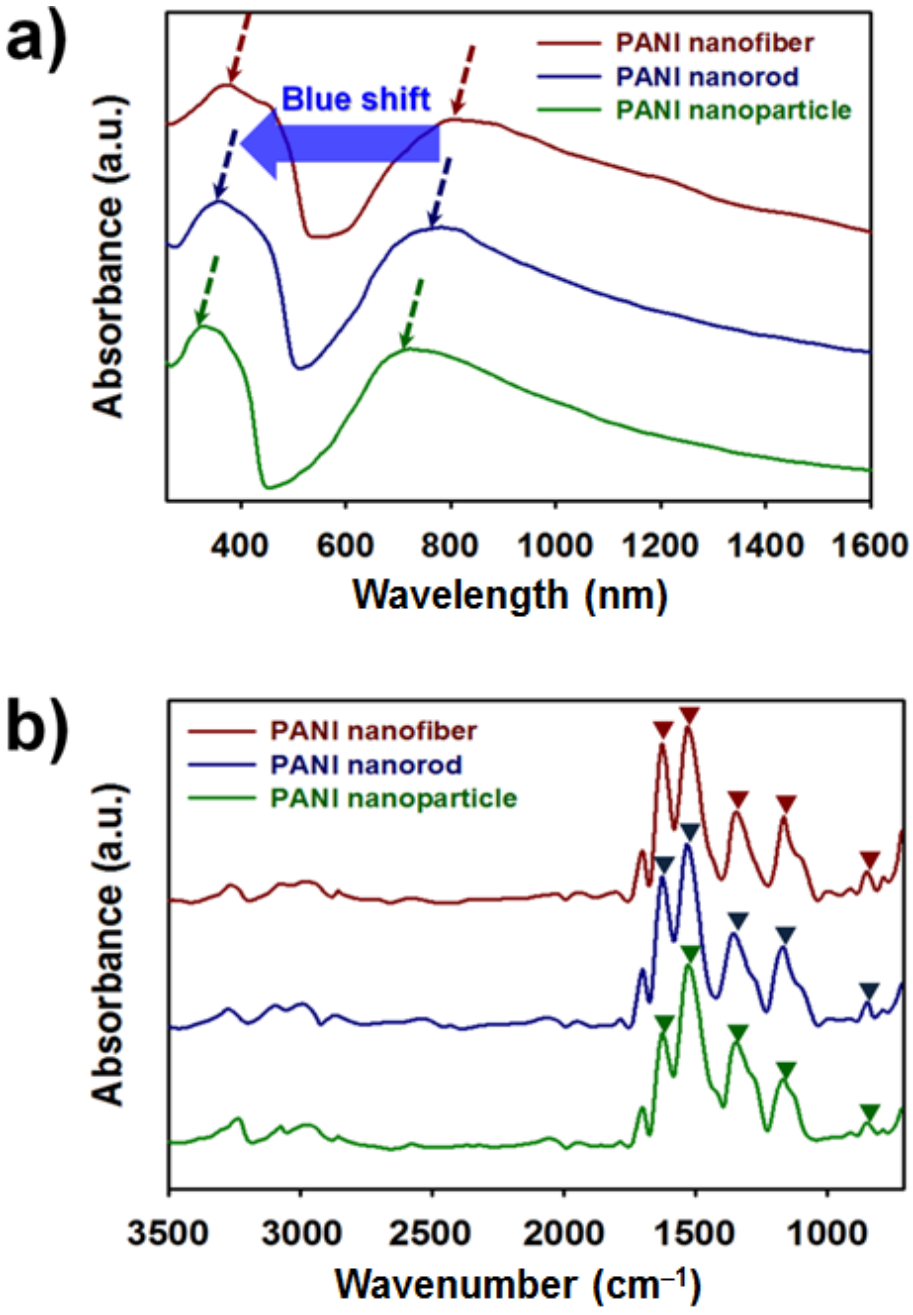

Figure 23. Distinctive bands in (a) UV/VIS/NIR and (b) FT-IR spectra of PANI nanomaterials with different shapes.

shorter wavelengths for the PANI NPs. The bands for the–B–NH–B– and the –N=Q=N– of the nanoparticles were slightly blueshifted to 340 and 720 nm. This blueshift is usually observed during a change from the half-oxidized form (conductor) to the fully oxidized form (insulator) [130,131]. The decrease in the maximum absorption wavelength of the PANI nanoparticles is attributable to a reduced extent of π conjugation within the PANI structure [132]. Hence, the conjugation length within the PANI structure increased in the order of NPs < NRs < NFs. FT-IR spectra provide information on the influence of chemical bonding on the charge-transport properties of the PANI nanomaterials (Figure 23b). Several distinctive bands were observed for the NFs, NRs, and NPs, i.e., at 825, 1145, 1299, 1498, and 1581 cm^{-1} [129,131–133]. The band at 825 cm^{-1} originates from the C–H out-of-plane bending of 1,4-disubstituted ring structures (*para*-coupling); these structures result from the favored head-to-tail (HT) coupling during aniline polymerization. The bands at 1145 and 1581 cm^{-1} are attributable to the stretching vibration of the –N=Q=N–. These two bands appeared more prominently in the oxidized form of the NFs and NRs than in the overoxidized PANI NPs. This implies that the PANI nanomaterials become conductive through protonation of the –N=. Additionally, the peaks at 1145 and 1581 cm^{-1} are indicative of the ability to delocalize electrons within the PANI structure [132,133]. The peak at the 1299 cm^{-1} originates from the stretching

vibration of C–N in the secondary aromatic amine. This band was more intense for the NFs and NRs than for the NPs, indicating the presence of higher amounts of amine nitrogen that could participate in hydrogen bonding with DMMP. The band at about 1498 cm^{-1} was assigned to C=C stretching in the –B–NH–B–. The ratio of the intensities of the bands at 1581 and 1498 cm^{-1} (I_{1581}/I_{1498}) was strongly related to the protonation state of the PANI structure [133]. In this work, the intensity of the 1581 cm^{-1} band increased as the doping level of PANI increased. The I_{1581}/I_{1498} intensity ratio was 0.96, 0.90, and 0.70 for the NFs, NRs, and NPs, respectively. These results also indicate that the conjugation length of the PANI nanomaterials increased in the order of NPs < NRs < NFs.

Cyclic voltammograms (CVs) were carried out in a 1 M H_2SO_4 electrolyte at 20 mV s^{-1} to clarify how the charge-transport properties influence the electrochemical properties of the PANI structure (Figure 24). The upper and lower peaks are ascribed to the redox behavior of PANI and correspond to leucoemeraldine/emeraldine and emeraldine/pernigraniline transitions, respectively [133]. The electric current increased with increasing aspect ratio of the PANI nanomaterials, suggesting that the morphologies of the nanomaterials affected the redox conversion between the LS, ES, and PS forms. The rapid redox transition at the transducer/electrolyte surface suggests enhanced

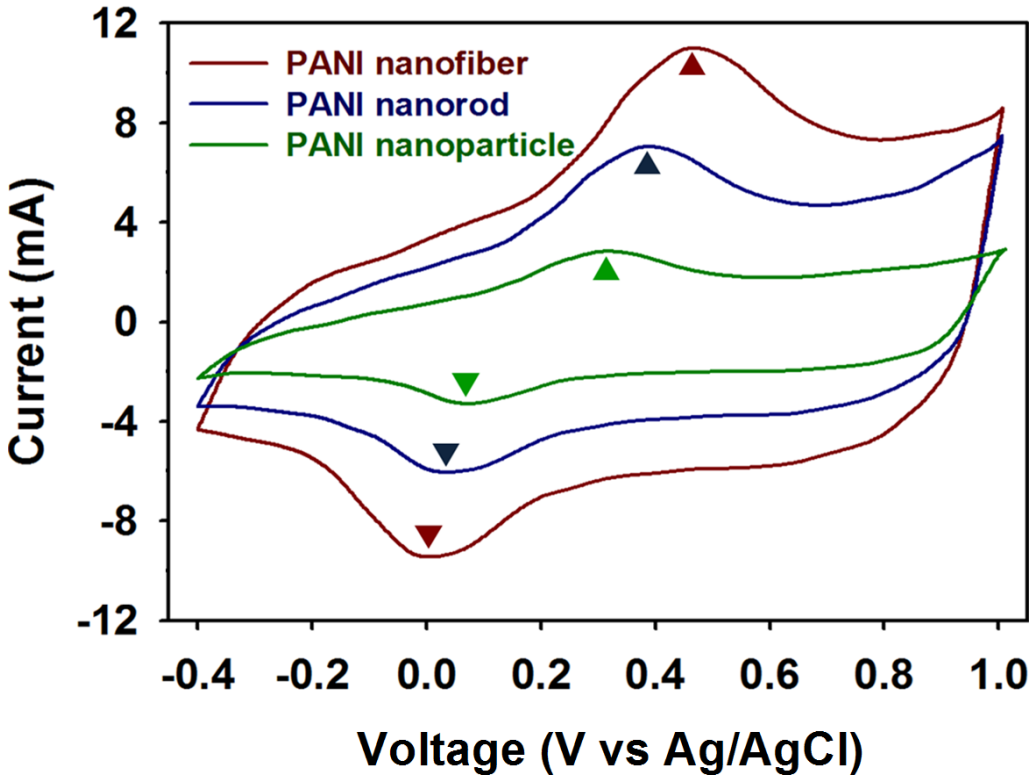

Figure 24. Cyclic voltammograms of PANI nanomaterials in a 1M H_2SO_4 electrolyte at a scan rate of 20 mV s^{-1}.

interaction between the nanomaterials and DMMP vapor. Therefore, the PANI NFs seemed to have less resistance with DMMP vapor than the nanorods and nanoparticles.

3.1.2. DMMP sensors based on PANI nanomaterials

Recently, chemiresistive sensors have been developed for the detection of chemical warfare agents (CWAs), which include blister agents and nerve agents [185,186]. Nerve agents such as sarin (GB), soman (GD), tabun (GA), and VX are organophosphate-based CWAs that inhibit the enzyme cholinesterase by forming covalent bonds with a serine residue at the active site of the enzyme. Dimethyl methylphosphonate (DMMP), a relatively nontoxic simulant for chemical agents, has been widely used as a model system for the detection of organophosphorus CWAs. Because of its easy synthesis and the low cost of aniline monomers, PANI nanomaterials can be attractive sensing elements for detecting the DMMP.

A mechanism for the detection of DMMP vapor by the PANI structure is illustrated in Figure 25. Amine nitrogens along the PANI backbone can form hydrogen bonds with the –P=O group of DMMP. This strong hydrogen bonding promotes absorption of the DMMP molecules into the PANI structure. In addition, the $–CH_3O$ group of DMMP can also form weak hydrogen bonds

with the PANI backbone [113]. Although H_2O molecules can interact with the same sites, H_2O appears to have little effect or no effect on the total amount of DMMP absorbed into the PANI structure, at a low relative humidity (RH) (<30%) [114]. DMMP vapors were introduced into PANI-nanomaterial-based sensors at a RH of 25%. This lack of interference from RH indicates the diminished binding affinity of H_2O molecules to the –N–H linkages along the PANI backbone.

To evaluate the sensing capability of the PANI nanomaterials as transducers for the detection of DMMP vapor, very small amounts of PANI NFs, NRs, and NPs were deposited onto separate gold-interdigitated microelectrodes (Figure 26). PANI nanomaterials bridge the gap between the microelectrodes, providing conductive channels. Moreover, the high aspect ratio of PANI NFs compared with that of the NRs and NPs is advantageous for bridging adjacent microelectrodes. Smaller amounts of NFs than NRs and NPs were required to form the conductive pathway (Figure 26a). In the case of the NRs and NPs, conductive pathways between microelectrodes were formed by laterally contacting aggregates of individual NRs and NPs, which made it more difficult to minimize the contact resistance (Figure 26b and c, respectively). The ability to generate a conductive channel on a microelectrode is important for the sensing capability of the PANI nanomaterials.

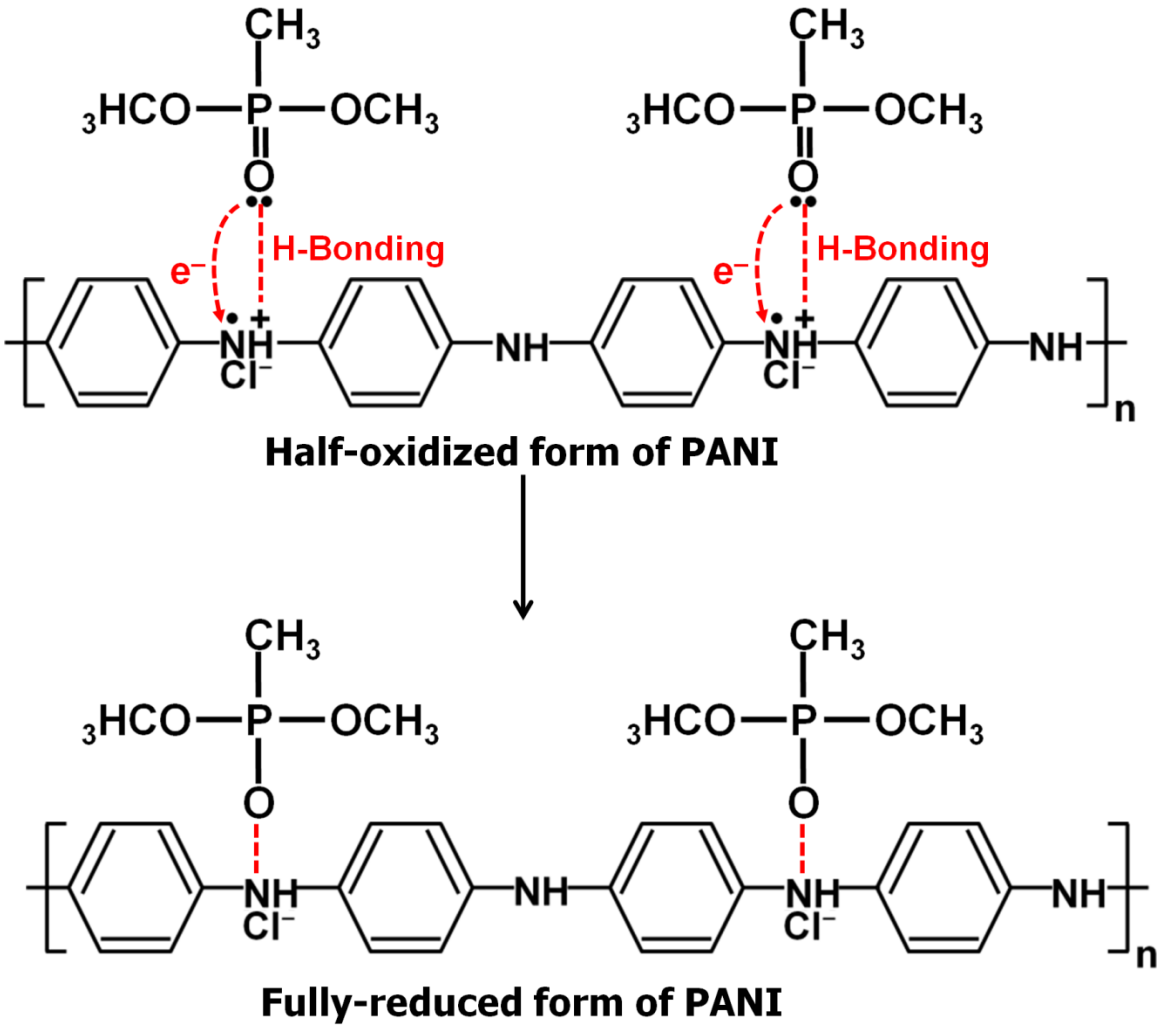

Figure 25. Possible mechanism for hydrogen bonding between HCl-doped PANI and DMMP vapor.

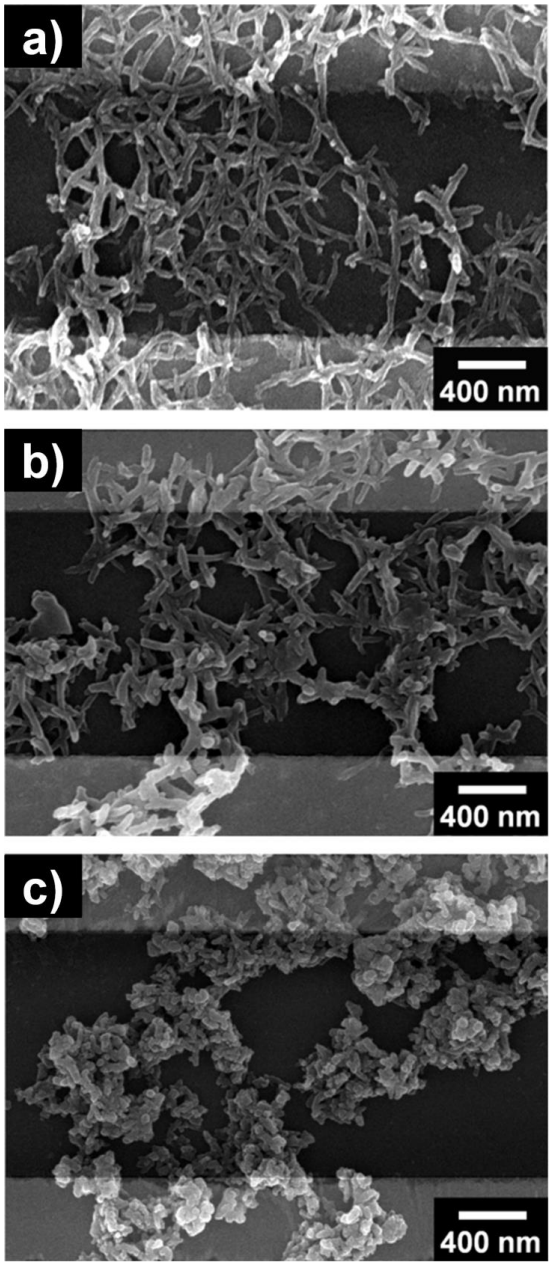

Figure 26. FE-SEM images of gold-interdigitated electrodes employing the PANI nanomaterials synthesized at different $m_{APS}/m_{aniline}$ ratios: (a) 0.25, (b) 1.0, and (c) 2.0.

Figure 27 illustrates the *I*–*V* characteristics of PANI NFs, NRs, and NPs deposited as the conductive channels on the microelectrode substrates. The linear *dI*/*dV* values imply that reliable electrical contacts were present at the PANI/gold electrode interfaces [117]. The *dI*/*dV* value increased in the order of NPs < NRs < NFs, i.e., with decreasing interparticle contact resistance. This indicates that the decreased contact resistance between the nanomaterials is highly correlated with the contact improvement between the nanomaterials and microelectrodes. Assuming that the microelectrodes used for sensor device remain unchanged, the resistance contact between the nanomaterial-microelectrode mainly depends on the charge-transport within the PANI structures. PANI NFs, NRs, and NPs possess different degree of protonation (doping level) and conjugation length, which mainly determine the intrinsic conductivity of the PANI. Hence, the contact resistance between the PANI and microelectrode could be minimized with increasing aspect ratio of the PANI, and the values were in accordance with the conductivity of the PANI nanomaterials. When relatively small amounts (0.05 wt%) of the nanomaterials were deposited on the microelectrodes, the electric current through the PANI NFs was approximately 10 times larger than that for the other nanomaterials (Figure 27a). On depositing more nanomaterial (0.1 wt%) on the microelectrodes, the electric current through nanorods and nanoparticles

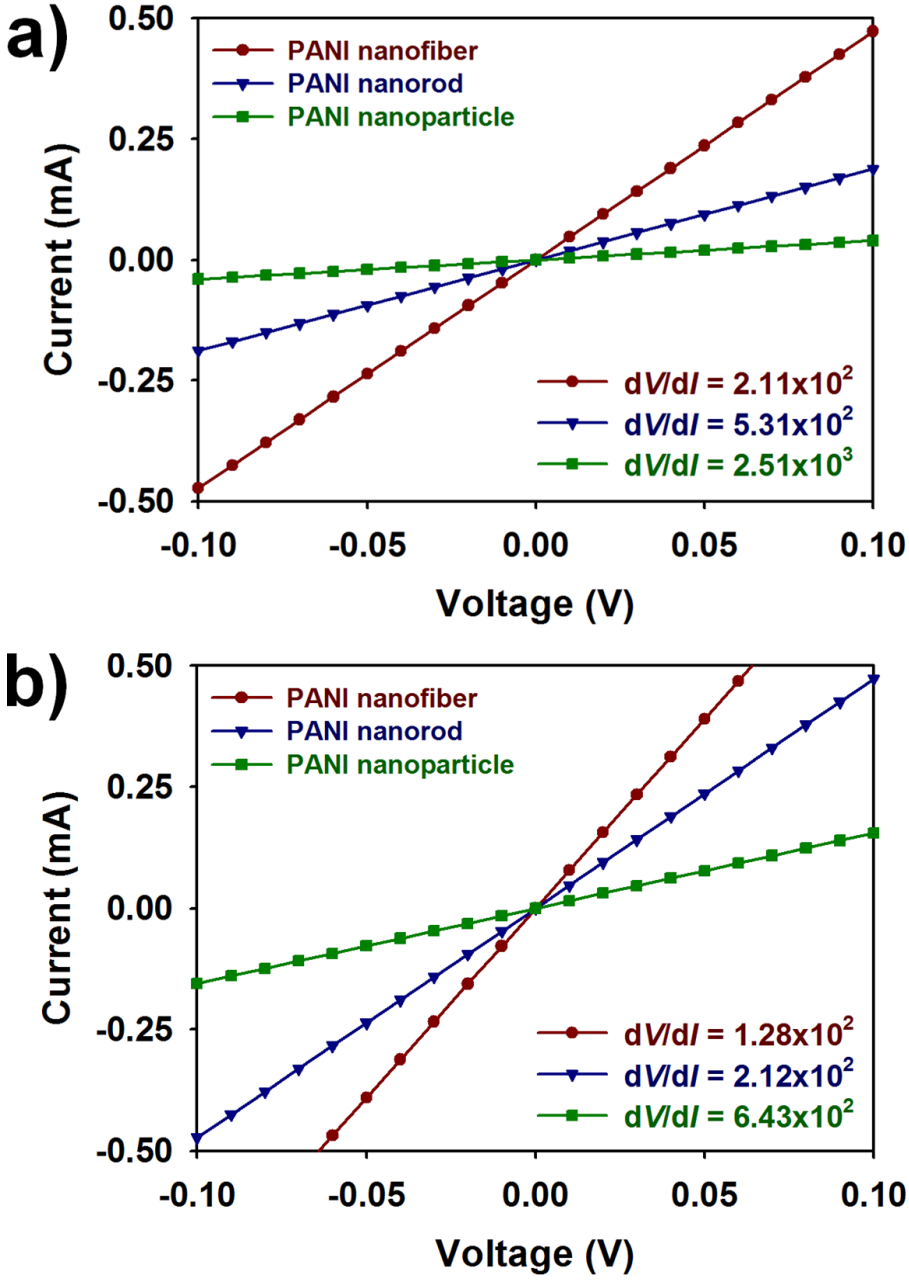

Figure 27. *I-V* characteristics of PANI nanomaterials integrated in the sensor substrate at a scan rate of 10 mV s^{-1}: (a) 0.05 wt% and (b) 0.1 wt% in ethanol.

increased dramatically, while the *I–V* characteristic of the nanofibers was similar to the results at 0.05 wt% concentration (Figure 27b). Relatively smaller amounts of NFs are required to form contacts between the PANI and DMMP compared to the NRs and NPs. Taking the facts into account, the results are attributed to the enhanced charge transport properties within the PANI NFs. The difference in the *I–V* characteristics thus provide valuable insight into the relationship between inter-material contact resistance and aspect ratio of the nanomaterials, and indeed differentiates the responses of sensors made with the different PANI nanomaterials.

The real-time responses of the PANI nanomaterials were systematically investigated to clarify the influence of morphological variation on their DMMP-sensing capabilities (Figure 28 and 29). The $\Delta R/R_0$ of the PANI-based sensor was monitored in real time when the saturated value was reached after exposure to DMMP. The $\Delta R/R_0$ of the PANI nanomaterials is given by Equation (1),

$$\frac{\Delta R}{R} = \frac{R\text{-}R_0}{R_0} \qquad (1)$$

where R_0 is the initial resistance and R is the measured real-time resistance [74.117]. Furthermore, R_0 and R can be expressed as Equations (2) and (3),

$$R_0 = \sum^{n} R_I + \sum^{n-1} R_S \quad (2)$$

$$R = \sum^{n} R_I + \sum^{n-1} R_S + \sum^{n} R_C \quad (3)$$

where R_s, R_I, and R_c denote the resistance of the single nanomaterial, the inter-material contact resistance, and the resistance change for the nanomaterial–DMMP interaction, respectively; n is the number of nanomaterials creating the conductive channel [117]. The R_s is related to intrinsic factors such as the protonation state and conjugation length for a single PANI nanomaterial. The R_I and R_c are related to extrinsic factors, which affect the nanomaterial–microelectrode and nanomaterial–DMMP interactions, respectively. It is reasonable to assume that facile redox transition in the PANI structure is advantageous for reducing R_c. Extensively aggregated PANI nanorods and nanoparticles resulted in higher R_I values than for the NFs. The R_I is ascribed to aggregation between the nanomaterials deposited on the microelectrodes. Conductive areas within the conducting polymer films become less connective with increasing aggregation between the nanomaterials [16]. Low connectivity between the conductive regions may also reduce carrier mobility along the PANI thin film, which may lead to a decrease in conductivity [134]. Accordingly, formation of the PANI nanostructures should be less aggregated

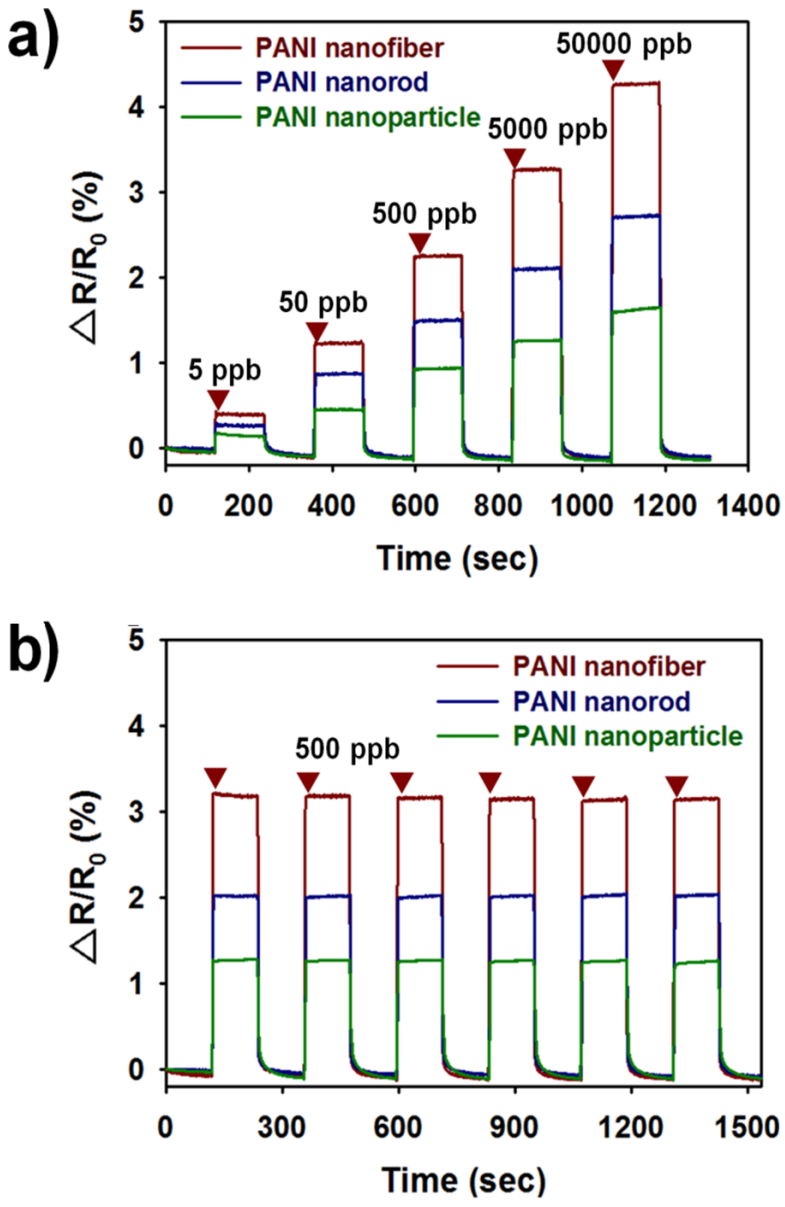

Figure 28. (a) Real-time responses of PANI nanomaterials upon cyclic exposure to DMMP (5 ppb to 50000 ppb) and N_2 streams. (b) Real-time responses of PANI nanomaterials upon periodic exposure to 500 ppb DMMP.

to minimize R_I between the nanomaterials within the film. As mentioned above, PANI nanostructures become less aggregated with increasing aspect ratio of the nanomaterials. Thus, both intrinsic and extrinsic factors affected the $\Delta R/R_0$ ratio, affecting the sensitivity. Figure 28a plots the change in $\Delta R/R_0$ as a function of sequential exposure to DMMP (5, 50, 500, 5000, and 50,000 ppb). When the PANI nanomaterial was exposed to DMMP vapor, the resistance kept rising. After the DMMP vapor was removed, the resistance rapidly recovered to the original level. The sensor device had a short response time (less than 1 s) and recovered to nearly the initial conductivity within *ca.* 40 s. The detection limits of the PANI-based sensors were 5 ppb, which is three orders of magnitude better than that of PPy-based devices (Table 3) [135–138]. This high sensitivity and rapid response and recovery times are primarily due to a higher effective surface areas and shorter penetration depths with the PANI nanomaterials [11,119]. The Brunauer–Emmett–Teller (BET) surface areas increased in the order of NF (35 $m^2 g^{-1}$) < NR (40 $m^2 g^{-1}$) < NP (46 $m^2 g^{-1}$). In general, BET surface areas around 10^1 $m^2 g^{-1}$ were sufficient for reasonable sensing behavior (Table 4). In addition to the high sensitivities and fast responses, the sensitivities increased with an increasing concentration of DMMP and increasing aspect ratio of the PANI nanomaterial. This is consistent with the sensitivity being closely linked to the charge-transport properties,

Table 3. Chemiresistive sensor performance of this work toward DMMP compared with the literatures.

sensing materials	MDL (ppb)[a]	response/ recovery (s)	reference
PPy-CuPC	5000	10/80	[135]
PPy-POP	2000	1200/-	[136]
NDSA-PPy/Cu^{2+}	26000	-	[137]
NDSA-PPy	28000	-	[138]
PANI nanomaterials	5	1/40	This work

[a] Minimum detection limit.

Table 4. BET Surface areas of PANI nanomaterials obtained by N_2 adsorption/desorption characteristics.

sensing materials	aspect ratio	surface area ($m^2\ g^{-1}$)	total pore volume ($cm^3\ g^{-1}$)
NFs	≈25	35.3	0.15
NRs	≈7.5	40.2	0.17
NPs	≈1.5	46.4	0.19

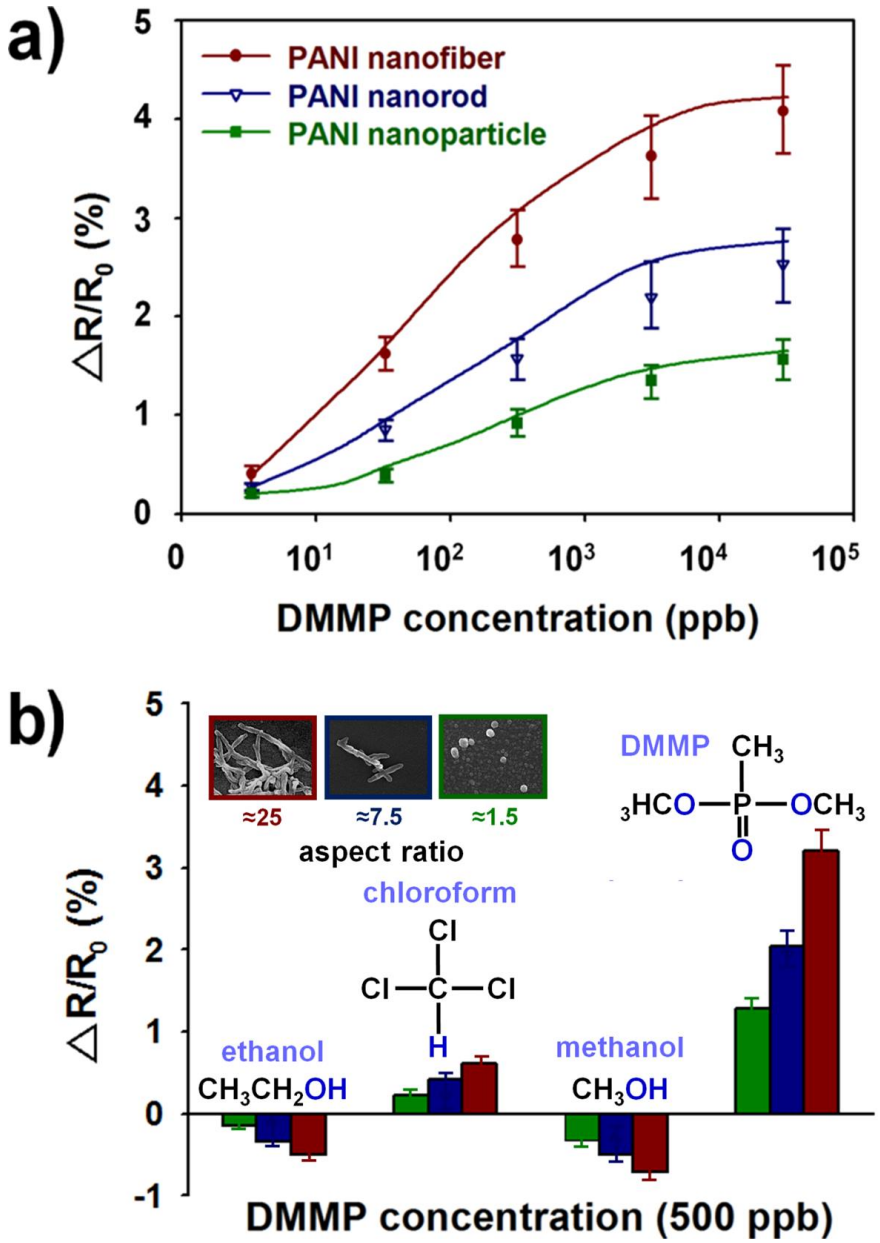

Figure 29. (a) Changes in saturated sensitivity of PANI nanomaterials as a function of DMMP vapor concentration. (b) Normalized response graphs of the PANI nanomaterials to different organic vapors at 500 ppb.

which are affected by the PANI nanomaterial morphology. The nanomaterials were exposed periodically to DMMP vapor to further investigate the real-time response of the PANI-based sensors (Figure 28b). After repeated cycles of exposure and recovery to 500 ppb DMMP, the PANI-based sensors exhibited stable and sustained sensitivities. The PANI NFs had better response toward DMMP vapor than the NRs and NPs. The results were highly repeatable, indicating that these nanomaterials could be used over a long period.

The changes in saturated signal responses as a function of vapor concentration are plotted in Figure 29a. The curve for each of the nanomaterials saturated at *ca.* 10^4 ppb. The slope of the curve increased in the order of NP < NR < NF, which is consistent with the sensing performance upon exposure to DMMP vapor. The PANI nanomaterials were tested against several organic vapors including methanol, ethanol, and chloroform to evaluate their selectivity (Figure 29b). It is considered that the different sensitivity to organic vapor depends on the dipole moment (μ) [139]. The μ value was 3.62, 1.7, 1.69, and 1.04 D for DMMP, methanol, ethanol, and chloroform, respectively. Relatively polar molecule like DMMP produce large resistance change, whereas less polar molecules such as methanol, ethanol, and chloroform produce only small response. In addition, $-CH_3O$ groups in the nerve agents can act as weak hydrogen bond acceptors, rendering increased

hydrogen bonding interaction between the PANI structure and DMMP [113]. Consequently, the ability of PANI nanomaterials to perceive DMMP vapors was successfully examined.

3.2. Fabrication of organic solvent-dispersible porous PANI/CSA nanostructures and their applications

3.2.1. Fabrication of porous PANI/CSA nanostructures

The overall procedure for fabricating porous PANI/CSA electrodes from a solution of PANI/CSA is illustrated in Figure 30. In the first step, highly conductive PANI ES powders were created using a SSDP method [40,41]. The SSDP method was designed to promote the *para*-direction polymerization at -30˚C to achieve higher conductivity than the conventional methods. In this method, the protonated anilinium ions, which contain hydrophobic, hydrophilic, polar, and organic parts, act as interfacial stabilizers, allowing the excellent dispersion of organic phases into the aqueous medium [40,41]. The chloroform solvents separate insoluble oligomers and grown PANI chains in the aqueous phase, forming the PANI nanostructures, suppressing the undesirable side reactions, such as *ortho*-coupling and Michael reductive addition of aniline monomers. Importantly, the *para*-directed polymerization is induced by the SSDP method, which may result in the high quality PANI nanostructures with

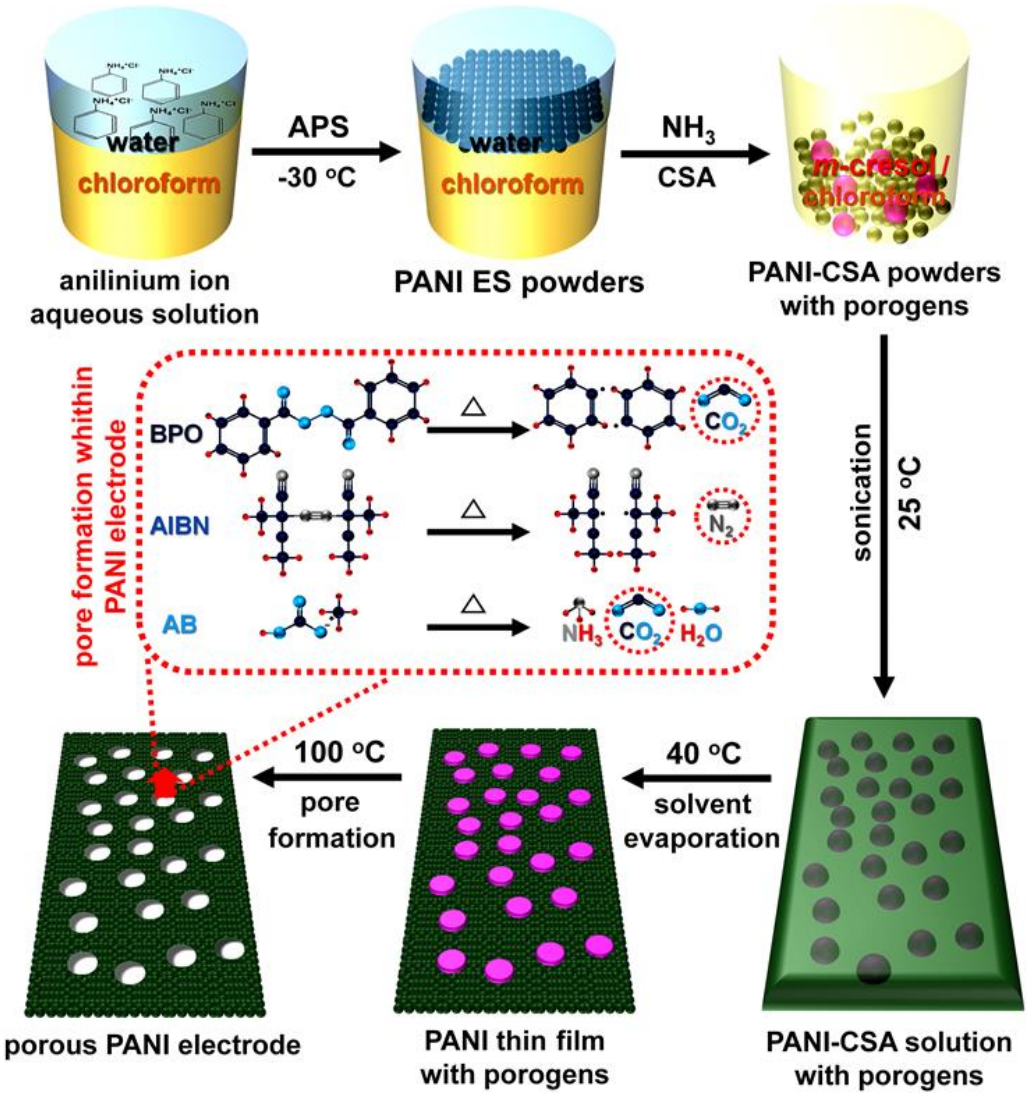

Figure 30. Overall procedure for fabricating porous PANI/CSA nanostructured electrodes.

lower defects and enhanced charge transport properties compared to the conventional methods [30,140]. NH_3 was used as the reducing agent to remove the primary dopant (HCl) from the PANI ES while the nitrogen atoms along the quinone diamine segment (–N=Q=N–) within the PANI structure for secondary doping. CSA was selected as a secondary dopant for the PANI emeraldine base (EB). Secondary doping changes the structure of PANI from a compact coil to an expanded coil [39].

Perforated and porous nanostructures were observed in both PANI ES and PANI/CSA powders (Figure 31). Such porous structures may increase the solubility of the polymer in organic solvents such as *m*-cresol [40]. Furthermore, the nanostructures obtained from the SSDP method appeared to be grown radially, promoting the successive couplings of *para*-mode on benzene rings of aniline monomers, as mentioned above [40]. The sulfonic acid group ($–SO_3H$) of CSA forms a strong hydrogen bond with the hydroxyl group (–OH) of *m*-cresol, facilitated by the strong polarity and acidity of *m*-cresol. This strong compatibility of CSA molecules with the *m*-cresol solvents is a key reason for a dramatic increase in the conductivity of the PANI/CSA nanostructure [39−41]. This can slow CSA doping at the –N=Q=N– unit of PANI EB. Chloroform is capable of forming a hydrogen bond with *m*-cresol, which indicates that more CSA molecules can form hydrogen bonds with

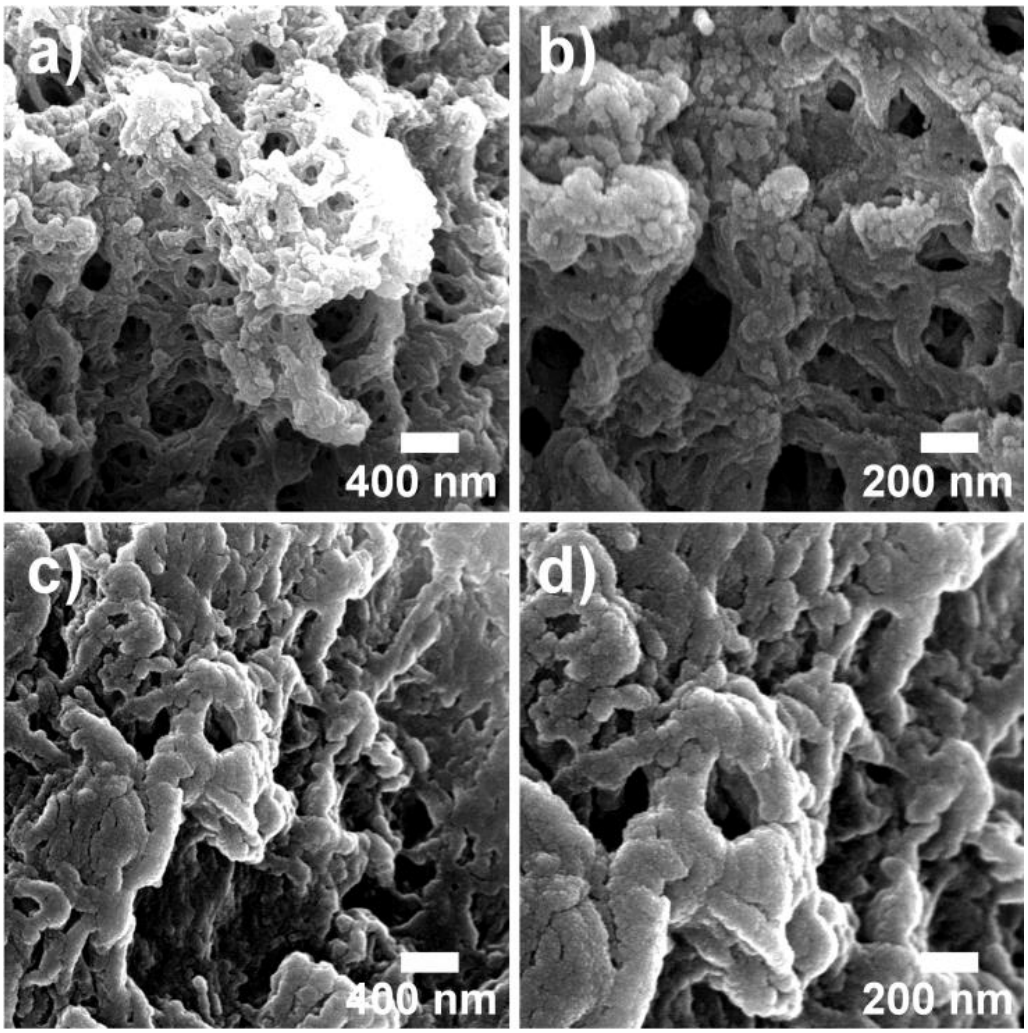

Figure 31. FE-SEM images of PANI powders: PANI ES before secondary-doping (a,b), PANI-CSA after secondary doping (c,d). Magnifications: ×45 (a,c) and ×90 (b,d).

$CHCl_3$ molecules. The increased interaction between CSA and $CHCl_3$, facilitates the diffusion of CSA in the system during aging. For these reasons, a co-solvent system composed of *m*-cresol/$CHCl_3$ (v/v=4:1) was used for dissolution of the PANI/CSA powders. Sonication was used to increase the solubility of PANI/CSA powders in the *m*-cresol/$CHCl_3$ co-solvent. The high viscosity of the PANI/CSA solution, 1.53×10^3 centipoise (cP), is also attributable to the sonication-assisted dissolution of PANI/CSA in *m*-cresol/$CHCl_3$ solvents. This high viscosity of the PANI/CSA solution is associated with increased hydrodynamic volume and rapid changes in the molecular conformation of PANI/CSA from a compact coil to an expanded coil [39]. Taking these facts into account, the *m*-cresol/chloroform co-solvent system was necessary to achieve both high conductivity of the PANI/CSA nanostructures and their practical applicability in the capacitor device. After dissolution in organic solvent, the porous aggregates of PANI/CSA changed to film-type nanostructures with a flat surface composed of nanoscale grains with diameters of ~40−60 nm. Thermally decomposing compounds, including BPO, AIBN, and AB, were added to the CSA-doped PANI as porogens, and the entire system was dissolved in the same solvent. As-prepared PANI/CSA solutions were cast as thin-film electrodes onto stainless steel mesh. The high compatibility of PANI/CSA with various substrates can be attributed to the

high surface polarity and wettability of the *m*-cresol solvent. Pore formation in the PANI thin films was induced thermally. Upon heating, gases (CO_2 from BPO and AB, and N_2 from AIBN) were emitted from the surface of the PANI/CSA electrode, generating pores of various diameters and shapes. The porous PANI/CSA thin films were presumed to benefit from the resulting enhancement of the surface area, which facilitates charge transfer and charge-discharge between the PANI electrode and the surrounding electrolyte.

Figure 32 and 33 show FE-SEMs of the PANI thin films. Grain size was ~40−60 nm in both pristine film and those that had been made porous by BPO, AB, and AIBN (Figure 32). Pore sizes in the BPO- and AB-PANI/CSA were ~ 45 and 50 nm, respectively, indicating that CO_2 gas had been released by decomposition of the porogen (Figure 32b, d, 33b, and d). The AIBN-PANI/CSA film had two types of pores with diameters of about 50 and 150 nm (Figure 32c). Pores 50 nm in diameter were found in specific regions at the film surface, while the larger pores were observed throughout the AIBN-PANI/CSA thin film (Figure 33c). These characteristics are thought to be due to the release of N_2 by the thermal decomposition of AIBN. Another factor affecting pore sizes may be associated with the decomposition rate (K_d) of the porogen agents. According to previous studies, the K_d value of AIBN is more than 10 times higher than the BPO at the same decomposition temperature

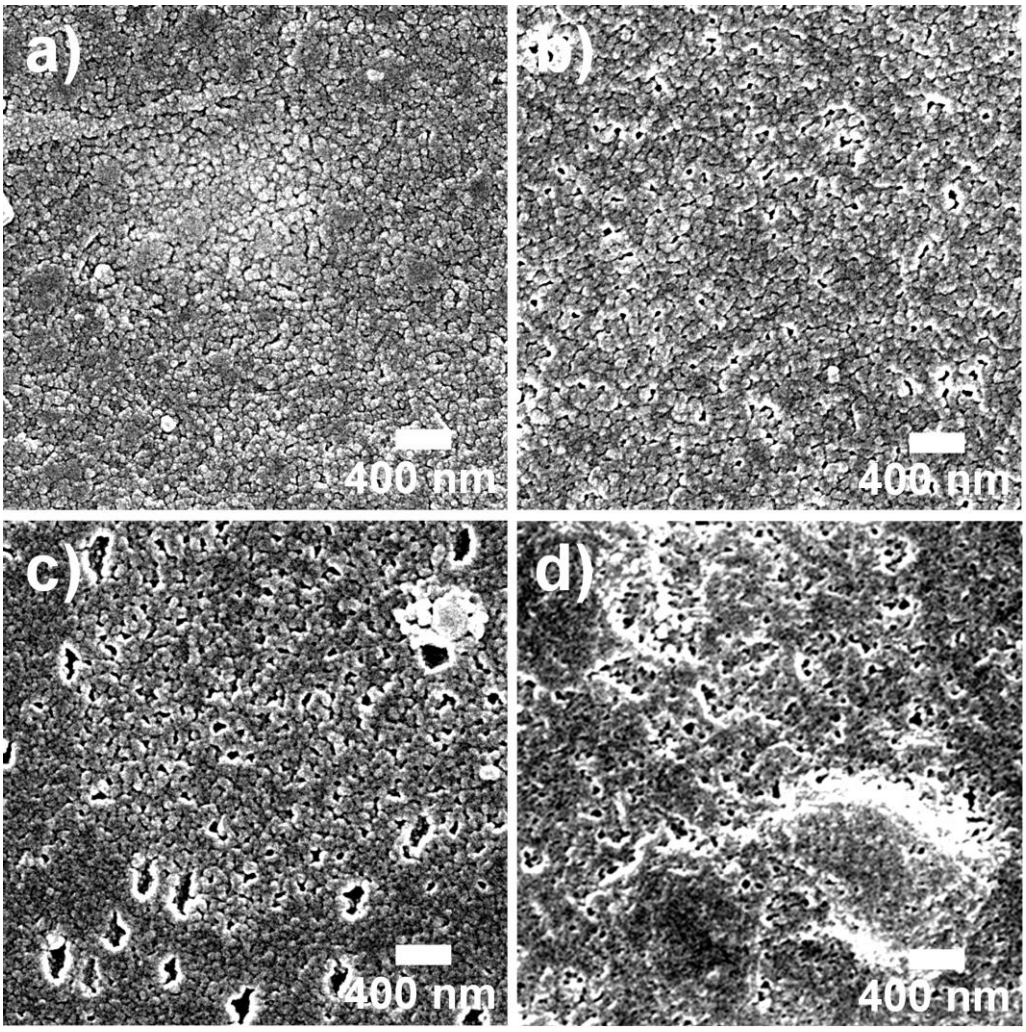

Figure 32. FE-SEM images of PANI/CSA thin films prepared by pore-forming process using different porogens: (a) pristine, (b) BPO, (c) AIBN, and (d) AB. Magnification: ×40k.

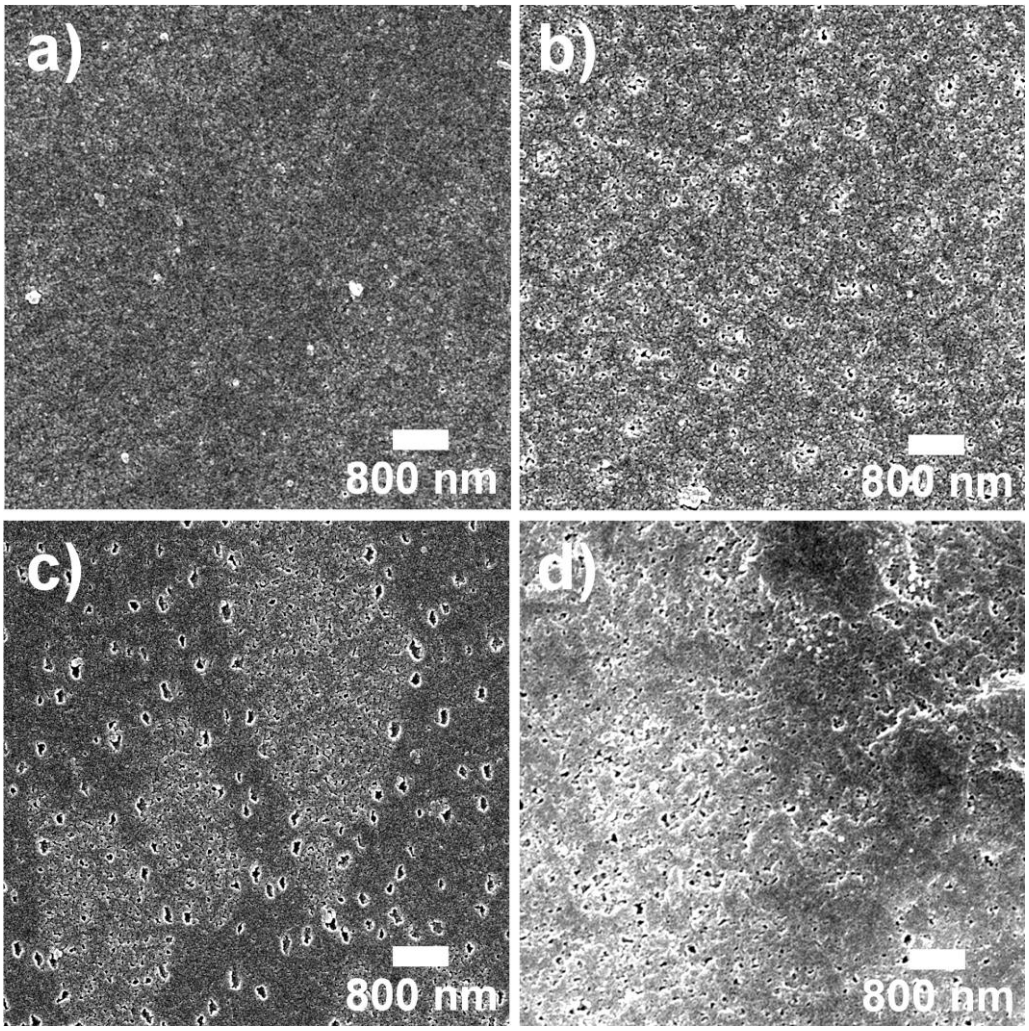

Figure 33. FE-SEM images of PANI/CSA thin films prepared by pore-forming process using different porogens: (a) pristine, (b) BPO, (c) AIBN, and (d) AB. Magnification: ×20k.

[141]. This indicates that the AIBN is more reactive than the BPO at the same temperature, resulting in wider pore size distributions and rougher surfaces. The AB molecules within the PANI/CSA thin films are decomposed at a lower temperature (60^{o}C) compared to the BPO (70^{o}C) and AIBN (65^{o}C) [142]. In addition, the NH_3 released from the thermal decomposition of the AB may also participate in the pore-forming reaction within the AB-PANI/CSA as well as the CO_2 gas [143]. Accordingly, the AB-PANI/CSA seemed to have rougher surfaces than the BPO- and AIBN-PANI/CSA. Based on these data, it is reasonable to assume that the use of all three porogens in a single film would result in entirely porous PANI/CSA thin films.

AFM was used to study the surface morphologies of the PANI/CSA thin films (Figures 34 and 35). The AFM images of the PANI/CSA thin films in Figure 34 show grain and pore sizes that are consistent with those determined by FE-SEM. Figure 35 shows the AFM images of the pristine and porous PANI/CSA thin films over a relatively wide area (10×10 μm^2). Highly porous nanostructures formed over the entire PANI/CSA surface. Interestingly, the AB-PANI/CSA seemed to have a rougher surface than did the BPO-PANI/CSA, although they exhibited similar pore sizes. Surface roughness (R_a) is a crucial factor affecting the electrical properties of PANI/CSA electrodes [16]. R_a values of the PANI electrodes increased as follows: pristine (2.37 nm)

< BPO (4.05 nm) < AIBN (4.67 nm) < AB (5.83 nm). Compared to the pristine PANI/CSA, surface roughness increased significantly as a result of porogenesis. However, the conductive regions within the porous PANI/CSA were well-connected, regardless of which porogen was applied. Moreover, porogen decomposition within the PANI/CSA thin films is thought to have contributed further to the increase in surface roughness during solvent evaporation. The effective surface area of the electrode increases with increasing surface roughness, which facilitates faster electron transfer between the electrode and the surrounding electrolyte. However, increasing surface roughness may also reduce carrier mobility along the PANI/CSA thin film, which may lead to a decrease in conductivity. The observed dependence of conductivity on R_a is shown in Table 5 [111,112]. The conductivity of the electrode material is important for collecting currents within the capacitor and DSSC devices. The internal resistance of PANI/CSA is assumed to increase with increasing R_a. This increased internal resistance makes it more difficult to form conductive channels within the PANI/CSA thin film. Therefore, the electrical properties of PANI/CSA thin films are strongly affected by R_a. Jung et al. [134] reported that very small changes in surface roughness can enhance charge transport. Accordingly, R_a must be high enough to facilitate electro-catalytic activity at the PANI/CSA electrode/electrolyte surface. The results of the present study

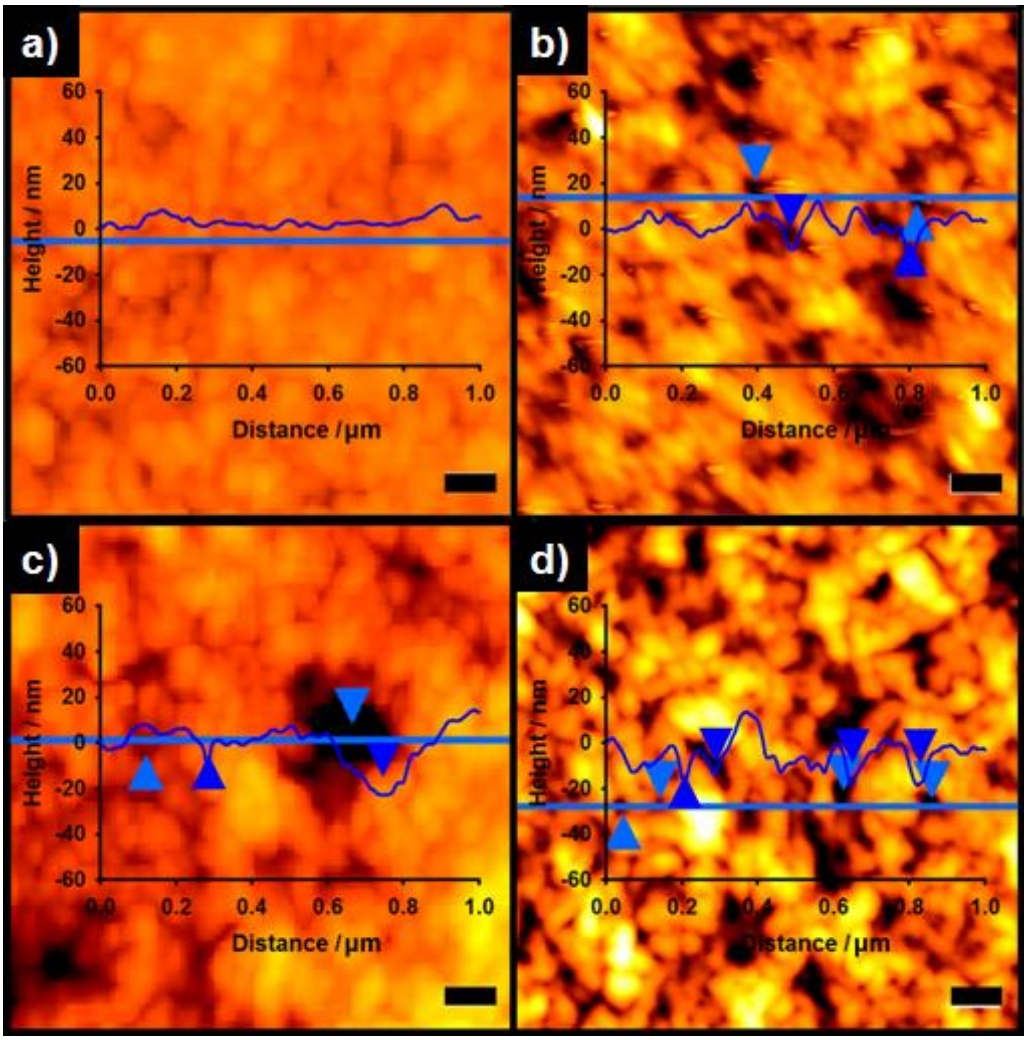

Figure 34. AFM images of PANI/CSA thin films with cross-sectional analyses (1×1 μm^2 scale): (a) pristine, (b) BPO-, (c) AIBN-, and (d) AB-PANI/CSA.

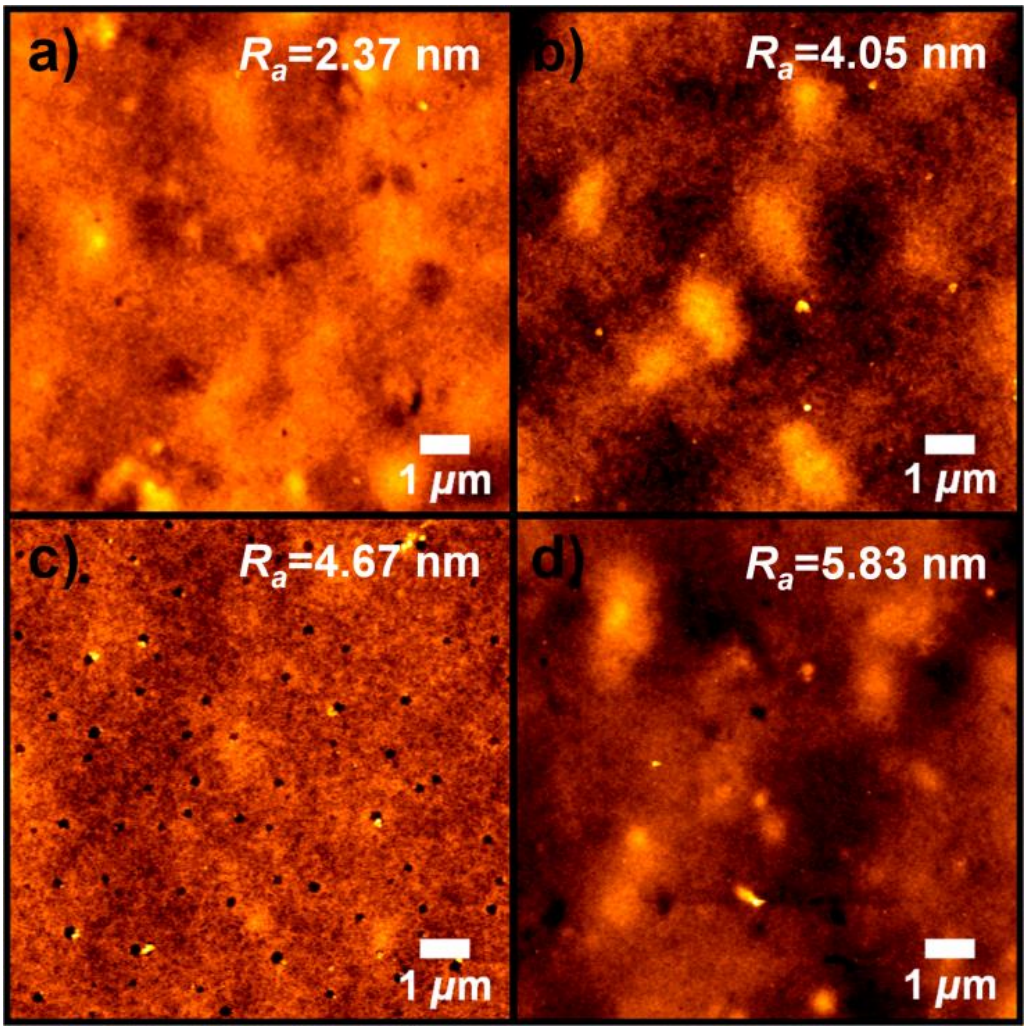

Figure 35. AFM images of PANI/CSA thin films after pore formation (10×10 μm^2 scale): (a) pristine, (b) BPO-, (c) AIBN-, and (d) AB-PANI/CSA.

show only a small loss in conductivity caused by varying amounts of porogen. This indicates that the porous PANI/CSA films possessed sustainable electrical properties. These data indicate that the BPO-, AB-, and AIBN-PANI/CSA films have high relative conductivities and large contact surface areas, making them suitable for use in supercapacitors (Table 5).

The XRDs in Figure 36 show the changes in crystallinity associated with increasing porosity and surface roughness. Three distinctive peaks were observed with PANI/CSA at 2θ = 15.2°, 20.8° and 25.5°. Previous reports [39,41], have shown that when a PANI/CSA sample becomes more metallic, the broad background decreases while the relative intensity of these three peaks changes with increasing conductivity, the peaks at 15.2° and 20.8° decrease and the peak at 25.5° increases. The diffractograms of the pristine, BPO-, AB-, and AIBN-PANI/CSA samples did not differ from each other and were similar to that of PANI/CSA [39,41]. The dominant peak at 25.5° is attributed to the degree of π-electron delocalization and the effective conjugation length of the PANI chains [39]. Increased delocalization results in better π-π* interchain stacking within the PANI/CSA structure and higher conductivity [41]. These results suggest that the degree of crystallinity in PANI/CSA was preserved throughout the film-forming process, resulting in good agreement with measured electrical conductivities.

Table 5. Relationship between surface roughness and conductivity of PANI/CSA thin films fabricated by using different porogens.

porogens	surface roughness (nm)[a]	conductivity (S cm^{-1})	relative conductivity (σ_{rel})[b]
pristine	2.37	628.5	1.00
BPO	4.05	603.7	0.96
AIBN	4.67	596.8	0.95
AB	5.83	573.5	0.91

[a] PANI/CSA thin films with 10 μm thickness were deposited onto the substrate.
[b] relative conductivity compared to pristine PANI: $\sigma_{rel} = \sigma/\sigma_0 \times 100$ (%).

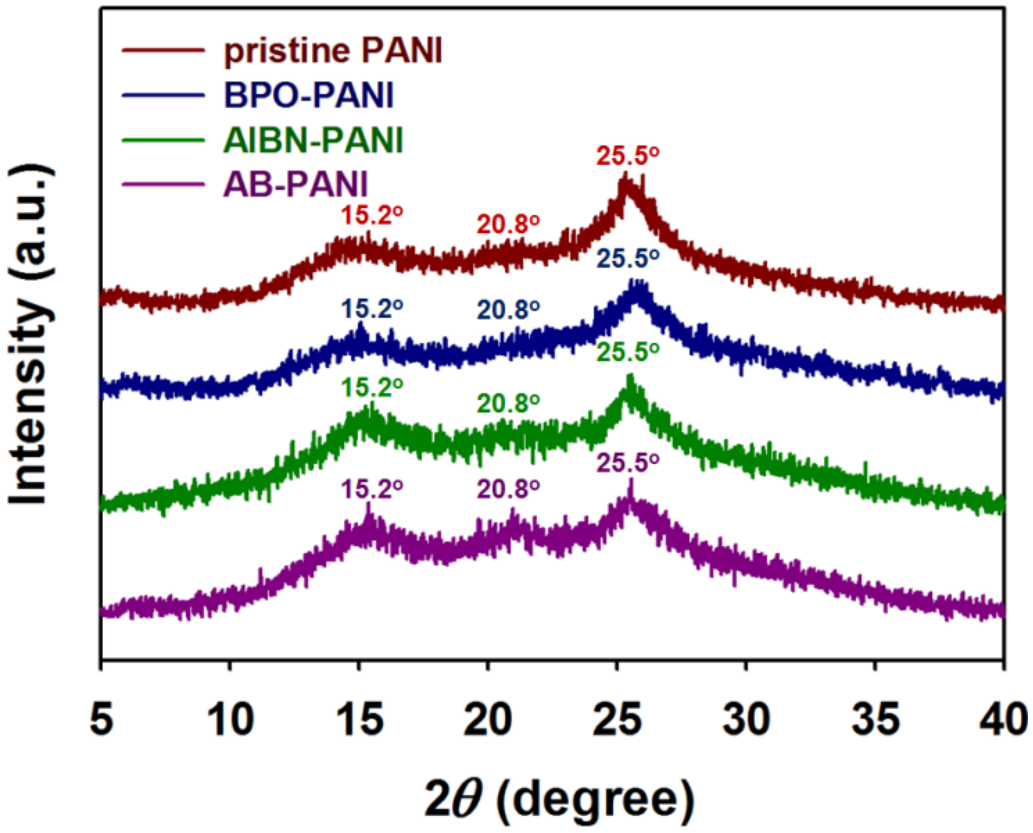

Figure 36. XRD patterns of PANI/CSA thin films fabricated by using different porogens.

UV/VIS/NIR and FT-IR spectroscopies were used to observe variation in the charge transport and chemical bonding properties of PANI/CSA thin films prepared with the different porogens (Figures 37 and 38). Figure 37 shows UV/VIS/NIR spectra of pristine and porous PANI/CSA thin films. Distinctive peaks at 320, 430, and 850 nm were assigned to π-π* transitions of the benzenoid ring (–N=B=N–), a localized polaron to π* transition and a π to polaron transition, respectively. Free-carrier tails, which extended from 1000 nm to beyond 2000 nm, were observed in every UV/VIS/NIR spectrum of the PANI/CSA thin films [39]. The presence of free carriers is characteristic of delocalized polaron band structures possessing longer conjugation lengths within PANI/CSA. This type of delocalized band structure is assumed to be originate from an expanded coil-like PANI structure. Solvation of dopant counterions is promoted by the diffusion of *m*-cresol molecules into the PANI/CSA chains, resulting in a local conformational change from a compact coil-like structure to an expanded coil-like one [39]. In PANI/CSA, this conformational change reduces twisting defects between polymer chains and elongates conjugation length. However, in the present study, no such changes occurred in pristine, BPO-, AB-, or AIBN-PANI/CSA. The charge transport properties of pristine PANI/CSA were retained in all of the porous PANI thin films.

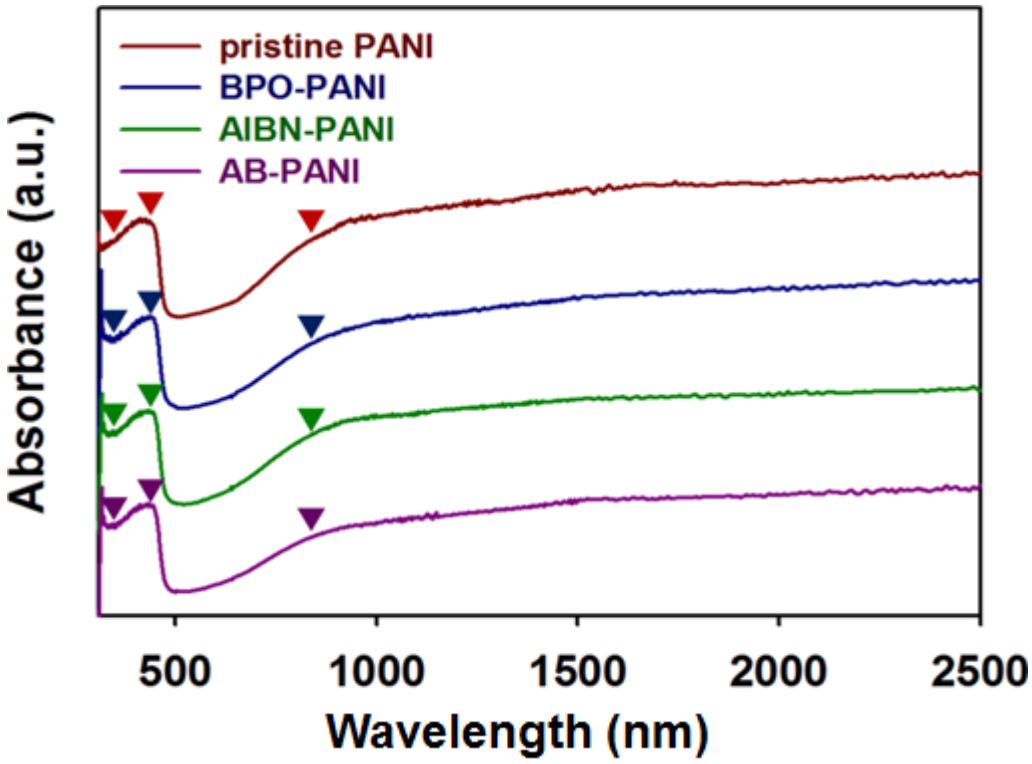

Figure 37. Distinctive bands in UV/VIS/NIR spectra of PANI/CSA thin films with different porogens.

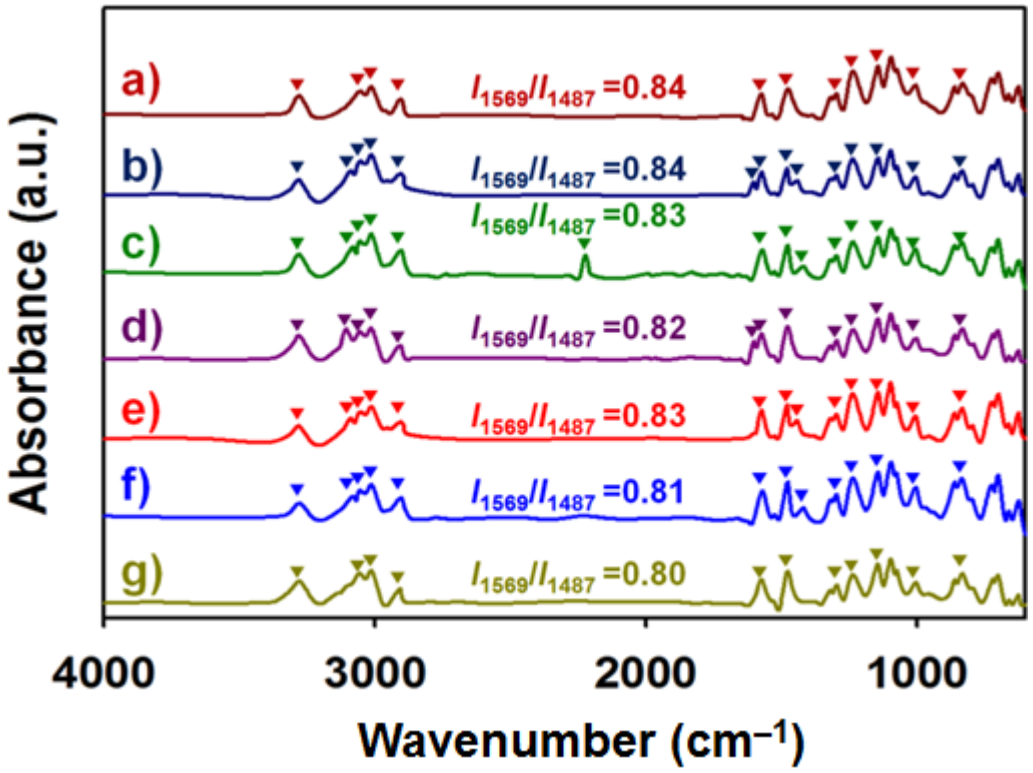

Figure 38. Distinctive bands in FT-IR spectra before pore formation of (a) pristine, (b) BPO-, (c) AIBN-, and (d) AB-PANI/CSA, and after pore formation of (e) BPO-, (f) AIBN-, and (g) AB-PANI/CSA.

To further investigate the changes in the chemical bonding properties associated with the pore formation, FT-IR spectra of the PANI/CSA are shown in Figure 38. Several bands that are assigned to the porogen agents were found in the FT-IR spectra of nanostructures. Absorption bands at 3085 cm^{-1} and 3091 cm^{-1} in the spectra of the BPO- and AB-PANI/CSA, respectively, are assigned to C−H symmetric stretching of the phenyl rings and the methylene unit [144,145]. The peaks for C–C stretching of the BPO and AIBN appeared at 1443 cm^{-1} and 1421 cm^{-1}, respectively [144,145]. The band at 2226 cm^{-1} is attributed to the C–N stretching of the C–N=N–C unit [145]. The band at 1603 cm^{-1} in the spectra of the BPO-PANI/CSA is ascribed to asymmetric stretching of the C−O bonds, and the peak also appeared in the spectra of the AB-PANI/CSA [143,144]. The absorption band at 3120 cm^{-1} in the spectrum of the AB-PANI/CSA was due to the stretching of the NH_4^+ [143]. After the pore-forming reactions within the thin films, the bands associated with the stretching of C−O, C−N, and NH_4^+ species were significantly reduced. These results indicate that the CO_2 (BPO and AB), N_2 (AIBN), and NH_3 (AB) gases were emitted from the PANI/CSA surface throughout the porogen decomposition. Several characteristic bands of PANI/CSA were observed in the FT-IR spectra of both nonporous and porous PANI/CSA samples. The band at 831 cm^{-1} was assigned to C-H out-of-plane bending of the 1,4-disubstituted rings. This band

is also indicative of *para*-position coupling of the benzene rings of aniline. The bands of 1293 cm^{-1} and 3282 cm^{-1} were ascribed to C−N and N–H stretching of the secondary aromatic amine, respectively [133,146,147]. The absorption bands for C−H symmetric stretching of both the quinoid (–N=Q=N–) and the benzenoid unit (–N=B=N–) appeared at 2906, 3012, and 3058 cm^{-1} [133]. The bands at 1142 cm^{-1} and 1569 cm^{-1} were designated to C=C stretching of the –N=Q=N– unit. These two bands are also associated with delocalization of electrons within PANI/CSA. The spectra also contain bands at 1487 cm^{-1}, which are attributed to C=C stretching of the –N=B=N– unit. Note that the intensity ratio of the bands at 1569 cm^{-1} (I_{1569}) and 1487 cm^{-1} (I_{1487}) indicates the conjugation length and doping level of the PANI structure [133]. The I_{1569}/I_{1487} ratios of the pristine, BPO-, AIBN-, and AB-PANI/CSA thin films were almost the same, indicating that charge transport properties were not significantly affected by pore formation. The band at 1010 cm^{-1} can be ascribed to the sulfate anion ($–SO_3^-$) of the CSA dopant. The band at 1234 cm^{-1} originated from the bipolaron structure and may be indicative of the conducting, protonated form. These results demonstrate that the charge transport properties of pristine PANI/CSA, such as doping level and conjugation length, were preserved in the porous PANI/CSA thin films.

3.2.2. Supercapacitors based on porous PANI/CSA nanostructures as electrode materials

The electrochemical performance of cells based on porous PANI/CSA thin-film electrodes were evaluated by CV and galvanostatic charge/discharge tests (Figure 39 and 40). Voltammograms of pristine and porous PANI/CSA electrodes were performed in 0.5 M H_2SO_4 from 0 to 1.0 V at a scan rate of 20 mV s^{-1} (Figure 39a). The anodic and cathodic peaks were attributed to leucomeraldine/emeraldine and emeraldine/pernigraniline transitions, respectively [65,115]. The electrochemical behavior of the PANI/CSA electrodes may be the result of Faradaic reactions at the PANI/CSA electrode/electrolyte surface. The BPO-PANI/CSA exhibited the highest electrochemical response. The area under the CV peaks obtained with pristine PANI/CSA electrode was smaller than those of the BPO-, AIBN, and AB-PANI/CSA electrodes. The results suggest that the formation of porous structures within the PANI/CSA thin films increases the electrode surface area, which results in faster redox reactions between the PANI electrode and electrolyte. The cells based on PANI/CSA thin-film electrodes also exhibited symmetric charge/discharge curves, which implies that their electrochemical behavior originates from pseudocapacitance (Figure 39b) [148]. The discharge time of the PANI/CSA electrodes were measured from the charge/discharge

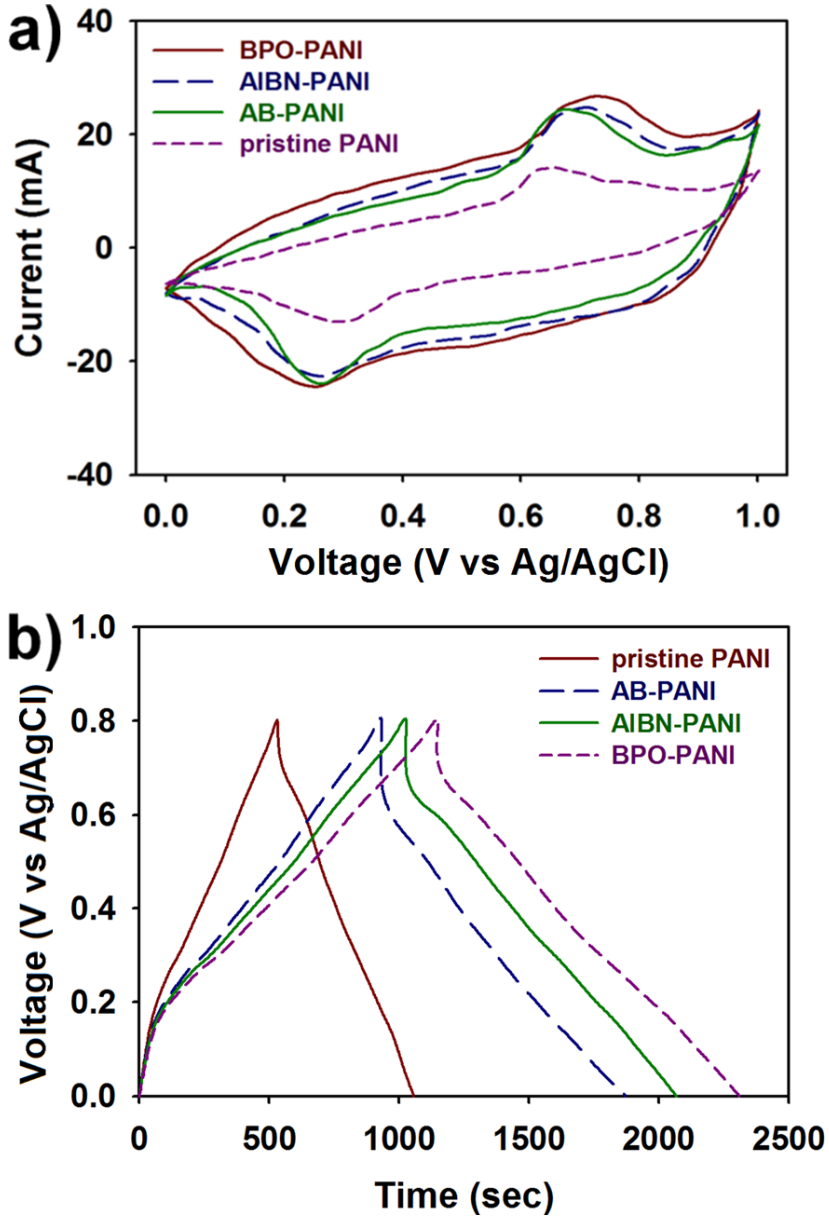

Figure 39. (a) Cyclic voltammograms of PANI/CSA thin-film electrodes scanned at 20 mV s^{-1} in 0.5 M H_2SO_4 electrolyte, (b) Galvanostatic charge/discharge plots of PANI thin-film electrodes at current density of 0.25 A g^{-1}.

Table 6. Specific capacitances and discharge times of PANI/CSA thin-film electrodes prepared by different porogens at a current density of 0.25 A g^{-1}.

porogen	specific capacitance (F g^{-1})[a,b]	discharge time (sec)[a,b]
pristine	165	532
BPO	361	1149
AIBN	323	1028
AB	293	933

[a] 0.025 mL of PANI/CSA solutions were used for forming thin films, resulting in a thickness of about 10 μm.

[b] The values were measured using a three-electrode system.

curves and the BPO-, AIBN-, and AB-PANI/CSA electrodes exhibited relatively longer discharge time than the pristine PANI/CSA electrode (Table 6). The results suggest that the highly porous structure at the PANI/CSA surface leads to a larger capacity. Overall, discharge times were proportional to the specific capacitance of the PANI/CSA electrodes [115,149]. The specific capacitances were 361, 323, 293, and 165 F g^{-1} for the BPO-, AIBN-, AB-, and pristine-PANI/CSA electrodes, respectively, at a current density of 0.25 A g^{-1} (Table 6).

Rate performance was evaluated by performing charge/discharge cycles at different current densities (Figure 40). The specific capacitances of the porous electrodes were higher than that of the pristine electrode. Specific capacitance decreased with increasing discharge current density. This decrease can be ascribed to diffusion of the supporting electrolyte. This suggests that a proportion of the electrode surface may be inaccessible at higher current densities. The BPO-, AB-, and AIBN-PANI/CSA electrodes maintained 69%, 67%, and 65% of their capacitance, respectively, with increasing current density while the pristine PANI/CSA film lost about 46% of its capacity in the same range of current densities. It is assumed that the porous structure facilitates their charge transfer during discharge. According to previous reports [71,150], the long-term stability of conductive polymer electrodes is restricted

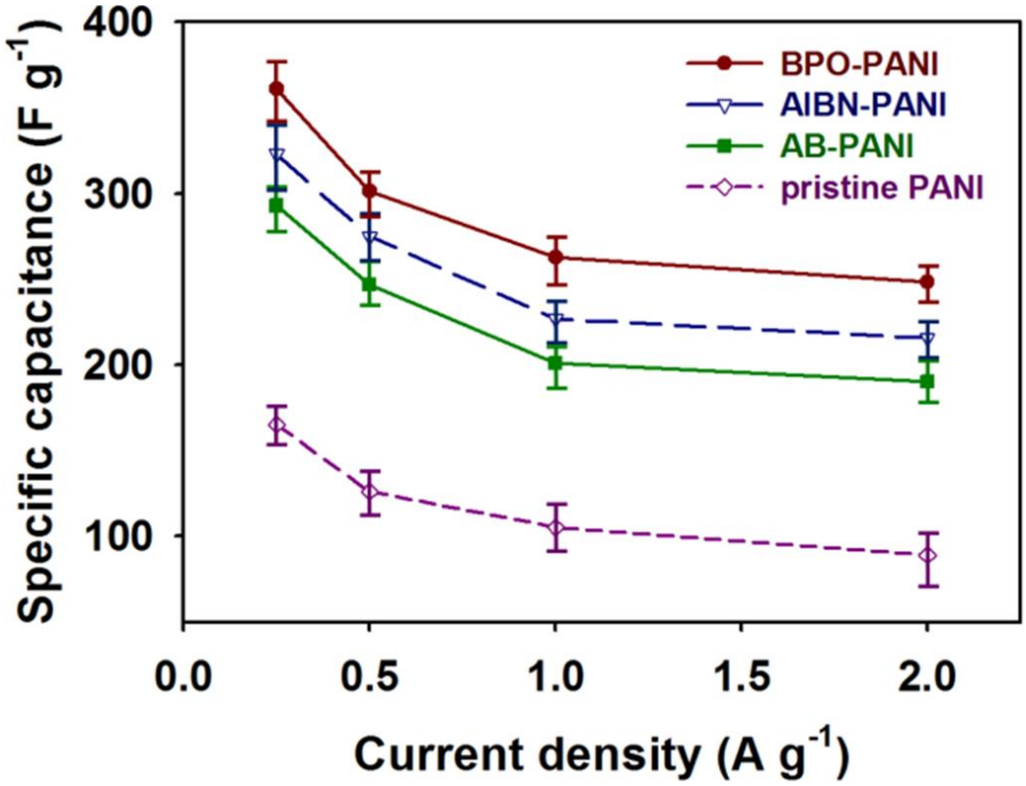

Figure 40. Specific capacitances of PANI/CSA thin-film electrodes at different current densities.

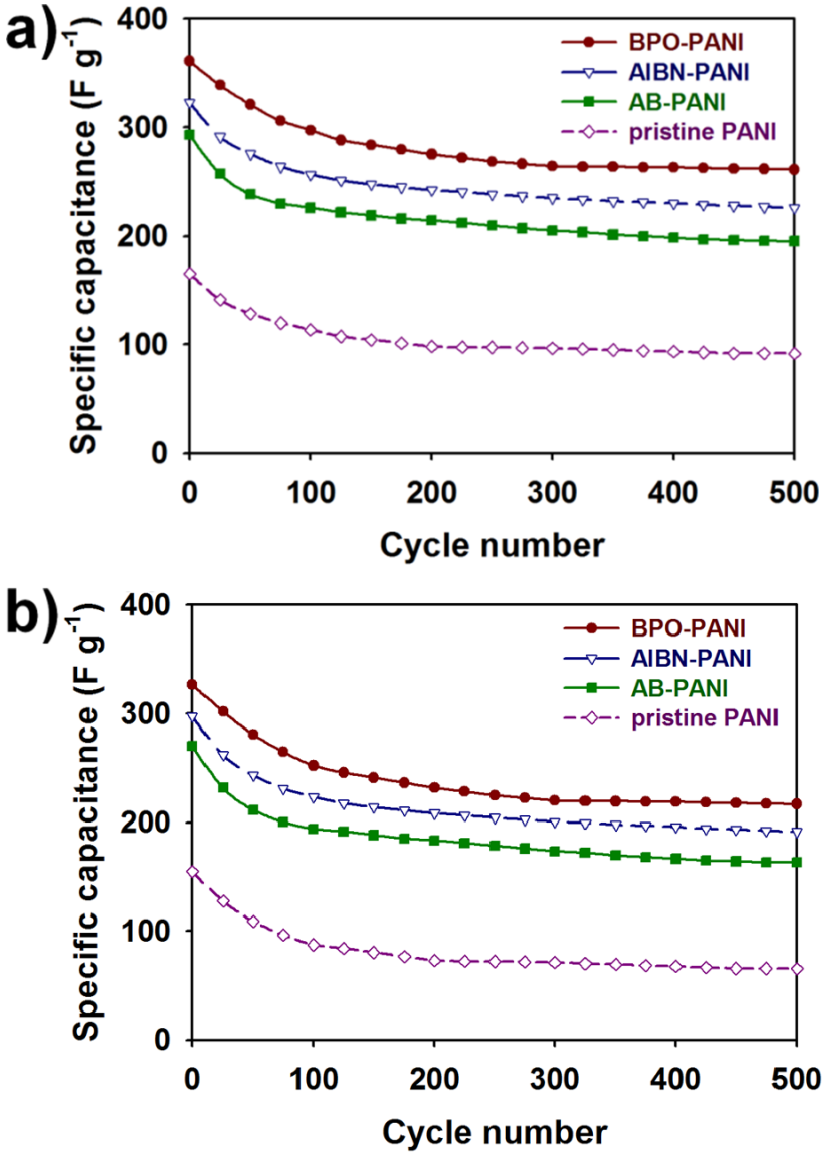

Figure 41. Cycling stability of PANI/CSA thin-film electrodes with different film thicknesses upon charge/discharge at a current density of 0.25 A g^{-1} (three-electrode cells): (a) 10 μm and (b) 50 μm. 0.025 and 0.25 mL of PANI solutions were used for forming thin films, resulting in a thickness of about 10 and 50 μm, respectively.

by degradation caused by swelling and shrinkage that occurs during voltage cycling.

The cyclic stability of the PANI/CSA thin-film electrodes was evaluated with galvanostatic charge/discharge cycles at a current density of 0.25 A g^{-1} (Figure 41). After 500 such cycles, the specific capacitances of the BPO-, AIBN-, AB-, and pristine PANI/CSA electrodes with a thickness of 10 μm decreased to 261, 226, 195, and 91 F g^{-1}, respectively, from their initial levels (Figure 41a). On depositing more PANI/CSA solutions (0.25 mL) on the electrodes (thickness of 50 μm), the specific capacitances of the BPO-, AIBN-, AB-, and pristine PANI/CSA after the 500 cycles decreased to 217, 191, 163, and 65 F g^{-1}, respectively (Figure 41b). Although the electrode surface seemed to become inaccessible with increasing mass loading of the electrode material, the increased mass loading only resulted in a small decrease in the specific capacitances of the samples [151,152]. The results suggest that these porous architectures facilitate redox reactions at the electrode/electrolyte surface while effectively minimizing the capacitance losses caused by degradation and shrinkage of the electrode materials.

3.2.3. DSSCs based on porous PANI/CSA nanostructures CEs

The overall procedure for the fabrication of porous PANI/CSA nanostructured CEs is illustrated in Figure 42. The prepared PANI/CSA solution was added to non-conducting glass substrates as a thin film by spin-coating. To produce high-PCE DSSCs, it is necessary to control the thickness of PANI/CSA. Catalytic material that is too thick has low connectivity between domains of the conductive area. The optimized thickness of porous PANI/CSA for CEs was chosen as *ca*. 10 μm.

The AFMs in Figure 43 and 44 show the changes in the surface roughness of PANI/CSA CEs resulted from different amounts (4.8−19.2wt% relative to that of PANI/CSA) of the BPO and AIBN. These porous PANI/CSA CEs were compared by comparing their heights using cross-sectional analysis. As the amount of porogen increased, the surface roughness of the PANI/CSA CEs increased, indicating that porogen decomposition within PANI/CSA causes incremental increases in surface roughness as well as solvent evaporation. Figure 45 displays the dependence of conductivity versus surface roughness for varying amounts of porogens. Conductivity of PANI/CSA CEs were measured using the four-line probe method [111,112]. Conductivity of PANI/CSA CE is susceptible to surface roughness, which involves the morphological information of PANI/CSA CEs. Although rougher surfaces of BPO- and AIBN-PANI/CSA CEs results in larger surface areas than that of pristine PANI/CSA

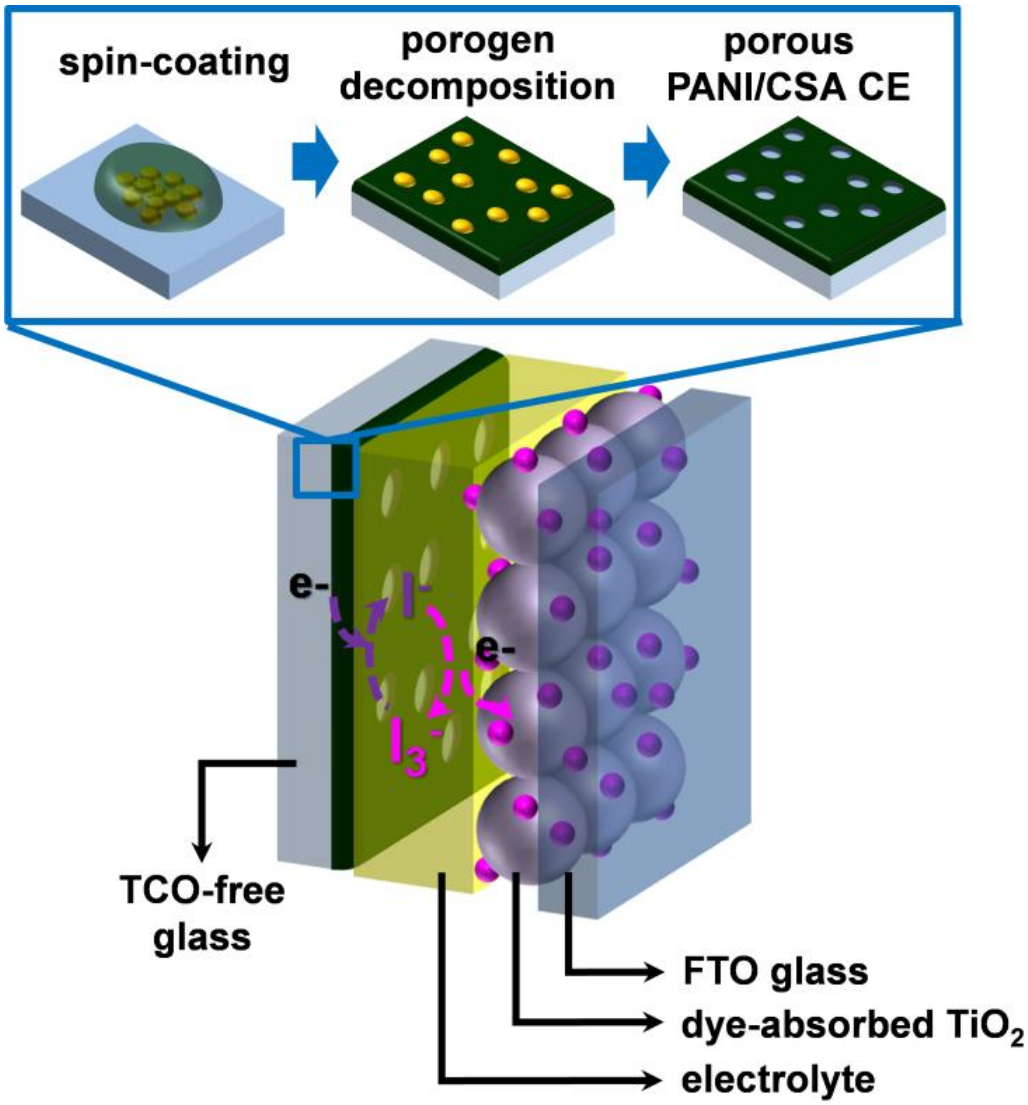

Figure 42. Overall procedure for the fabrication of PANI/CSA porous CEs for DSSCs.

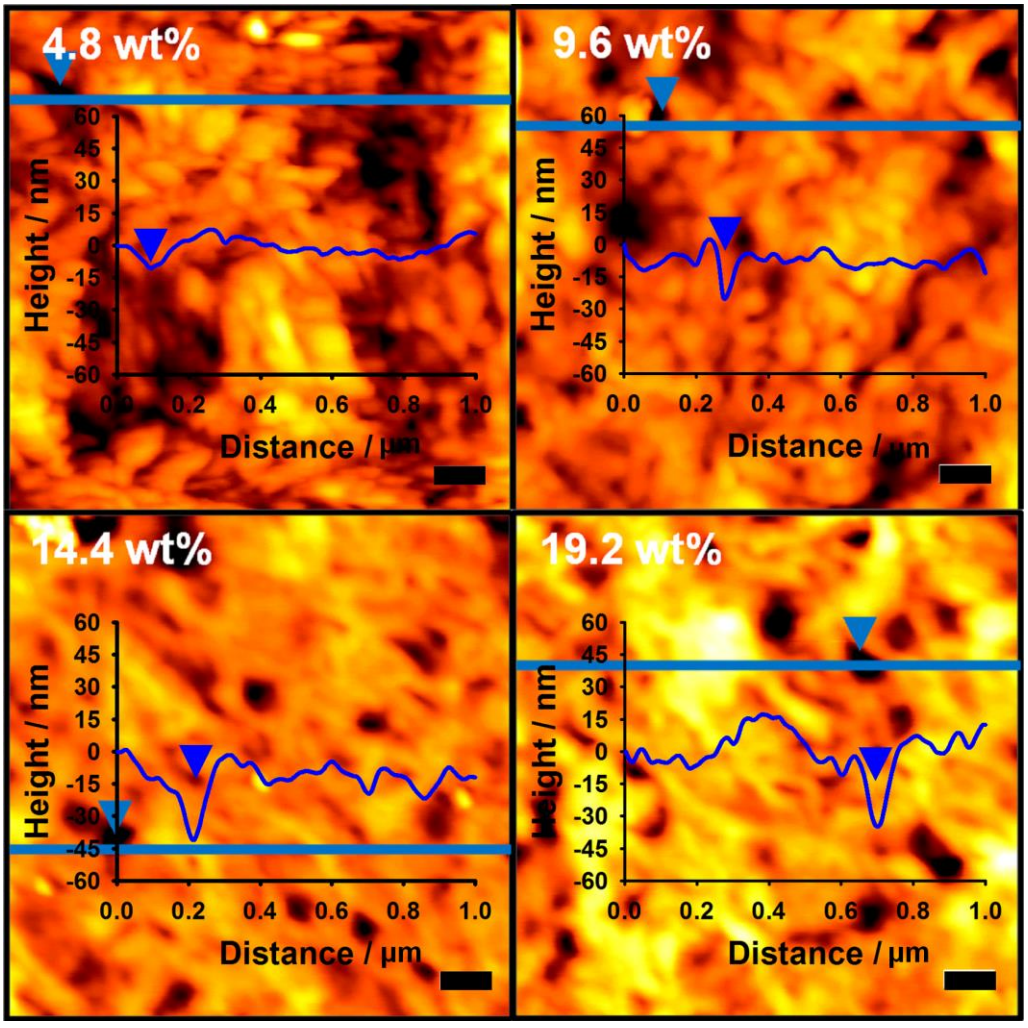

Figure 43. AFM images of PANI/CSA CEs fabricated by adding different amounts of BPO (bar size: 100 nm).

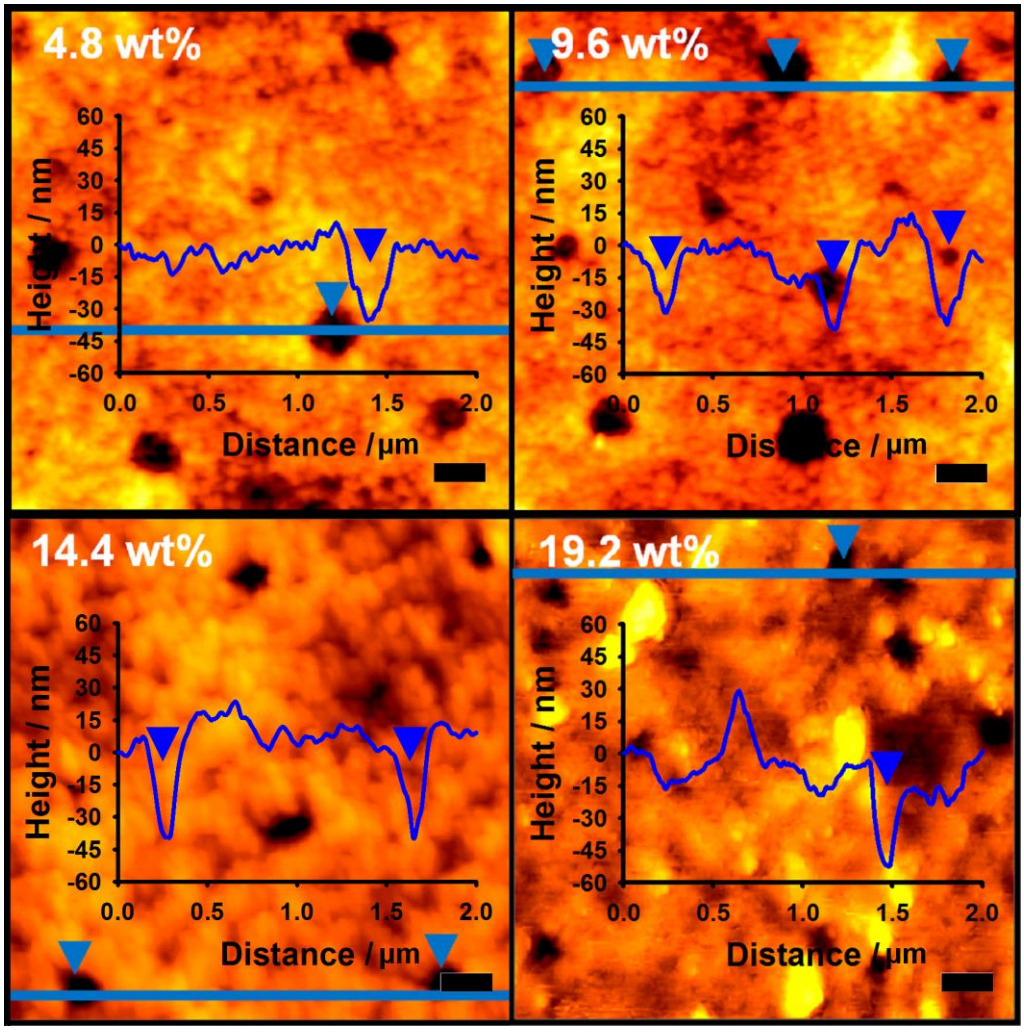

Figure 44. AFM images of PANI/CSA CEs fabricated by adding different amounts of AIBN (bar size: 200 nm).

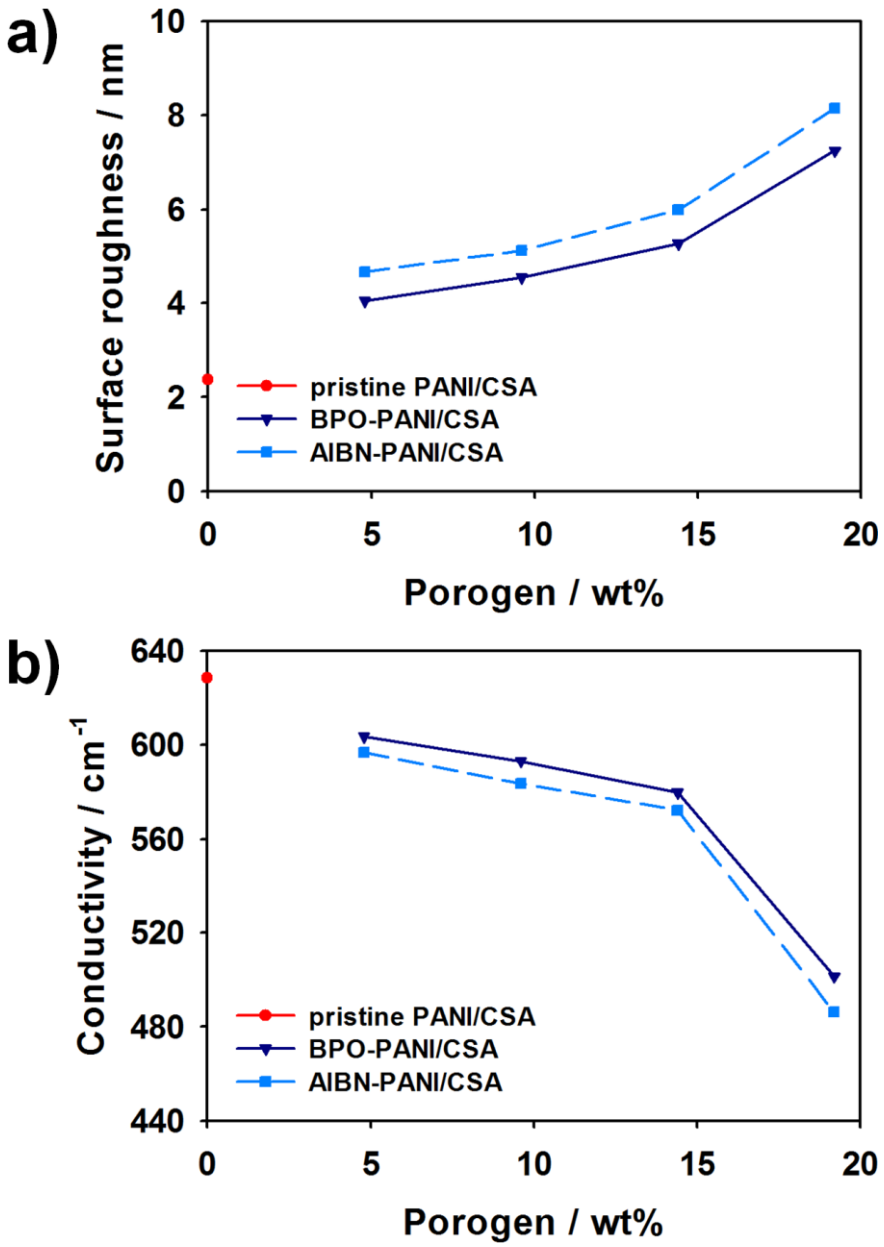

Figure 45. (a) Surface roughness and (b) conductivity of porous PANI/CSA nanostructured CEs fabricated by adding different amounts of porogens.

CE, the increase of surface roughness is a reason for reduced connectivity between conductive areas within PANI/CSA CEs (Figure 45a). Therefore, surface roughness of PANI/CSA CEs should be controlled properly to obtain well-retained conductivity of PANI/CSA CEs. More retained conductivity of BPO-PANI/CSA than that of AIBN-PANI/CSA is attributed to better connectivity between grains within BPO-PANI/CSA CEs, resulting in lower sheet resistance for the facile electron transfer and higher electro-catalytic activity at the CEs [16,134] (Figure 45b). In the present study, BPO (Figure 43) resulted in not only a porous structure, but also less surface roughness and thus a better connection between grains than AIBN (Figures 44). Therefore, our results suggest that BPO is more desirable porogen than AIBN. Importantly, favorable morphology of surface was achieved by optimizing the amount of porogen; this is a crucial factor for obtaining high-performance CEs in DSSCs, as discussed below.

CV, IPCE, and photocurrent density–voltage (*J*–*V*) tests were performed (Figures 46–51, and Table 7) to compare the overall performances of DSSCs with porous PANI/CSA nanostructures to that of Pt-coated ITO. To understand the influence of the porous structure on the electrochemical activity, cyclic voltammograms of PANI/CSA CEs and the Pt-coated ITO CE for the triiodide/iodide (I_3^- / I^-) redox couple were measured (Figures 46 and 47). The

Pt-coated ITO CE had cathodic and anodic peaks at -0.086 V and 0.46 V, respectively. The cathodic peak of Pt was assigned to the reaction of equation (4), and the anodic peak of Pt was assigned to the reaction of equation (5).

$$3I_2 + 2e^- \leftrightarrows 2I_3^- \quad (4)$$

$$I_3^- + 2e^- \leftrightarrows 3I^- \quad (5)$$

The cathodic peaks of the PANI/CSA CEs ranged from –0.14 to 0.04 V and corresponded to the reaction of eq. (4), and the anodic peaks of PANI/CSA CEs ranged from 0.68 to 0.92 V and corresponded to the reaction of eq. (5). Moreover, every PANI/CSA CE showed a different CV curve with different current density. The shapes of the CV curves were attributed to the redox-sensitive characteristic of PANI/CSA [133]. BPO-PANI/CSA CEs showed a strong anodic peak current in the range of 3.89 to 5.89 mA cm^{-2} and a cathodic peak current in the range of –3.04 to –4.26 mA cm^{-2} (Figure 46). The Pt-coated ITO CE and pristine PANI/CSA CE had anodic peak currents of −0.81 and 2.44 mA cm^{-2} and cathodic peak currents of −2.19 and −2.38 mA cm^{-2}, respectively. The increased photocurrent density for the anodic and cathodic peaks of porous PANI/CSA CEs indicates not only increased ability for transitions between leucomeraldine, emeraldine, and pernigraniline within the PANI structure [133] but also reflects rapid reduction of I_3^- to I^- at the porous

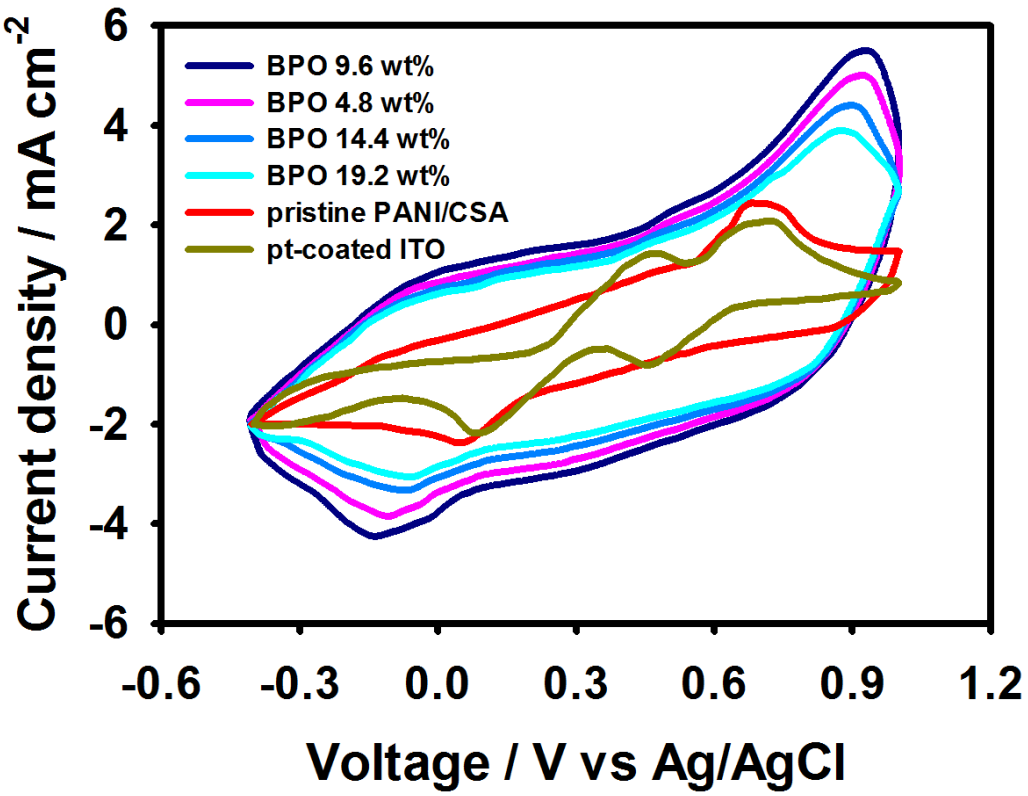

Figure 46. Cyclic voltammograms of porous PANI/CSA nanostructured CEs fabricated by adding different amounts of BPO and Pt-coated ITO CE at a scan rate of 50 mV s^{-1} under iodide redox electrolyte.

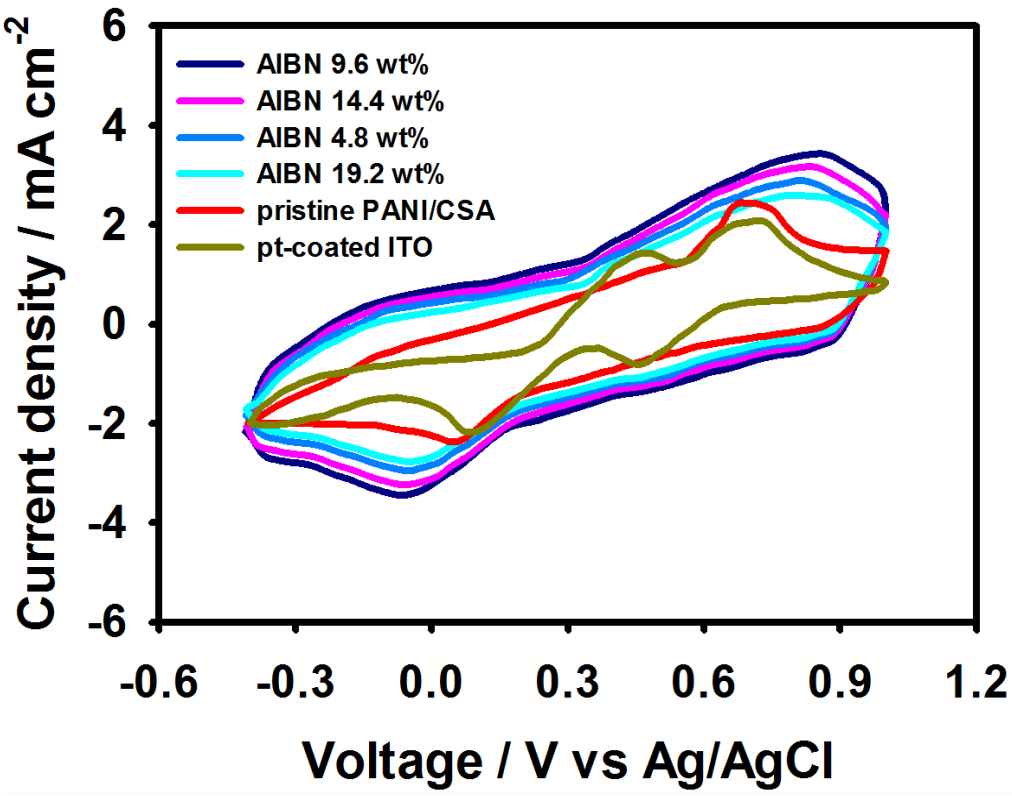

Figure 47. Cyclic voltammograms of porous PANI/CSA nanostructured CEs fabricated by adding different amounts of AIBN and Pt-coated ITO CE at a scan rate of 50 mV s^{-1} under iodide redox electrolyte.

PANI CEs. Although AIBN-PANI/CSA CEs had weaker current densities than BPO- PANI/CSA CEs, the anodic peak values (2.59 to 3.43 mA cm^{-2}) and the cathodic peak values (–2.78 to –3.45 mA cm^{-2}) were higher than those of Pt-coated ITO and pristine PANI/CSA CEs (Figure 47). Importantly, the higher electro-catalytic activities at BPO- and AIBN-PANI/CSA CEs than Pt-coated ITO and pristine PANI/CSA CEs are likely due to favorable roughness and porous structures resulting from the addition of optimal amounts of porogens. Consequently, porous PANI/CSA CEs with favorable surface morphologies offered larger surface area, resulting in higher electro-catalytic activity for diffusion of I_3^- and I^- ions in the CEs than do pristine PANI/CSA and Pt-coated CEs [90].

The IPCE spectra of DSSCs with PANI/CSA CEs and the Pt- coated ITO CE are shown in Figures 48 and 49. The IPCE curves of the CEs were measured by using the reported method [82]. The IPCE curve (λ) could be defined as equation (6),

$$IPCE\ (\%) = 1240(J_{sc} / \lambda \emptyset) \qquad (6)$$

where λ is the wavelength, J_{sc} is the current at short circuit (mA cm^{-2}), and $\emptyset$ is the incident radiative flux. BPO-PANI/CSA CEs had higher IPCEs than AIBN-PANI/CSA CEs. Every DSSC with a porous PANI/CSA CE had a higher IPCE than those containing pristine PANI/CSA. The optimized DSSC with the BPO-

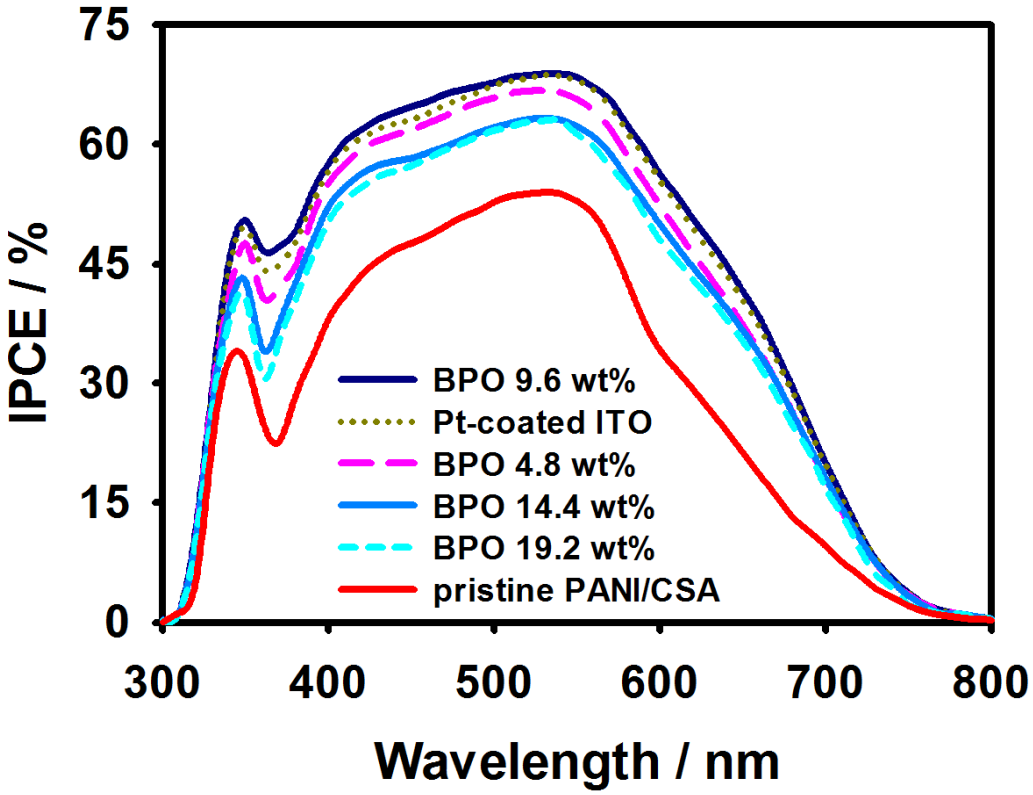

Figure 48. IPCE spectra of DSSCs with porous PANI/CSA nanostructured CEs fabricated by adding different amounts of BPO and Pt-coated ITO CE.

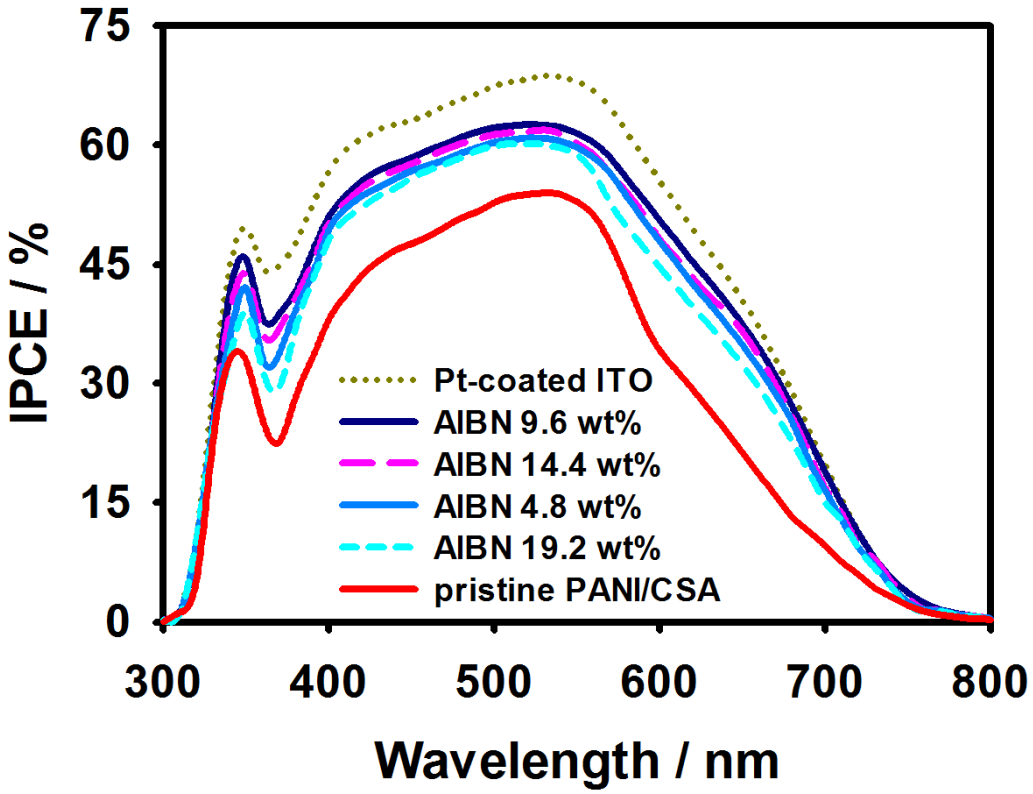

Figure 49. IPCE spectra of DSSCs with porous PANI/CSA nanostructured CEs fabricated by adding different amounts of AIBN and Pt-coated ITO CE.

PANI CE exhibited an equivalent IPCE, 68.86%, compared to the Pt-coated ITO cell (68.70%). The IPCE results indicate that the increased active surface area of porous PANI/CSA enhanced the ability of CEs to harvest light in the broad spectral region with increased emission of electrons per induced photons. Moreover, the photo-catalytic performances of PANI/CSA CEs were consistent with the results of surface roughness and electro-catalytic activity of PANI/CSA CEs.

The *J*–*V* characteristics of DSSCs with PANI/CSA CEs and the Pt-coated ITO CE are shown in Figure 50 and 51. Table 7 summarizes the photovoltaic parameters such as short-circuit photocurrent density (J_{sc}), open-circuit voltage (V_{oc}), fill factor (FF), IPCE (%), and overall PCE (η). As mentioned above, the DSSCs containing PANI/CSA CEs with appropriate surface roughness showed optimal DSSC performance. The DSSC containing the BPO-PANI CE showed the best performance of η = 6.23%, J_{sc} = 12.4 mA cm^{-2}, and V_{oc} = 0.80 V (Figure 50). The DSSC with the pristine PANI/CSA CE had η = 4.02%, J_{sc} = 9.16 mA cm^{-2}, and V_{oc} = 0.67 V. DSSCs containing AIBN-PANI/CSA CEs also exhibited enhanced PCEs of 5.24% compared to the DSSC with the pristine PANI/CSA CE (Figure 51). As aforementioned, higher J_{sc} of BPO- and AIBN-PANI/CSA than that of pristine PANI/CSA CE is due to enhanced electro-catalytic activity for facile reduction of I_3^- ions at the CEs, resulting

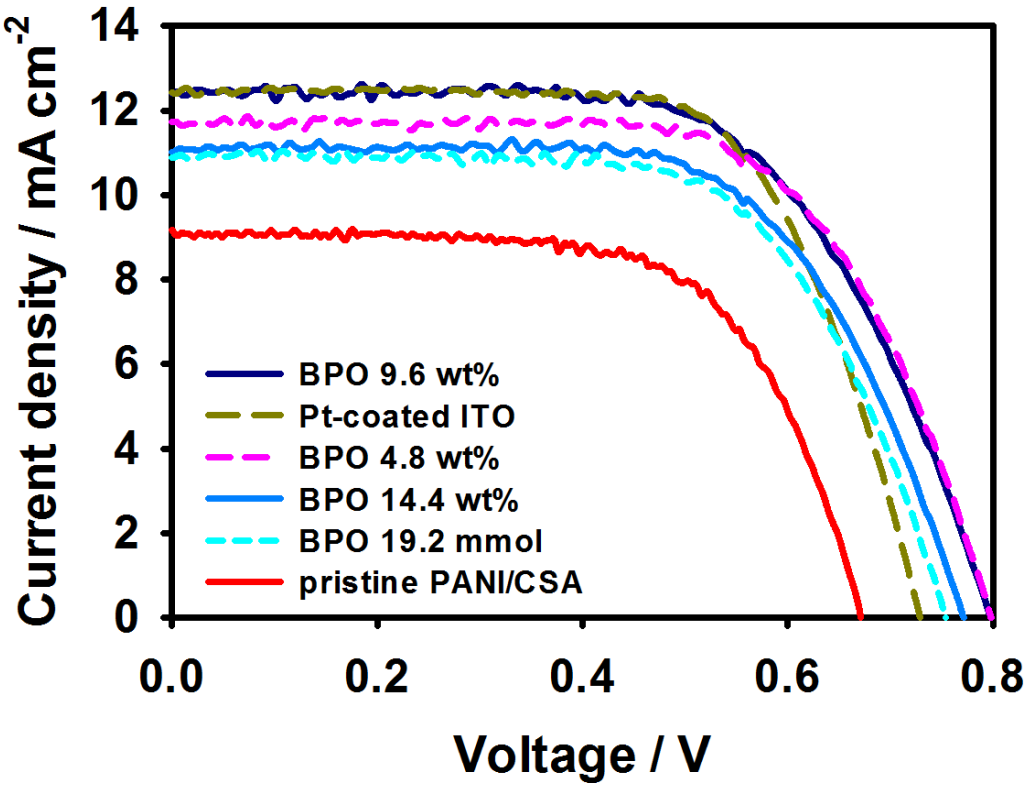

Figure 50. *J*−*V* characteristics of DSSCs with porous PANI/CSA nanostructured CEs fabricated by adding different amounts of BPO and Pt-coated ITO CE.

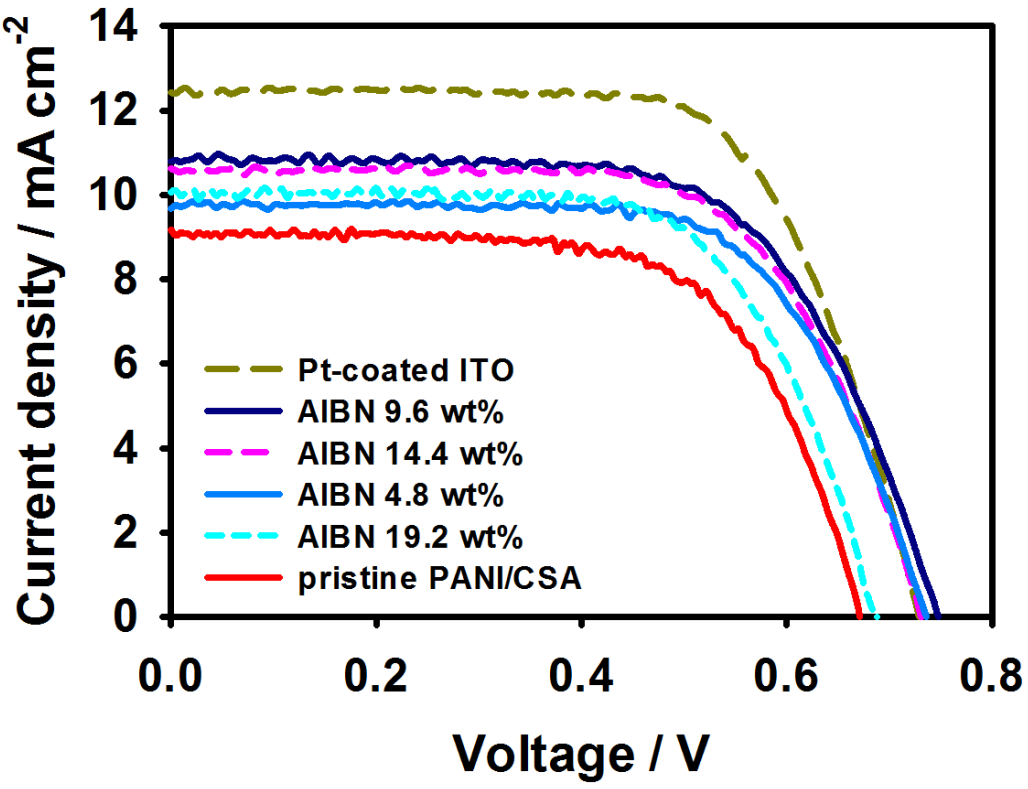

Figure 51. *J*−*V* characteristics of DSSCs with porous PANI/CSA nanostructured CEs fabricated by adding different amounts of AIBN and Pt-coated ITO CE.

Table 7. Photovoltaic performances of DSSCs with PANI/CSA nanostructured CEs and Pt-coated ITO CE.

porogen (wt%)	V_{oc} (V)	J_{sc} (mA cm^{-2})	FF	η (%)	IPCE (%)
Pt-coated ITO	0.73	12.4	0.68	6.17	68.70
pristine	0.67	9.16	0.65	4.02	53.98
BPO (4.8)	0.80	11.7	0.70	6.13	66.78
BPO (9.6)	0.80	12.4	0.67	6.23	68.86
BPO (14.4)	0.77	11.0	0.69	5.53	63.25
BPO (19.2)	0.75	10.9	0.70	5.38	62.98
AIBN (4.8)	0.74	9.69	0.72	4.82	60.83
AIBN (9.6)	0.75	10.8	0.69	5.24	62.49
AIBN (14.4)	0.73	10.6	0.69	5.11	61.90
AIBN (19.2)	0.69	10.1	0.67	4.62	60.09

from favorable surface morphologies of BPO- and AIBN-PANI/CSA CEs [68,73]. In addition, higher J_{sc} of BPO-PANI/CSA CE compared to AIBN-PANI CE could be attributed to small loss of conductivity, indicating that better electron transfer at the BPO-PANI/CSA CE. Moreover, the increased electro-catalytic ability for fast reduction of I_3^- ions at the BPO- and AIBN-PANI/CSA CEs renders the reduced availability of I_3^- ions for recombination with photoinjected electrons, resulting in higher V_{oc} of BPO- and AIBN-PANI/CSA CEs than the pristine PANI/CSA CE [107]. However, pristine PANI/CSA CE has insufficient pores for diffusion of I_3^- and I^- ions compared to BPO- and AIBN-PANI/CSA CEs. Therefore, the structure of pristine PANI/CSA CE reduces effective sites for I_3^- reduction, resulting in the increased availability of recombination between I_3^- ions and the photoinjected electrons at the CE. According to equation (7), V_{oc} is the difference between the Fermi level of TiO_2 semiconductor (E_{F,TiO_2}) and the formal potential of the I_3^-/I^- ($\varphi_{I_3^-I^-}$) couple in the redox electrolyte [91].

$$V_{oc} = \left| E_{F,TiO_2} - \varphi_{I_3^-I^-} \right| \quad (7)$$

Assuming that the TiO_2 semiconductor in the DSSCs remains unchanged, V_{oc} depends on the $\varphi_{I_3^-I^-}$ of the CE. Because of enhanced diffusion and adsorption of I_3^- ions at the porous PANI/CSA CEs, $\varphi_{I_3^-I^-}$ of the porous PANI/CSA CEs shifts more positively than the pristine PANI/CSA CE. Thus, the higher V_{oc} of the

BPO- and AIBN-PANI/CSA CEs than the pristine PANI/CSA CE is attributed to the positive shift of formal potential of I_3^-/I^- redox reaction at the CEs [90,91]. Accordingly, porous PANI/CSA CEs had much higher electro-catalytic abilities than the pristine PANI/CSA CE. The maximum PCE of the Pt-coated ITO cell was η = 6.17%, and the value was almost the same as the maximum PCE of the porous PANI/CSA CE-based cell. In addition, the porous PANI/CSA CE-based cell had a higher V_{oc} of 0.80 V and the same J_{sc} of 12.4 mA cm^{-2} compared to the Pt-coated ITO cell (V_{oc} = 0.73 V and J_{sc} = 12.4 mA cm^{-2}). Although no significant trends in FF were observed, the overall FF of porous PANI/CSA CE-based cells was slightly higher than that of the pristine PANI/CSA CE-based cell. Notably, the relative efficiency of the porous PANI/CSA CE-based cell was 101.0% compared to the Pt-coated ITO CE-based cell. Thus, porous PANI/CSA CEs offered significantly enhanced DSSC performance, and thus offer new possibilities for obtaining high-performance DSSCs without using TCO or Pt.

3.3. Fabrication of water-dispersible PSS-based conducing polymer nanostructures and their applications

3.3.1. Fabication of Pd NPs-decorated porous P(ANI-*co*-ASA):PSS nanostructures for H_2 sensors

3.3.1.1. Fabrication of Pd NPs-decorated porous P(ANI-*co*-ASA):PSS nanostructures

The overall procedure for fabricating Pd NPs-decorated porous P(ANI-*co*-ASA):PSS, which is based on electrostatic polymerization followed by a porogen decomposition process, is illustrated in Figure 52a. In the first step, –SO_3H groups were introduced into the aniline (ANI) monomer by dissolving aniline-2-sulfonic acid (ASA) in the liquid monomer. Although the ASA has a high affinity for the aniline monomer, insoluble salts were formed when excess –SO_3H reacted with the protonated aniline groups (–NH_3). For this reason, a *co*-monomer system composed of ANI/ASA (8:2 by volume) was used for preparing the –SO_3H bearing monomer. The ANI-*co*-ASA *co*-monomers were protonated onto the positively charged anilinium ions (–NH_3^+) using HCl and subsequently incorporated into the negatively charged PSS ions [33]. $PdCl_2$ was used as a catalyst in the interaction with H_2 molecules, and Pd^{2+} ions of the $PdCl_2$ electrostatically combined with the –SO_3H groups of both the *co*-monomer and the PSS ions. The Pd^{2+} ions attached along the co-monomer/PSS

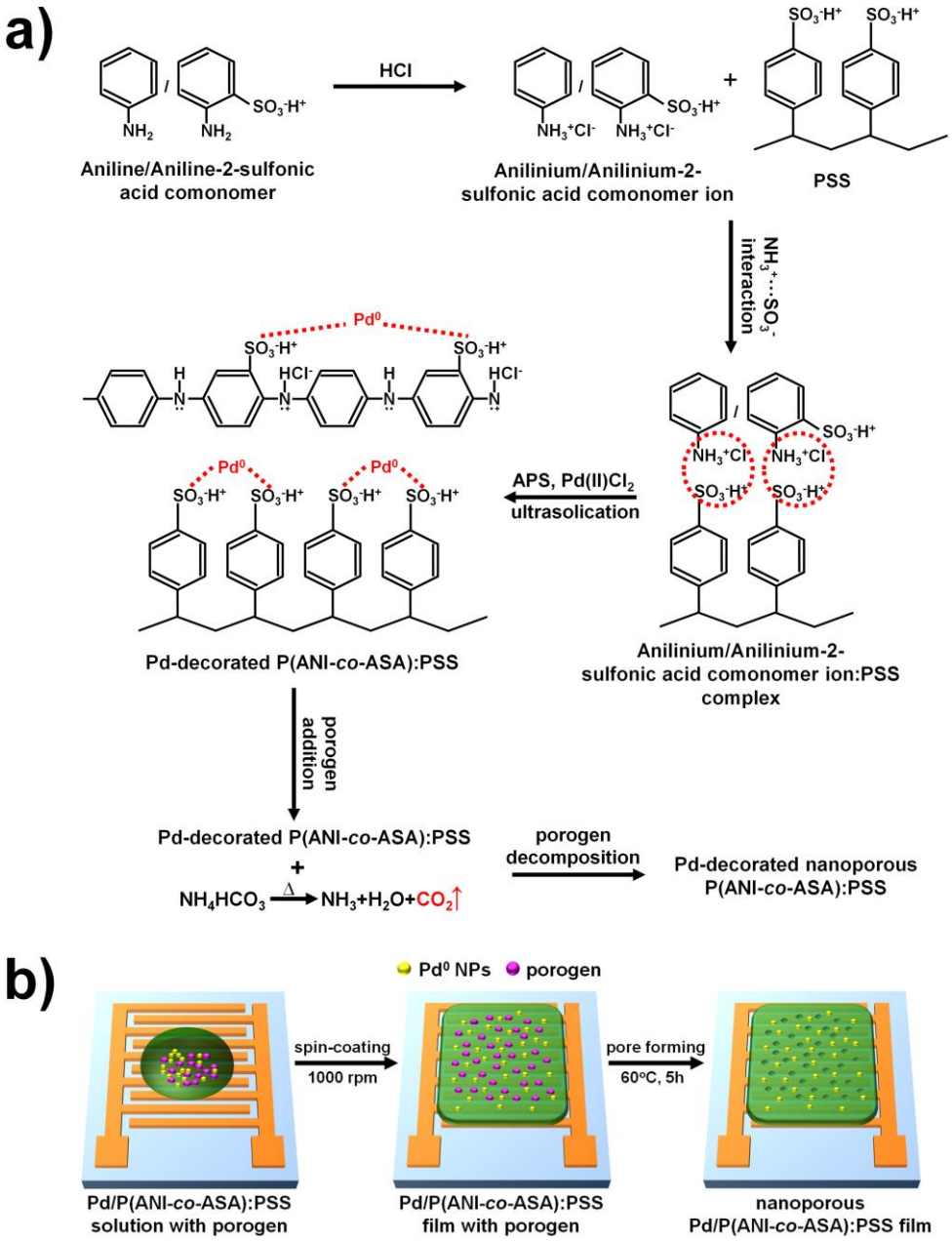

Figure 52. (a) Synthetic procedure for Pd NPs-decorated porous P(ANI-*co*-ASA):PSS nanostructure and (b) schematic illustration of porous P(ANI-*co*-ASA):PSS nanostructure in sensor application.

complexes were reduced to neutral Pd via sonication [153]. The polymerization of the Pd NPs-decorated co-monomer was facilitated using APS as an oxidizing agent. AB, a water-soluble porogen, was dissolved in the synthesized Pd NPs-decorated P(ANI-*co*-ASA):PSS solution. Upon heating, CO_2 gases from AB were emitted from the surface of the Pd NPs-decorated P(ANI-*co*-ASA):PSS electrode, generating pores on the surface. Figure 52b illustrates the fabrication of the sensor electrode employing the Pd NPs-decorated porous P(ANI-*co*-ASA):PSS. As-prepared Pd NPs-decorated P(ANI-*co*-ASA):PSS solutions were cast as thin films onto separate gold-interdigitated microelectrodes. Spin-coating was used to spread the Pd NPs-decorated P(ANI-*co*-ASA):PSS solutions evenly over the microelectrode, resulting in a uniform thickness of the nanostructures. Pore formation in the Pd NPs-decorated P(ANI-*co*-ASA):PSS thin films was conducted thermally, resulting in pores of 10–30 nm in diameter throughout the Pd NPs-decorated nanoporous P(ANI-*co*-ASA):PSS nanostructure. This porous structure is expected to increase the surface area, allowing improved H_2 diffusion compared with the material without the porogen and compared with the pristine P(ANI-*co*-ASA):PSS.

Figure 53a shows transmission electron microscope (TEM) images of the Pd NPs-decorated P(ANI-*co*-ASA):PSS nanostructures. The TEM method was

more advantageous for identifying the Pd NPs from the the P(ANI-*co*-ASA):PSS NPs than that of the FE-SEM and AFM method. In the TEM image of the Pd NPs-decorated P(ANI-*co*-ASA):PSS, tiny NPs, 3–10 nm in diameter, were well dispersed throughout the P(ANI-*co*-ASA):PSS NPs, which were 20–30 nm in diameter (Figure 53a). According to previous results, the particle sizes of the Pd are known as *ca.* 5 nm [153,156−159]. Hence, the NPs with diameters of 3–10 nm are assigned to the Pd NPs. The sizes and shapes of the Pd and P(ANI-*co*-ASA):PSS NPs shown in the TEM image were consistent with the FE-SEM and AFM images as will be discussed below. The size distribution of the Pd NPs-decorated P(ANI-*co*-ASA):PSS nanostructures in aqueous solution was characterized using DLS, as shown in Figure 53b. The P(ANI-*co*-ASA):PSS NPs exhibited a narrow size distribution centered at 30 nm in diameter; the percentage of the Pd NPs-decorated P(ANI-*co*-ASA):PSS NPs with a diameter of 25–40 nm was more than 90%. A low-intensity peak corresponding to diameters in the range 3–10 nm is ascribed to Pd NPs. Based on these data, most Pd NPs were successfully loaded into the P(ANI-*co*-ASA):PSS surfaces and the Pd NPs-decorated P(ANI-*co*-ASA):PSS NPs have a narrow particle-size distribution [154,157].

Figure 54 shows FE-SEM images of the P(ANI-*co*-ASA):PSS nanostructures. The diameter of the pristine P(ANI-*co*-ASA):PSS NPs was

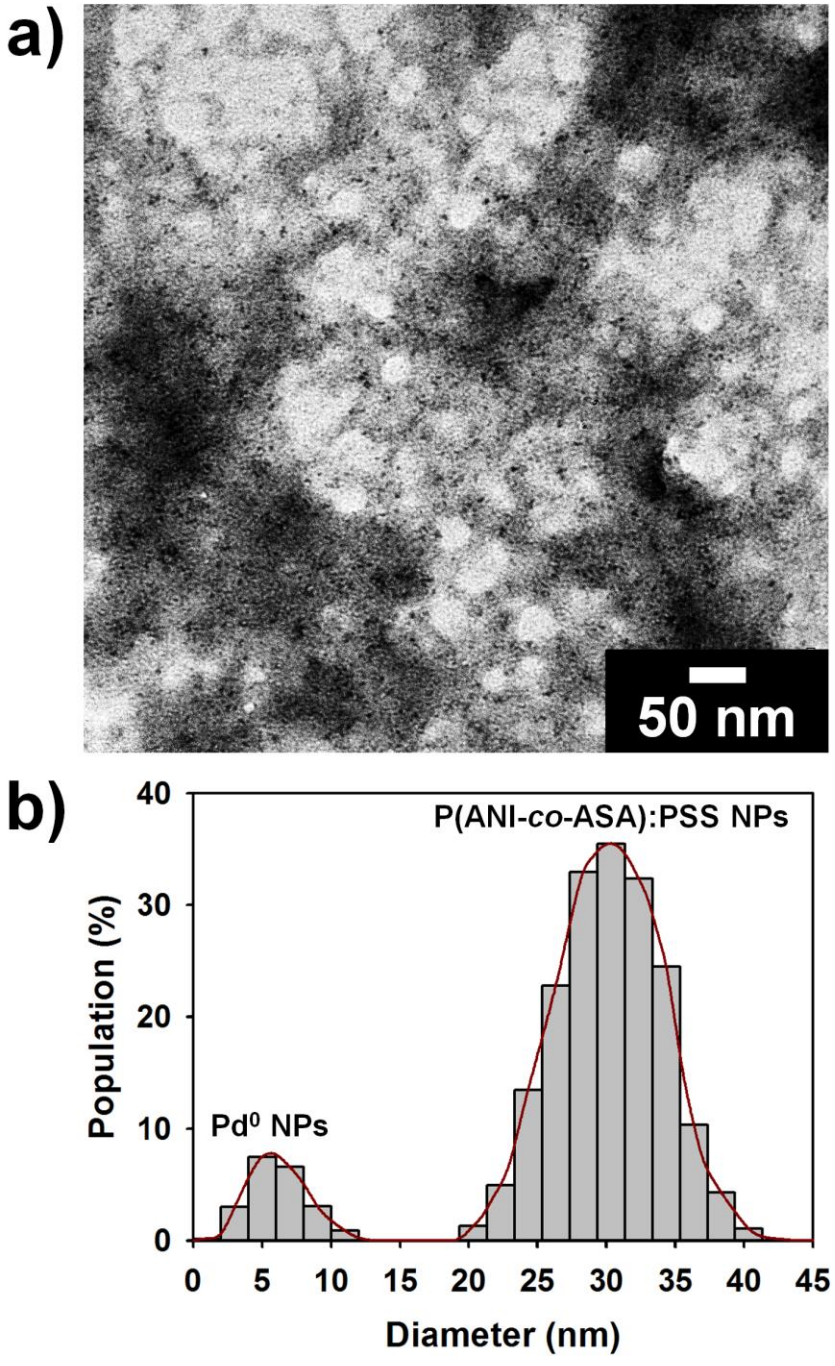

Figure 53. (a) A TEM image and (b) Particle size distribution curve of the Pd NPs-decorated P(ANI-*co*-ASA):PSS NPs.

around 25 nm, which is in agreement with the TEM image and the DLS results shown in Figures 54a and b. Following Pd loading, the diameter did not appear to significantly increase, based on the SEM images of the Pd NPs-decorated P(ANI-*co*-ASA):PSS over a wide area (Figure 54c). NPs that were 3–10 nm in diameter are thought to be Pd NPs and were observed throughout the Pd NPs-decorated P(ANI-*co*-ASA):PSS nanostructure over a smaller area, as shown in Figure 54d. After thermally inducing pore formation, pores that were 10–30 nm in diameter were observed throughout the Pd NPs-decorated P(ANI-*co*-ASA):PSS nanostructure (Figures 54e and f). As discussed above, this is expected to result from the release of CO_2 by the thermal decomposition of AB.

AFM was used to study the surface morphologies of the nanostructures, as shown in Figure 55. These cross-sectional analyses of the nanostructures show particle and pore sizes that are consistent with those determined by TEM, DLS, and FE-SEM. The Pd NPs-decorated P(ANI-*co*-ASA):PSS nanostructures appeared to have a rougher surface than the pristine P(ANI-*co*-ASA):PSS nanostructure, which had a flat surface composed of NPs with diameters of 20–30 nm. The presence of the pores was confirmed by cross-sectional analysis, and a highly porous network formed over the entire P(ANI-*co*-ASA):PSS surface following porogen decomposition. The increase in the surface roughness, R_a, may have resulted from porogen decomposition within the Pd

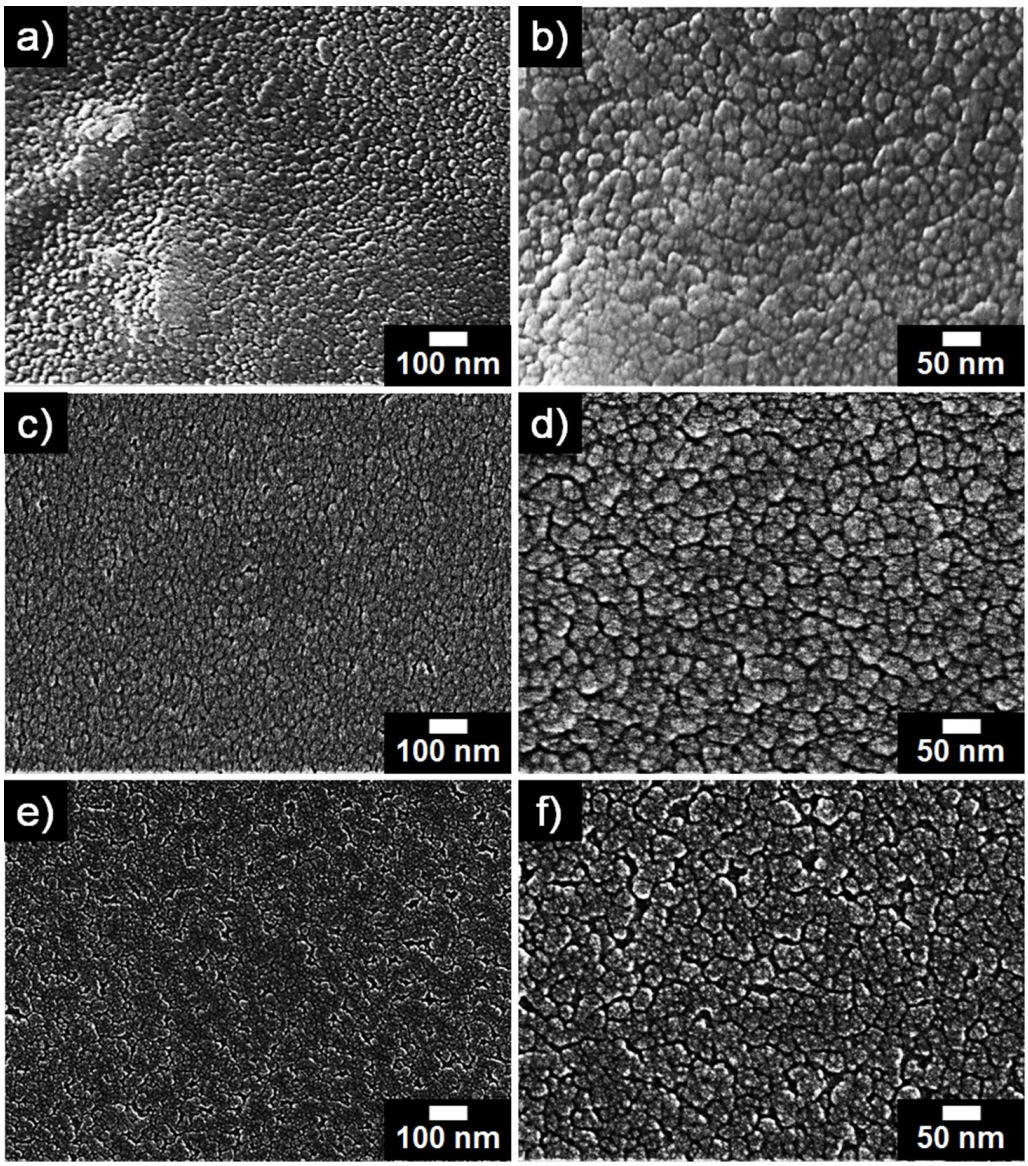

Figure 54. FE-SEM images of nanostructures: pristine (a,b), Pd NPs-decorated non-porous (c,d), Pd NPs-decorated porous P(ANI-*co*-ASA):PSS (e,f). Magnifications: ×40k (a,c,e) and ×80k (b,d,f).

NPs-decorated P(ANI-*co*-ASA):PSS during evaporation of the solvent. The surface roughness of the nanostructures was as follows: pristine P(ANI-*co*-ASA):PSS (R_a = 3.05 nm); Pd NPs-decorated non-porous P(ANI-*co*-ASA):PSS (R_a = 3.81 nm); Pd NPs-decorated porous P(ANI-*co*-ASA):PSS (R_a = 5.03 nm). The increase in the surface roughness is associated with an increase in the effective surface area of the nanostructures. Therefore, it is reasonable to expect that the Pd NPs-decorated porous P(ANI-*co*-ASA):PSS would have larger surface areas for faster electron transfer between the transducer and the surrounding analyte than the non-porous Pd NPs-decorated surface or the pristine P(ANI-*co*-ASA):PSS [159]. However, the charge carrier mobility along the nanostructure also reduced with increasing surface roughness [160]. To improve understanding of the electrical properties of the nanostructures, the conductivity of the pristine, non-porous, and Pd NPs-decorated porous P(ANI-*co*-ASA):PSS nanostructures was measured using the four-point probe method (Table 8) [111,112]. The conductivity of the nanostructure is important for signal transduction at the device microelectrode. The increased surface roughness of the nanostructure is expected to have contributed to an increase in the sheet resistivity of nanostructure. This increased sheet resistivity is associated with a reduced number of conducting channels within the nanostructure. Very small changes in surface roughness can significantly affect

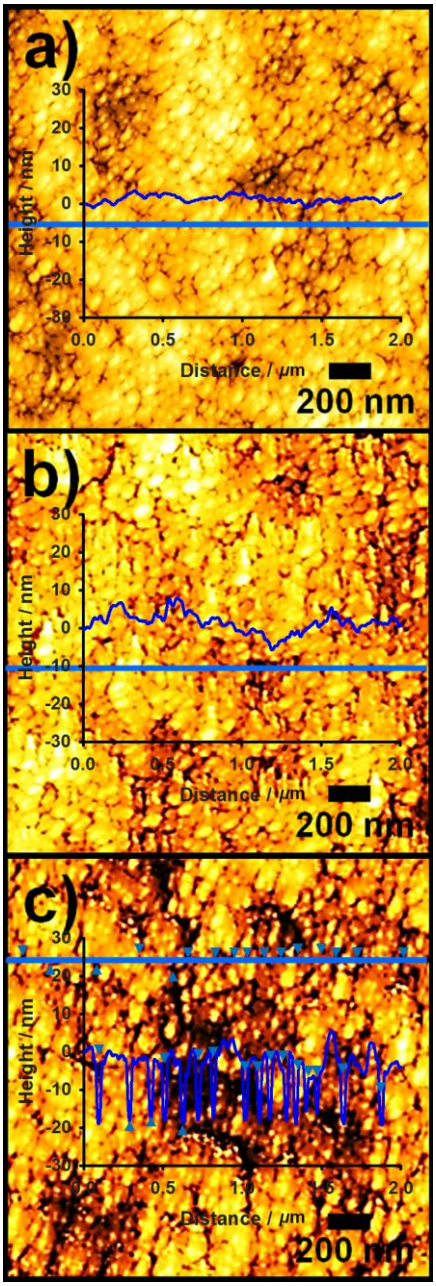

Figure 55. AFM images of nanostructures with cross-sectional analyses (1×1 μm^2 scale): (a) pristine, (b) Pd NPs-decorated non-porous, and (c) Pd-NPs decorated porous P(ANI-*co*-ASA):PSS.

charge transport [16,160]. Accordingly, a small increase in the surface roughness may be desirable to achieve both high electro-catalytic activity and conductivity of the P(ANI-*co*-ASA):PSS nanostructures upon exposure to H_2 gas. These results represent only a small loss in conductivity caused by the Pd NPs and pore formation, indicating that the additional resistance caused by the Pd NPs and pore formation was relatively low.

To predict the effects of temperature on the sensing performances, we conducted measurements of the conductivity of the Pd NPs-decorated porous P(ANI-*co*-ASA):PSS nanostructure at different heating temperature in a N_2 atmosphere for 1 h (Table 9). The conductivity of the Pd NPs-decorated porous P(ANI-*co*-ASA):PSS nanostructure retained more than 65 % of its initial value at the temperature below 150 ℃, whereas the conductivity began to decrease significantly at the temperature above 150 ℃. According to previous reports, PANI-based materials are known to exhibit typical two-steps of thermal degradation behaviors [161,162]. During the first thermal degradation, which occurs between 100 and 150 ℃, the P(ANI-*co*-ASA) structure usually loses water and only small proportion of the HCl molecules from slight deprotonation. Hence, the first thermal degradation results in only a small decrease in the conductivity of the Pd NPs-decorated porous P(ANI-*co*-ASA):PSS. Most of HCl molecules are lost during the second thermal

Table 8. Relationship between surface roughness, conductivity, and surface resistance of P(ANI-*co*-ASA):PSS nanostructures.

Sample	surface roughness[a]	conductivity[a] (S cm^{-1})	surface resistance[a] (Ω)
Pristine	3.05	6.8±0.25	66±3.0
Pd NPs-decorated non-porous	3.81	6.4±0.25	70±3.0
Pd NPs-decorated porous	5.03	6.2±0.30	73±3.5

[a] P(ANI-*co*-ASA):PSS nanostructures with thickness of 5 μm were measured.

Table 9. Conductivity of Pd NPs-decorated porous P(ANI-*co*-ASA):PSS nanostructure as a function of heating temperature.

heating temperature (℃)	conductivity[a] (S cm^{-1})
25	6.20±0.30
50	6.15±0.30
100	5.40±0.35
150	4.20±0.40
200	0.75±0.45

[a] P(ANI-*co*-ASA):PSS nanostructures with thickness of 5 μm were measured.

degradation, which commences at the temperature above 150−170 ℃, together with an oxidation of the polymer backbone and a chlorination of the rings within the polymer backbone. Judging from these facts, the electric responses of the Pd NPs-decorated porous P(ANI-*co*-ASA):PSS to the H_2 gases would not be seriously reduced at the temperature below 150 ℃.

UV/VIS/NIR and FT-IR spectroscopy were used to identify changes in the charge transport properties of pristine and Pd NPs-decorated porous P(ANI-*co*-ASA):PSS nanostructures, as shown in Figure 56. UV/VIS/NIR spectra show the spectral change before and after Pd NPs-decoration of the P(ANI-*co*-ASA):PSS (Figure 56a). The broad spectral region from 340–420 nm in the UV/VIS/NIR spectrum of the pristine P(ANI-*co*-ASA):PSS is attributed to π–π excitation of the *para*-substituted benzenoid segment (–B–NH–B–), and π–π excitation of the quinone diamine structure (–N=Q=N–) appeared at 758 nm [156,164]. Pd NPs-decorated P(ANI-*co*-ASA):PSS samples also demonstrated characteristic features of PANI-ES, i.e., the two bands of PANI-ES in the spectra at 415 nm and 758 nm are present, which are similar to those of pristine P(ANI-*co*-ASA):PSS. In the P(ANI-*co*-ASA) structure, the complex ion of the Pd NPs interacts with PANI through the π–π conjugate chains, prohibiting protonation at the imine nitrogen sites, which results in a reduced conjugation length of delocalized electrons. However, in this work, no such changes

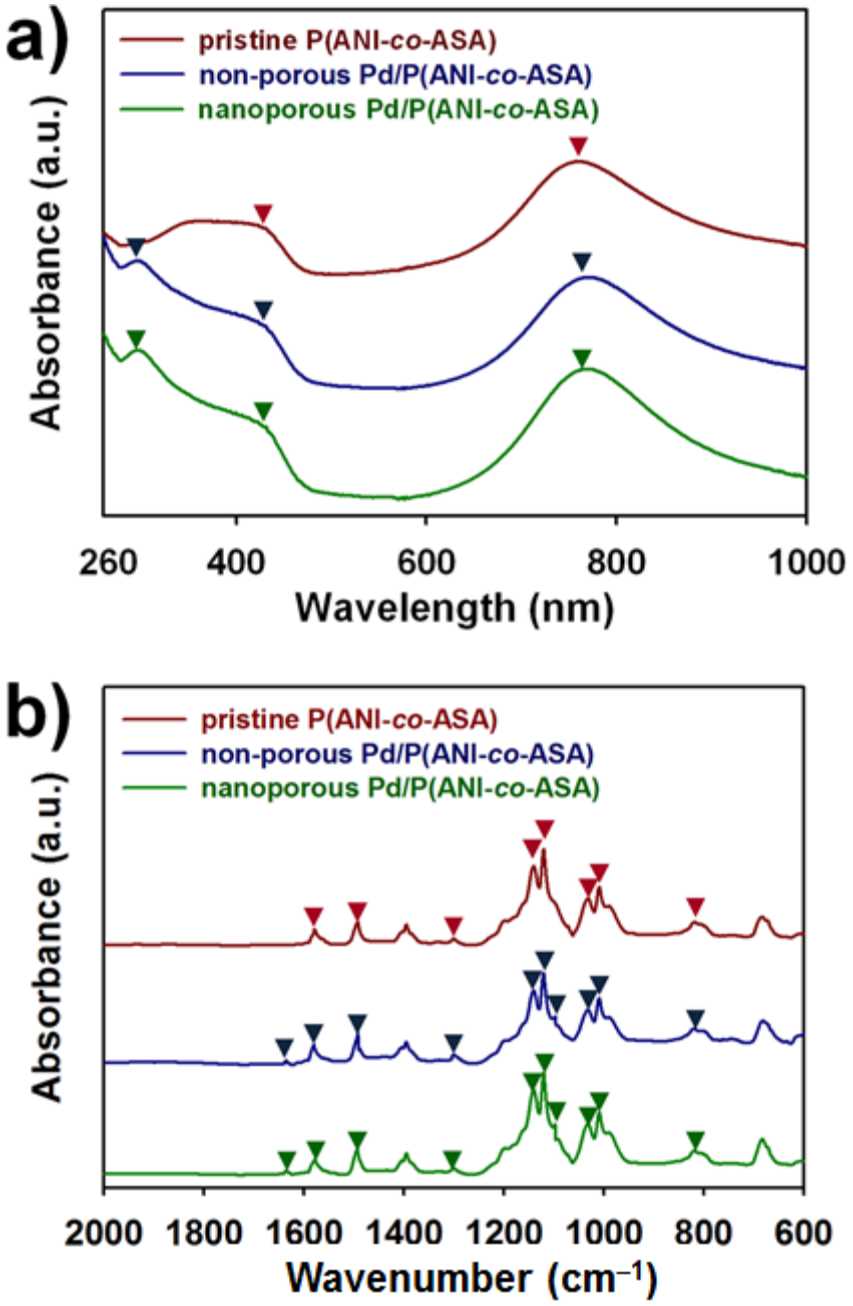

Figure 56. (a) UV/VIS/NIR and (b) FT-IR spectra of P(ANI-*co*-ASA):PSS nanostructures.

occurred in the Pd NPs-decorated P(ANI-*co*-ASA):PSS. These spectral results indicate that the $–SO_3H$ groups of the *co*-monomer and PSS had a higher affinity for the Pd NPs than that of the nitrogen atoms of the PANI structure. Therefore, the conjugation length and the protonation levels were retained in the Pd NPs-decorated P(ANI-*co*-ASA):PSS nanostructures. In particular, an additional peak at 290 nm was observed; no absorption bands are expected at this wavelength for PANI-ES. Metal NPs usually absorb in the spectral region from 280–290 nm, because of the excitation of surface plasmons. This peak appeared to be closer to neutral Pd than to Pd^{2+} [154,156]. Hence, the spectral change is attributed to the formation of complex ions of Pd NPs by P(ANI-*co*-ASA):PSS. Following pore formation, no significant changes in the distinctive absorption peaks were found, implying that the conjugation length of P(ANI-*co*-ASA):PSS was not significantly deteriorated by the Pd NPs-decoration or pore formation. The FT-IR spectra reveal the influence of chemical bonding on the charge transport properties of the P(ANI-*co*-ASA):PSS nanostructures (Figure 56b) [33,133,154,156]. The band at 820 cm^{-1} was assigned to the C–H out-of-plane bending of 1,4-disubstituted ring structures (*para*-coupling) and is attributed to favorable head-to-tail coupling during polymerization. The peaks for bending modes of the benzene ring and C–N stretching of the secondary aromatic amine appeared at 1010 and 1300 cm^{-1}, respectively. The bands at

1040 and 1140 cm^{-1} are attributed to $–SO_3H$, which are associated with the PSS and *co*-monomer. In addition, the peak at 680 cm^{-1} is attributed to S–O stretching of the PSS. The peaks for C=C stretching of the quinoid unit (−N=Q=N−) appeared at 1122 and 1580 cm^{-1}. The band at 1492 cm^{-1} is attributed to C=C stretching of the benzenoid unit (−N=B=N−). The intensity ratio of the bands at 1580 cm^{-1} (I_{1580}) and 1492 cm^{-1} (I_{1492}) is associated with the conjugation length and doping level of the PANI structure. The ratio I_{1580}/I_{1492} was 0.66 for pristine P(ANI-*co*-ASA):PSS, 0.64 for Pd NPs-decorated non-porous P(ANI-*co*-ASA):PSS, and 0.63 for the Pd NPs-decorated porous P(ANI-*co*-ASA):PSS [37]. These results indicate that the charge transport properties were not significantly affected by Pd NPs-decoration and pore formation. In the spectra of the Pd NPs-decorated P(ANI-*co*- ASA):PSS nanostructures, characteristic bands were present at 1097 and 1635 cm^{-1}, indicating that complex ions of PANI and Pd NPs were formed in both porous and non-porous structures [154].

The elemental compositions and doping levels of the P(ANI-*co*-ASA):PSS nanostructures were measured using X-ray photoelectron spectroscopy (XPS) (Figure 57 and 58). The elemental compositions of the P(ANI-*co*-ASA):PSS nanostructures were determined from the full-scan XPS patterns shown in Figure 57a. Relatively high fractions of sulfur and oxygen in the samples

suggest that sufficient $–SO_3H$ groups were available within the co-monomers [133]. The presence of the peak around 335–341 eV in the spectra of Pd NPs-decorated samples is attributed to Pd NPs incorporated on the P(ANI-*co*-ASA):PSS surface [153]. The Pd 3*d* core spectrum was fitted using two components, as shown in Figure 57b. The prominent peaks at 335 and 341 eV are assigned to the neutral Pd state, whereas the weaker features at 335 and 341 eV are attributed to PdO. No obvious peak for Pd^{2+} species was found (which has a binding energy of approximately 338 eV), indicating that most Pd species of $PdCl_2$ were reduced to neutral Pd during sonication [153]. Figure 58 show the N(1s) core spectra of pristine, Pd NPs-decorated non-porous, and Pd NPs-decorated porous P(ANI-*co*-ASA):PSS. The N(1s) spectra of the PANI showed three components with peaks at 399.3 eV (–NH–, benzenoid amine nitrogen), 400.4 eV ($–NH•^+$, radical cation), and 401.6 eV ($=NH^+$, imine cation) [125,126]. The proportion of positively charged nitrogen of the $–NH•^+$ and $=NH^+$ groups decreased slightly following addition of the Pd NPs, whereas the proportion of –NH–increased slightly after addition of Pd NPs. The ratio of N^+ species (sum of $–NH•^+$ and $=NH^+$) to N species (sum of – N=, –NH–, $–NH•^+$, and $=NH^+$) was calculated to estimate the protonation states of P(ANI-*co*-ASA):PSS. This ratio was 0.79, 0.77, and 0.75 for the pristine, Pd NPs-decorated non-porous, and Pd NPs-decorated porous P(ANI-*co*-ASA):PSS,

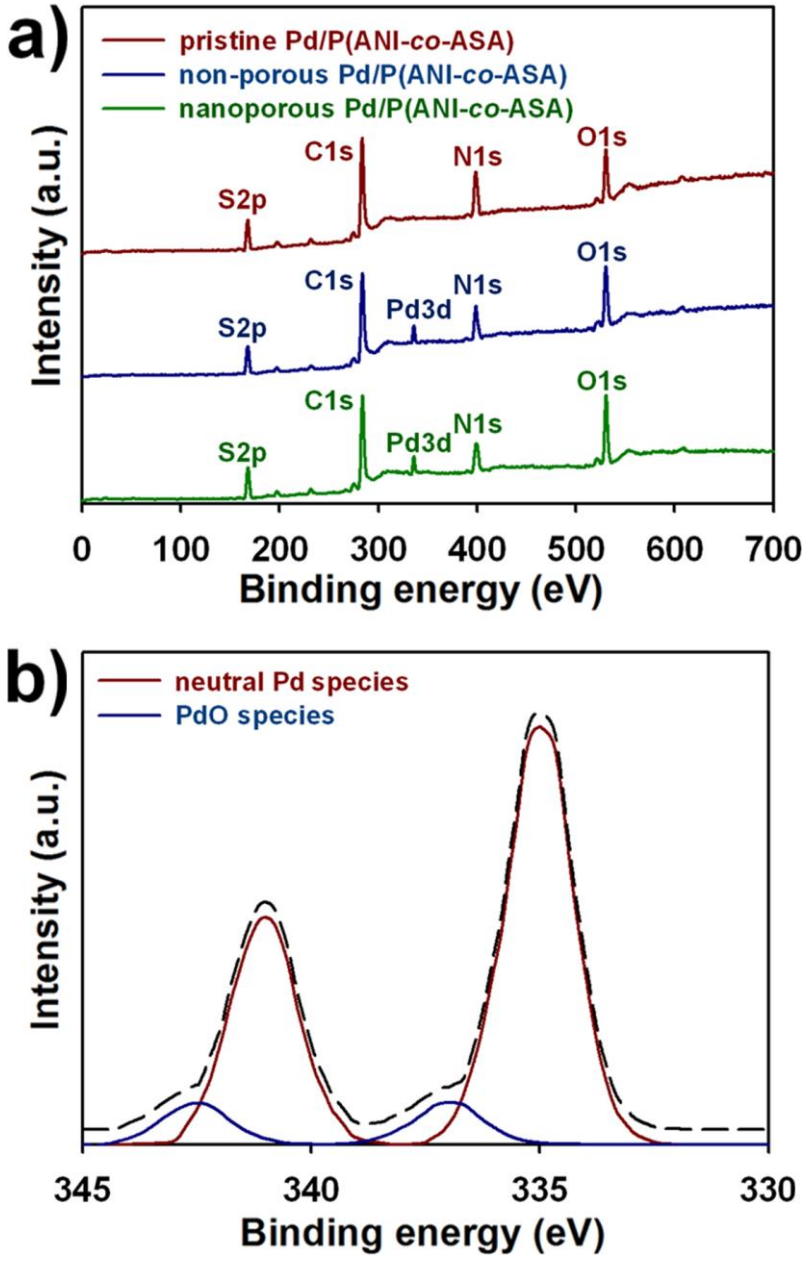

Figure 57. (a) Fully scanned XPS spectra of P(ANI-*co*-ASA):PSS nanostructures. (b) XPS core spectrum of Pd 3d in Pd NPs-decorated P(ANI-*co*-ASA):PSS nanostructures.

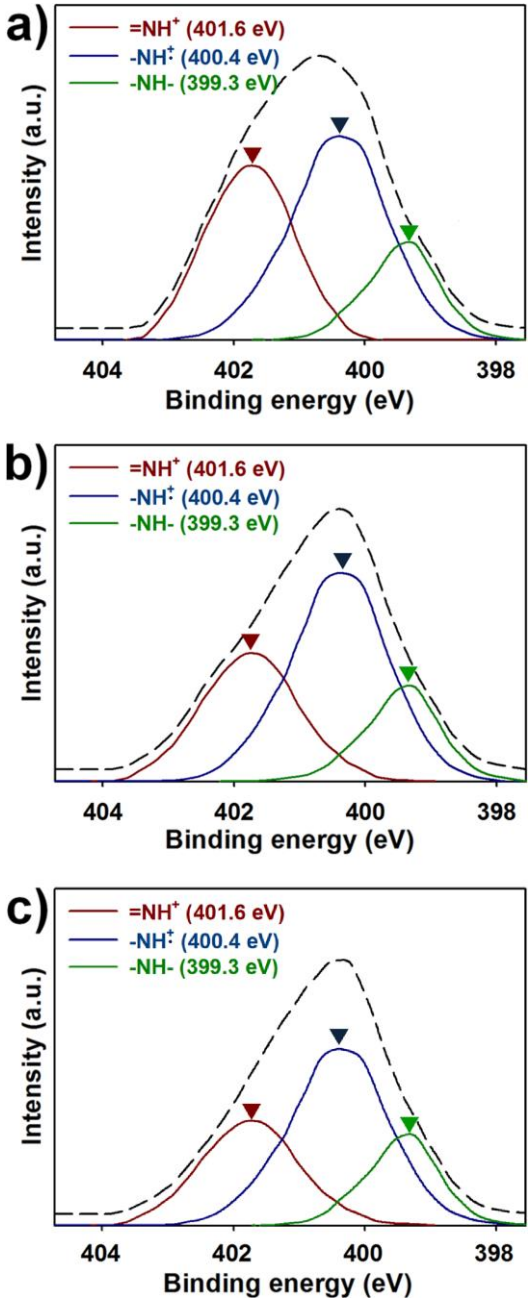

Figure 58. XPS core spectra of N1s in (a) pristine, (b) Pd NPs-decorated non-porous, and (c) Pd NPs-decorated porous P(ANI-*co*-ASA):PSS.

Table 10. XPS atomic ratios of P(ANI-*co*-ASA):PSS nanostructures.

Samples	XPS atomic ratio			
	$=NH^{+a}$	$–NH•^{+a}$	$–NH–^{a}$	N^{+}/N ratio^{a}
pristine	0.38	0.41	0.21	0.79
Pd NPs-decorated non-porous	0.29	0.48	0.23	0.77
Pd NPs-decorated porous	0.28	0.47	0.25	0.75

[a] The values were calculated using the XPS core spectra of N1s in the samples.

respectively (Table 10). When the N^+/N ratio exceeded 50%, the H^+ of the HCl dopant not only protonated the –NH–, but also the –N= in the P(ANI-*co*-ASA):PSS structure [125,126]. Therefore, the peak for –N= was assumed to be absent from the spectra. These results indicate that most of the Pd NPs interacted with the P(ANI-*co*-ASA):PSS structure via the $–SO_3H$ groups; thus, the protonation of the amine nitrogen sites, which generates the $–NH•^+$ and $=NH^+$ groups, was less affected by the Pd NPs–nitrogen complex ion. Furthermore, no significant changes in the spectra were observed due to pore formation. Accordingly, the protonation level of the Pd NPs-decorated porous P(ANI-*co*-ASA):PSS was similar to that of the pristine and the Pd NPs-decorated non-porous P(ANI-*co*-ASA):PSS; however the coupling between the Pd NPs caused an increase in the electron transport upon exposure to H_2 gas.

CV was carried out in a 1M H_2SO_4 electrolyte at 20 mV s^{-1} to identify how the porous structures influenced the electrochemical properties of the Pd NPs-decorated P(ANI-*co*-ASA):PSS, as shown in Figure 59. The upper (anodic) and lower (cathodic) peaks are attributed to the redox behavior of the P(ANI-*co*-ASA):PSS nanostructures, corresponding to leucoemeraldine /emeraldine and emeraldine/pernigraniline transitions, respectively [157,164]. Following Pd NPs-decoration through the co-monomers and PSS, the anodic and cathodic peaks of P(ANI-*co*-ASA):PSS shifted towards the positive and negative

regions, respectively. These results suggest strong electrochemical interactions between the electrolyte and Pd NPs on the P(ANI-*co*-ASA):PSS surface, which promotes a reversible interaction at the Pd NPs-decorated P(ANI-*co*-ASA):PSS/electrolyte interface [157]. In addition, the Pd NPs-decorated porous P(ANI-*co*-ASA):PSS structure exhibited significantly enhanced electro-catalytic activity compared with both the pristine and non-porous Pd NPs-decorated P(ANI-*co*-ASA):PSS. This suggests that porous structures within the Pd NPs-decorated P(ANI-*co*-ASA):PSS had an increased electrode surface area, which results in more rapid redox reactions between the P(ANI-*co*-ASA) electrode and electrolyte. This faster redox transition at the transducer/ electrolyte surface suggests an enhanced interaction between the Pd NPs-decorated porous P(ANI-*co*-ASA):PSS and H_2 gas.

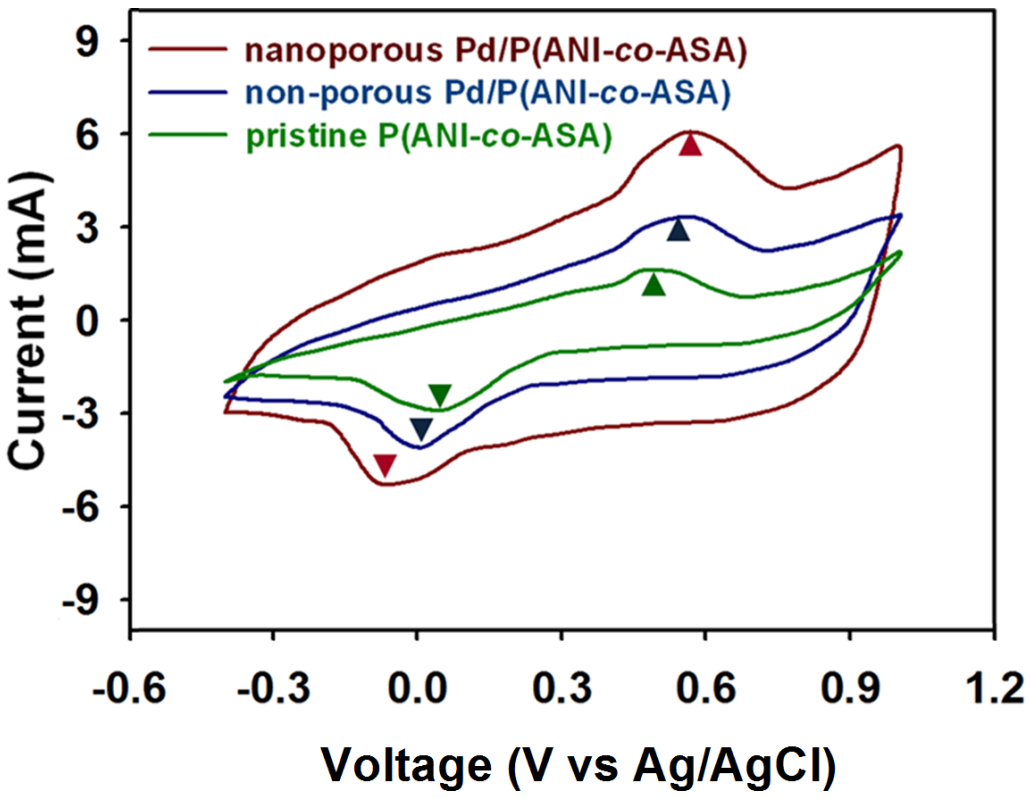

Figure 59. Cyclic voltammograms of P(ANI-*co*-ASA):PSS nanostructures in a 1M H_2SO_4 electrolyte at a scan rate of 20 mV s^{-1}.

3.3.1.2. H_2 Sensors based on Pd NPs-decorated porous P(ANI-*co*-ASA):PSS nanostructures

Hydrogen (H_2) is a non-toxic, odorless, colorless, and tasteless analyte and has been extensively investigated as an environmentally-friendly renewable energy resource [187,188]. However, safe storage and transportation remain significant issues due to the hazards associated with H_2 gas, which forms flammable mixtures over a wide range of concentrations (from 4 to 75% in air), and only small activation energy is required to ignite hydrogen–air mixtures [32,187,188]. Designing and constructing effective sensors for H_2 detection has become an important aspect of ensuring safe storage and transportation of H_2.

Possible mechanisms for sensing H_2 gas using the Pd NPs-decorated porous P(ANI-*co*-ASA):PSS nanostructure are illustrated in Figure 60. The Pd NPs-decorated P(ANI-*co*-ASA):PSS nanostructure provides two sensing mechanisms for H_2 detection. Amine nitrogens along the P(ANI-*co*-ASA) backbone can form hydrogen bonds with H_2 gas. This strong hydrogen bonding promotes H_2 bond dissociation to form new N–H bonds with the amine nitrogen sites of the P(ANI-*co*-ASA) chains [32]. Charge transfer between the amine nitrogen sites then creates half-oxidized P(ANI-*co*-ASA), and ES forms with the release of H_2 molecules. This reversible interaction at the amine nitrogen sites leads to the possibility of a resistivity change for H_2 sensing.

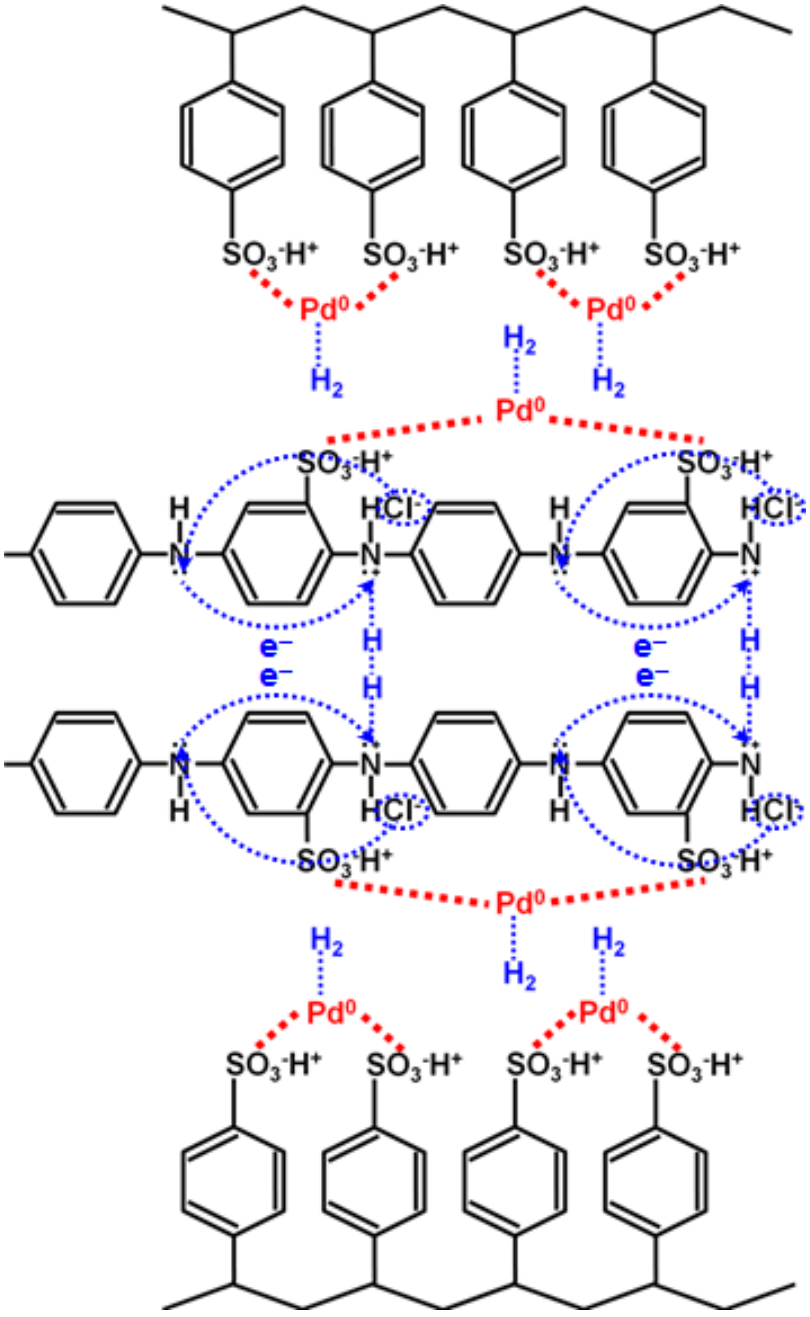

Figure 60. Possible mechanism for molecular interactions between the Pd NPs-decorated P(ANI-*co*-ASA):PSS and H_2 gas molecules.

Another method of detecting H_2 gas is to use the neutral Pd NPs that are attached on the $–SO_3H$ groups of the nanostructure [154]. The H_2 atoms can occupy octahedral interstitial positions within the face-centered cubic (FCC) lattice structures of Pd. The Pd surface absorbs H_2 gas to form palladium hydride (PdH_x), leading to electrical resistivity changes when H_2 is incident on the structure [155]. Accordingly, the Pd NPs-decorated P(ANI-*co*-ASA):PSS nanostructures can use both P(ANI-*co*-ASA):PSS−H_2 and Pd−H_2 interactions, resulting in improved H_2 sensitivity compared with that of pristine P(ANI-*co*-ASA):PSS. Moreover, the porosity of the P(ANI-*co*-ASA):PSS surface provides a larger surface-area-to-volume ratio, which increases the probability of interactions between Pd NPs-decorated P(ANI-*co*-ASA):PSS and H_2 gas.

Figure 61 show current–voltage (*I*–*V*) curves of the pristine, non-porous Pd NPs-decorated, and Pd NPs-decorated porous P(ANI-*co*-ASA):PSS deposited as transducers on microelectrode substrates. The linearity of *dI*/*dV* indicates that good electrical contacts were formed [74,117]. Although *dI*/*dV* was lower for the Pd NPs-decorated porous P(ANI-*co*-ASA):PSS than the non-porous Pd NPs-decorated P(ANI-co-ASA):PSS, which in turn was lower than that of the pristine P(ANI-*co*-ASA):PSS, the differential resistances were within the same range (Figure 61a). These results indicate that the contact resistance between the P(ANI-*co*-ASA) and microelectrode was not affected by the Pd NPs or the

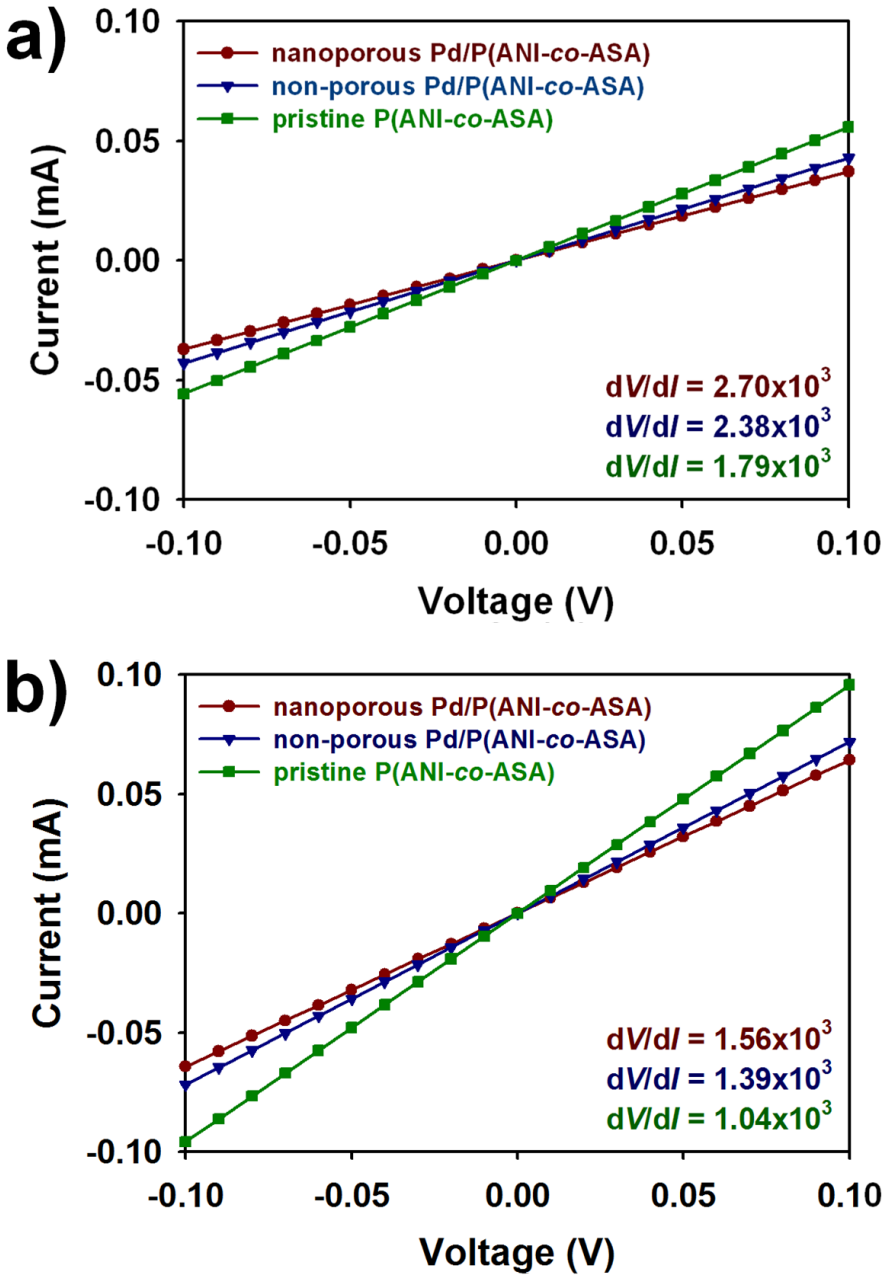

Figure 61. *I-V* characteristics of P(ANI-*co*-ASA):PSS nanostructures with thickness of (a) 5 μm and (b) 10 μm integrated in the sensor substrate at a scan rate of 10 mV s^{-1}.

porous structure. Assuming that the microelectrodes used for the sensor devices remain unchanged, *dI*/*dV* was consistent with the interparticle resistances being closely linked to the charge transport properties, which are affected by the P(ANI-*co*-ASA):PSS nanostructure morphology [74,117]. Upon depositing more P(ANI-*co*-ASA):PSS (so that the layer was 10 μm thick) on the microelectrodes, the *I*–*V* characteristics of the samples were similar to those of the 5 μm-thick P(ANI-*co*-ASA):PSS layer (Figure 61b). Notably, only a very thin layer of Pd NPs-decorated porous P(ANI-*co*-ASA):PSS was required to form good electrical contacts between the P(ANI-*co*-ASA):PSS and microelectrode.

The real-time responses of the P(ANI-*co*-ASA):PSS nanostructures were systematically investigated to identify the influence of Pd NPs-decoration and pore formation on the H_2 sensing capabilities, as shown in Figure 62 and 63. The normalized change in resistance, $\Delta R/R_0$, of the P(ANI-*co*-ASA):PSS-based sensors was monitored in real time following exposure to H_2. $\Delta R/R_0$ was calculated using the equation $\frac{\Delta R}{R_0} = \frac{R - R_0}{R_0}$, where R_0 is the initial resistance before exposure to H_2 and R is the measured real-time resistance after exposure to H_2. Furthermore, R_0 and R can be written as $R_0 = \sum^{n} R_I + \sum^{n-1} R_S$ and $R = \sum^{n} R_I + \sum^{n-1} R_S + \sum^{n} R_C$, respectively, where R_s, is the resistance of the

single P(ANI-*co*-ASA):PSS NP, R_I is the interparticle contact resistance of the Pd NPs-decorated P(ANI-*co*-ASA):PSS NPs, R_c the resistance change for the Pd NPs-decorated P(ANI-*co*-ASA):PSS–H_2 interaction, and *n* is the number of P(ANI-*co*-ASA):PSS NPs creating the conducting channel. R_s is associated with the protonation state and conjugation length for a single Pd NPs-decorated P(ANI-*co*-ASA):PSS NP [117]. R_I is related to the charge carrier mobility of the nanostructures deposited on the microelectrodes. As discussed above, we can consider that R_I and R_s are similar. Accordingly, it is reasonable to expect that the resulting sensitivity depends mainly on R_c, and the Pd NPs-decorated porous P(ANI-*co*-ASA):PSS is advantageous for reducing R_c because of the increased interactions with H_2 gas molecules. Following the removal of H_2 gas using a compressed synthetic air flow, the resistance rapidly recovered to the original level due to the fully-reversible P(ANI-*co*-ASA)−H_2 and Pd NPs−H_2 interactions. Figure 62a shows the change in the electrical responses upon sequential exposure to H_2 gases at five different concentrations (5, 10, 20, 50, and 100 ppm). Interestingly, the resistance continued to decrease when the P(ANI-*co*-ASA):PSS nanostructures were exposed to H_2 gas. This decrease in resistance can be explained by the interaction between H_2 gas and amine nitrogen sites of P(ANI-*co*-ASA). As mentioned previously and shown in Figure 60, additional N–H bonds are formed at the amine nitrogen sites when

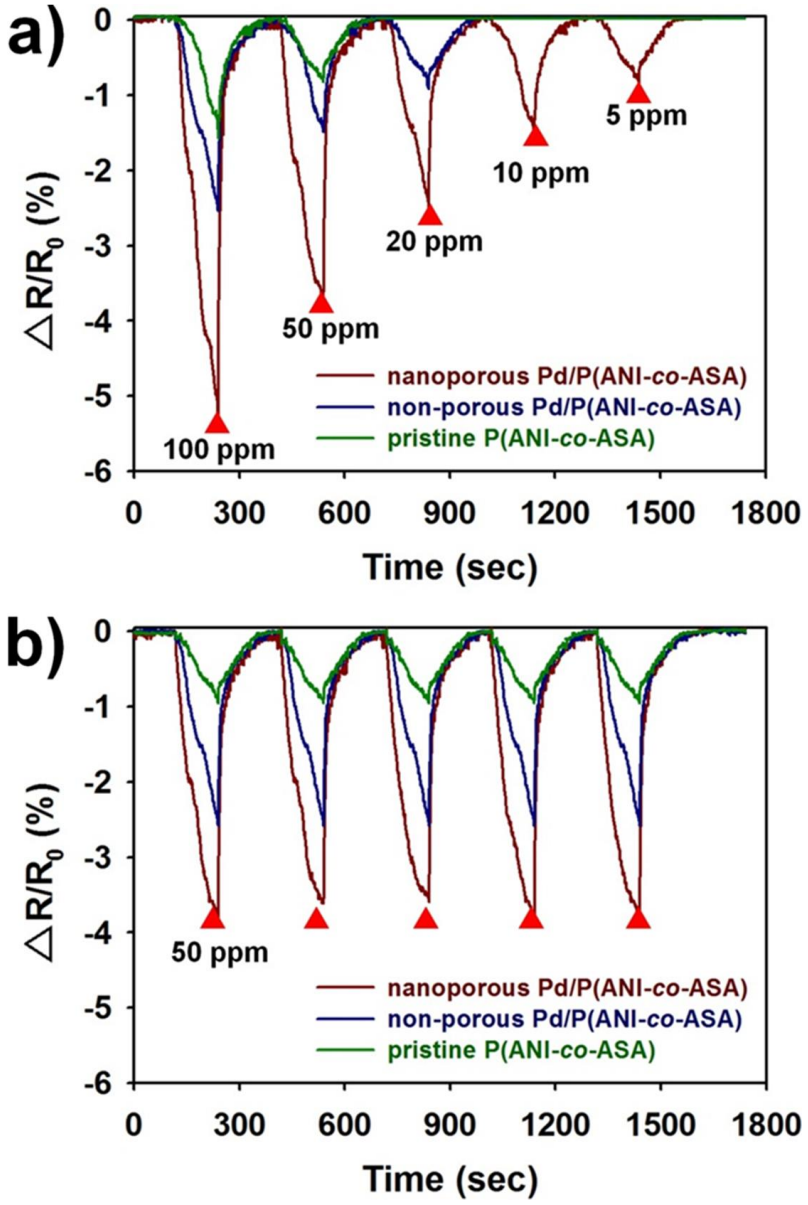

Figure 62. (a) Real-time responses of P(ANI-*co*-ASA):PSS nanostructures upon cyclic exposure to H_2 (5 to 100 ppm) and synthetic air streams, (b) Real-time responses of P(ANI-*co*-ASA):PSS nanostructures upon periodic exposure to 50 ppm H_2.

Table 11. Chemiresistive sensor performance of Pd NPs-decorated porous P(ANI-*co*-ASA):PSS toward H_2 compared with the literatures.

sensing materials	MDL[a]	response / recovery (s)	reference
This work	5	90 / 40	-
Pd NWs	27	5-30 / -	[167]
Pd/RGO	50	700 / -	[168]
Pd/SWNT	100	420 / 1200	[169]

[a] Minimum detection limit.

P(ANI-*co*-ASA) is exposed to H_2 molecules. These new N–H bonds enhance the charge transfer within the P(ANI-*co*-ASA), resulting in a decrease of $\Delta R/R_0$ in the P(ANI-*co*-ASA):PSS nanostructures. These hydrogen responses and limits of H_2 detection were significantly improved following Pd NPs-decoration and pore formation on the P(ANI-*co*-ASA):PSS surface. It was clear that well-dispersed Pd NPs on the P(ANI-*co*-ASA):PSS contributed to attract more H_2 gas molecules than on the pristine P(ANI-*co*-ASA):PSS in the same time. The Pd NPs-decorated porous P(ANI-*co*-ASA):PSS exhibited a reduced limit of detection (5 ppm) compared with that of the non-porous Pd NPs-decorated P(ANI-*co*-ASA):PSS (20 ppm), which is attributed to the enhanced surface area for H_2 diffusion within the P(ANI-*co*-ASA):PSS. Moreover, the detection limit of the Pd NPs-decorated porous P(ANI-*co*-ASA):PSS sensor was significantly lower than that of conventional Pd-based H_2 sensors (Table 11) [167−169]. Furthermore, slight increases in baseline resistances of the pristine and non-porous Pd NPs-decorated P(ANI-*co*-ASA):PSS occurred at the H_2 concentrations below 20 and 50 ppm, respectively. The results can be explained by several follwing reasons. In general, carrier mobility along the *p*-type conducting polymers is also affected by the applied electric currents and current-applying time [3,74,117,134,160]. Assuming that the applied current for sensor devices remains unchanged (10^{-6}

A), the carrier mobility of pristine P(ANI-*co*-ASA):PSS may be slightly deteriorated with applying time, resulting in a small increase in the baseline resistance. In addition, sufficient surface area of materials and H_2 amounts were also important factors affecting the baseline resistances of the sensor devices. An increase in the electron transport between the P(ANI-*co*-ASA):PSS structure and H_2 molecules was important for minimizing the carrier mobility losses within the P(ANI-*co*-ASA):PSS structure caused by the applied electric currents. It is reasonable to expect that the porous structures induce an increased electron transport upon exposure to the H_2 gases due to the increased surface areas available for the interaction with H_2 molecules. Thus, the baseline resistance of the porous device remained constantly over a wide range of the H_2 concentrations compared to the pristine and Pd NPs-decorated non-porous samples. The sensors with the P(ANI-*co*-ASA):PSS nanostructures had a response time of less than 90 s, and the initial resistance recovered within approximately 40 s. To investigate the reproducibility of the response of the P(ANI-*co*-ASA):PSS-based sensors, the P(ANI-*co*-ASA):PSS nanostructures were exposed to periodically fluctuating H_2 gas concentrations between 50 ppm and 0 ppm, as shown in Figure 62b. The P(ANI-*co*-ASA):PSS-based sensors exhibited repeatable and stable sensitivities after cycles of exposure to H_2 and recovery of the initial resistance, indicating that the Pd NPs-decorated

porous P(ANI-*co*-ASA):PSS are viable for long-term use [74,117]. Upon exposure to the 50 ppm H_2, the baseline resistances of the pristine and nonporous P(ANI-*co*-ASA):PSS also remained constantly as well as the Pd-decoarated porous P(ANI-*co*-ASA):PSS. This indicates that the sufficient amounts of the H_2 molecules were provided for minimizing losses in the charge transport properties along the P(ANI-*co*-ASA):PSS nanostructures.

Figure 63a shows the calibration curves of changes in the sensitivity as a function of H_2 gas concentration. The response of the sensors significantly increased at the 50 ppm in every sample, indicating that the amounts of H_2 introduced were enough to promote the electron transport within the P(ANI-*co*-ASA):PSS structure. The slope of the response curve was lowest for the pristine P(ANI-*co*-ASA):PSS and highest for the Pd NPs-decorated porous P(ANI-*co*-ASA):PSS, which is consistent with the sensitivities to H_2 gas. The Pd NPs-decorated porous P(ANI-*co*-ASA):PSS was tested against several analytes including ammonia (NH_3), carbon dioxide (CO_2), *N*,*N*-dimethylformamide (DMF), ethanol (EtOH), and methanol (MeOH) to evaluate their selectivity (Figures 63b). The H_2 could be detected at a lower concentration than that of the other analytes due to effective Pd- anchoring on the P(ANI-*co*-ASA) surface. At the same concentration of the analytes, negative changes in the $\Delta R/R_0$ were observed upon exposure to the H_2, EtOH,

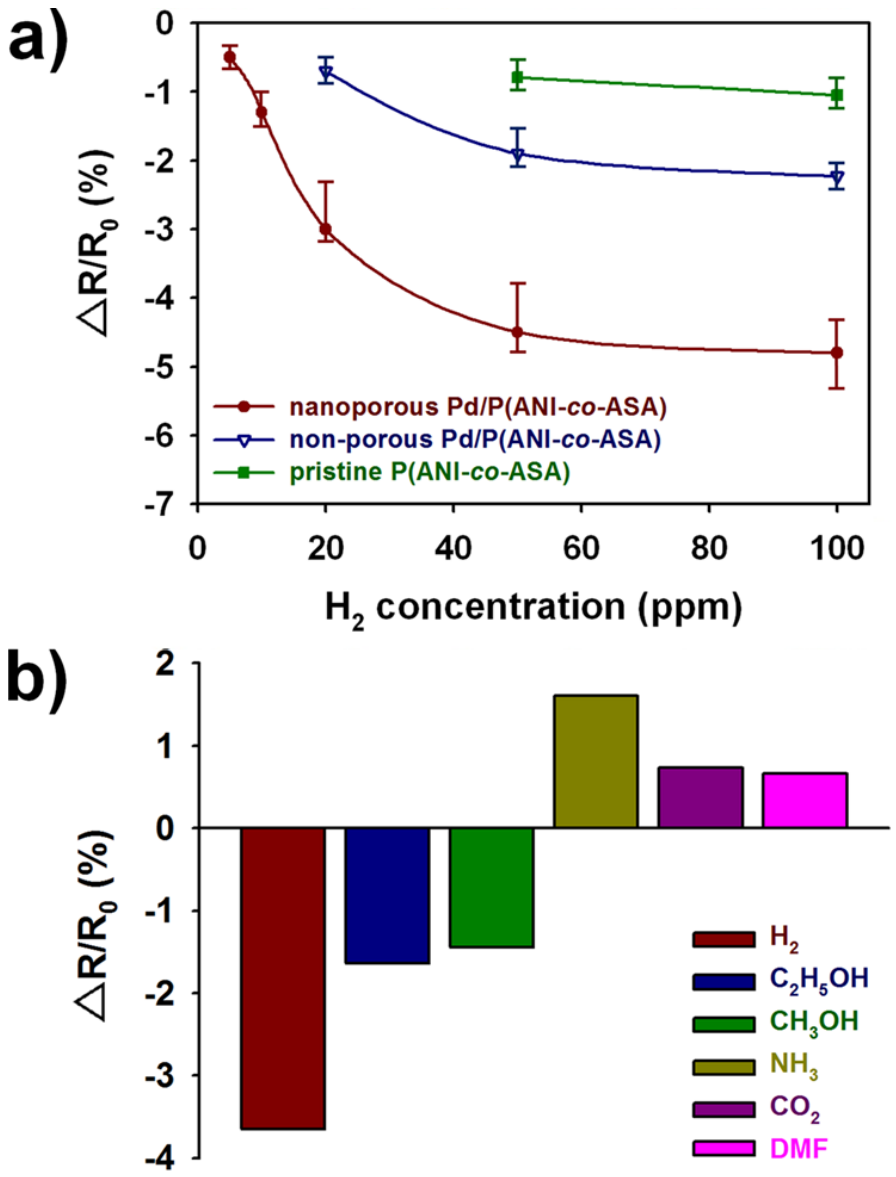

Figure 63. (a) Calibration curves of changes in sensitivity of P(ANI-*co*-ASA):PSS nanostructures as a function of H_2 gas concentration. (b) Normalized response graphs of Pd NPs-decorated porous P(ANI-*co*-ASA):PSS to different analytes: Each analyte concentration was fixed at 50 ppm.

and MeOH, whereas the resistance changes were positive when the Pd NPs-decorated porous P(ANI-*co*-ASA):PSS was exposed to the NH_3, CO_2, and DMF. It is considered that the different sensitivity to analyte depends on their chemical structure. The H_2, EtOH, and MeOH diffuse into the Pd NPs-decorated porous P(ANI-*co*-ASA):PSS structure through the hydrogen bonding interactions (–H···H–N– and –O–H···H–N–) at the amine nitrogen sites along the P(ANI-*co*-ASA) backbone, enhancing the charge transfer within the P(ANI-*co*-ASA):PSS [32,165]. Therefore, negative changes in the $\Delta R/R_0$ were observed upon exposure to the H_2, EtOH, and MeOH. However, the P(ANI-*co*-ASA):PSS structure becomes deprotonated when the Pd NPs-decorated porous P(ANI-*co*-ASA):PSS is exposed to the NH_3 and thereby results in resistance increases [33]. The NH_3 provides both high polarity and strong hydrogen bonding forces, resulting in a larger $\Delta R/R_0$ response than that of the CO_2 and DMF. Judging from these results, the ability of Pd NPs-decorated porous P(ANI-*co*-ASA):PSS to perceive H_2 molecules was successfully examined.

3.3.2. Fabrication of PSS-doped PANI/graphene nanocomposites for H_2S sensors

3.3.2.1. Fabrication of PSS-doped PANI/graphene nanocomposites

Figure 64a shows the overall procedure for producing PSS-doped PANI/graphene nanocomposites. The process is based on electrostatic polymerization combined with modified SSDP [40,51]. In the first step, high-molecular-weight PSS was synthesized *via* a free-radical polymerization using AAPH as a water-soluble azo-initiator. The AAPH molecules decomposed with a first-order rate constant of $K_d = 6.6\times10^{-5}$ min^{-1} at 37°C, which enabled the free-radical polymerization to proceed at a relatively low temperature [181,182]. In addition, compared with previous work, much lower concentrations of initiator were consumed during the polymerization of 4-styrenesulfonate [33,45]. This may result in higher degrees of polymerization (DP). Therefore, our experimental conditions were sufficient to obtain high-molecular-weight PSS ($M_w > 10^6$ Da) in the aqueous phase. Although PSS was used as a low- acidity doping agent, its polymeric counter ions are less likely to dissociate protons for aniline doping. Therefore, the polymerization of aniline was conducted according to a modified SSDP method. Overall reactions were carried out in a distilled water/$CHCl_3$ (2:1, v/v) co-solvent at the relatively low temperature of –50°C in order to promote *para*-direction polymerization. This method typically results in higher conductivities than conventional methods

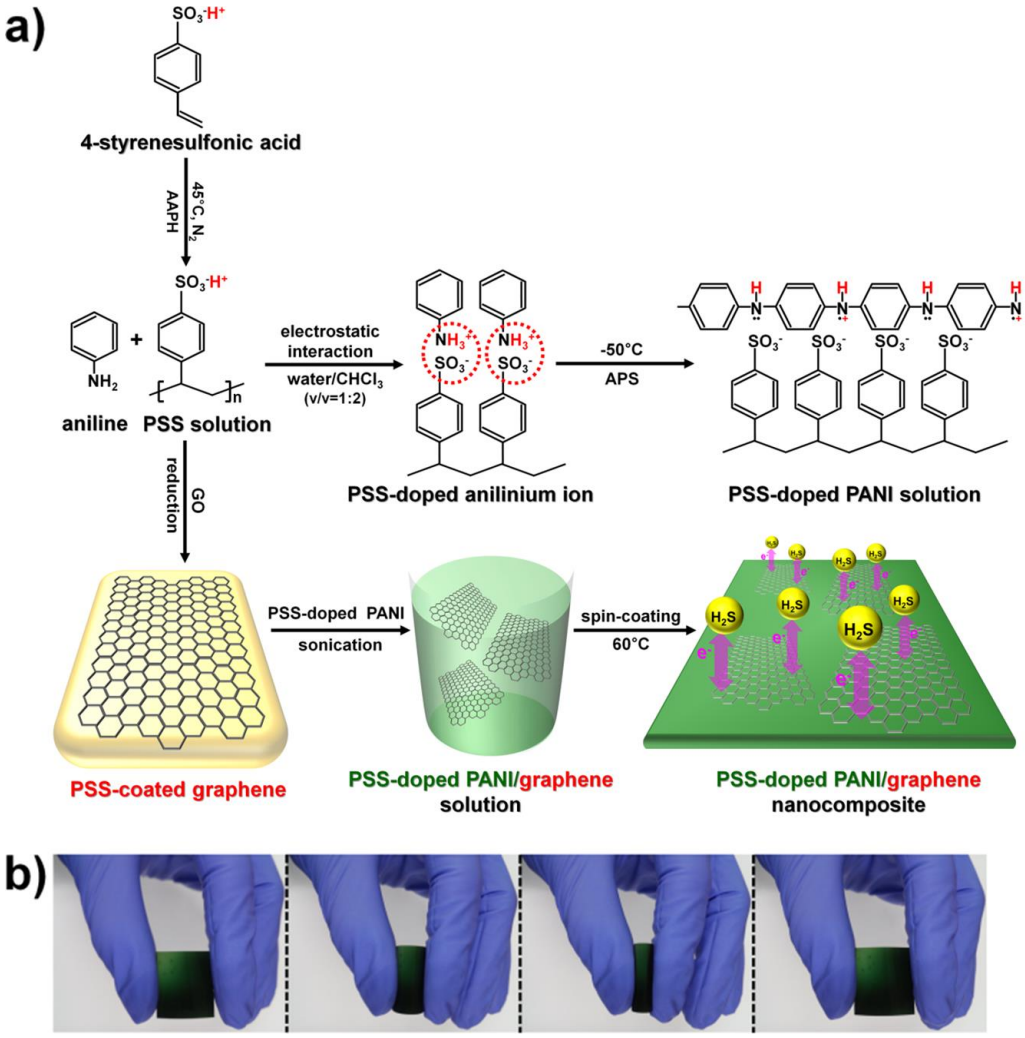

Figure 64. (a) Schematic illustration for synthetic processes of PSS-doped PANI/graphene nanocomposites and (b) digital images of a PSS-doped PANI/graphene sensor electrode for used as H_2S detection.

[40]. In the first step of this method, aniline (ANI) monomer was protonated to anilinium ions ($–NH_3^+$) by PSS. These were subsequently electrostatically combined with the negatively charged sulfonate ions ($–SO_3^–$) of PSS [33,45,51]. The ionic interactions between $–NH_3^+$ and $–SO_3^–$ resulted in an excellent dispersion of monomer along the PSS structure. Thus, PSS may be used as both a dopant and a dispersing agent without the use of highly acidic hydrogen chloride (HCl). In addition, polar $–NH_3^+$ ions promoted the dispersion of organic phases within the aqueous medium. Chloroform in the co-solvent system solvated oligomers in the aqueous phase, thereby suppressing undesirable side reactions, such as *ortho*-coupling and Michael reductive additions [40]. Hence, our method resulted in *para*-directed polymerization of PSS-doped PANI, which resulted in highly dispersed PANI solutions with enhanced charge-transport properties. Graphene sheets were prepared by reducing graphene oxide (GO), which was synthesized according to Hummer's method, in the PSS-dispersed aqueous solution [51]. Performing the GO reduction in the presence of PSS resulted in $–SO_3^–$ functionalized graphene that was easily dispersed in the PSS-doped PANI solution. Thus, the sulfonate anions ($–SO_3^–$) of PSS facilitated interfacial interactions and mechanical interlocking between the graphene sheets and PSS-doped PANI, thereby intensifying the π–π stacking interactions and enhancing conductivity

[45]. The final PSS-doped PANI/graphene solution was used to fabricate thin-film electrodes by spin-coating the solution onto flexible PET substrates (Figure 64b). Spin-coating resulted in thin films of uniform thickness. The PET substrates were wet evenly by the polymer solution, and the resulting films showed good adhesion to the flexible PET, even after repeated bending. The absence of tears or cracks in the spin-cast films implies that the co-solvent system was compatible with the carbonyl groups (C=O) on the surface of the PET. Based on these observations, the PSS-doped PANI/graphene solutions described above are suitable for easy fabrication of flexible sensor electrodes to detect H_2S gas.

GPC results of PSS prepared with various amounts of radical initiator (1.5–15 mg) are summarized in Table 12. Each radical dissociated from the initiator reacts with monomers during the polymerization of 4-styrenesulfonic acid. Therefore, the molecular weight of PSS can be controlled by adjusting the relative amount of radical initiator. Weight-average molecular weights (M_w) were calculated using the GPC method. The M_w of PSS using 1.5, 3.0, 7.5, and 15 mg of initiator were 1.96×10^6, 1.79×10^6, 1.59×10^6, and 1.46×10^6 Da, respectively. The M_w of PSS prepared by our method was much higher than the M_w of commercially available PSS, indicating that the polymerization of 4-styrenesulfonic acid proceeded as expected.

Table 12. GPC results for PSS prepared with different amounts of initiators.

AAPH (mg)[a]	M_w (Da)[b]	M_n (Da)[c]	M_w/M_n[d]
1.5	1.96×10^6	5.90×10^5	3.32
3.0	1.79×10^6	4.59×10^5	3.90
7.5	1.59×10^6	4.57×10^5	3.48
15.0	1.46×10^6	3.25×10^5	4.50

[a] AAPH: 2,2′-Azobis(2-amidinopropane) dihydrochloride.

[b] M_w: weight average molecular weight.

[c] M_n: number average molecular weight.

[d] M_w/M_n: polydispersity index.

FE-SEM images of PSS-doped PANI with different M_w are shown in Figure 65. The PSS-doped PANI with M_w of 1.96×10^6 Da was synthesized by our experimental method. The other samples are commercially available with PSS M_w of 7.00×10^4, 2.00×10^5, and 1.00×10^6 Da. These PSS-doped PANI films consisted of nanosized grains resulting from electrostatic interactions between the anilinium ions and the negatively charged PSS. The PANI grains became larger with increasing the M_w of the PSS: 1.96×10^6 Da (45–50 nm), 1.00×10^6 Da (30–35 nm), 2.00×10^5 Da (20–25 nm), and 7.00×10^4 Da (15–20 nm). These results suggest that the growth of PANI particles depends on the molecular weight of the PSS. Different weights of PSS result in different levels of interparticle connectivity [16,174]. Thus, the overall conductivity of the composite film can be tailored by controlling the M_w of PSS.

AFM was used to investigate the morphology of PSS-doped PANI as a function of the M_w of PSS. Figure 66 shows that the PANI particle size increased and the surface roughness decreased with the M_w of PSS: 1.96×10^6 Da (2.83 nm), 1.00×10^6 Da (3.88 nm), 2.00×10^5 Da (5.02 nm), and 7.00×10^4 Da (7.86 nm). It is reasonable to assume that the larger PANI grains were more densely packed, allowing the conductive areas in the PSS-doped PANI to become more connected. In addition, the lower surface roughness of the nanostructures would further enhance electrical connectivity and charge-

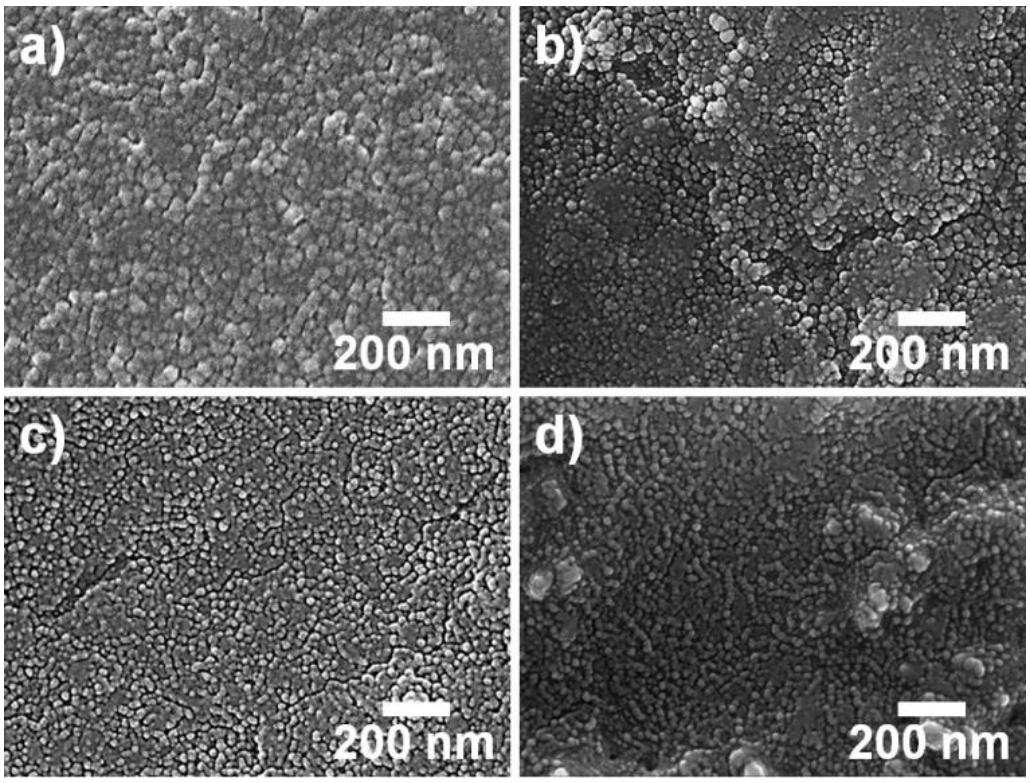

Figure 65. FE-SEM images of PSS-doped PANI having different M_w of PSS: (a) 1.96×10^6, (b) 1.00×10^6, (c) 2.00×10^5, and (d) 7.00×10^4. Magnification: ×80k.

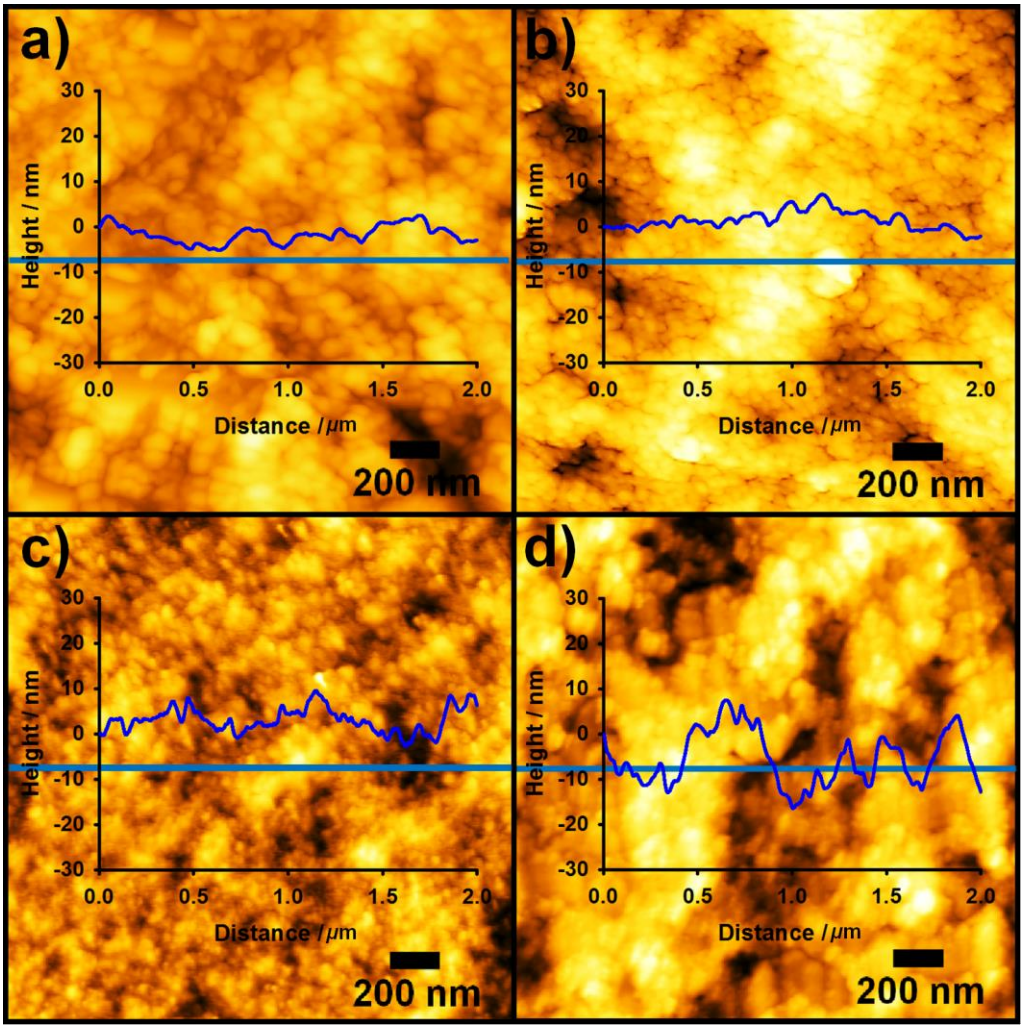

Figure 66. AFM images of PSS-doped PANI having different M_w of PSS: (a) 1.96×10^6, (b) 1.00×10^6, (c) 2.00×10^5, and (d) 7.00×10^4.

carrier mobility [16,174]. The latter variable may lower the surface resistance of the polymer electrodes. Accordingly, an increase in the M_w of PSS results in improved conductive pathways within PSS-doped PANI nanostructures that ultimately results in increased conductivity.

To identify the optimal set of experimental conditions, PSS-doped PANI was synthesized with various M_w of PSS and at various weight ratios of aniline to PSS (w_{PSS}/w_{ANI}) at temperatures from –50 to 25°C (Figure 67). Figure 67a and Table 13 shows the conductivity of PSS-doped PANI fabricated with different M_w of PSS. The conductivity of the PSS-doped PANI increased with the M_w of the PSS: 1.96×10^6 Da (11.2 S cm^{-1}), 1.00×10^6 Da (2.68 S cm^{-1}), 2.00×10^5 Da (0.0535 S cm^{-1}), and 7.00×10^4 Da (0.00894 S cm^{-1}), which is consistent with the AFM measurements. Further enhancement in the conductivity of PSS-doped PANI was realized by lowering the polymerization temperature. Lower temperatures facilitate *para*-directed polymerization, which results in the more electrically favorable head-to-tail bonding of monomers [40]. In addition, the conductivity increased with the w_{PSS}/w_{ANI} ratio from 2.5 to 10 (Figure 67b and Table 14). The conductivity of the PSS-doped PANI decreased slightly at w_{PSS}/w_{ANI} ratios greater than 10. This suggests that PSS is able to protonate aniline monomers under optimal conditions, but that excess PSS can act as a dispersing agent rather than a doping agent. Changes in

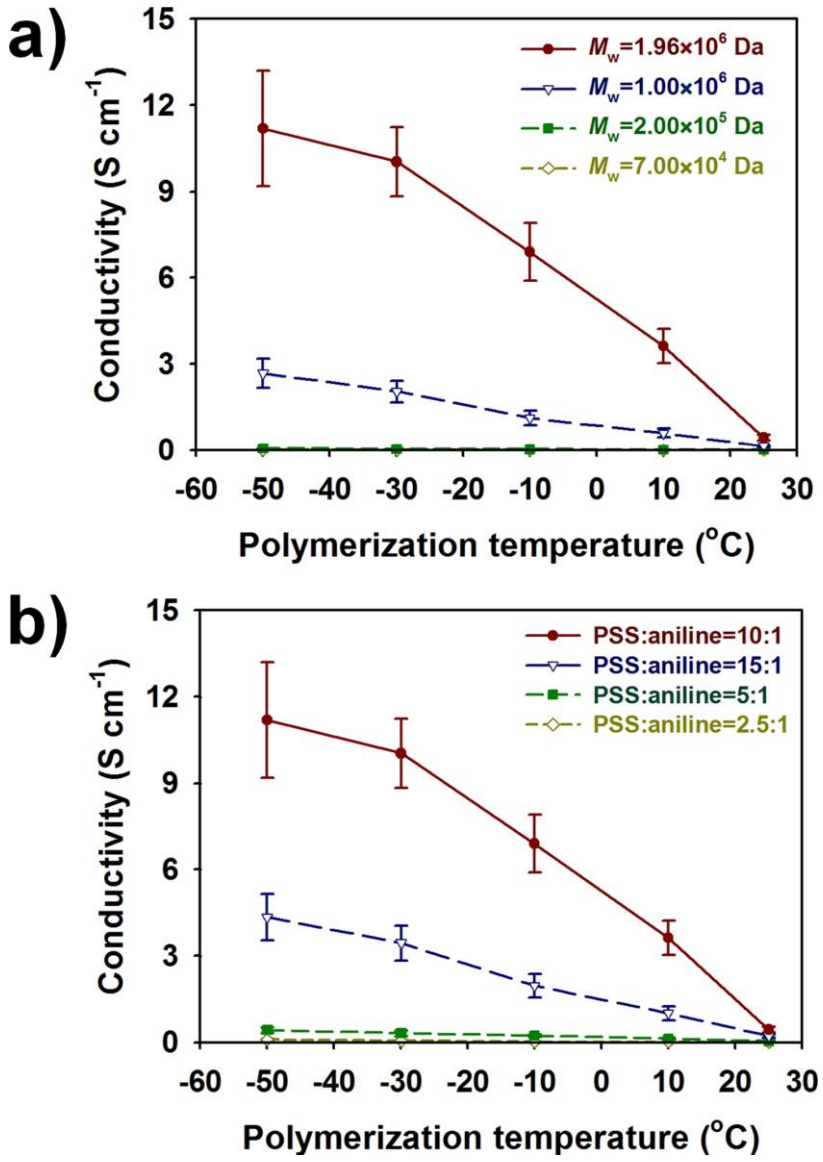

Figure 67. (a) Conductivity of PSS-doped PANI polymerized with different M_w of PSS at various polymerization temperature. A w_{PSS}/w_{ANI} ratio was fixed at 10. (b) Conductivity of PSS-doped PANI polymerized with different w_{PSS}/w_{ANI} ratios and various polymerization temperature. A M_w of PSS was fixed at 1.96×10^6.

Table 13. Electrical properties of PSS-doped PANI polymerized with different M_w of PSS at various polymerization temperature. A w_{PSS}/w_{ANI} ratio was fixed at 10.

M_w (Da)[a]	polymerization temperature (℃)	surface resistance (Ω)[a]	conductivity (S cm^{-1})[a]
1.96×10^6	−50	1.97×10^2	11.2±2.00
	−30	2.20×10^2	10.0±1.20
	–10	3.20×10^2	6.91±1.00
	10	6.09×10^2	3.63±0.60
	25	5.00×10^3	0.44±0.10
1.00×10^6	–50	8.24×10^2	2.68±0.50
	–30	1.08×10^3	2.05±0.38
	–10	1.96×10^3	1.13±0.25
	10	3.67×10^3	0.60±0.16
	25	1.57×10^4	0.14±0.031
2.00×10^5	–50	4.13×10^4	0.054±0.013
	–30	5.48×10^4	0.040±0.013
	–10	7.48×10^4	0.030±0.0063
	10	1.32×10^5	0.017±0.0031
	25	4.04×10^5	0.0055±0.0031
7.00×10^4	–50	2.47×10^5	0.0089±0.0023
	–30	4.25×10^5	0.0052±0.0023
	–10	9.82×10^5	0.0023±0.0093
	10	1.34×10^6	0.0017±0.00074
	25	2.11×10^6	0.0011±0.00056

[a] PSS-doped PANI with a thickness of 1 μm were measured.

Table 14. Electrical properties of PSS-doped PANI polymerized with different w_{PSS}/w_{ANI} ratios and various polymerization temperature. M_w of PSS was fixed at 1.96×10^6.

w_{PSS}/w_{ANI} ratio	polymerization temperature (℃)	surface resistance (Ω)[a]	conductivity (S cm^{-1})[a]
10	−50	1.97×10^2	11.2±2.00
	−30	2.20×10^2	10.0±1.20
	−10	3.20×10^2	6.91±1.00
	10	6.09×10^2	3.63±0.60
	25	5.00×10^3	0.44±0.10
15	−50	5.07×10^2	4.35±0.80
	−30	6.41×10^2	3.45±0.60
	−10	1.12×10^3	1.96±0.40
	10	2.19×10^3	1.01±0.25
	25	9.79×10^3	0.22±0.050
5	−50	5.18×10^3	0.43±0.10
	−30	6.88×10^3	0.32±0.10
	−10	9.39×10^3	0.24±0.050
	10	1.66×10^4	0.13±0.025
	25	5.07×10^4	0.044±0.025
2.5	−50	2.29×10^4	0.096±0.025
	−30	3.95×10^4	0.056±0.025
	−10	9.12×10^4	0.024±0.010
	10	1.25×10^5	0.018±0.0080
	25	1.97×10^5	0.011±0.0060

[a] PSS-doped PANI with a thickness of 1 μm were measured.

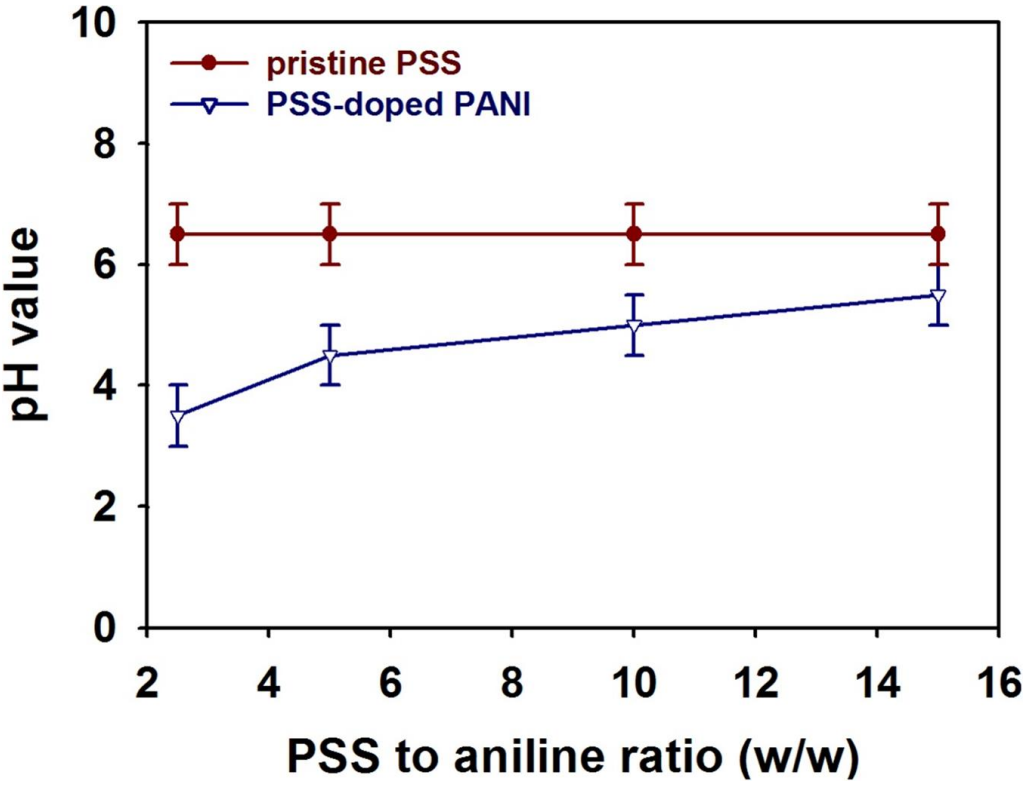

Figure 68. pH value of pristine PSS and PSS-doped PANI polymerized at different w_{PSS}/w_{ANI} ratios.

the w_{PSS}/w_{ANI} ratio also changed the acidity of the PSS-doped PANI (Figure 68). With increasing w_{PSS}/w_{ANI}, the pH of the PSS-doped PANI solution also increased. This indicates that polymeric anions, which are almost neutral (pH = 7.0), cannot only act as aniline dopants, but can also reduce the acidity of the reaction medium. Conventional PANI solutions that are doped with HCl are highly acidic (pH = 1.0). These results show that the conductivity of PSS-doped PANI could be improved under less acidic conditions by optimizing the w_{PSS}/w_{ANI} ratio and polymerization temperature.

FT-IR and XRD was utilized to further investigate changes in the chemical bonding and charge-transport properties of PSS-doped PANI having the different PSS M_w (Figure 69 and 70). In the FT-IR spectra of PSS with M_w of 1.96×10^6, 1.00×10^6, 2.00×10^5, and 7.00×10^4, characteristic bands of PSS were appeared at 621, 676, 699, 773, 826, 1004, 1036, 1125, 1177, ,1414, 1451, 1494, 1596, 1651, 2848, 2921, 3025, 3055, and 3439 cm^{-1} (Figure 69a) [33,46]. The bands at 622 and 676 cm^{-1} are assigned to the stretching vibration modes of the $C-SO_3^-$ and C−S benzenoid ring, respectively. The peaks at 1036 and 1177 cm^{-1} are attributed to the symmetric and asymmetric stretching modes of the SO_3^-, respectively. The in plane bending and stretching of benzene ring are present at 1004 and 1125 cm^{-1}, respectively. The bands at 699 and 774 cm are indicative of the benzene ring monosubstituted. The peak at 825 cm^{-1}

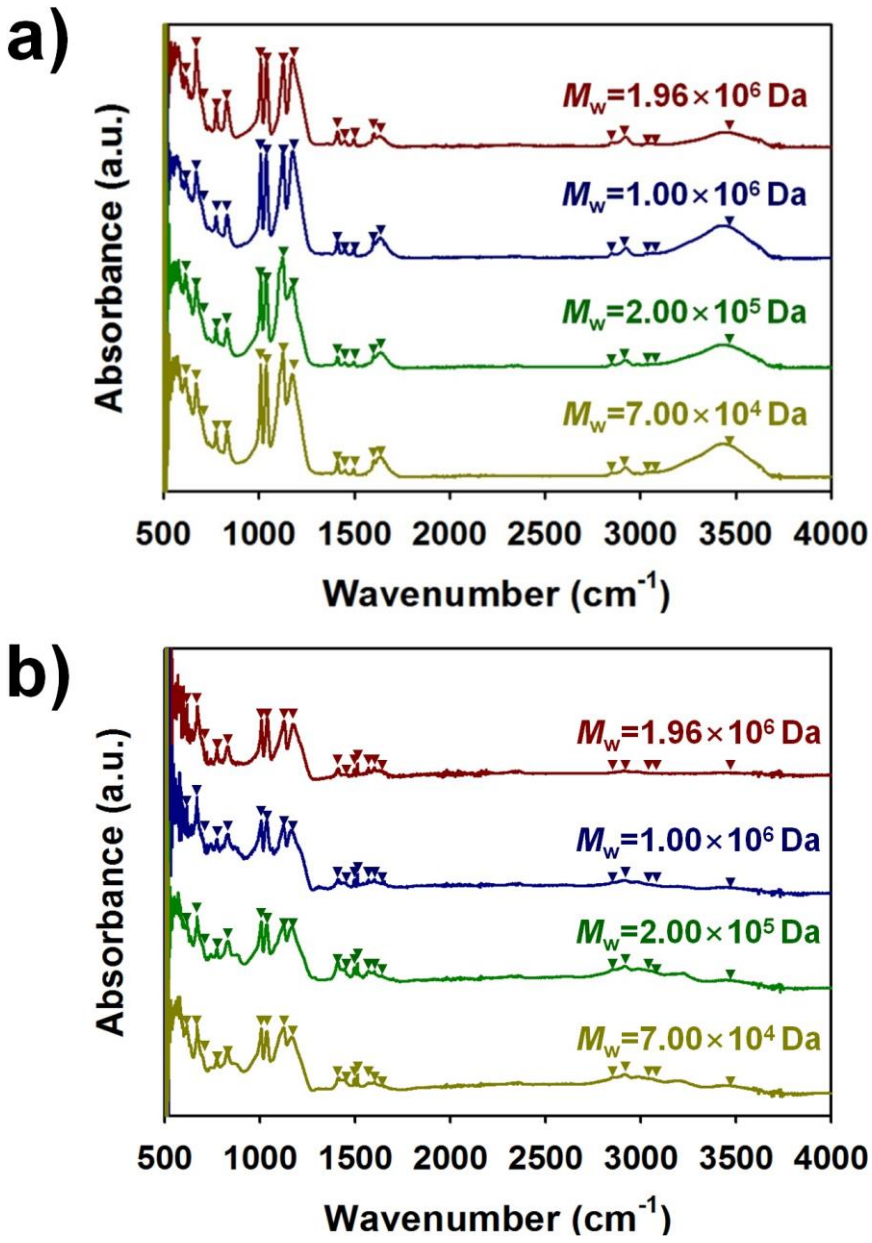

Figure 69. FT-IR spectra of (a) PSS having different M_w and (b) PSS-doped PANI polymerized with different M_w of PSS at a polymerization temperature of –50℃. All samples were polymerized at the w_{PSS}/w_{ANI} ratio of 10.

corresponds to the out of plane bending mode for the *para*-disubstituted benzene. The asymmetric bending of CH_2 is present at 1414 and 1451 cm^{-1}. The bands at 1494 and 1596 cm^{-1} originate from the carbon−carbon stretching aromatic ring stretching. The peaks for the bending and stretching of the H_2O are observed at 1651 and 3439 cm^{-1}, respectively. The symmetric and asymmetric stretching of the CH_2 can be assigned to the bands at 2848 and 2921 cm^{-1}, respectively. The stretching mode of the aromatic C−H bonds is appeared at 3025 and 3053 cm^{-1}. There were no significant differences between the FT-IR spectra of the PSS with the different M_w, implying that the every PSS sample has almost same chemical compositions. Thus, the FT-IR spectra of the PSS-doped PANI synthesized using the PSS with different M_w were further investigated to understand the effects of PSS M_w on the growth of the resulting PANI structures (Figure 69b). In comparison to the FT-IR results of PSS, two distinctive peaks were found at around 1513 and 1571 cm^{-1} in the spectra of the PSS-doped PANI samples, which originate to the C=C stretching vibration modes of the benzenoid unit (–N=B=N–) and quinoid unit (–N=Q=N–), respectively [33,46]. The other characteristic peaks for the PANI structure, such as C–N and N–H stretching vibration modes of the secondary aromatic amine, could not be clearly distinguishable from the peaks of PSS because of the predominant amounts of the PSS than the aniline monomers.

The intensity ratio of the peaks at 1571 cm^{-1} (I_{1571}) and 1513 cm^{-1} (I_{1513}) is related to the conjugation length and doping level of the PANI structure.[6] The ratio I_{1571}/I_{1513} of the PSS-doped PANI increased with the M_w of the PSS: 1.96×10^6 Da (0.71), 1.00×10^6 Da (0.66), 2.00×10^5 Da (0.60), and 7.00×10^4 Da (0.53), which is consistent with the electrical conductivity of the samples. These results suggest the following points: 1) The higher M_w PSS contains smoother surfaces for attracting the aniline monomers through the electrostatic interactions ; 2) The smoother surfaces of PSS lead to an increased connectivity between the monomeric units ; 3) These connectively linked monomeric units can be doped by more $–SO_3H$ units on the PSS surfaces ; 4) As a result of the improved doping efficiency of aniline, the PANI structures with extended π−conjugated systems can be formed [16,174]. For these reasons, the protonation level of the PSS-doped PANI increased with increasing M_w of PSS, allowing the effective delocalization of π-electrons within the PANI structure.

XRD was used to identify the influnces of the M_w of the PSS on the crystalline structures of the PSS-doped PANI (Figure 70). Characteristic bands were observed with the PSS-doped PANI at 2θ = 15.8°, 20.3°, and 25.5°. The band at 2θ = 25.5 ° became stronger with increasing M_w of PSS, whereas the peak intensities at 15.8° and 20.3° decreased. The results indicate that the

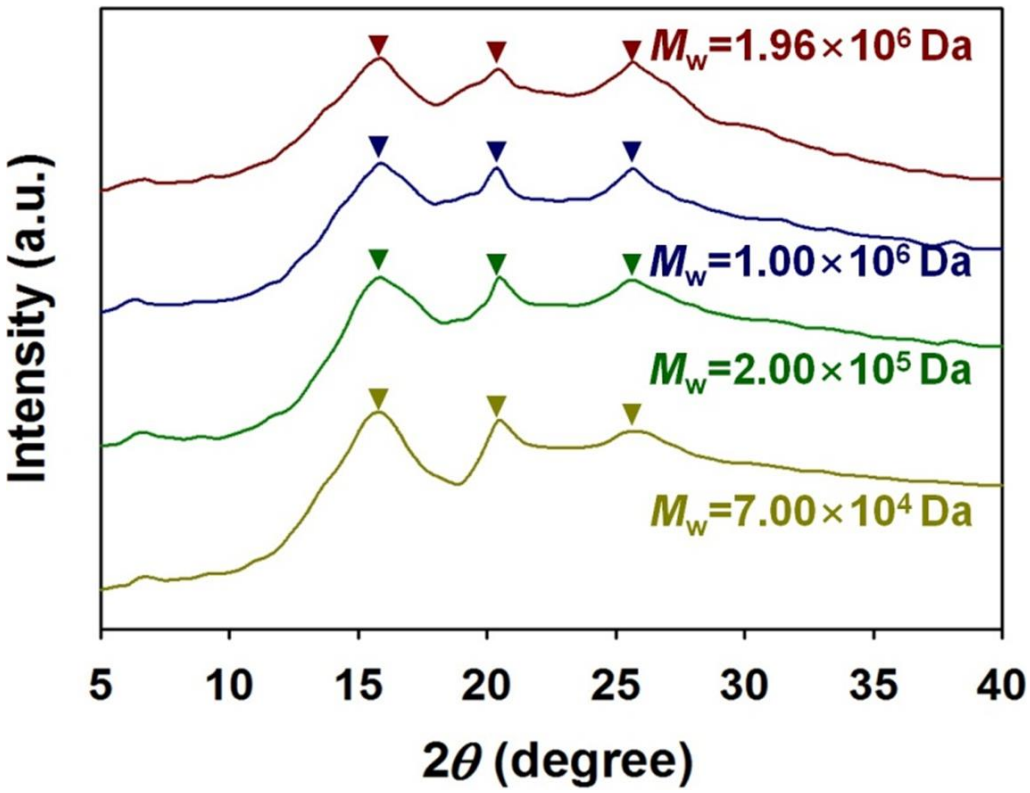

Figure 70. (a) XRD spectra of PSS-doped PANI polymerized with different M_w of PSS at a polymerization temperature of −50°C. All samples were polymerized at the w_{PSS}/w_{ANI} ratio of 10.

higher M_w PSS promote the linear chain conformation necessary for crystallization within the PANI structure, thus permitting both the increased π-π interchain stacking and extent of π-conjugation in the PANI backbone [39,66]. Therefore, the PANI doped by PSS with M_w of 1.96×10^6 has more effective conjugation length of the PANI chains to delocalize more π-electrons than the other samples prepared by using the PSS having lower M_w. Judging from these results, the higher M_w PSS efficiently doped the aniline monomers under the less acidic conditions, and resulted in improved charge transport properties and crystallinity of the PSS-doped PANI.

The morphological features of PSS-doped PANI/graphene nanocomposites were characterized by FE-SEM and AFM (Figure 71 and 72). An FE-SEM micrograph of PSS-doped PANI after introducing the graphene sheets is shown in Figure 71a and b. Graphene sheets with dimensions ranging from 2 to 10 μm were dispersed throughout the PSS-doped PANI/graphene nanocomposites (Figure 71a). Relative to the surfaces of pristine graphene sheets, the surfaces of the graphene sheets dispersed in the PSS-doped PANI/graphene were covered with PANI NPs with diameters of 45−50 nm, nearly identical to the diameter of pristine PSS-doped PANI NPs (Figures 71b and c). This suggests that the underlying graphene sheets in PSS-doped PANI/graphene may be highly dispersible in the aqueous PSS-doped PANI solution as a result of

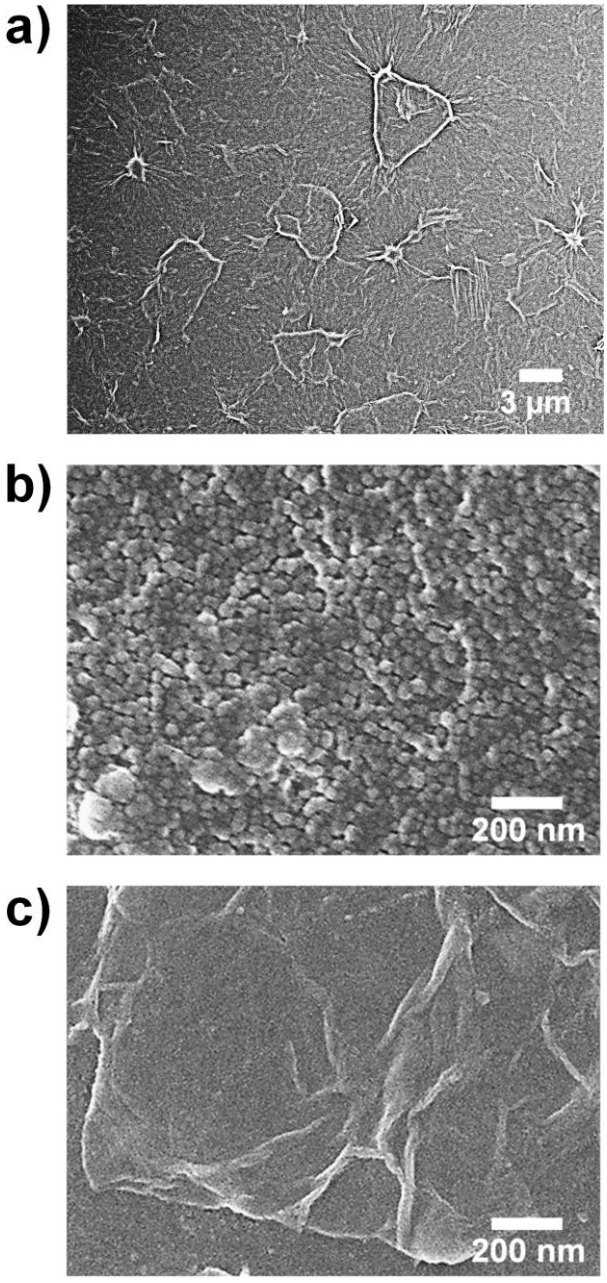

Figure 71. FE-SEM images of (a) PSS-doped PANI/graphene nanocomposite with 30 wt% graphene (a,b) and graphene sheet (c). Magnifications: ×2k (a) and ×80k (b, c).

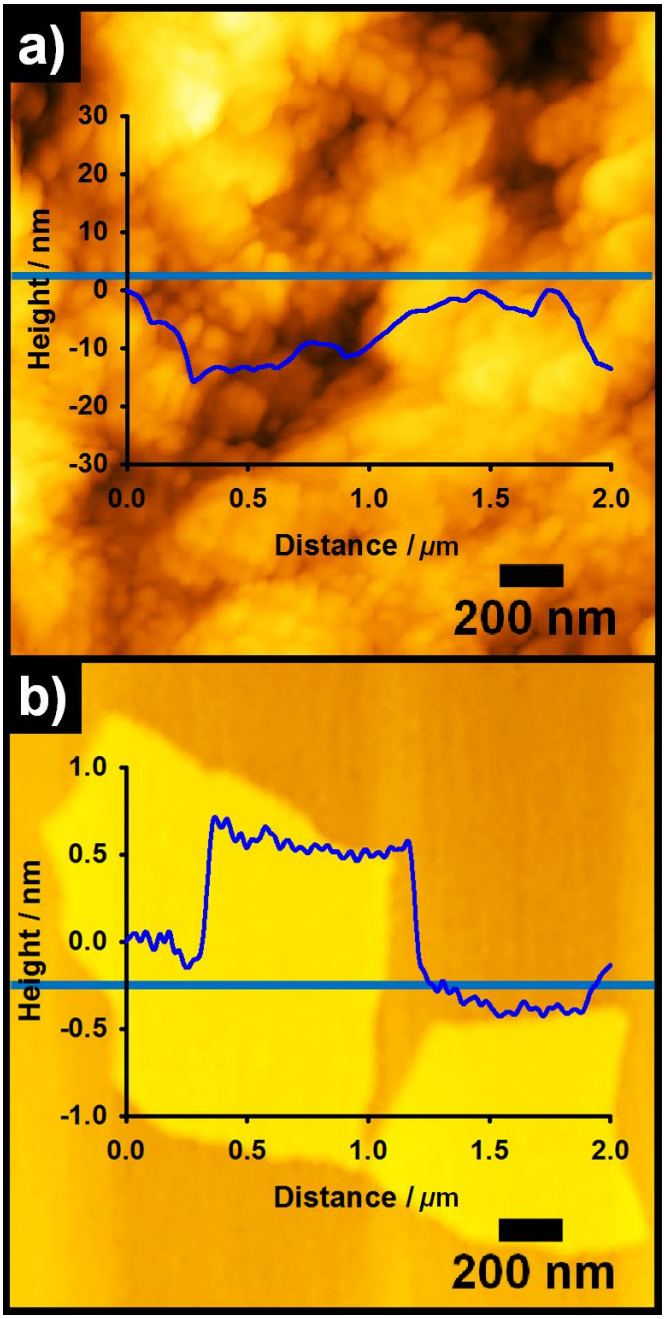

Figure 72. AFM images of (a) PSS-doped PANI/graphene nanocomposite with 30 wt% graphene and (b) graphene sheet.

electrostatic repulsion between PSS and the graphene sheets [51]. AFM micrographs are shown in Figure 72. Note that the incorporation of graphene sheets into the PSS-doped PANI results only in a small increase in the surface roughness (4.87 nm) compared with that of pristine PSS-doped PANI (Figure 72a). This implies that graphene sheets with atomic layer thickness may not significantly contribute to the surface roughness of the composite films (Figure 72b). Thus, the underlying graphene sheets that form strong π–π stacking interactions with PSS-doped PANI provide better conductive pathways, resulting in lower surface resistance [45,66].

Figure 73a shows the narrow surface resistance distribution observed for each 2-cm^2 thin-film of PSS-doped PANI/graphene nanocomposite containing 30-wt% graphene sheet. This suggests that spin-coating was effective in forming highly uniform PSS-doped PANI/graphene thin-films on the flexible PET substrates. The conductivity and surface resistance of PSS-doped PANI/graphene-coated flexible electrodes on a number of repeatable bends were evaluated using the four-point probe method (Figure 73b). In chemical sensor devices, the conductivity of the sensor electrodes is an important factor since higher currents result in larger changes in resistance upon exposure to an analyte gas. The conductivities of pristine PSS-doped PANI, G-PANI 1 (with 10-wt% graphene), G-PANI 2 (with 20-wt% graphene), and G-PANI 3 (with

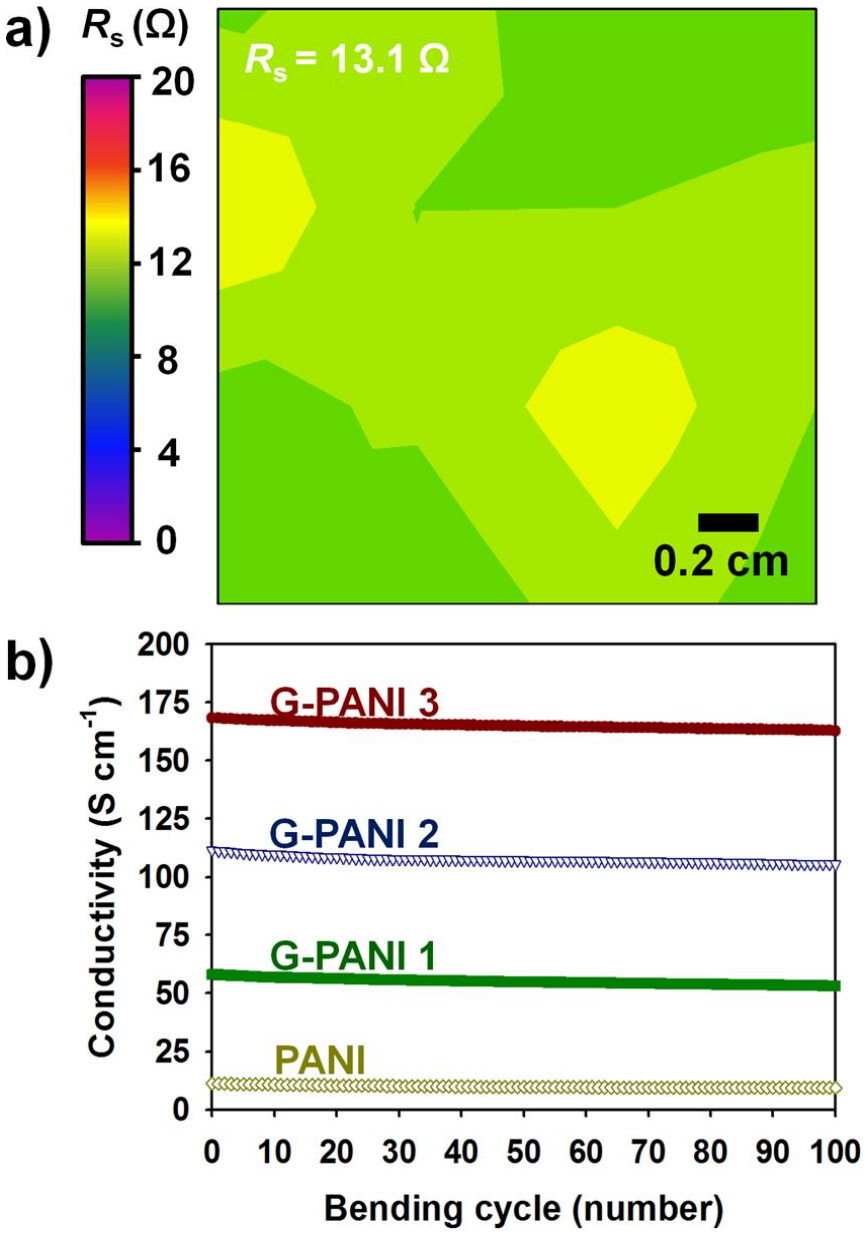

Figure 73. (a) Surface resistance distribution of PSS-doped PANI/graphene nanocomposite with 30 wt% graphene. (b) Conductivity of the flexible electrodes based on PSS-doped PANI/graphene nanocomposites with different amounts of graphene upon a number of bends.

Table 15. Electrical properties of PSS-doped PANI/graphene nanocomposites with different amounts of graphene.

sample	surface resistance (Ω)[a]	conductivity (S cm^{-1})[a]
PANI	1.97×10^{2}	11.2
G-PANI 1 (10-wt%)	3.81×10^{1}	58.0
G-PANI 2 (20-wt%)	1.98×10^{1}	111.4
G-PANI 3 (30-wt%)	1.31×10^{1}	168.4

[a] PSS-doped PANI/graphene nanocomposites with a thickness of 1 μm were measured.

30-wt% graphene) were 11.2, 58.0, 111.4, and 168.4 cm^{-1}, respectively (Table 15). These data show that the underlying graphene sheets were successfully incorporated into the PSS-doped PANI nanocomposites and greatly enhanced the charge transport within the PSS-doped PANI/graphene hybrid nanocomposites, as discussed above. Furthermore, no obvious decreases in conductivity were observed, even after 200 bending cycles. This shows that the electrical roperties of the PSS-doped PANI/graphene nanocomposites were stabilized through enhanced interfacial interactions and mechanical interlocking of the graphene sheets and the PSS-doped PANI.

XRD, UV/VIS/NIR, and Raman spectroscopies were utilized to further elucidate the effects of graphene sheets on charge transport in PSS-doped PANI (Figure 74–76). Distinctive peaks were observed at 2θ = 15.8° (5.61 Å), 20.3° (4.38 Å), and 25.5° (3.50 Å) in the X-ray diffractogram of pristine PSS-doped PANI (Figure 74). Interestingly, the peaks at 2θ = 15.8° and 20.3° decreased with increasing amounts of graphene, while the peak at 25.5° became much sharper and stronger relative to the analogous peak observed in the diffractogram of pristine PSS-doped PANI. The strength of the peak at 25.5° (*d*-spacing of 3.50 Å) indicates the face-to-face π–π stacking distance between neighboring phenyl rings within the crystalline structure of PSS-doped PANI [65,66]. However, the intrinsic band corresponding to RGO at around 24.5°

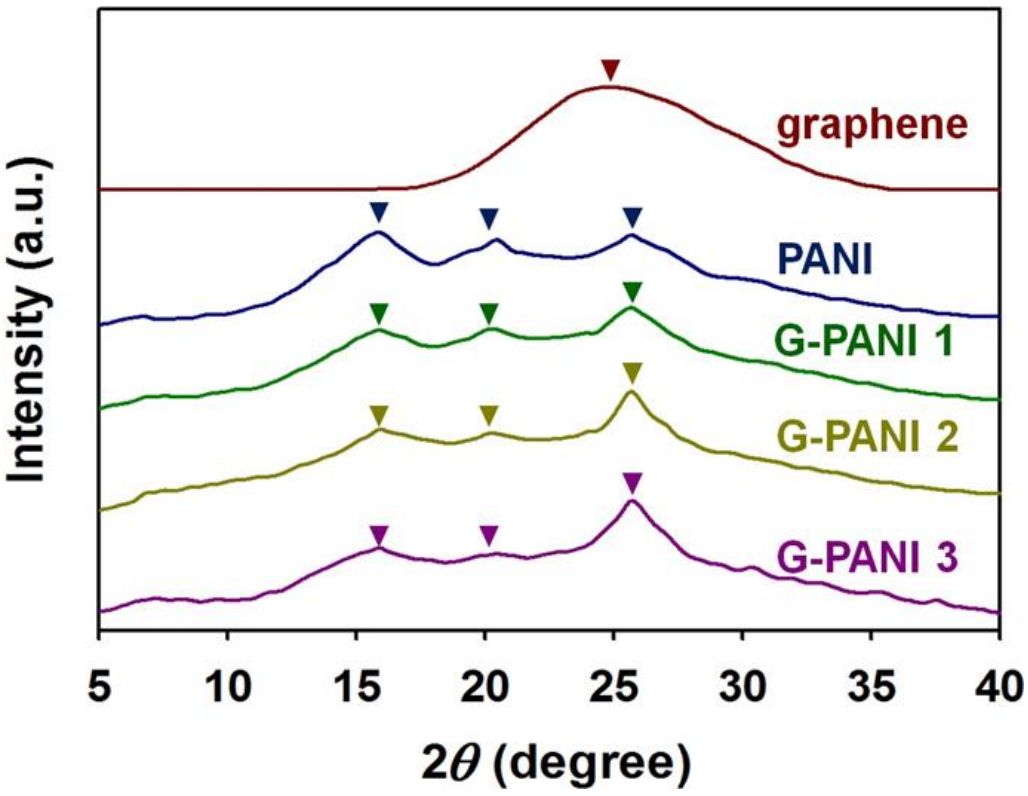

Figure 74. XRD spectra of PSS-doped PANI/graphene nanocomposites.

(3.63 Å) was not observed in every diffractogram, suggesting that, in those cases, the graphene sheets were intercalated into the PSS-doped PANI structure. Thus, the sharp peak at 25.5° indicates improved crystallinity and π–π inter-chain stacking within the PANI/graphene structure [65,66]. Improved crystallinity implies better charge transport between the PSS-doped PANI and the graphene sheets.

To further characterize this charge transfer, UV/VIS/NIR spectra of PSS-doped PANI/graphene nanocomposites containing various amounts of graphene sheets are shown in Figure 75. Two bands characteristic of PANI (π–π excitation of the benzenoid (–B–NH–B–) and quinoid diamine (–N=Q=N–) units) were observed at 390 and 730 nm, respectively, in the spectrum of pristine PSS-doped PANI [39,129]. Interestingly, both peaks shifted to longer wavelengths with increasing amounts of graphene in the composite. This red shift implies an increased extent of π–conjugation within the PANI structure [129]. More specifically, it indicates an enhancement in the intermolecular interactions between PSS-PANI and the graphene sheets that facilitate charge transfer within the samples. Interestingly, the peak around 730 nm became indistinctive with increasing addition amounts of the graphene sheets, whereas the very intense bands commencing at around 1000 nm increased steadily in intensities. These intense free-carrier tails, which are indicative features of

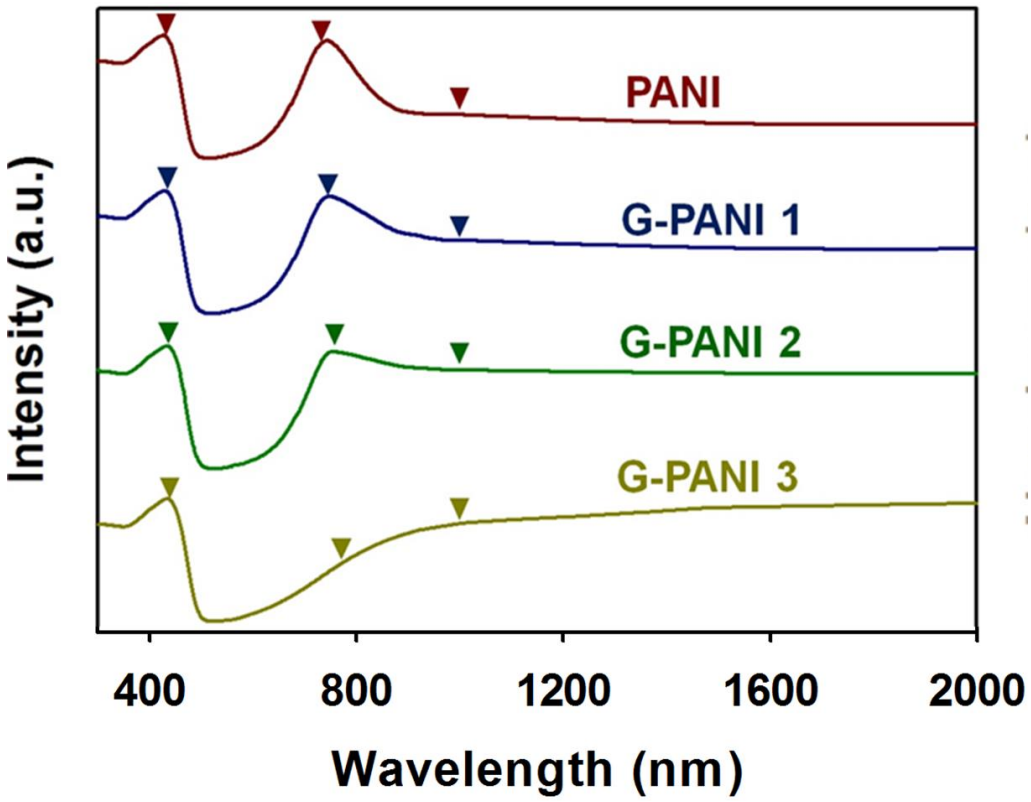

Figure 75. UV/VIS/NIR spectra of PSS-doped PANI/graphene nanocomposites.

delocalized band structures with relatively long conjugation lengths, extended from 1000 nm and became more pronounced with increasing proportions of graphene in the PSS-doped PANI. Conformational changes in PANI from a compact coil-like structure (pristine PSS-doped PANI) to an expanded coil-like structure (G-PANI 3 with 30-wt% graphene) are caused by π–π overlap between the basal planes of the graphene sheets and the quinoid rings of PANI [39].

Figure 76 shows Raman spectra of pristine graphene, pristine PSS-doped PANI, and PSS-doped PANI/graphene nanocomposites. In the spectrum of pristine graphene, the D band, corresponding to structural defects, and the G band, which is related to vibrations of sp^2-hybridized carbon atoms, appeared at 1351 and 1598 cm^{-1}, respectively. The D/G ratio of graphene was higher than that of non-reduced GO, indicating that the proportion of defects increased during the reduction of GO. Distinctive PANI bands were also observed at 1162, 1313, 1337, 1486, 1586, and 1594 cm^{-1} [65,66,175]. In addition, bands at 1003, 1134, and 1600 cm^{-1} were assigned to the $–SO_3H$ group of PSS [176]. The bands at 1162, 1486, and 1586 cm^{-1} correspond to C–H bending vibrations of the quinoid ring, C=N stretching, and C=C stretching of the quinoid ring, respectively [65,175]. These bands became more pronounced with increasing amounts of graphene sheet, suggesting that the conjugation length of the PANI

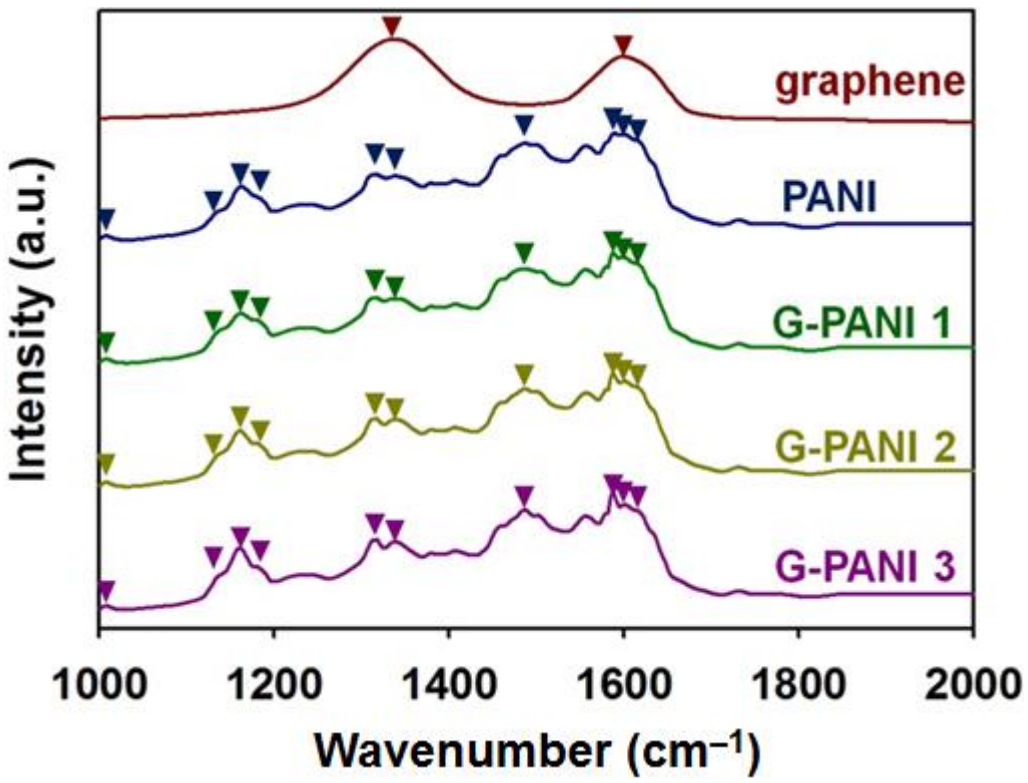

Figure 76. Raman spectra of PSS-doped PANI/graphene nanocomposites.

structure was elongated through strong π–π interactions between the graphene sheets and the quinoid rings of PANI. More specifically, the bands at 1313 and 1337 cm^{-1}, which are attributed to $=NH^{+}$ (protonated imine) stretching and $–NH•^{+}$ (protonated amine) stretching of the bipolaron structure, respectively, became more distinct after incorporation of the graphene sheets [65,175]. These data show that the presence of graphene sheets highly affected the protonation level of PSS-doped PANI.

The FT-IR spectra of the GO, RGO, PSS-coated GO, and PSS-coated RGO were measured to identify the changes in the chemical bonding of the GO during the reduction processes in the presence of PSS (Figure 77a). In the spectrum of pristine GO, characteristic bands appeared for the C–OH stretching (1225 cm^{-1}), C–O stretching (1040 and 1382 cm^{-1}), C=O stretching (1618 and 1725 cm^{-1}), C–H stretching (2844 and 2915 cm^{-1}), and O–H stretching (3439 cm^{-1}) [177,178]. Most distinctive peaks for the PSS were found in the spectrum of the PSS-coated GO, indicating that the PSS was successfully incorporated into the GO. In the spectrum of pristine RGO, most distinctive bands of the GO disappeared and the bands for the residual C–OH (1225 cm^{-1}), C–O (1382 cm^{-1}), and aromatic C=C (1514 and 1640 cm^{-1}) were found [177,178]. Moreover, these bands for the RGO became even more indistinctive in the spectrum of the PSS-coated RGO, indicating that the GO

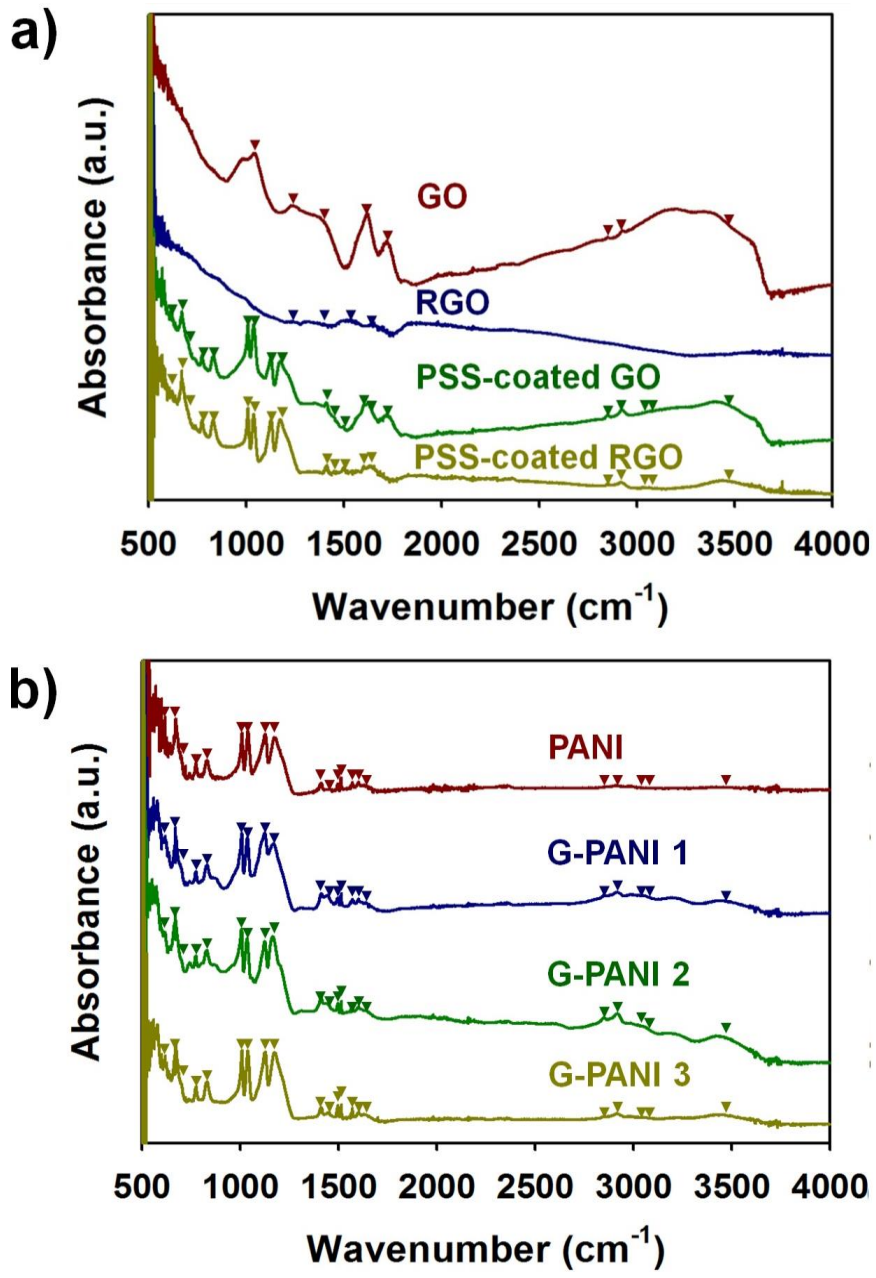

Figure 77. (a) FT-IR spectra of GO, RGO, PSS-coated GO, and PSS-coated RGO. (b) FT-IR spectra of PSS-doped PANI/graphene nanocomposites.

could be successfully reduced in the presence of PSS. To identify the effects of graphene sheets on the chemical bonding and charge transport properties of the PANI structure, the FT-IR spectra of PSS-doped PANI/graphene nanocomposites are shown in Figure 77b. Although the bands for the graphene sheets were not clearly observed in the spectra of PSS-doped PANI/graphene nanocomposites, the ratio I_{1571}/I_{1513} of the PSS-doped PANI increased with the adding amounts of the PSS-coated graphene: G-PANI 3 (with 30-wt% graphene) (0.85), G-PANI 2 (with 20-wt% graphene) (0.80), G-PANI 1 (with 10-wt% graphene) (0.73), and pristine PSS-doped PANI (0.71), which are in good agreement with the results of conductivity measurement, UV-VIS/NIR spectroscopy, and Raman spectroscopy . The results indicate that the graphene sheets extend the π–conjugated structures in the PANI backbone through the strong π–π stacking interactions with the quinoid rings of PANI [65,66,172]. Accordingly, more electrons in the PANI backbone can be delocalized in the presence of graphene sheets, thus permitting the higher protonation level and conductivity of the PSS-doped PANI structure.

X-ray photoelectron spectroscopy (XPS) was used to obtain detailed elemental information and to determine protonation levels in PSS-doped PANI/graphene (Figures 78 and 79). Since graphene sheets are composed of sp^2-hybridized carbon networks, samples containing graphene exhibited higher

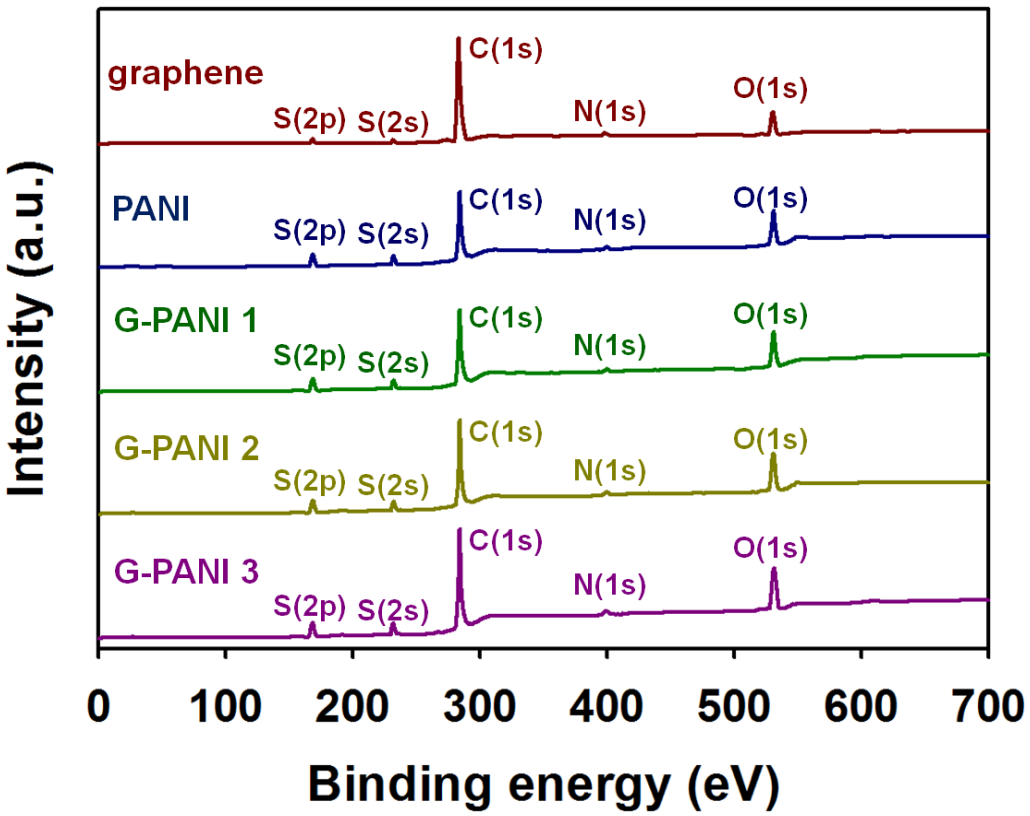

Figure 78. Fully scanned XPS spectra of PSS-doped PANI/graphene nanocomposites.

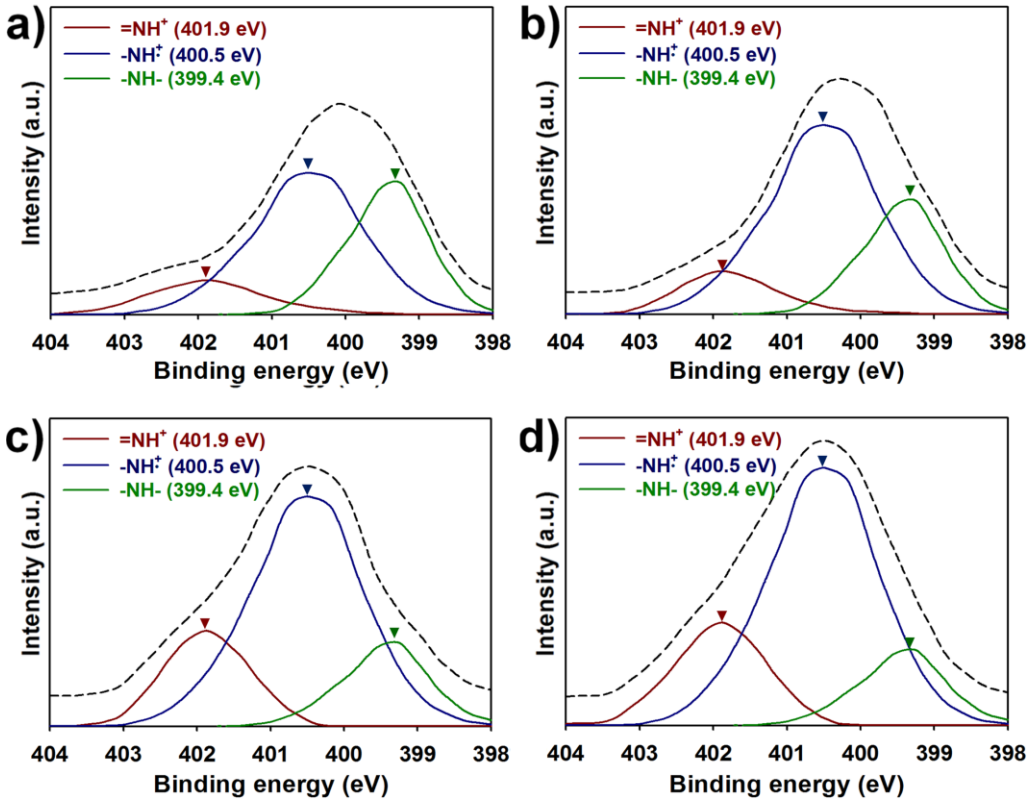

Figure 79. XPS patterns of PSS-doped PANI/graphene nanocomposites: N1s core spectra of (a) pristine PSS-doped PANI, (b) G-PANI 1 (with 10 wt% graphene), (c) G-PANI 2 (with 20 wt% graphene), and (d) G-PANI 3 (with 30 wt% graphene).

Table 16. XPS atomic ratios of PSS-doped PANI/graphene nanocomposites.

Samples	XPS atomic ratio			
	$=NH^{+a}$	$–NH•^{+a}$	$–NH–^{a}$	N^{+}/N ratio^{a}
PANI	0.11	0.46	0.43	0.57
G-PANI 1	0.12	0.55	0.33	0.67
G-PANI 2	0.23	0.56	0.20	0.79
G-PANI 3	0.24	0.59	0.17	0.83

[a] The values were calculated using the N1s core spectra of the samples.

C (1s) peak intensity (Figure 78) [65,175]. In addition, small peaks assigned to S(2p) (164 eV), S(2s) (231 eV), and N1s (400 eV) were found in the survey spectrum of graphene; this suggests that the reduction of graphene sheets were carried out in the presence of hydrazine (N_2H_4) and PSS. Judging from sulfur content (~5.7%) in the XPS analysis of graphene, the amount of PSS, which is contained in the graphene sheets, was estimated as ~33% [51]. N (1s) spectra of the PSS-doped PANI and graphene-incorporated samples contained three peaks at 399.4 eV (–NH–, benzenoid amine nitrogen), 400.5 eV ($–NH•^+$, protonated amine), and 401.9 eV (=NH+, protonated amine) (Figure 79) [127,176]. The ratio of N^+ species (sum of $–NH•^+$ and =NH+) to N species (sum of –N=, –NH–, $–NH•^+$, and $=NH^+$) in the N (1s) spectra was calculated to estimate the protonation states of PSS-doped PANI/graphene nanocomposites. The N^+/N ratios of pristine PSS-doped PANI, G-PANI 1 (with 10-wt% graphene), G-PANI 2 (with 20-wt% graphene), and G-PANI 3 (with 30-wt% graphene) were 0.57, 0.67, 0.79, and 0.83, respectively (Table 16). Most –N= and –NH– units exist as N^+ species when the N^+/N ratio exceeds 50%. These data agree with the results obtained via XRD, Raman, and FT-IR analyses, and are consitent with an enhancement in the π–π interaction between the graphene sheets and the quinoid unit of PANI, resulting in longer paths for delocalized electrons within the PANI structure and an elevated doping level.

3.3.2.2. H_2S Sensors based on PSS-doped PANI/graphene nanocomposites

Figure 80 describes the possible mechanisms by which H_2S gas is detected using PSS-doped PANI/graphene nanocomposite electrodes. Note that H_2S is colorless, toxic, and flammable with a low threshold limit value of 10 ppm [171,189]. Strong hydrogen bonding between amine nitrogens on the PANI backbone and H_2S gas promotes dissociation of the H_2S molecule into H^+ and HS^- ions [170,171]. The H^+ ions form new N–H bonds with the amine nitrogen sites of PANI. This protonation produces charge carriers (semiquinone radicals), resulting in an increase in the conductivity of the PSS-doped PANI. Reversible charge transfer then occurs between the amine nitrogen atoms of the PANI backbone, generating ES with release of H_2S. These reversible interactions within the PANI backbone result in changes in the resistivity of the PSS-doped PANI/ graphene film. In addition, sulfonate anions ($–SO_3^-$) on PSS may induce additional hydrogen bonding, which may attract additional H_2S molecules [173]. Graphene sheets further enhance face-to-face ring stacking interactions within the PANI structure, and lead to a higher degree of charge transfer relative to that of pristine PSS-doped PANI in the presence of H_2S [65,66,172].

Prior to evaluating the PSS-doped PANI/graphene nanocomposites as H_2S sensor films, the films were characterized by CV and EIS in order to clarify the

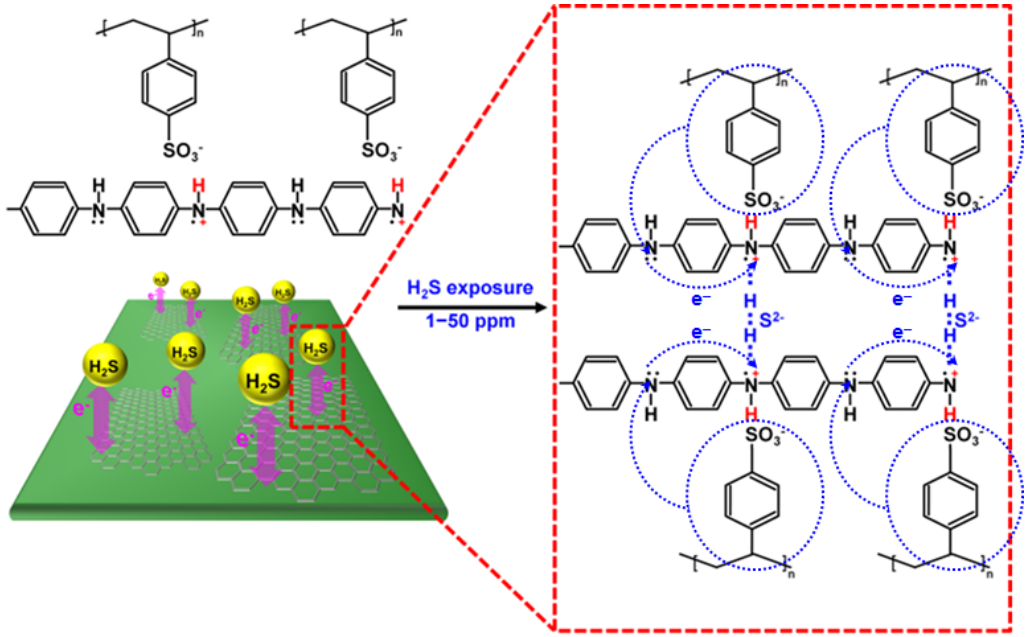

Figure 80. Possible mechanism for molecular interactions between the PSS-doped PANI/graphene nanocomposites and H_2S molecules.

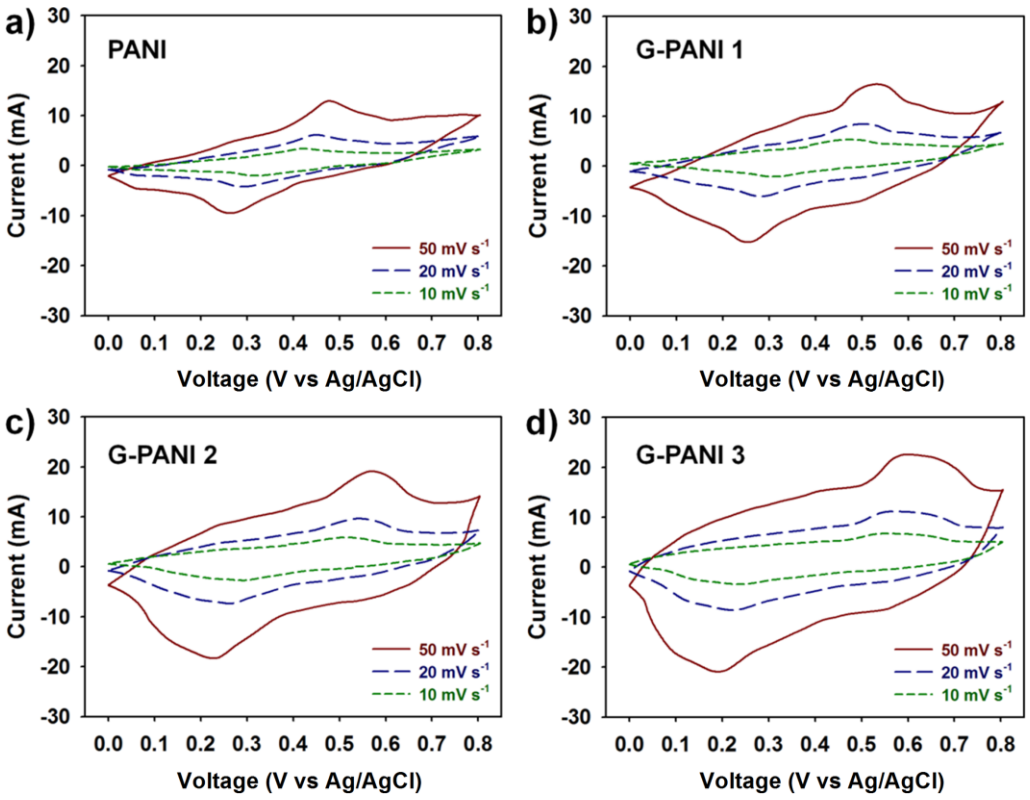

Figure 81. Cyclic voltammograms of (a) pristine PSS-doped PANI, (b) G-PANI 1 (with 10 wt% graphene), (c) G-PANI 2 (with 20 wt% graphene), and (d) G-PANI 3 (with 30 wt% graphene) in a 0.5M H_2SO_4 electrolyte at different scan rates (10, 20, and 50 mV s^{-1}).

effect(s) of graphene sheets on the electrical and electrochemical properties of PSS-doped PANI, and the *I–V* curves were acquired in the absence of H_2S (Figure 81–83). Voltammograms were acquired from 0 to 0.8 V at a scan rate of 20 mV s^{-1} (Figure 81), and showed two distinct peaks at 0.44–0.56 and 0.22–0.30 V, corresponding to the anodic (oxidization) and cathodic (reduction) electron transfer of PSS-doped PANI, respectively [65,178]. The redox equations are

$$PANI^{+}\cdot PSS^{-} + e^{-} + H^{+}\ (\text{oxidized state}) \leftrightarrows PANI^{0}\cdot PSS^{-}\cdot H^{+}\ (\text{reduced state}) \quad (8)$$

where e^{-} and H^{+} indicate the electron and proton of the H_2SO_4 electrolyte, respectively. With increasing proportions of graphene sheet in the PSS-doped PANI composites, the area under the CV peaks increased and both the anodic and cathodic peaks shifted to higher voltages. The PSS-doped PANI electrodes showed better electrochemical performance at every scan rate after the addition of graphene. This suggests that electron transport between PANI and protons from PSS was enhanced by strong intermolecular interactions between PANI and the graphene sheets, resulting in larger currents at the sensor electrode. An increased ability to interact with H^{+} is related to an enhanced sensitivity for H_2S gas, which facilitates the formation of additional amine nitrogen bonds along the PANI structure.

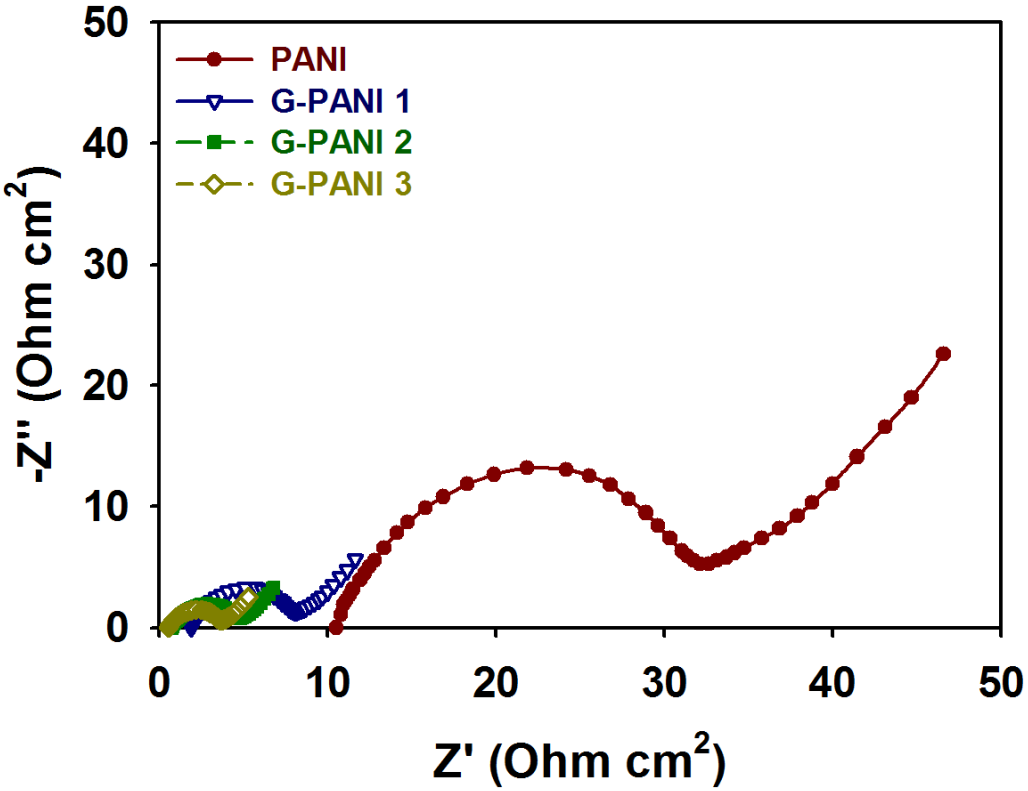

Figure 82. Electrochemical Impedance Spectra (EIS) of PSS-doped PANI/graphene nanocomposites in the frequency range from 100 kHz to 10 mHz.

Series (R_s) and charge-transfer resistances (R_{ct}) were measured using EIS (Figure 82). Nyquist impedance plots of the electrodes showed semicircular curves in the high-frequency region and linear curves at low frequencies. R_{ct} of the samples increased in the following order: G-PANI 3 (with 30-wt% graphene) (3.64×10^0 Ω cm^2) < G-PANI 2 (with 20-wt% graphene) (4.65×10^0 Ω cm^2) < G-PANI 1 (with 10-wt% graphene) (8.00×10^0 Ω cm^2) < pristine PSS-doped PANI (3.21×10^1 Ω cm^2). The reduced size of the semicircle and the lower R_{ct} values indicate that charger transfer within the samples was enhanced after the addition of graphene sheets [179].

The *I*–*V* characteristics of the PSS-doped PANI/graphene electrodes are shown in Figure 83. Contact resistance was estimated from the slope of the *I*–*V* curves. At a scan rate of 20 mV s^{-1}, contact resistance (*R*) decreased as the proportion of graphene in the nanocomposite increased (Figure 83a). After depositing additional PSS-doped PANI/graphene nanocomposites (5-μm thick) onto the flexible PET substrate, the *I*–*V* characteristics of the film samples were similar to those of the 1-μm-thick nanocomposites. This suggests that only a small amount of PSS-doped PANI/graphene solution is needed to form a good electric contact with the sensor electrode (Figure 83b) [29,74,117]. The CV, EIS, and *I*–*V* results of the PSS-doped PANI/graphene electrodes indicate that synergetic effects between the polymer matrix and the graphenes enhance

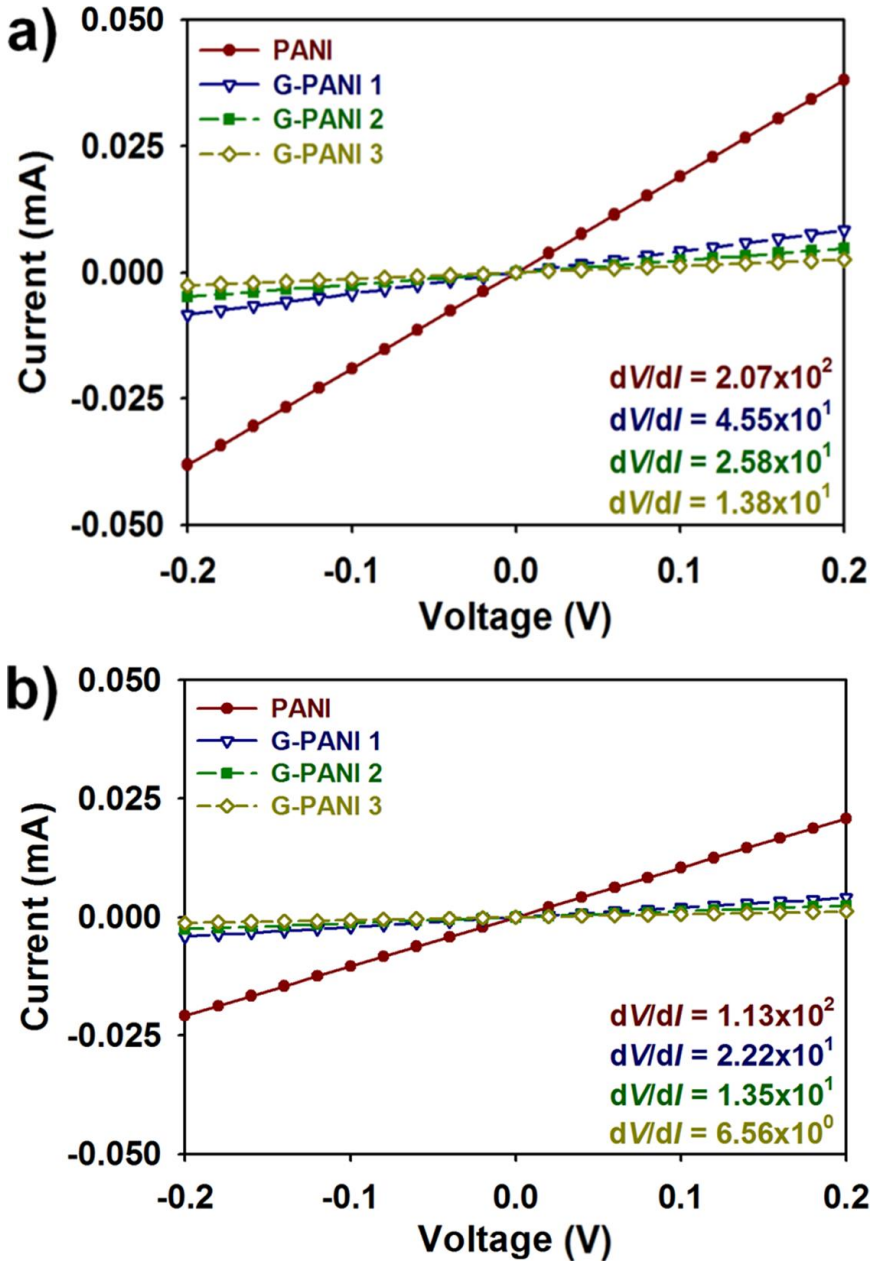

Figure 83. *I-V* characteristics of PSS-doped PANI/graphene nanocomposites with thickness of (a) 1 μm and (b) 5 μm integrated in the sensor substrate at a scan rate of 20 mV s^{-1}.

charge transfers in the sensor electrodes, which can improve the sensing performance for detecting H_2S.

The real-time response of PSS-doped PANI/graphene nanocomposites to H_2S was systematically investigated in order to gauge the influence of graphene content on sensing ability (Figure 84). $\Delta R/R_0$ recovered rapidly to its initial value after H_2S was purged from the system with compressed air, demonstrating the full reversibility of PANI−H_2S interactions. The electrical response to sequential exposures to H_2S at five concentrations (1, 2, 5, 20, and 50 ppm) is shown in Figure 84a. Negative changes in $\Delta R/R_0$ were observed when pristine PSS-doped PANI and PSS-doped PANI/graphene were exposed to H_2S gas. As above, the initial $\Delta R/R_0$ was recovered after the H_2S was replaced with air. As described above and shown in Figure 80, additional N–H bonds are formed within the PSS-doped PANI structure by interactions between H_2S and amine nitrogen atoms within PANI. The result is a decrease in $\Delta R/R_0$ of the PSS-doped PANI structure in response to H_2S. The sensor response and limit of H_2S detection were significantly improved by incorporating graphene sheets into PSS-doped PANI. The highly dispersed graphene sheets allowed greater electric currents to flow simultaneously through the sensor electrode. Note that H_2S gas was not detected using pristine graphene sheets. This suggests that the PSS-doped, PANI-based sensor

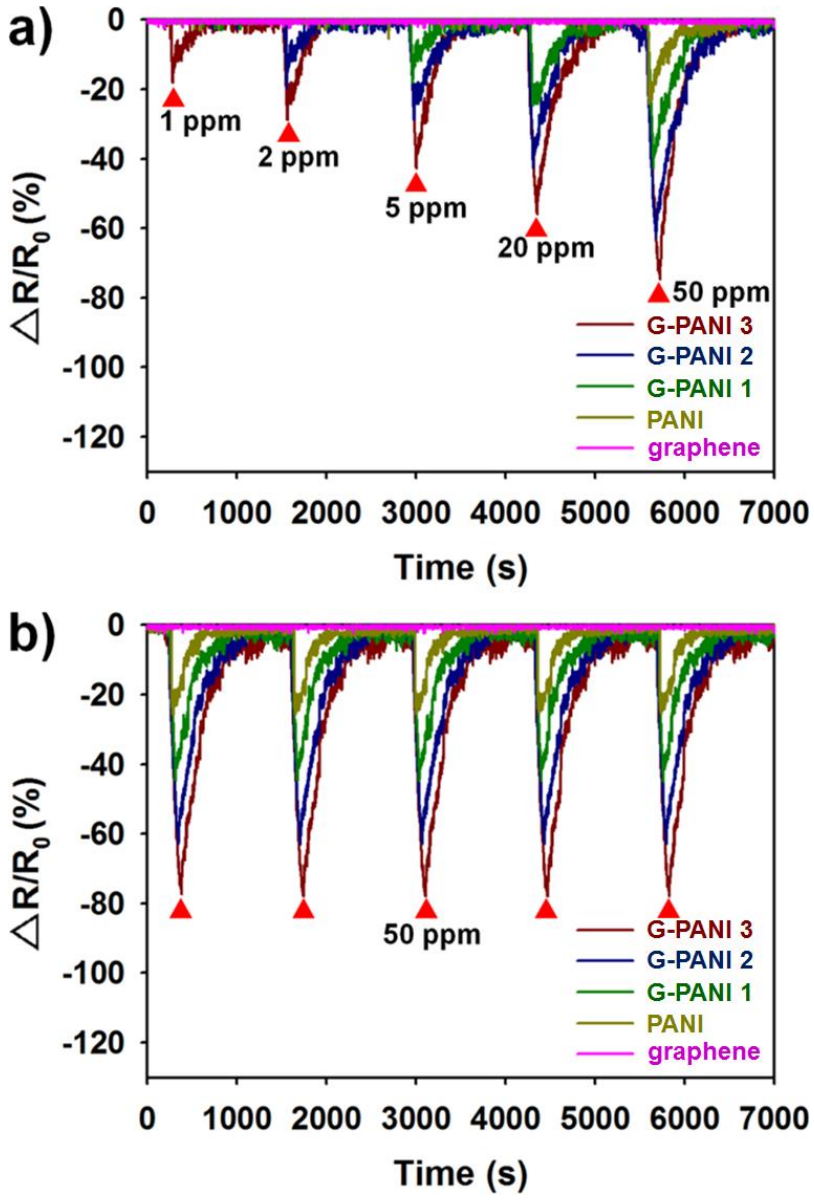

Figure 84. (a) Real-time responses of PSS-doped PANI/graphene nanocomposites upon cyclic exposure to H_2S (1 to 50 ppm) and synthetic air streams. (b) Real-time responses of PSS-doped PANI/graphene nanocomposites upon periodic exposure to 50 ppm H_2S.

electrodes detect H_2S *via* hydrogen bonding interactions between H_2S and amine nitrogen sites [32]. Such interactions increase charge transfer within the PSS-doped PANI structure, resulting in negative changes in $\Delta R/R_0$. G-PANI 3 (with 30-wt% graphene) boasted a significantly lower limit of detection (1 ppm) than those of pristine PSS-doped PANI (50 ppm), G-PANI 1 (with 10-wt% graphene) (5 ppm), and G-PANI 2 (with 20-wt% graphene) (2 ppm). This can be attributed to the significant conductivity enhancement in the 30-wt% composite. In addition, the detection limit of the PSS-doped PANI/graphene nanocomposites was significantly lower than those of conventional conducting polymers and conducting polymer/transition metal oxide-based H_2S sensors. The PSS-doped PANI/graphene nanocomposite sensors exhibited a response time of less than 90 s with a recovery time of 150 s. To evaluate the response reproducibility, the PSS-doped PANI/graphene nanocomposites were exposed to periodically fluctuating H_2S gas concentrations between 50 and 0 ppm (Figure 84b).

The data show that the PSS-doped PANI/graphene nanocomposites are viable for long-term use. To evaluate selectivity, G-PANI 3 (with 30-wt% graphene) was exposed to ammonia (NH_3) and ethanol (EtOH) at concentrations of 20 ppm (Figure 85). Interestingly, negative changes in $\Delta R/R_0$ were observed upon exposure to H_2S and EtOH while positive changes in

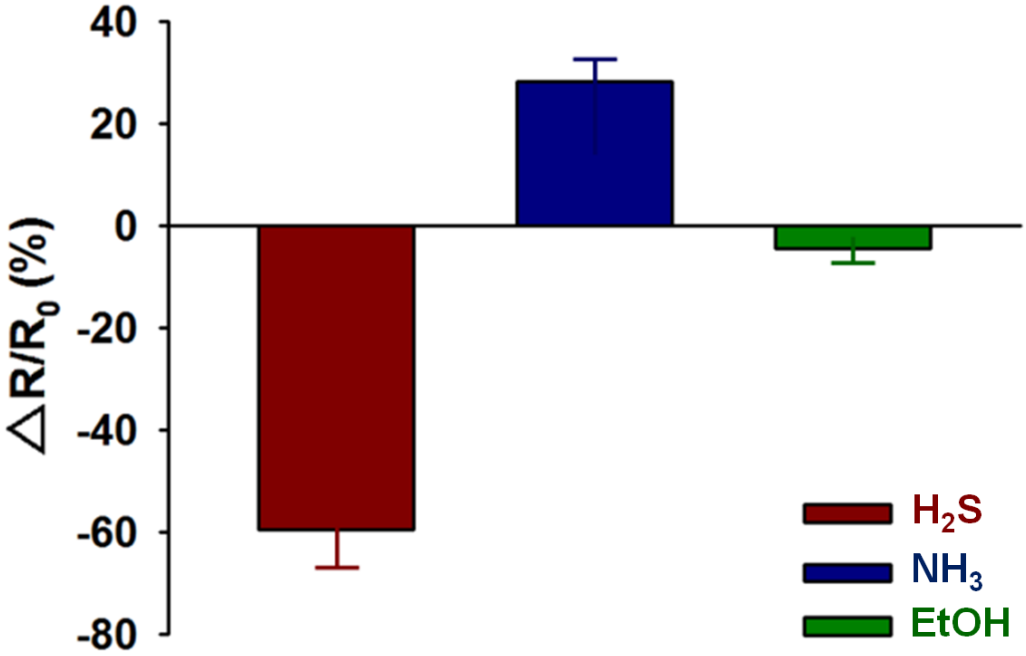

Figure 85. Normalized response graphs of PSS-doped PANI/graphene nanocomposites to different analytes: Each analyte concentration was fixed at 20 ppm.

$\Delta R/R_0$ were observed upon exposed to NH_3. Note that with these sensors, the detection sensitivity to a particular analyte depends on the molecular structure of the analyte. When H_2S or EtOH diffuse into the sensor film, charge transfer within the PSS-doped PANI/graphene is enhanced through hydrogen bonding interactions at the amine nitrogen sites on the PANI backbone, resulting in negative resistance changes. However, NH_3 deprotonates the PSS-doped PANI, resulting in increased resistance of the PSS-doped PANI film. Lower bond energies are required to break bonds in H_2S (381 kJ mol^{-1}) compared to EtOH (436 kJ mol^{-1}), indicating that protons can be more easily dissociated from the H_2S [180]. For these reasons, the PSS-doped PANI/graphene sensors exhibited higher responses to H_2S compared to the EtOH. Furthermore, $-SO_3-$ groups in PSS have a larger chemical affinity for H_2S than for NH_3. Accordingly, the PSS-doped PANI/graphene sensor was more sensitive to H_2S than to NH_3. Thus, H_2S can be differentiated from other analytes based on the magnitude and direction of the resistance change upon analyte exposure.

3.3.3. Fabrication of RuO_2 NPs-decorated PEDOT:PSS/graphene nanocomposites for screen-printable and flexible electrodes in supercapacitors

3.3.3.1. Fabrication of RuO_2 NPs-decorated PEDOT:PSS/graphene nanocomposites

Figure 86 describes the fabrication methods of RuO_2/PEDOT:PSS/graphene nanocomposites. DMSO (5 wt%), which is known to enhance the conductivity of PEDOT:PSS by reducing the Coulomb interactions between PEDOT NPs and PSS molecules, was added to the PEDOT:PSS solution [15]. According to Hansen's equation, the DMSO/water co-solvent system provided appropriate hydrogen bonding (δ_h) and polarity interaction (δ_p) parameters, which are related to the stable dispersion of PSS-coated graphenes and hydrous RuO_2 NPs in the co-solvent system [62,69]. GO was prepared according to Hummer's method, and graphene sheets were produced by reducing GO in the presence of PSS [51]. In this study, PSS was synthesized in an aqueous phase using AAPH as a water-soluble initiator for free-radical polymerization [181]. During the reduction of GO, the PSS electrostatically covered both sides of the graphene sheets through electrostatic repulsion interactions between the anionic head groups ($-SO_3^-$) of PSS and the graphene; thus, the PSS-coated graphene sheets became directly dispersible in the aqueous phase. The PSS-coated graphene sheets were inserted and

dispersed in PEDOT:PSS solutions doped with 5 wt% DMSO via mechanical stirring and sonochemical treatment. The 30-wt% PSS aqueous solutions were introduced to the PEDOT:PSS/graphene solutions to obtain sufficient viscosity (more than 10^3 cp) for screen-printing. Although increasing the amount of PSS reduces the conductivity of PEDOT:PSS, loading of PSS can minimize and sometimes prevent serious agglomeration of the graphene sheets due to the van der Waals forces between them [51]. This intensifies the π–π interactions between the thiophene rings of PEDOT:PSS and the graphene sheets due to the improved compatibility [21,27,63,64,183]. Hydrous, amorphous RuO_2 NPs formed as a result of the reaction between $RuCl_3$ and NaOH, followed by low-temperature annealing (150℃) [109,110]. These hydrous RuO_2 NPs were anchored to the surface of PEDOT:PSS/graphene by chemical interactions between the residual oxygen-containing functional groups on graphene sheets and the RuO_2 NPs, or through the electrostatic interaction between the Ru^{4+} cations of RuO_2 and the SO_3^- anions of the PSS molecules [55,109]. Thus, the PSS molecules acted as electrostatic stabilizers that reduced the particle aggregation of RuO_2 NPs and facilitated redox reactions between RuO_2 NPs and the PEDOT:PSS/graphene surfaces. The ternary RuO_2/PEDOT:PSS/graphene, having an optimized solution viscosity, were formed as thin-film patterns on flexible plastic substrates using screen-printing

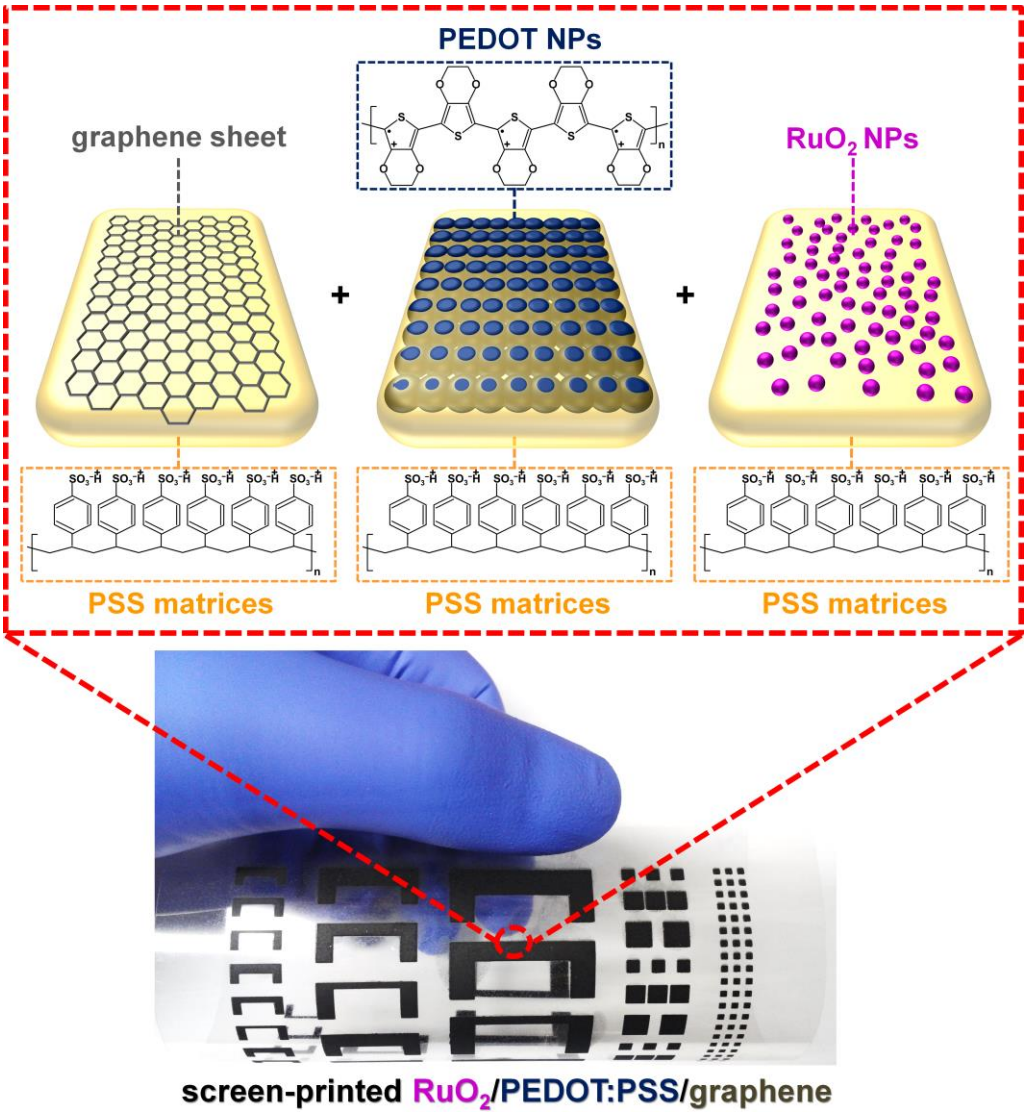

Figure 86. Overall procedure for fabricating RuO_2/PEDOT:PSS/graphene screen-printed electrode and a digital camera image of screen-printed electrode with different sizes and shapes of patterns.

method; the patterned films has a uniform thickness of *ca*. 5 μm. Accordingly, the synergetic effects from PEDOT:PSS, graphene sheets, and RuO_2 NPs resulted in a higher specific capacitance for the system. The patterns obtained, which consisted of three components (PEDOT:PSS, graphene, and RuO_2), were used as the working electrode of an supercapacitor. The prepared RuO_2/PEDOT:PSS/graphene solutions showed good adhesion with PET, which was attributed to the optimized solution viscosity caused by PSS binders within the conducting inks. It was evident that the screen-printing method could be a facile means for forming thin-film electrodes of different shapes, sizes, and thicknesses on flexible plastic substrates.

Figures 87 and 88 shows FE-SEM images of PEDOT:PSS, PEDOT:PSS/graphene, and RuO_2/PEDOT:PSS/graphene nanocomposites prepared by screen-printing. In addition, TEMs of graphene sheet and RuO_2 NPs are further investigated in order to confirm successful incorporation of RuO_2 NPs and graphene sheets into the PEDOT:PSS nanostructure (Figure 89). PEDOT:PSS was composed of nanoscale grains (diameter: *ca.* 20−30 nm) (Figures 87a and 88a). The sizes of the graphene sheets ranged from ~2−10 μm (Figures 87b, 88b, and 89a); these graphene sheets were mixed with the PEDOT:PSS grains and became highly dispersed throughout the PEDOT:PSS surface, demonstrating that the graphene sheets could be successfully

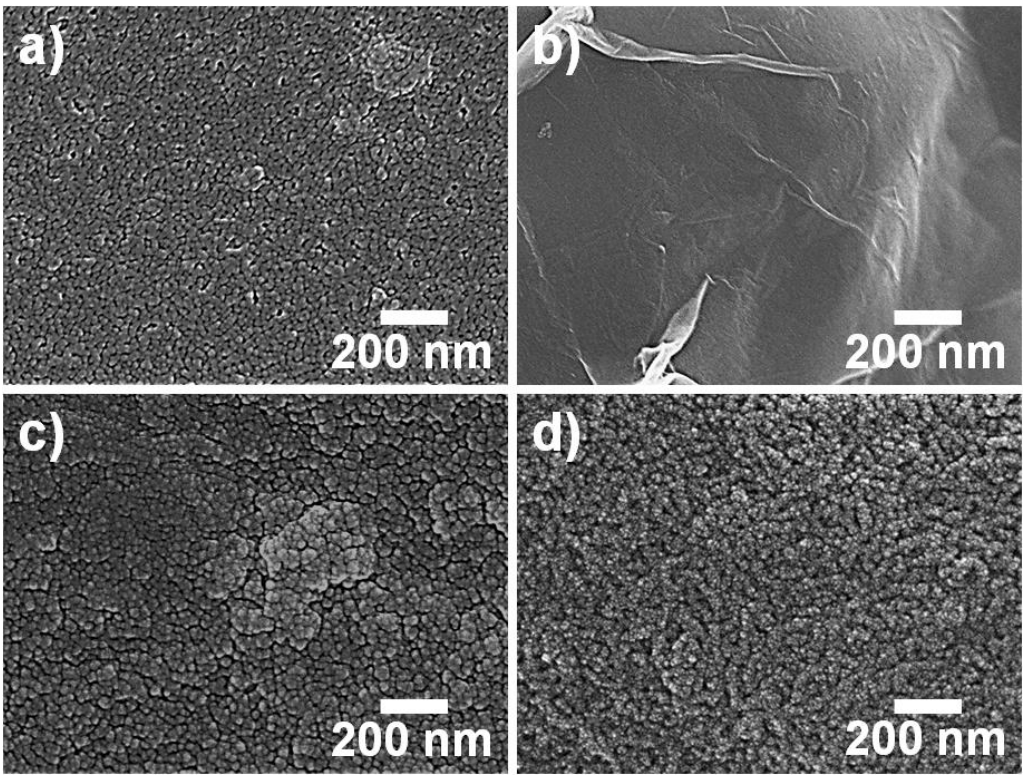

Figure 87. FE-SEM images of (a) PEDOT:PSS, (b) graphene, (c) PEDOT:PSS/graphene, and (d) RuO_2/PEDOT:PSS/graphene. Magnification: ×80k.

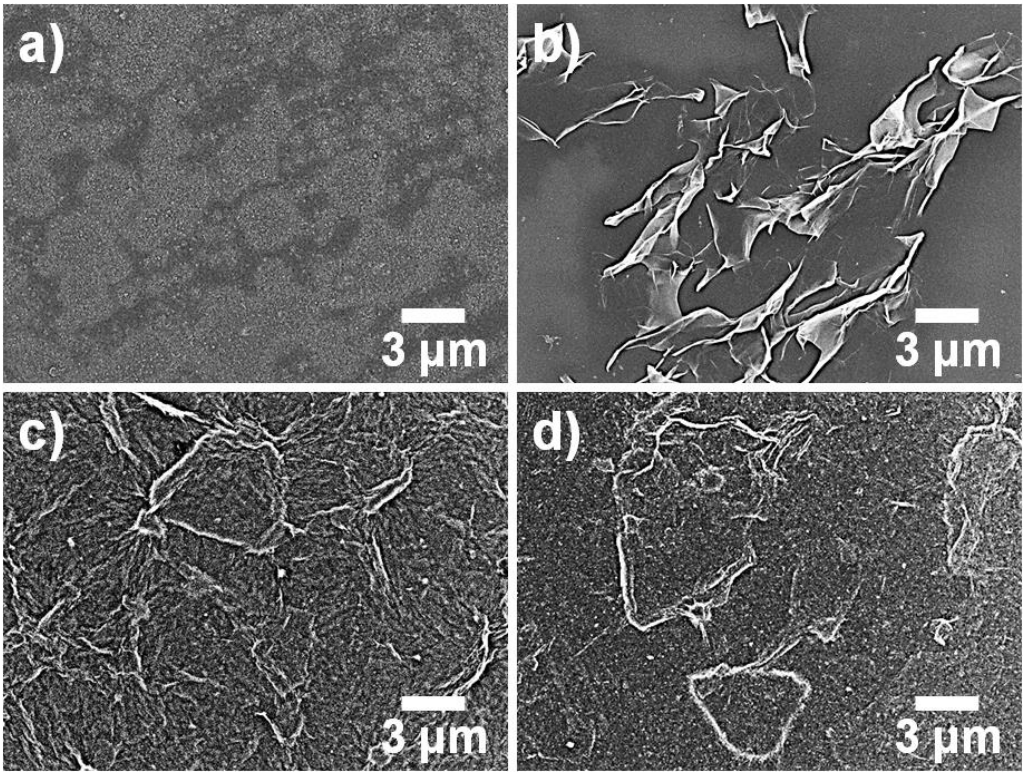

Figure 88. FE-SEM images of (a) PEDOT:PSS, (b) graphene, (c) PEDOT:PSS/graphene, and (d) RuO_2/PEDOT:PSS/graphene. Magnification: ×5k.

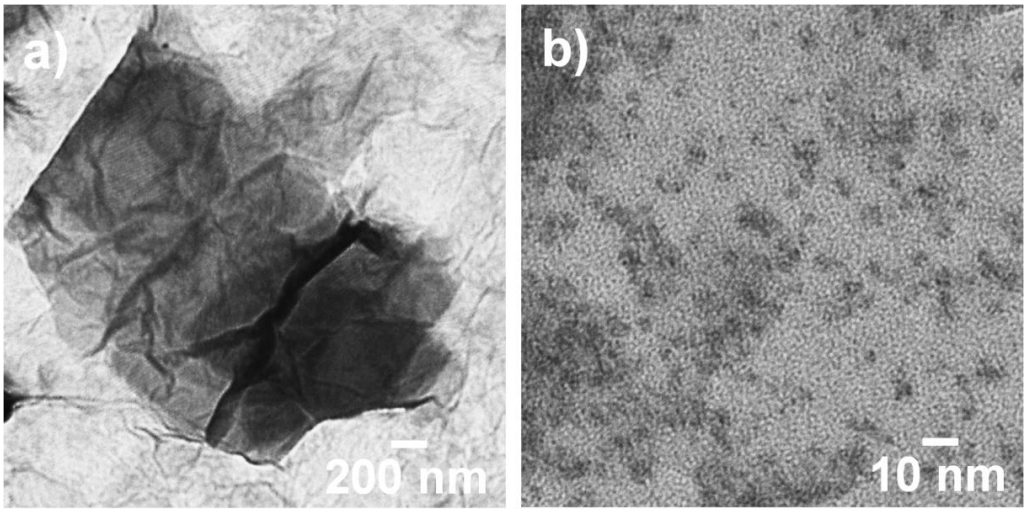

Figure 89. TEM images of (a) graphene and (b) RuO_2 NPs.

incorporated into the PEDOT:PSS system in the presence of amphiphilic PSS molecules (Figures 87c and 88c). An increased number of anionic groups per unit chain length of PSS molecules should enhance the interfacial interactions and mechanical interlocking between the graphene sheets and PEDOT:PSS nanograins, which would eventually lead to good dispersion of hydrophobic graphene sheets in an aqueous PEDOT:PSS system [21,27,45,51,183]. This, in turn, may increase the π–π interactions between the PEDOT:PSS and graphene sheets, which is an important factor for increasing the conductivity of the nanocomposite. The RuO_2 NPs (< 5 nm in size) were highly dispersed over the PEDOT:PSS/graphene surface (Figures 87d and 88d), and the sizes of the NPs were identical to those of RuO_2 NPs (Figure 89b) [109]. These RuO_2 NPs may become thermodynamically stable through electrostatic interactions between the cations (Ru^{4+}) and anions (SO_3^-), preventing incomplete redox reactions of RuO_2 NPs [55].

AFM was used to further investigate the morphological features of PEDOT-PSS nanocomposites affected by the RuO_2 NPs and graphene sheets (Figure 90). Compared with PEDOT:PSS (3.75 nm), the PEDOT:PSS/graphene (5.05 nm) exhibited rough surfaces due to the presence of graphene sheets (< 5-nm-thick sheets) (Figures 90a–c). Only a slight increase in the surface roughness should not have a significant effect on the charge carrier mobility

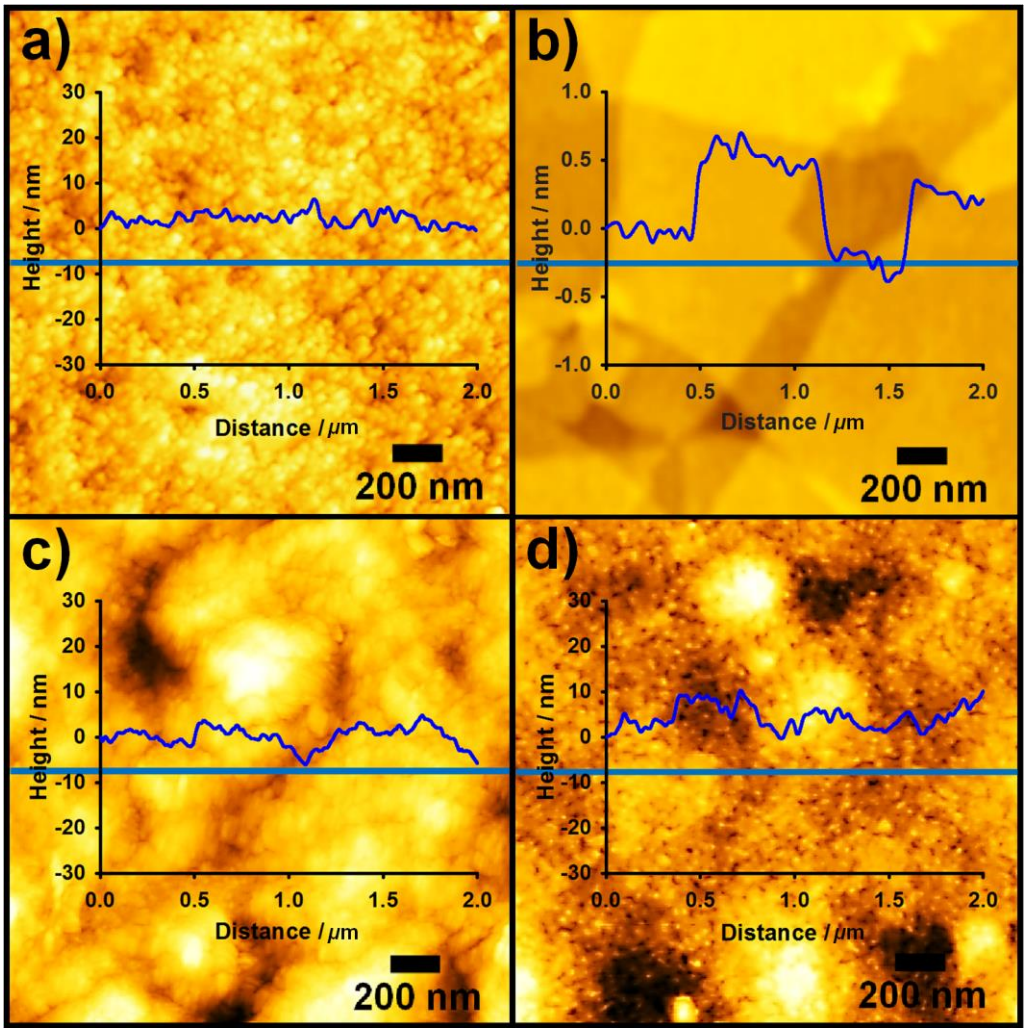

Figure 90. AFM images of (a) PEDOT:PSS, (b) graphene, (c) PEDOT:PSS/graphene, and (d) RuO_2/PEDOT:PSS/graphene nanocomposites.

within the nanostructures. However, the π–π stacking between the PEDOT:PSS and graphene sheets resulted in a higher charge-carrier mobility within the nanocomposites [21,27,63,64,183]. Upon exposure to the electrolyte, this very small change in surface roughness can increase the contact surface area available for transporting electrons [16]. The increase in surface roughness (5.75 nm) induced by the RuO_2 NPs was relatively small, while the RuO_2 NPs provided faster, facile redox reactions of the PEDOT:PSS/graphene nanocomposite with the electrolyte (Figure 90d). Thus, it is reasonable to assume that the graphene sheets and RuO_2 NPs induced optimized morphologies to achieve better charge transport within the nanocomposites.

Raman spectroscopy was used to confirm the chemical bonding between PEDOT:PSS, graphene, and RuO_2 NPs (Figure 91). In the spectrum of PEDOT:PSS, the major peaks for PEDOT indicated SO_2 bending (436 cm^{-1}), symmetric C–S–C deformation (701 cm^{-1}), oxyethylene ring deformation (575 and 987 cm^{-1}), C–O–C deformation (1093 cm^{-1}), C–C inter-ring stretching (1258 cm^{-1}), single C–C stretching (1364 cm^{-1}), C=C symmetrical stretching (1441 cm^{-1}), C=C asymmetrical stretching (1510 cm^{-1}), and C=C anti-symmetrical stretching (1567 cm^{-1}) [18,21,27,63]. The peaks of PSS observed at 1001, 1133, and 1600 cm^{-1}, were assigned to the vibration modes of C–C aromatic stretching, SO_2, and aromatic C–CH quadrant stretching, respectively

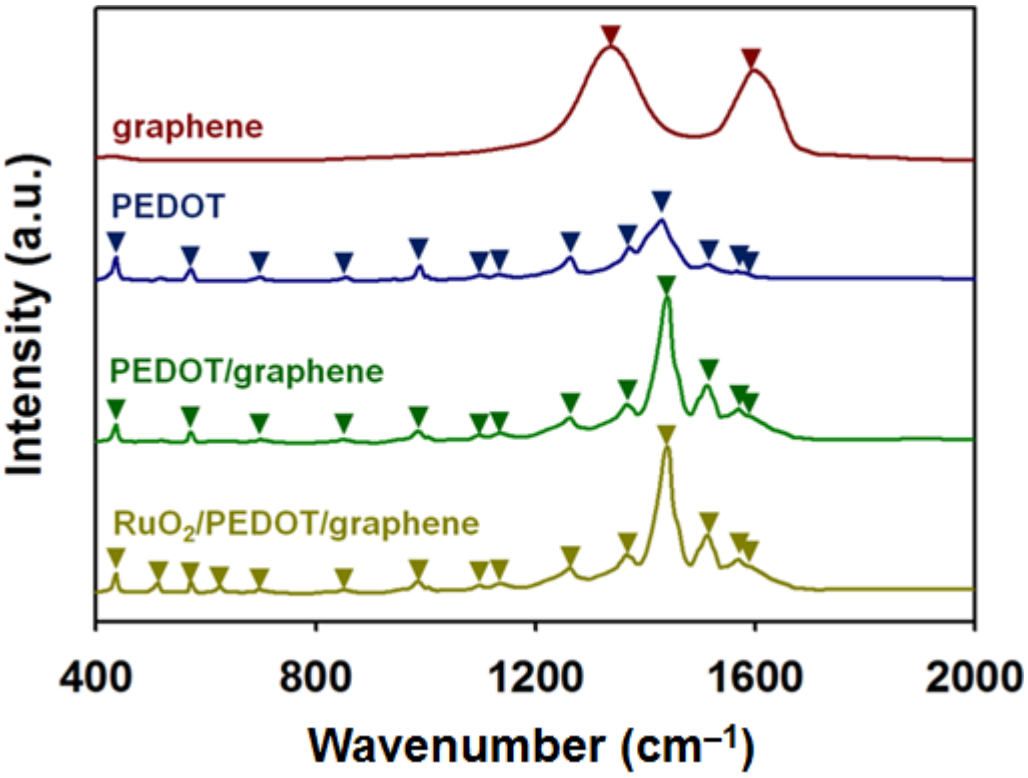

Figure 91. Raman spectra of graphene, PEDOT:PSS, PEDOT:PSS/graphene, and RuO_2/PEDOT:PSS/graphene nanocomposites.

[110]. The spectrum of graphene indicated two distinctive peaks: D mode (corresponding to structural defects (1351 cm^{-1})) and G mode (related to the vibration of sp^2-hybridized carbon (1598 cm^{-1})) [21,27,63,109]. The D/G ratio of graphene was higher than that for non-reduced GO, suggesting that the defects in the graphene sheets were caused by GO reduction. When the graphene sheets were added to the PEDOT:PSS, the peaks associated with C=C symmetric and C=C asymmetric stretching in PEDOT:PSS became dominant, and the peak associated with C=C symmetrical stretching shifted from 1441 to 1446 cm^{-1}. These results suggest that the expanded-coil conformation became dominant within the PEDOT:PSS/graphene structure through strong π–π interactions between the PEDOT:PSS and graphene sheets [21,63]. The structural change of the PEDOT:PSS is expected to increase the π–conjugation lengths of delocalizing electrons along the PEDOT:PSS backbone. When the RuO_2 NPs were incorporated into the PEDOT:PSS/graphene, weak peaks at 513, 625, and 692 cm^{-1}, ascribed to hydrous RuO_2 with an amorphous structure, were observed [109]. Judging from these results, the PEDOT:PSS, graphene sheets, and RuO_2 NPs coexisted and maintained their individual electronic properties within the RuO_2/PEDOT:PSS/graphene nanocomposite.

Figure 92 shows XRD patterns of PEDOT:PSS, graphene, PEDOT:PSS/graphene, and RuO_2/PEDOT:PSS/graphene nanocomposites. Two

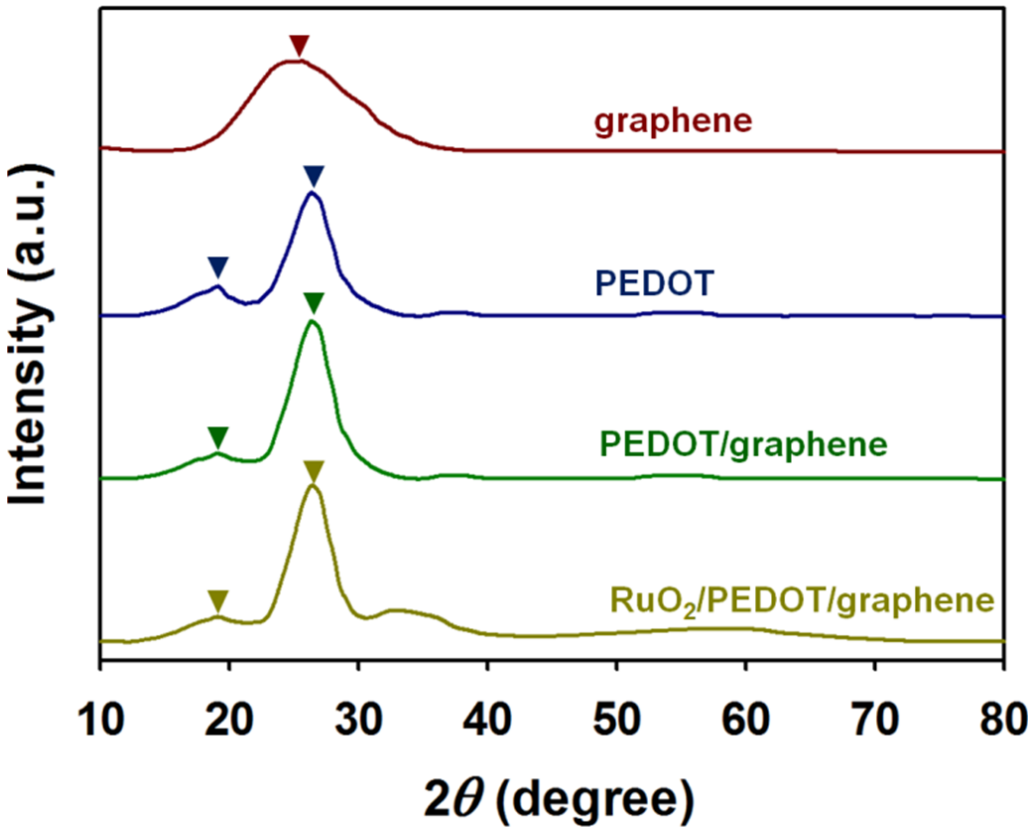

Figure 92. XRD spectra of graphene, PEDOT:PSS, PEDOT:PSS/graphene, and RuO_2/PEDOT:PSS/graphene nanocomposites.

distinctive peaks were observed at 2θ = 18.0° (4.93 Å) and 26.4° (3.38 Å) for PEDOT:PSS, which were identical to the distances associated with interchain packing of the pseudo-orthobromic crystal structure and the face-to-face interchain stackings of thiophene rings, respectively [21,184]. In the spectrum of graphene, a broad peak at 2θ = 24.5° with an interlayer distance of 3.63 Å was observed, which is close that of that of graphite (3.39 Å) [21,66]. After the addition of graphene sheets into PEDOT:PSS, the peak intensity at 2θ = 26.4° became more prominent, whereas the characteristic features of the graphene sheets became indistinguishable. This indicates that the graphene sheets were highly dispersed by the PSS [21]. Additionally, the distinct peak at 2θ = 26.4° in the spectrum of PEDOT:PSS/graphene indicated that the interchain stacking between thiophene rings of the PEDOT:PSS intensified through π–π interactions between PEDOT and the graphene sheets. Hence, the enhanced crystallinity of PEDOT:PSS/graphene nanocomposites is an indication of more compact packing of the PEDOT:PSS chains, resulting in extensive delocalization of the electrons and improved conductivity of the electrode material [66]. After the addition of RuO_2 NPs into the PEDOT:PSS/graphene nanocomposite, no significant peaks for crystalline RuO_2 were found, as opposed to the prominent peaks that appeared in the spectrum of pure RuO_2 NPs. Thus, these results revealed that the RuO_2 NPs decorating the

PEDOT:PSS/graphene nanocomposite were hydrous and amorphous, leading to better electrical conductivity and enhanced charge–discharge performance of the electrode system [109].

XPS was used to identify the binding energy that reflects the elemental information and protonation states of the PEDOT:PSS-based nanocomposites (Figures 93 and 94). Figure 93 shows fully-scanned XPS patterns of graphene, PEDOT:PSS, PEDOT:PSS/graphene, and RuO_2/PEDOT:PSS/graphene nanocomposites. The spectra of the PEDOT:PSS-based nanocomposites exhibited four peaks located at 285, 533, 164, and 231 eV corresponding to C(1s), O(1s), S(2p), and S(2s), respectively [184]. In the XPS survey spectrum of graphene, weak peaks were observed at S(2p) (164 eV), S(2s) (231 eV), and N1s (400 eV); this indicates that the graphene sheets have been successfully reduced with hydrazine in the presence of PSS molecules. Considering sulfur content (~5.7%) in the XPS survey spectrum of graphene, the PSS-coated graphene sheets contained ~33% PSS molecules [51]. For the PEDOT:PSS/graphene, the peak intensity at 285 eV, which prominently appeared in the survey spectrum of graphene, intensified compared with PEDOT:PSS [109]. After the introduction of hydrous RuO_2 NPs into the PEDOT:PSS/graphene nanocomposite, a small peaks assigned to Ru(4p) (44.5 eV), Ru(4s) (75.0 eV), Ru(3d) (281.3 eV), Ru(3p) (463.0 and 485.0 eV), and

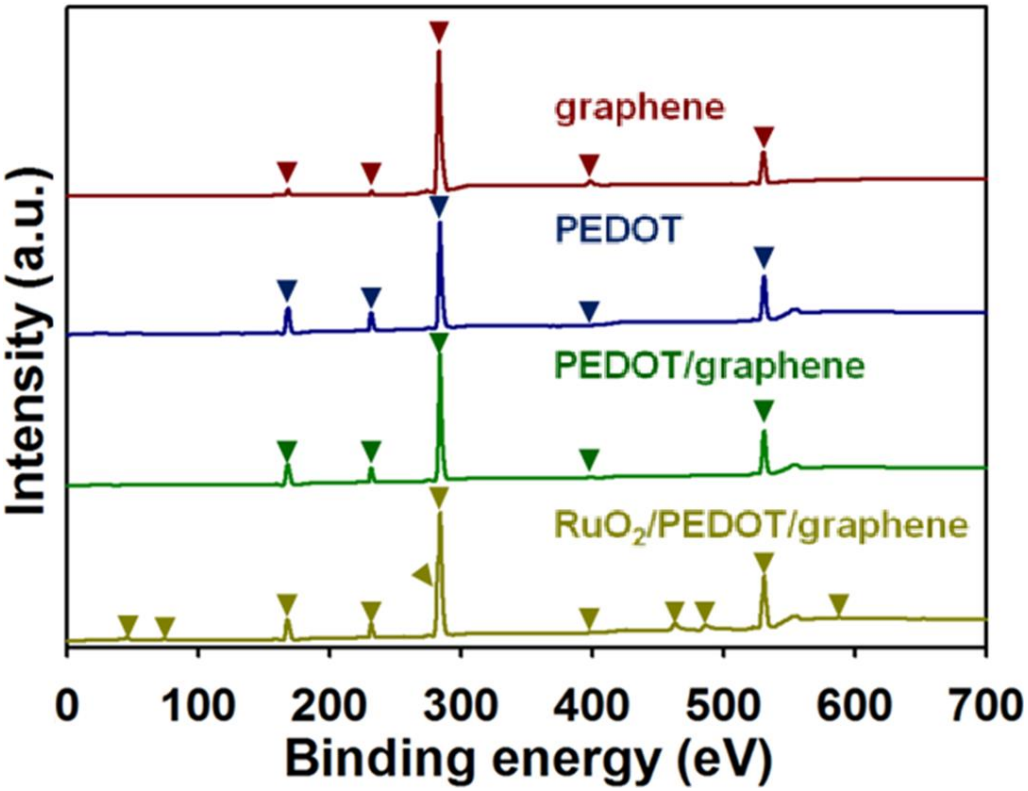

Figure 93. Fully-scanned XPS patterns of graphene, PEDOT:PSS, PEDOT:PSS/graphene, and RuO_2/PEDOT:PSS/graphene nanocomposites.

Ru(3s) (588.0 eV) newly appeared in the survey spectrum. In particular, the binding energy of Ru3d (281.3 eV) corresponded to the binding energy of Ru^{4+}, suggesting the presence of RuO_2 on the electrode surfaces [109]. In addition, the O1s peak became more prominent compared with that of the PEDOT:PSS/graphene nanocomposite. The intensified intensity of the O1s peak was attributed to the presence of Ru–O in RuO_2. Figures 94 show the C(1s) spectra of PEDOT:PSS, PEDOT:PSS/graphene, and RuO_2/PEDOT:PSS/graphene nanocomposites, consisting of three components with peaks at 284.5 eV (C–C), 285.9 eV (C–O–C), and 288.1 eV (C=C). These peaks shifted slightly towards higher binding energy levels when graphene and RuO_2 NPs were added to the PEDOT:PSS. Such red shifts of the C(1s) spectra is indicated the enhanced face-to-face interchain stackings of thiophene rings within the PEDOT:PSS structure through strong π–π intermolecular interactions between the basal plane of the graphene sheets and the thiophene rings of the PEDOT:PSS structure [27]. Furthermore, the results also showed that the carrier concentrations in the graphene sheets were enhanced by additional electrons from PEDOT:PSS and hydrous RuO_2 NPs, consequently resulting in a blue shift in the Fermi level. These results, taken as a whole, suggest that the charge transport in the electrode material is enhanced by the synergetic effects from PEDOT:PSS, graphene sheets, and RuO_2 NPs.

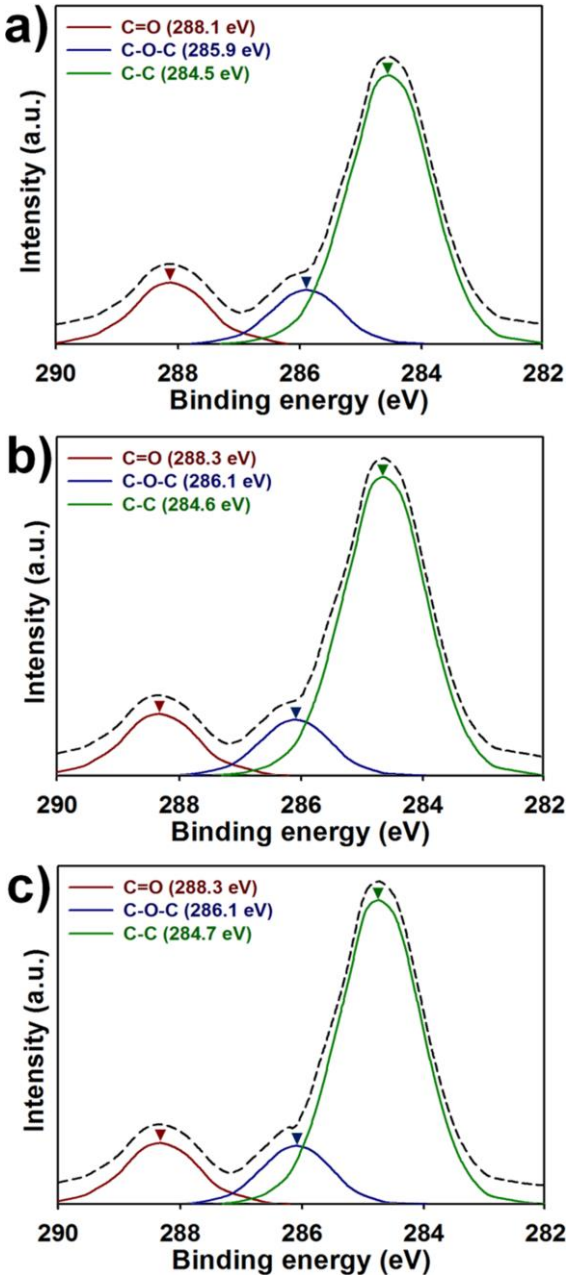

Figure 94. XPS core spectra of C1s in (a) PEDOT:PSS, (b) PEDOT:PSS/graphene, and (c) RuO_2/PEDOT:PSS/graphene nanocomposites.

3.3.3.2. Supercapacitors based on RuO_2 NPs-decorated PEDOT:PSS/graphene nanocomposites as electrode materials

To identify the optimal amount of graphene sheets to enhance the electrical and electrochemical properties of PEDOT:PSS/graphene nanocomposites, various amounts of graphene sheets (0−40 wt% in comparison with the nanocomposites) were incorporated into the PEDOT:PSS (Figures 95 and 96). The surface resistance distribution for each 1-cm square sample pattern of the samples was investigated to obtain reliable conductivity values for the samples (Figure 96). It was notable that every sample exhibited a narrow surface resistance distribution. This indicated that the highly uniform thin films could be deposited onto flexible PET substrates using the screen-printing method, resulting in enhanced connectivity between the conductive areas within the PEDOT:PSS thin-films. Based on the data in Figure 95, the conductivity of the PEDOT:PSS/graphene nanocomposites was measured using the four-point probe method (Figure 96). The electrode material is required to be highly conductive to enhance the charge collection capability of the capacitor [63]. The conductivity of PEDOT:PSS (680 S cm^{-1}) used in our work was lower than the conductivity reported by Heraeus (900 S cm^{-1}) due to the presence of PSS binders that were added to PEDOT:PSS for the screen-printing process [19]. In comparison with the PEDOT:PSS, the conductivity of PEDOT:PSS/graphene nanocomposites increased with the amount of graphene

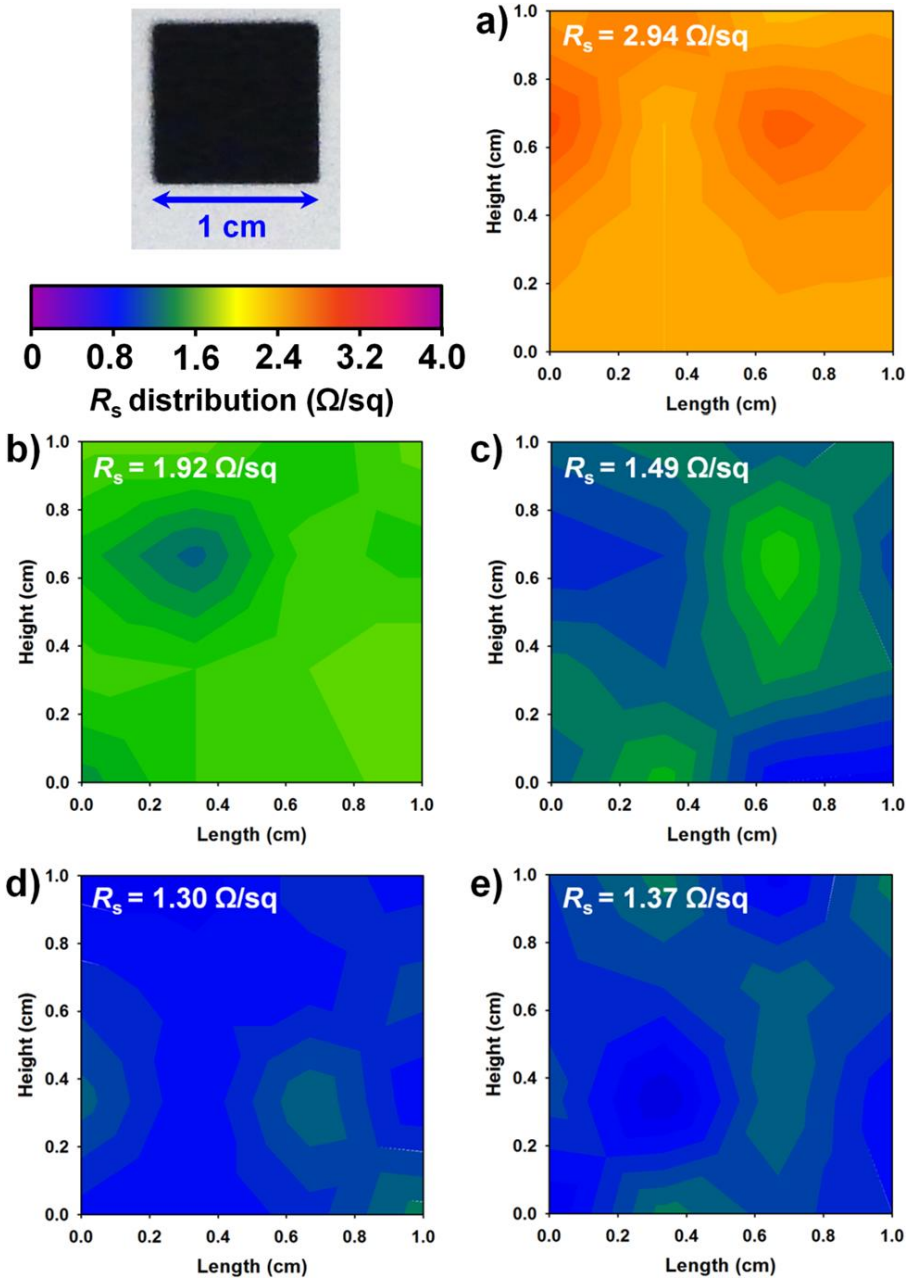

Figure 95. Distribution of surface resistances of PEDOT:PSS/graphene nanocomposites having different graphene sheets concentration: (a) PEDOT:PSS, (b) 10 wt%, (c) 20 wt%, (d) 30 wt%, and (e) 40 wt%.

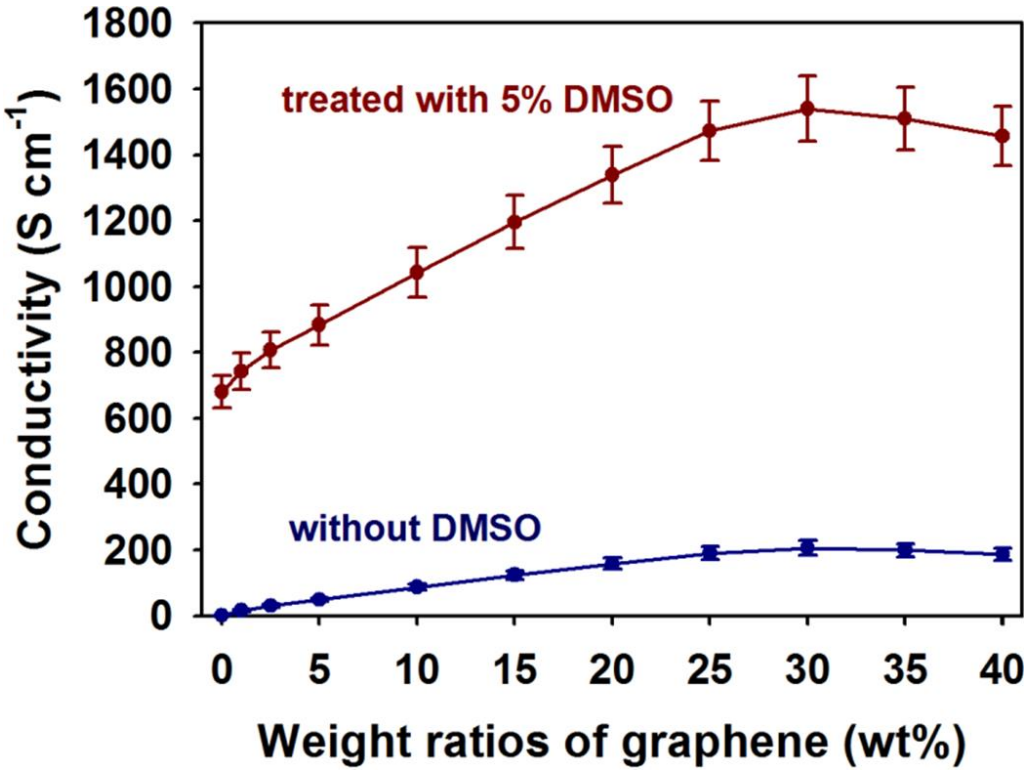

Figure 96. Conductivity of PEDOT:PSS/graphene nanocomposites as a function of graphene sheets concentration.

sheets, up to 30 wt%. Specifically, we observed that the conductivity of PEDOT:PSS/graphene sheets increased two fold (1540 S cm^{-1}) compared with PEDOT:PSS (Figures 95d and 96). These results suggest that the appropriate amount of graphene sheets greatly enhanced the current collection of the PEDOT:PSS-based nanocomposites. This enhanced current collection may be attributed to strong π–π stacking interactions between the aromatic structures of the PEDOT:PSS and graphene sheets, which may have elongated the conjugation lengths of delocalizing electrons within the PEDOT:PSS structure [21,27,63,183]. However, the conductivity of PEDOT:PSS/graphene became smaller after adding graphene sheets at concentrations that exceeded 30 wt%, implying that excessive amounts of graphene sheets may induce aggregation, which, in turn, would degrade the electrical performance of the electrode materials (Figures 95e and 96). Thus, this concentration was chosen to enhance the conductivity of the PEDOT:PSS nanostructure.

CV studies were also carried out to determine the optimum additive graphene-sheet concentration (Figure 97). The anodic peaks ranging from 0.40 to 0.50 V and the cathodic peaks ranging from 0.25 to 0.35 V in the CV curves were ascribed to oxidization and reduction reactions, respectively, given by

$$PEDOT^{+}\cdot PSS^{-} + e^{-} + H^{+}\ (\text{oxidized state}) \leftrightarrows PEDOT^{0}\cdot PSS^{-}\cdot H^{+}\ (\text{reduced state}) \quad (9)$$

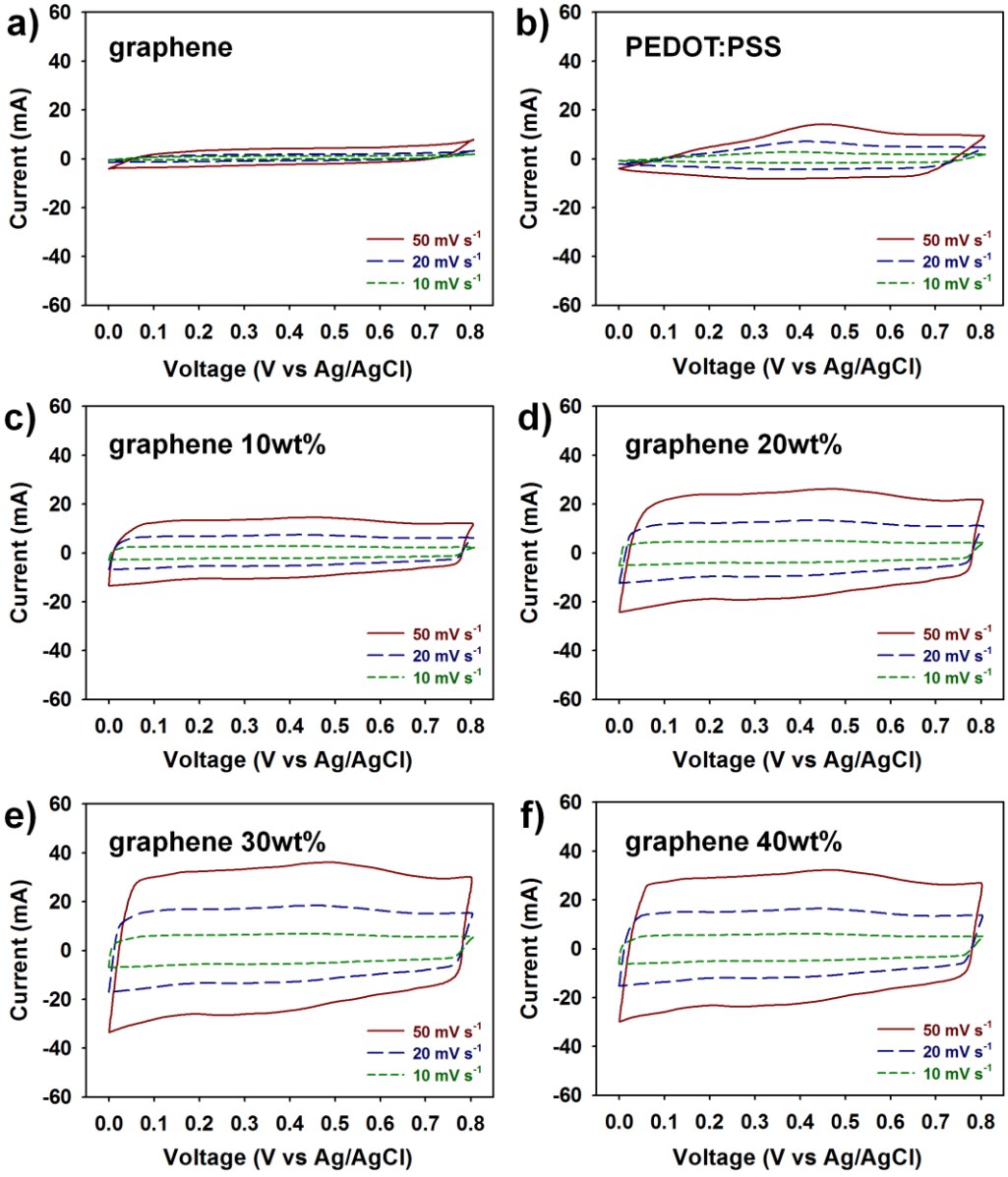

Figure 97. Cyclic voltammograms of PEDOT:PSS/graphene nanocomposites having different graphene sheets concentration at various scan rates (10 to 50 mV^{-1}): (a) graphene, (b) PEDOT:PSS, (c) 10 wt%, (d) 20 wt%, (e) 30 wt%, and (f) 40 wt% (0.5 M H_2SO_4 was used as an electrolyte).

where the e^- and H^+ denote the electron and proton in the H_2SO_4 electrolyte, respectively [26]. With increasing amounts of graphene sheets within the PEDOT:PSS, the pair of redox peaks became indistinguishable and the shape of the CV curves became more rectangular compared with PEDOT:PSS (Figure 97). These rectangular-shaped CV curves may be associated with the electrochemical double-layer capacitance (EDLC) mechanism of the graphene sheets. Furthermore, it was obvious that the PEDOT:PSS/graphene nanocomposite, with 30-wt% graphene sheets, exhibited the largest CV area among the prepared samples at every scan rate, in accordance with the conductivity results (Figure 97e). This implies that a sufficient amount of π-electrons in the graphene sheets promotes π–π stacking interactions with the thiophene rings of PEDOT:PSS, resulting in enhanced charge transfer in the PEDOT:PSS-based nanocomposites with the H_2SO_4 electrolyte [21,27,63,64,183]. The electrochemical activity between the electrode material and H_2SO_4 decreased when the added graphene-sheet concentration exceeded 30 wt% (Figure 97f), which may be related to the aggregation of excessive amounts of graphene sheets. Considering the conductivity and CV results, 30 wt% of graphene sheets was selected as the optimal amount for the PEDOT:PSS-based nanocomposite.

To confirm the effects of graphene sheets and RuO_2 NPs on the

conductivity of samples, the surface resistance distribution for each 1-cm square pattern of the PEDOT:PSS, PEDOT:PSS/graphene, and RuO_2/PEDOT:PSS/graphene electrodes was further analyzed (Figure 98). As described previously, the screen-printing method provided good interplanar contact. The surface resistances decreased after the addition of graphene sheets to the PEDOT:PSS structure (Figures 98a and b). These results imply that the restored graphitic network of sp^2 bonds played an important role in enhancing the π-interactions between the graphene sheets and PEDOT nanostructure, which eventually extended the conjugation length of the PEDOT chain [21,27,60,63,64,183]. Hence, PEDOT:PSS/graphene nanocomposites could conduct more current at the working electrode of the supercapacitor, which is an important factor for obtaining high specific capacitances. After the addition of infinitesimal amounts of RuO_2 NPs, a slight decrease in the surface resistance was observed (Figure 98c). Based on the data, the conductivity of RuO_2/PEDOT:PSS/graphene was 1570 S cm^{-1}, which was slightly larger than that of PEDOT:PSS/graphene (1540 S cm^{-1}). This indicates that the RuO_2 NPs, having metallic conductivity (*ca.* 10^{-5} Ω cm) and interlinked with the PEDOT:PSS chains, resulted in better electrical connectivity of the conductive areas within the nanocomposite [55,110].

The CVs of the RuO_2, RuO_2/graphene, and RuO_2/PEDOT:PSS/graphene

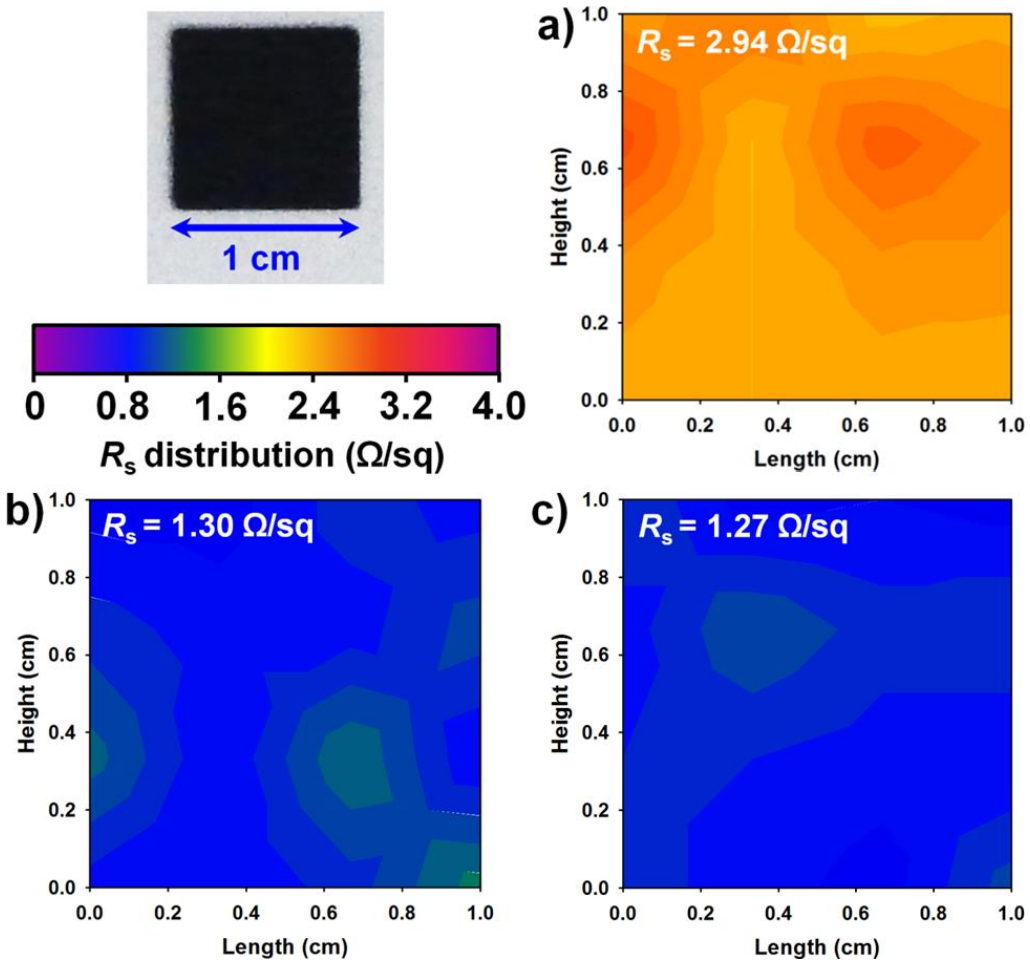

Figure 98. Distribution of surface resistances of (a) PEDOT:PSS, (b) PEDOT:PSS/graphene, and (c) RuO_2/PEDOT:PSS/graphene nanocomposites.

were measured in a 0.5 M H_2SO_4 electrolyte at scan rates from 10 to 50 mV s^{-1} (Figure 99). In comparison with the CV curve of the PEDOT:PSS/graphene nanocomposite, a pair of very pronounced and reversible redox peaks are observed for RuO_2, RuO_2/graphene, RuO_2/PEDOT:PSS/graphene nanocomposite at every scan rate. In the CV curve of RuO_2, the anodic peaks ranging from 0.40 to 0.75 V and the cathodic peaks ranging from 0.26 to 0.62 V were ascribed to oxidization and reduction reactions, respectively, given by

$$RuO_2 + 2e^- + 2H^+ \text{ (oxidized state)} \leftrightarrows Ru(OH)_2 \text{ (reduced state)} \quad (10)$$

where the e^- and H^+ indicate the electron and proton in the H_2SO_4 electrolyte, respectively [190,191]. The CV area became larger in the following order: graphene < PEDOT:PSS < PEDOT:PSS/graphene < RuO_2/graphene < RuO_2/PEDOT:PSS/graphene < RuO_2 (Figures 97 and 100). These results indicate that hydrous RuO_2 NPs are redox-active, capable of faradaic energy storage via their pseudocapacitive behavior [109]. Thus, the RuO_2 NPs enabled faster oxidation/reduction reactions and charge transport into/out of the electrode, resulting in enhanced charge–discharge performance and larger specific capacitances of the samples. Hence, the synergetic effects from the PEDOT:PSS, graphene sheets, and RuO_2 NPs delivered the expected enhancement in electrochemical performance.

Figure 100a shows the galvanostatic charge–discharge curves of the RuO_2,

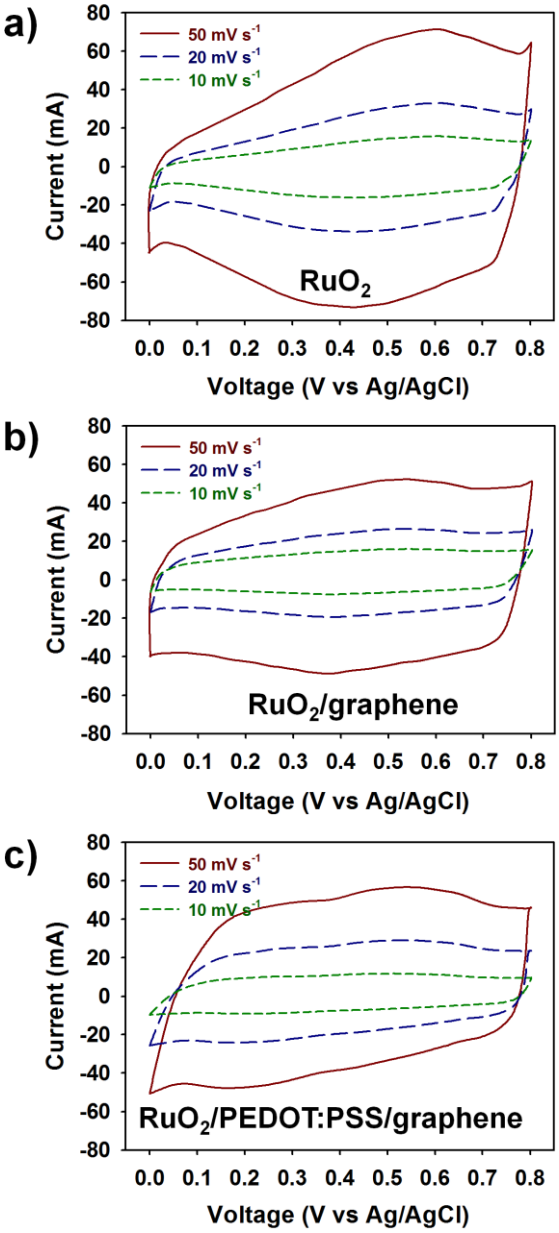

Figure 99. Cyclic voltammograms of RuO_2, RuO_2/graphene, and RuO_2/PEDOT:PSS/graphene nanocomposites at different scan rates (10 to 50 mV^{-1}) in 0.5 M H_2SO_4.

RuO_2/PEDOT:PSS/graphene, RuO_2/graphene, PEDOT:PSS/graphene, and PEDOT:PSS at a current density of 0.5 A g^{-1} over the voltage range of 0 to 0.8 V. The linear voltage–time profile and the highly symmetric charge–discharge characteristics imply facile redox reactions and charge transport into/out of the PEDOT:PSS-based nanocomposites during the charge/discharge process. The discharge time of the nanocomposites (given in seconds (s)) increased in the following order: graphene (542) < PEDOT:PSS (936) < PEDOT:PSS/graphene (2525) < RuO_2/graphene (3490) < RuO_2/PEDOT:PSS/graphene (3936) < RuO_2 (4641); and these discharge times were proportional to the specific capacitances of the PEDOT:PSS-based nanocomposites. The specific capacitances were 967, 820, 727, 526, 195, and 113 F g^{-1} for the RuO_2, RuO_2/PEDOT:PSS/graphene, RuO_2/graphene, PEDOT:PSS/graphene, PEDOT:PSS, and graphene nanocomposites respectively, at a current density of 0.5 A g^{-1} (Figure 100b). The discharge time and specific capacitances of graphene, PEDOT:PSS/graphene, RuO_2/graphene, and RuO_2/PEDOT:PSS/graphene gradually decreased with increasing current density, whereas the PEDOT:PSS and RuO_2 exhibited a rapid decrease in its specific capacitance when higher currents were applied. At the inner active sites of the electrodes, it became difficult to sustain the redox reactions completely at higher current densities,thus resulting in reduced electrochemical

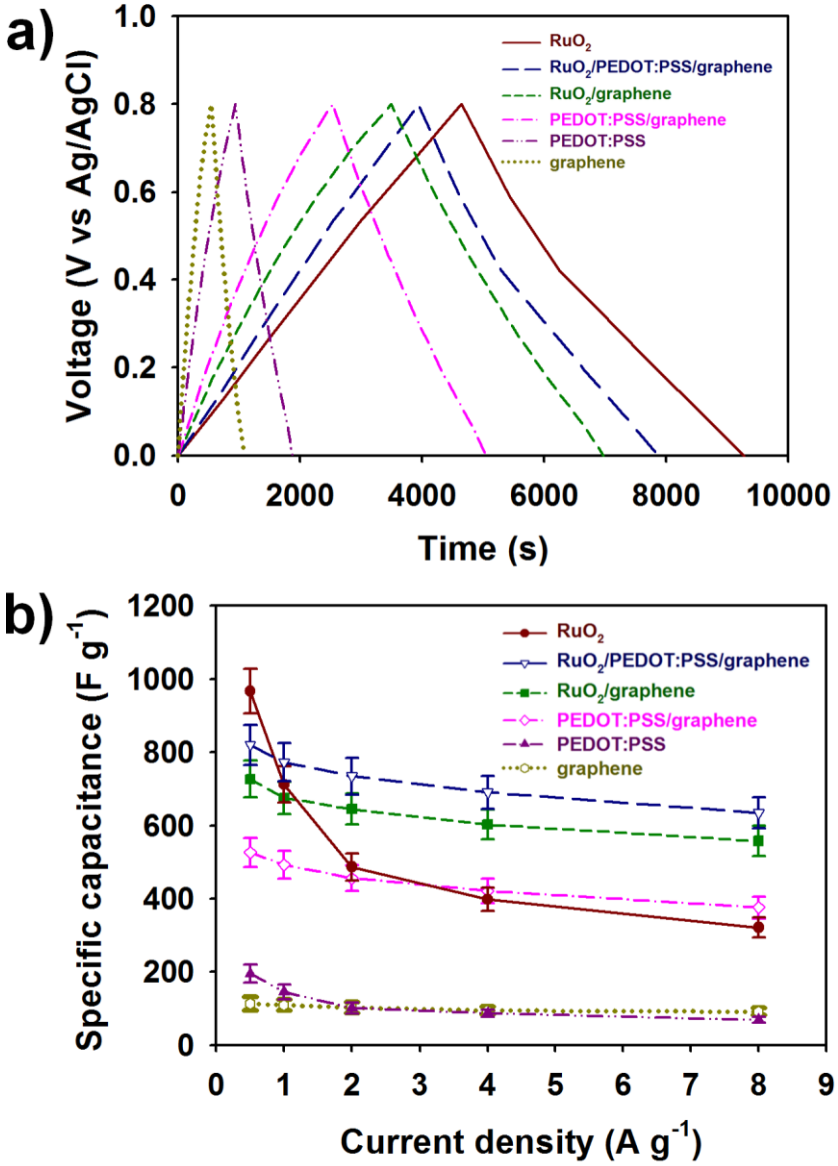

Figure 100. (a) Galvanostatic charge-discharge characteristics of four different electrode systems having a thickness of about 5 μm at a current density of 0.5 A g^{-1}. (b) Specific capacitances (SCs) of four different electrode systems having a thickness of about 5 μm at various current densities (0.5 to 8.0 A g^{-1}).

performances of the electrodes [55–57,63]. In addition, pseudocapacitive materials, including PEDOT:PSS and RuO_2 NPs, usually provide slower ion diffusions than the graphene sheets, which make the PEDOT NPs and RuO_2 NPs difficult to continue appropriate redox reactions at higher current densities [55,109,190–192]. This implies that the graphene sheet-incorporated electrodes have a better rate performance than PEDOT:PSS and RuO_2 due to the enhanced chemical and mechanical stability provided by the graphene sheets in maintaining the redox reactions at higher current densities [66]. Furthermore, the increased mass loading produced only a small decrease in the specific capacitance of the samples, suggesting that the π–π interactions between the graphene sheets and PEDOT:PSS, as well as the presence of RuO_2 NPs, facilitated charge transport at the electrode/electrolyte surface, while effectively minimizing the capacitance losses caused by degradation and shrinkage of the PEDOT:PSS structure (Figure 101) [55,63,66,109]. Consequently, the synergistic effects from the RuO_2 NPs, PEDOT:PSS nanostructures, and the graphene sheets led to higher specific capacitances, which were consistent with enhanced electrochemical performances.

To further identify the beneficial effects of the graphene sheets and the RuO_2 NPs on the charge transport within the ternary electrode system, series (R_s) and charge transfer resistances (R_{ct}) were measured using EIS analyses.

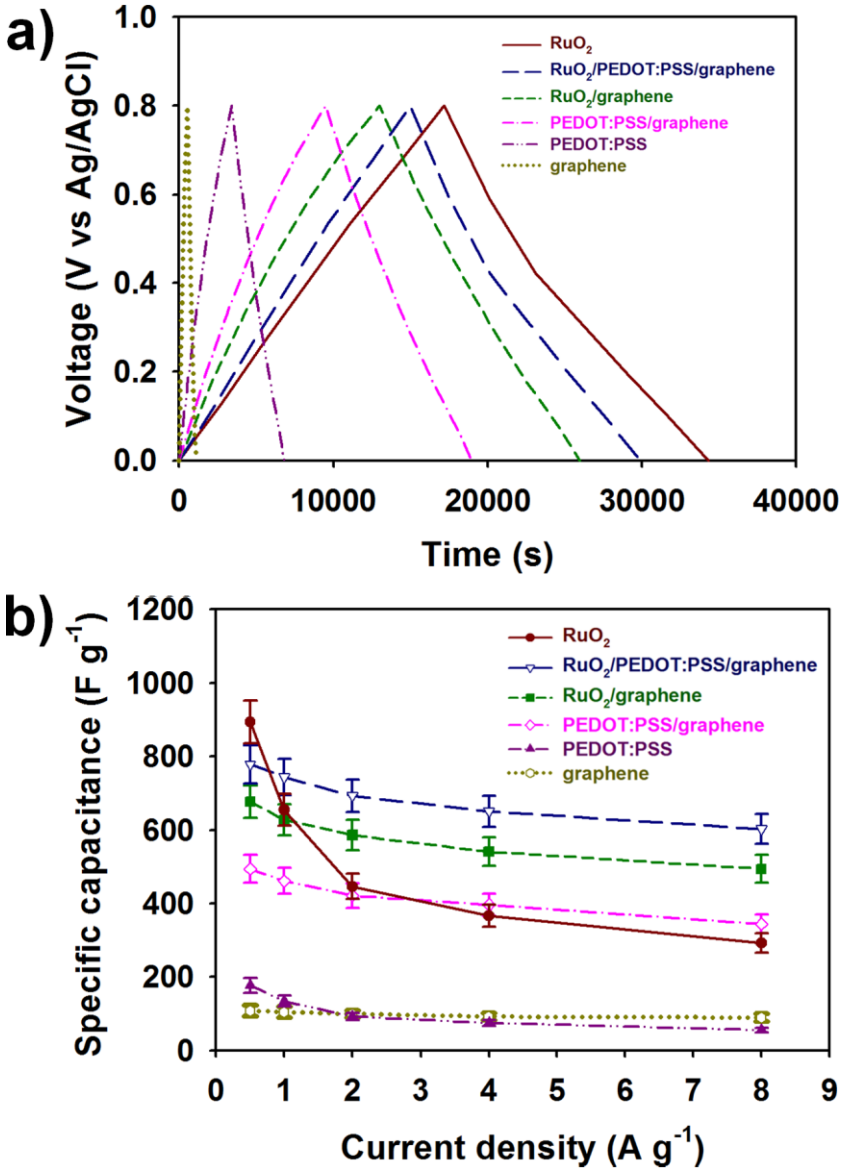

Figure 101. (a) Galvanostatic charge-discharge characteristics of four different electrode systems having a thickness of about 20 μm at a current density of 0.5 A g^{-1}. (b) Specific capacitances (SCs) of four different electrode systems having a thickness of about 20 μm at various current densities (0.5 to 8.0 A g^{-1}).

(Figure 102a). The Nyquist impedance plots consisted of semicircular curves for high frequencies and linear curves for low frequencies [26]. In particular, the DMSO-induced PEDOT:PSS exhibited lower R_s and R_{ct} than the graphene sheets and RuO_2 NPs. This indicates that the phase separation and uniform distribution of PEDOT and PSS in the PEDOT:PSS could be successfully achieved through the addition of DMSO, resulting in better charge transfer of the PEDOT:PSS [2,19]. As mentioned above, the low rate capability of the RuO_2 NPs in Figures 100b and 101b is also ascribed to its high R_{ct}. Importantly, using binary or ternary electrode systems, such as RuO_2/PEDOT:PSS/graphene, PEDOT:PSS/graphene, and RuO_2/graphene, were more effective to lower R_s and R_{ct} compared with one-component electrodes, including RuO_2, graphene, and PEDOT:PSS. The size of the semicircle and R_{ct} significantly decreased after the addition of the graphene sheets and RuO_2 NPs, which was consistent with the CV test results. Moreover, the EIS results indicated that the ideal combination of PEDOT:PSS, RuO_2 NPs, and graphene sheets improved the interfacial charge transfer within the nanocomposite, which could lead to a better capacitive performance for supercapacitors. To examine practical applicability of the RuO_2/PEDOT:PSS/graphene nanocomposites, Ragone plots of different electrode systems are shown in Figure 102b. The energy density (Wh kg^{-1}) of samples at the power density of 67 W kg^{-1} increased as following

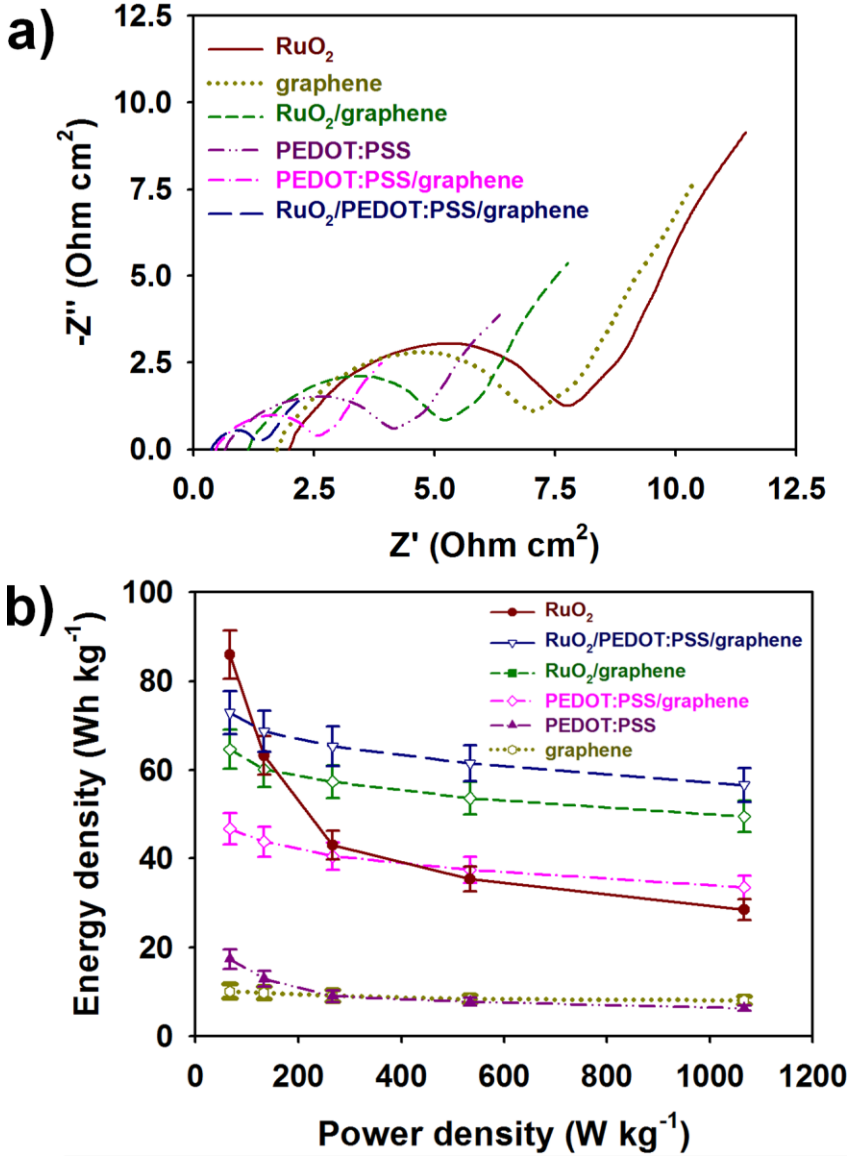

Figure 102. (a) Electrochemical Impedance Spectra (EIS) of RuO_2/PEDOT:PSS/graphene, PEDOT:PSS/graphene, RuO_2/graphene, PEDOT:PSS, graphene, and RuO_2 having a thickness of about 5 μm in the frequency range from 100 kHz to 10 mHz. (b) Ragone plots of electrochemical cells containing different electrode systems.

orders: graphene (10) < PEDOT:PSS (17) < PEDOT:PSS/graphene (47) < RuO_2/graphene (65) < RuO_2/PEDOT:PSS/graphene (73) < RuO_2 (86). Although the highest energy density was achieved by using RuO_2 NPs (86 Wh kg^{-1} at 67 W kg^{-1}), the energy density of RuO_2 rapidly decreased with increasing power density. On the other hand, the energy density of the RuO_2/PEDOT:PSS/graphene was highly preserved at higher power densities, and its energy density was the highest among the samples at the power density of 133, 266, 533, and 1067 W kg^{-1}. The results suggest that the RuO_2/PEDOT:PSS/graphene benefit from the advantages of each component: 1) The RuO_2 can store more energy than the graphene and PEDOT:PSS because of its excellent redox behaviors ; 2) PEDOT:PSS prevented RuO_2 NPs from aggregating and detaching from the substrate through the electrostatic interactions between PSS and Ru^{4+} cations ; 3) The graphene provides rapid sorption and desorption of ions at the electrode surfaces [51,55,63,109,190–192].

The cycling stabilities of the supercapacitors based on the RuO_2/PEDOT:PSS/graphene, PEDOT:PSS/graphene, and PEDOT:PSS nanocomposites were measured with galvanostatic charge–discharge cycles at a current density of 0.5 A g^{-1} (Figure 103). After 1000 such cycles, the specific capacitances of the RuO_2/PEDOT:PSS/graphene, RuO_2/graphene, RuO_2,

PEDOT:PSS/graphene, graphene, and PEDOT:PSS nanocomposites decreased to 668, 574, 469, 422, 98, and 95 F g^{-1} from their initial specific capacitance, respectively (Figure 103a). The retention rate of the nanocomposites (given in %) increased in the following order: RuO_2 (48.5) < PEDOT:PSS (50.2) < RuO_2/graphene (79.0) < PEDOT:PSS/graphene (80.3) < RuO_2/PEDOT:PSS/graphene (81.5) < graphene (84.2) (Figure 103b). Despite its high capacitance and energy density, the RuO_2 NPs exhibited the lowest retention rate among the samples due to its breaking and detaching from the PET substrate [55,109,191]. Furthermore, PEDOT usually suffer from degradation and shrinkage upon exposure to electrolyte during the repeated cycles [55,191]. These results indicated that the graphene sheets with high chemical, mechanical stabilities, and flexibility prevented the PEDOT:PSS and RuO_2 nanostructures from breaking, shrinking and collapsing upon repeated cycling [63,109,192]. Additionally, it can be assumed that the improved dispersion of the graphene sheets and hydrous RuO_2 NPs through the electrostatic interactions with anions of the PSS, resulted in better cycling performance of the RuO_2/PEDOT:PSS/graphene nanocomposite [51,55].

Overall performances of state-of-art electrodes and our work are summarized in radar plots (Figure 104) [42]. This work has shown higher capacitance, energy density, and electrical conductivity than the other

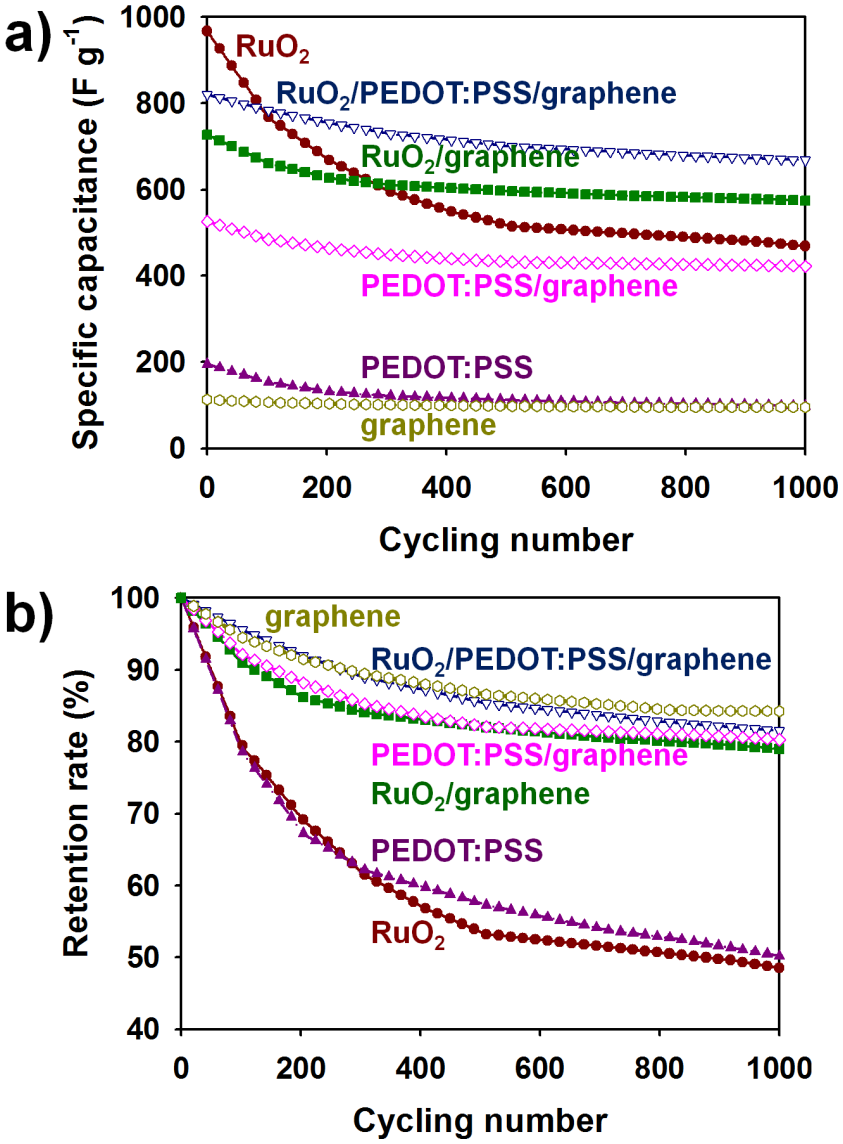

Figure 103. Long-term cycling stability of supercapacitors containing different electrode systems: (a) specific capacitance and (b) retention rate upon repeated cycles.

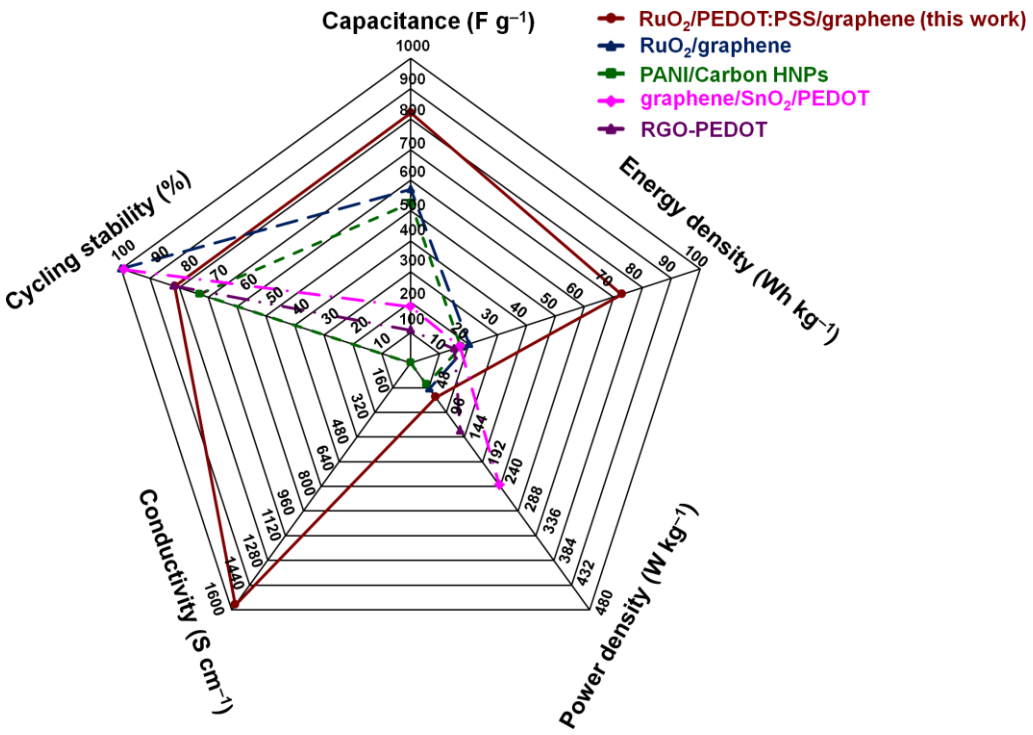

Figure 104. Radar plots comparing this work and four supercapacitors cited from [63,109,192,193].

conducting polymer-based supercapacitors [63,109,192,193]. In particular, the capacitance of RuO_2/PEDOT:PSS/graphene (820 F g^{-1}) was more than four times higher than that of the SnO_2/graphene/PEDOT ternary electrode (184 F g^{-1}). Compared with the other work, the improved electrochemical performances of this work can be attributed to two advantages: 1) The PSS played an important role to promote the effective utilizations of three different components, including PEDOT:PSS, graphene sheets, and RuO_2 NPs, by allowing electrostatic stabilization interactions with each component [51,55] ; 2) Morphological homogeneity of electrode materials could be achieved by a screen-printing method, which allows high connectivity between PEDOT:PSS chains and uniform distribution of each component, including PEDOT:PSS, graphene sheets, and RuO_2 NPs, in the nanocomposites [45,47,48].

4. CONCLUSIONS

1. PANI nanomaterials having different shapes were adjusting the amount of an oxidizing agent and a monomer during chemical oxidation polymerization. The aspect ratios of the nanomaterials could be controlled by adjusting the amount of added APS in a HCl-doped anilinium ion ($NH_3^+Cl^-$) solution. The morphologically different nanomaterials had different charge-transport properties. Intrinsic properties, such as doping level, oxidation level, and conjugation length, were systematically investigated using XPS, UV/VIS/NIR, and FT-IR techniques. The doping levels of the PANI nanomaterials increased in the order of nanoparticles < nanorods < nanofibers. Charge-transport properties were consistent with the conductivities of the nanomaterials. From CV tests, fast redox transitions seemed to enhance the interaction between the nanomaterials and DMMP vapor. The differently shaped PANI nanomaterials were suitable for creating conductive channels on microelectrodes, minimizing the contact resistance between the nanomaterials and the microelectrodes. Chemiresistive sensors based on the PANI nanomaterials had high sensitivity with a low minimum detection limit (MDL, 5 ppb), short recovery time (40 s), and rapid response (1 s) to exposure to various concentrations of DMMP. The PANI nanomaterials have great potential as

CWA sensors.

2. Highly porous PANI/CSA nanostructured thin films were fabricated by the incorporation of very small amounts of BPO, AIBN, and AB into the CSA-doped PANI dissolved in *m*-cresol/$CHCl_3$ co-solvent. Relatively large improvements in electrochemical performance were attributed to the enhanced surface area of the porous polymer electrode, which results in enhanced contact between the electrodes and the surrounding electrolyte. Small increases in the surface roughness of porous PANI provided higher electro-catalytic activity and sustainable conductivities, resulting in low internal resistance and fast redox diffusion at the electrode/electrolyte surface. The specific capacitance of the porous PANI electrodes was as high as 361 F g^{-1} in the three-electrode cell, which is significantly greater than that of pristine PANI. Furthermore, the best DSSC performance was achieved by adding optimal amounts of BPO and AIBN as porotons into the PANI/CSA. A PCE of η = 6.23%, which is an efficiency of 101.0% compared to the Pt-coated cell, and enhanced light harvesting ability with IPCE of 68.86 % could be obtained by empolying porous PANI/CSA nanostructured CEs in the DSSCs. The procedure described herein provides a new means for producing porous, conductive polymer thin films for use as electrode materials in solar cells, Li-ion batteries, supercapacitors, and

thin-film transistors.

3. Water-dispersible Pd-decorated porous P(ANI-*co*-ASA):PSS nanostructures as H_2 sensors were designed to benefit from the synergistic effects of enlarged surface areas due to the nanoporous structures, combined with effective Pd decoration on the P(ANI-*co*-ASA):PSS surface. Both ANI/ASA *co*-monomers and PSS provided sufficient numbers of $–SO_3H$ groups to couple with the Pd NPs. High porosity of the Pd-decorated P(ANI-*co*-ASA):PSS was achieved by introducing very small amounts of water-soluble AB porogens into the P(ANI-*co*-ASA):PSS solution. Pores that were 10–30 nm in diameter and Pd NPs that were 3–10 nm in diameter were successfully incorporated into the P(ANI-*co*-ASA):PSS nanostructure. Data obtained using XPS, UV/VIS/NIR, and FT-IR confirmed not only the successful incorporation of the Pd NPs into the nanoporous matrix, but also showed that the charge transport properties of the P(ANI-*co*-ASA):PSS were retained in the Pd-decorated nanoporous P(ANI-*co*-ASA):PSS nanostructure. CV tests were used to investigate the redox transitions at the P(ANI-*co*-ASA)/electrolyte interface, which became more rapid following pore formation and Pd decoration. Chemiresistive sensors employing Pd-decorated nanoporous P(ANI-*co*-ASA):PSS exhibited good selectivity for various analytes and high sensitivity with a limit of detection of 5 ppm, a

response time of 90 s, and a recovery time of 40 s. .

4. PSS-doped PANI/graphene nanocomposites for use in high-performance H_2S sensors were synthesized by using PSS as both a doping agent and a binding agent for the polymerization of aniline monomers in a biphasic system (water/chloroform) at −50℃. High M_w (1.96×10^6) PSS was synthesized using a low-temperature radical initiator and acted as both a doping agent and a compatibilizer between PSS-doped PANI and graphene sheets in an aqueous reaction mixture. As a result, π−π stacking interactions between the quinoid rings of PANI and the basal planes of graphene were intensified in the presence of PSS. Raman, UV-VIS absorption, XRD, and XPS data show that π−π stacking interactions between PANI and the graphene sheets facilitated compact packing of the PANI chains, higher protonation states, and longer π−conjugation lengths. Polymer solutions of PSS-doped PANI and graphene sheets were highly compatible with flexible PET substrates, and films deposited from such solutions exhibited electrical properties that were stable even after repeated bending. Conductivities of 168.4 S cm^{-1} and surface resistances of 13.1 Ω were obtained for PSS-doped PANI/graphene sensors with film thicknesses of 1 μm, demonstrating the suitability of solution-processed electrodes for H_2S sensing applications. The solution-processed, flexible sensors based on

PSS-doped PANI/graphene boasted high sensitivity to H_2S with a low minimum detection limit (MDL) of 1 ppm, short recovery time (150 s), and rapid response (90 s) to various concentrations of H_2S. In addition, the PSS-doped PANI/graphene sensors were able to differentiate H_2S gas from other analytes.

5. Water-dispersible RuO_2 NPs-decorated PEDOT:PSS/graphene nanocomposite inks for screen-printing was successfully fabricated by incorporating PSS-coated graphene sheets and RuO_2 NPs into the PEDOT:PSS solution. The present work describes an efficient way to obtain highly-defined electrode patterns for use as high-performance supercapacitors by magnifying the synergetic effects from PEDOT:PSS, graphene, and RuO_2 NPs in an aqueous phase. The graphene sheets (size: 2–10 μm) were readily reduced in the presence of high-M_w PSS, and greatly enhanced the charge-transport properties of electrode materials through strong π–π stacking interactions with the PEDOT:PSS structure. The RuO_2 NPs (diameter: ~5 nm) were also highly dispersible in the PEDOT:PSS/graphene system, and acted as efficient catalysts to facilitate redox reactions with the protons (H^+) of the H_2SO_4 electrolyte. The solution-processed RuO_2/PEDOT:PSS/graphene electrode system exhibited conductivity of 1570 S cm^{-1}, specific capacitance of 820 F g^{-1}, and energy

density of 73 Wh Kg^{-1} at a power density of 67 W kg^{-1}, significantly greater than that of PEDOT:PSS (conductivity: 680 S cm^{-1}; specific capacitance: 195 F g^{-1}; energy density: 17 Wh Kg^{-1} at 67 W kg^{-1}) and PEDOT:PSS/graphene (conductivity: 1540 S cm^{-1}; specific capacitance: 526 F g^{-1}; energy density: 47 Wh Kg^{-1} at 67 W kg^{-1}). Moreover, the RuO_2/PEDOT:PSS/graphene-based capacitor showed improved cycling (81.5% after 1000 cycles) and rate performance. Such improvements were highly correlated with the synergetic effects of the PEDOT:PSS, graphene, and hydrous RuO_2 NPs. The procedure described herein can be used as an efficient means to produce highly conductive, electrochemically active electrode patterns for use as electrode materials in various energetic and environmental applications, such as solar cells, batteries, chemical sensors, and thin-film transistors.

In summary, five different ways in the synthetic methodology of high-performance conducting polymer films using solution processes were demonstrated. First, shape-controlled PANI nanomaterials were fabricated by varying the ratio of an oxidizing agent with the monomer, and their charge transport properties were systematically investigated to identify optimal conditions for DMMP detection. Second, highly porous PANI/CSA nanostructures, prepared by inducing thermal decomposition of porogens, showed enhanced electro-catalytic activity than the pristine PANI/CSA, and the porous PANI/CSA thin films have been successfully employed as electrode materials in both an supercapacitor (specific capacitance: 361 F g^{-1}) and DSSC (η = 6.23% and IPCE of 68.86%). Third, pores that were 10–30 nm in diameter and Pd NPs that were 3–10 nm in diameter were successfully incorporated into the P(ANI-*co*-ASA):PSS nanostructure, and thus the resulting sensitivity to H_2 has been enhanced up to 5 ppm. Fourth, the conductivity of PSS-doped PANI/graphene has been successfully improved by increasing M_w of PSS and π–π stacking interactions between the quinoid rings of PANI and the basal planes of graphene, which led to significantly enhanced sensitivity (1 ppm) to H_2S. Lastly, water-dispersible and screen-printable RuO_2 NPs-decorated PEDOT:PSS/graphene nanocomposite showed significantly greater conductivity (1570 S cm^{-1}), specific capacitance (820 F g^{-1}), energy density

(73 Wh Kg^{-1}) than that of the pristine PEDOT:PSS (conductivity: 680 S cm^{-1}; specific capacitance: 195 F g^{-1}; energy density: 17 Wh Kg^{-1}). The conducting polymer thin films consisting of shape-controlled nanomaterials (PANI NFs, NRs, and NPs), organic solvent-dispersible (porous PANI/CSA), and water-dispersible conducting polymer nanostructures (Pd NPs-decorated P(ANI-*co*-ASA):PSS, PSS-doped PANI/graphene, and RuO_2 NPs-decorated PEDOT:PSS/graphene) nanostructures have been successfully applied as electrode materials for chemical sensors, supercapacitors, and DSSCs. Accordingly, these film-forming techniques for conducting polymers can be scaled up and have a great potential for mass productions of high-performance sensors, supercapacitors, and solar cells.

REFERENCES

[1] A. G. Macdiarmid, *Angew. Chem. Int. Ed.* **2001**, *40*, 2581.

[2] K. Matyjaszewski, Oxidative polymerization. In *Encyclopedia of polymer science and technology*. H. Higashimura, S. Kobayashi, 4th ed., John Wiley & Sons, Inc.: New York, 2004, pp 740–764.

[3] J. Jang, *Adv. Polym. Sci.*, **2006**, *199*, 189.

[4] H. S. Nalwa, *Advanced Functional Molecules and Polymers: Electronic and photonic properties*, 1st ed., CRC Press, 2001.

[5] H. Bai, G, Shi, *Sensors*, **2007**, *7*, 267.

[6] J. L. Brédas, G. B. Street, *Acc. Chem. Res.* **1985**, *18*, 309.

[7] S. Bhadra, D. Khastgir, N. K. Singha, J. H. Lee, *Prog. Polym. Sci.*, **2009**, *34*, 783.

[8] G. Ćirić-Marjanović, *Synth. Met.*, **2013**, *170*, 31.

[9] S. Kirchmeyer, K. Reuter, *J. Mater. Chem.*, **2005**, *15*, 2077.

[10] S. G. Im, K. K. Gleason, *Macromolecules* **2007**, *40*, 6552.

[11] H. Yoon, J. Jang, *Adv. Funct. Mater.*, **2009**, 19, 1567.

[12] J. Huang, R. B. Kaner, *Chem. Commun.*, **2006**, 367.

[13] L. B. Groenendaal, F. Jonas, D. Freitag, H. Pielartzik, J. R. Reynolds, *Adv. Mater.*, **2000**, *12*, 481–494.

[14] J. Y. Kim, J. H. Jung, D. E. Lee, J. Joo, *Synth. Met.*, **2002**, *126*, 311–316.

[15] J. Ouyang, C.-W. Chu, F.-C. Chen, Q. Xu, Y. Yang, *Adv. Funct. Mater.*, **2005**, *15*, 203.

[16] S. K. M. Jönsson, J. Birgerson, X. Crispin, G. Greczynski, W. Osikowicz, A.W. Denier van der Gon, W.R. Salaneck, M. Fahlman, *Synth. Met.*, **2003**, *139*, 1.

[17] J. Y. Kim, S. H. Kim, H.-H. Lee, K. Lee, W. Ma, X. Gong, A. J. Heeger, *Adv. Mater.*, **2006**, *18*, 572.

[18] J. P. Thomas, L. Zhao, D. McGillivray, K. T. Leung, *J. Mater. Chem. A*, **2014**, *2*, 2383.

[19] Y. H. Kim, C. Sachse, M. L. Machala, C. May, L. Müller-Meskamp, K. Leo, *Adv. Funct. Mater.*, **2011**, *21*, 1076.

[20] J.-G. Chen, H.-Y. Wei, K.-C. Ho, *Sol. Energy Mater. Sol. Cells*, **2007**, *91*, 1472.

[21] D. Yoo, J. Kim, J. H. Kim, *Nano Res.*, **2014**, *7*, 717.

[22] B. Zhang, G. Tan, C.-S. Lam, B. Yao, C.-L. Ho, L. Liu, Z. Xie, W.-Y. Wong, J. Ding, L. Wang, *Adv. Mater.*, **2012**, *24*, 1873.

[23] Z.-T. Zhu, J. T. Mabeck, C. Zhu, N. C. Cady, C. A. Batt, G. G. Malliaras, *Chem. Commun.*, **2004**, 1556.

[24] M. Kuş, S. Okur, *Sens. Act. B*, **2009**, *143*, 177.

[25] X. Crispin, F. L. E. Jakobsson, A. Crispin, P. C. M. Grim, P. Andersson, A. Volodin, C. van Haesendonck, M. Van der Auweraer, W. R. Salaneck, M. Berggren, *Chem. Mater.*, **2006**, *18*, 4354.

[26] H.-S. Park, S.-J. Ko, J.-S. Park, J. Y. Kim, H.-K. Song, *Sci. Rep.*, **2013**, *3*, 2454.

[27] G. H. Kim, D. H. Hwang, S. I. Woo, *Phys. Chem. Chem. Phys.*, **2012**, *14*, 3530.

[28] R. Gangopadhyay, B. Das, M. R. Molla, *RSC Adv.*, **2014**, *4*, 43912.

[29] H. Yoon, M. Chang, J. Jang, *Adv. Funct. Mater.*, **2007**, *17*, 431.

[30] J. Huang, R. B. Kaner, *J. Am. Chem. Soc.*, **2004**, *126*, 851.

[31] J. Huang, S. Virji, B. H. Weiller, R. B. Kaner, *Chem. Eur. J.*, **2004**, *10*, 1314.

[32] S. Virji, R. B. Kaner, B. H. Weiller, *J. Phys. Chem. B*, **2006**, *110*, 22266.

[33] J. Jang, J. Ha, J. Cho, *Adv. Mater.*, **2007**, *19*, 1772.

[34] J-Y. Hong, H. Yoon, J. Jang, *Small*, **2010**, *6*, 679.

[35] X. Li, X. Li, G. Wang, *Appl. Surf. Sci.*, **2005**, *249*, 266.

[36] L. Zhang, M. Wan, Y. Wei, *Macromol. Rapid Commun.*, **2006**, *27*, 366.

[37] Y. Fu, L. Elsenbaumer, *Chem. Mater.*, **1994**, *6*, 671.

[38] B. G. Gustafsson, Y. Cao, G. M. Treacy, F. Klavetter, N. Colaneri, A. J. Heeger, *Nature*, **1992**, *357*, 477.

[39] A. G. MacDiarmid, A. J. Epstein, *Synth. Met.*, **1994**, *65*, 103.

[40] S. Lee, D. Lee, K. Lee, C. Lee, *Adv. Funct. Mater.*, **2005**, *15*, 1495.

[41] K. Lee, S. Cho, S. H. Park, A. J. Heeger, C.-W. Lee, S.-H. Lee, *Nature*, **2006**, *441*, 65.

[42] N. M. Das, D. Roy, N. Clarke, V. Ganesan, P. S. Gupta, *RSC Adv.*, **2014**, *4*, 32490.

[43] Y. Kang, M. Lee, S. Rhee, *Synth. Met.*, **1992**, *52*, 319.

[44] J. Jang, J. Ha, K. Kim, *Thin Solid Films*, **2008**, *516*, 3152

[45] K.-Y. Shin, S. Cho, J. Jang, *Small*, **2013**, *9*, 3792.

[46] S. Bocchini, A. Chiolerio, S. Porro, D. Accardo, N. Garino, K. Bejtka, D. Perrone, C. F. Pirri, *J. Mater. Chem. C*, **2013**, *1*, 5101.

[47] J. Xu, M. G. Schwab, A. J. Strudwick, I. Henning, X. Feng, Z. Wu, K. Müllen, *Adv. Energ. Mater.*, **2013**, *3*, 1035.

[48] F. C. Krebs, Sol. Energy Mater. Sol. Cells, **2009**, 93, 465.

[49] J. Hu, H. Wang, X. Huang, *Electrochim. Acta*, **2012**, *74*, 98.

[50] X. Luo, A. J. Killard, M. R. Smyth, *Chem. Eur. J.*, **2007**, *13*, 2138.

[51] S. Stankovich, R. D. Piner, X. Chen, N. Wu, S. T. Nguyen, R. S. Ruoff, *J. Mater. Chem.*, **2006**, *16*, 155.

[52] Y.-H. Liao, K. Levon, *Polym. Adv. Tech.*, **1995**, *6*, 47.

[53] S.-A. Chen, H.-T. Lee, *Macromolecules*, **1995**, *28*, 2858.

[54] A. V. Caramyshev, E. G. Evtushenko, V. F. Ivanov, A. R. Barceló, M. G. Roig, V. L. Shnyrov, R. B. van Huystee, I. N. Kurochkin, A. Vorobiev, I. Y. Sakharov, *Biomacromolecules.*, **2005**, *6*, 1360.

[55] L.-M. Huang, H.-Z. Lin, T.-C. Wen, A. Gopalan, *Electrochim. Act.*, **2006**, *52*, 1058.

[56] L. Chen, C. Yuan, H. Dou, B. Gao, S. Chen, X. Zhang, *Electrochim. Act.*, **2009**, *54*, 2335.

[57] C.-Y. Chu, J.-T. Tsai, C.-L. Sun, Int. *J. Hydrogen Energy.*, **2012**, *37*, 13880.

[58] P. Novák, K. Müller, K. S. V. Santhanam, O. Haas, *Chem. Rev.*, **1997**, *97*, 207.

[59] T. Stöcker, A. Köhler, R. Moos, *J. Polym. Sci.*, **2012**, *50*, 976.

[60] V. Georgakilas, M. Otyepka, A. B. Bourlinos, V. Chandra, N. Kim, K. C. Kemp, P. Hobza, R. Zboril, K. S. Kim, *Chem. Rev.*, **2012**, *112*, 6156.

[61] H. Bai, C. Li, G. Q. Shi, *Adv. Mater.*, **2011**, *23*, 1089.

[62] S. Park, J. An, I. Jung, R. D. Piner, S. J. An, X. Li, A. Velamakanni, R. S. Ruoff, *Nano Lett.*, **2009**, *9*, 1593.

[63] J. Zhang, X. S. Zhao, *J. Phys. Chem. C*, **2012**, *116*, 5420.

[64] S. Liu, J. Tian, L. Wang, Y. Luo, X. Sun, *Analyst*, **2011**, *136*, 4898.

[65] N. A. Kumar, H.-J. Choi, Y. R. Shin, D. W. Chang, L. Dai, J.-B. Baek, *ACS Nano*, **2012**, *6*, 1715.

[66] M. Kim, C. Lee, J. Jang, *Adv. Funct. Mater.*, **2014**, *24*, 2489.

[67] X. Huang, X. Qi, F. Boey, H. Zhang, *Chem. Soc. Rev.*, **2012**, *41*, 666.

[68] B. He, Q. Tang, M. Wang, C. Ma, S. Yuan, *J. Power Sources*, **2014**, *256*, 8.

[69] C. M. Hansen, Hansen Solubility Parameters: A User's Handbook, 2nd ed., CRC Press, 2007.

[70] L, Pan, H. Qiu, C. Dou, Y. Li, L. Pu, J. Xu, Y. Shi, *Int. J. Mol. Sci.* **2010**, *11*, 2636.

[71] G. A. Snook, P. Kao, A. S. Best, *J. Power Sources*, **2011**, *196*, 1

[72] J. F. Mike, J. L. Lutkenhaus, *J. Polym. Sci., Part B: Polym. Phys.* **2013**, *51*, 468.

[73] T. N. Murakami, M. Grätzel, *Inorg. Chim. Acta*, **2008**, *361*, 572.

[74] H. Yoon, S. H. Lee, O. S. Kwon, H. S. Song, E. H. Oh, T. H. Park, J. Jang, *Angew. Chem. Int. Ed.*, **2009**, *48*, 2755.

[75] R. Liu, J. Duay, S. B. Lee, *ACS Nano*, **2010**, *4*, 4299.

[76] B. O'Regan, M. Grätzel, *Nature*, **1991**, *353*, 737.

[77] M. Grätzel, *Nature*, **2001**, *414*, 338.

[78] A. Yella, H. Lee, H. N. Tsao, C. Yi, A. K. Chandiran, M. K. Nazeeruddin, E. W. Diau, C. Yeh, S. M. Zakeeruddin, M. Grätzel, *Science*, 2011, **334**, 629.

[79] E. Ghadiri, N. Taghavinia, S. M. Zakeeruddin, M. Grätzel, J.-E. Moser, *Nano Lett.*, **2010**, *10*, 1632.

[80] S. H. Hwang, H. Song, J. Lee, J. Jang, *Chem. Eur. J.*, **2014**, *20*, 12974.

[81] A. Kay, M. Grätzel, *J. Phys. Chem.*, **1993**, *97*, 6272.

[82] M. K. Nazeeruddin, P. Péchy, T. Renouard, S. M. Zakeeruddin, R. Humphry-Baker, P. Comte, P. Liska, L. Cevey, E. Coasta, V. Shklover, L. Spiccia, G. B. Deacon, C. A. Bignozzi, M. Grätzel, *J. Am. Chem. Soc.*, **2001**, *123*, 1613.

[83] M. Wang, N. Chamberland, L. Breau, J.-E. Moser, R. Humphry-Baker, B. Marsan, S. M. Zakeeruddin and M. Grätzel, *Nat. Chem.*, **2010**, *2*, 385.

[84] N. A. Lewcenko, M. J. Byrnes, T. Daeneke, M. Wang, S. M. Zakeeruddin, M. Grätzel and L. Spiccia, *J. Mater. Chem.*, **2010**, *20*, 3694.

[85] C.-L. Chen, H. Teng and Y.-L. Lee, *J. Mater. Chem.*, **2011**, *21*, 628.

[86] A. Kay, M. Grätzel, *Sol. Energy Mater. Sol. Cells*, **1996**, *44*, 99.

[87] T. N. Murakami, S. Ito, Q. Wang, M. K. Nazeeruddin, T. Bessho, I. Cesar, P. Liska, R. Humphry-Baker, P. Comte, P. Péchy, M. Grätzel, *J. Electrochem. Soc.*, **2006**, *153*, A2255.

[88] C.-P. Lee, M.-H. Yeh, R. Vittala, K.-C. Ho, *J. Mater. Chem.*, **2011**, *21*, 15471.

[89] S. Das, P. Sudhagar, V. Verma, D. Song, E. Ito, S. Y. Lee, Y. S. Kang, W. Choi, *Adv. Funct. Mater.*, **2011**, *21*, 3729.

[90] B. Zhao, H. Huang, P. Jiang, H. Zhao, X. Huang, P. Shen, D. Wu, R. Fu, S. Tan, *J. Phys. Chem. C*, **2011**, *115*, 22615.

[91] X. Cai, S. Hou, H. Wu, Z. Lv, Y. Fu, D. Wang, C. Zhang, H. Kafafy, Z. Chu, D. Zou, *Phys. Chem. Chem. Phys.*, **2012**, *14*, 125.

[92] X. Xin, M. He, W. Han, J. Jung, Z. Lin, *Angew. Chem., Int. Ed.*, **2011**, *50*, 1.

[93] M. Wang, A. M. Anghel, B. Marsan, N.-L. Cevey Ha, N. Pootrakulchote, S. M. Zakeeruddin, M. Grätzel, *J. Am. Chem. Soc.*, **2009**, *131*, 15976.

[94] M. Wu, Q. Zhang, J. Xiao, C. Ma, X. Lin, C. Miao, Y. He, Y. Gao, A. Hagfeldt, T. Ma, *J. Mater. Chem.*, **2011**, *21*, 10761.

[95] S. Ahmad, J.-H. Yum, H.-J. Butt, M. K. Nazeeruddin, M. Grätzel, *ChemPhysChem*, **2010**, *11*, 2814.

[96] Y. Saito, T. Kitamura, Y. Wada, S. Yanagida, *Chem. Lett.*, **2002**, *31*, 1060.

[97] S. Ahmad, J.-H. Yum, Z. Xianxi, M. Grätzel, H.-J. Butta, M. K. Nazeeruddin, *J. Mater. Chem.*, **2010**, *20*, 1654.

[98] K. S. Lee, H. K. Lee, D. H. Wang, N.-G. Park, J. Y. Lee, O. O. Park, J. H. Park, *Chem. Commun.*, **2010**, *46*, 4505.

[99] A. J. Mozer, D. K. Panda, S. Gambhir, T. C. Romeo, B. Winther-Jensen, G. G. Wallace, *Langmuir*, **2010**, *26*, 1452.

[100] K. S. Lee, J. H. Yun, Y.-H. Han, J.-H. Yim, N.-G. Park, K. Y. Cho, J. H. Park, *J. Mater. Chem.*, **2011**, *21*, 15193.

[101] Q. Li, J. Wu, Q. Tang, Z. Lan, P. Li, J. Lin, L. Fan, *Electrochem. Commun.*, **2008**, *10*, 1299.

[102] S. Ameen, M. S. Akhtar, Y. S. Kim, O.-B. Yang, H.-S. Shin, *J. Phys. Chem. C*, **2010**, *114*, 4760.

[103] J. Xia, L. Chena, S. Yanagida, *J. Mater. Chem.*, **2011**, *21*, 4644.

[104] S. Jeon, C. Kim, J. Ko and S. Lim, *J. Mater. Chem.*, **2011**, *21*, 8146.

[105] N. Ikeda, K. Teshima, T. Miyasaka, *Chem. Commun.*, **2006**, 1733.

[106] C.-P. Lee, P.-Y. Chen, R. Vittala, K.-C. Ho, *J. Mater. Chem.*, **2010**, *20*, 2356.

[107] K.-C. Huang, J.-H. Huang, C.-H. Wu, C.-Y. Liu, H.-W. Chen, C.-W. Chu, J.-T. Lin, C.-L. Lin, K.-C. Ho, *J. Mater. Chem.*, **2011**, *21*, 10384.

[108] M.-H. Yeh, L.-Y. Lin, C.-P. Lee, H.-Y. Wei, C.-Y. Chen, C.-G. Wu, R. Vittala, K.-C. Ho, *J. Mater. Chem.*, **2011**, *21*, 19021.

[109] Z.-S. Wu, D.-W. Wang, W. Ren, J. Zhao, G. Zhou, F. Li, H.-M. Cheng, *Adv. Funct. Mater.*, **2010**, *20*, 3595.

[110] K.-H. Chang, C.-C. Hu, *Electrochem. Solid-State Lett.*, **2004**, *7*, A466.

[111] T. A. Skotheim, R. L. Elsenbaumer, L. W. Shacklette, *Handbook of Conducting polymers*, 2nd ed., Marcel Dekker, Inc.: New York, 1997.

[112] L. J. van der Paw, *Philips Tech. Rev.*, **1958**, *20*, 220.

[113] K. Kim, O. G. Tsay, D. A. Atwood, D. G. Churchill, *Chem. Rev.*, **2011**, *111*, 5345.

[114] V. M. Bermudez, *Langmuir*, **2010**, *26*, 18144.

[115] H. Park, T. Kim, M. Kang, J. Lee, H. Yoon, *ACS Nano*, **2012**, *6*, 7624.

[116] J. Stejskal, P. Kratochvil, *Langmuir*, **1996**, *12*, 3389.

[117] H. Yoon, J-Y. Hong, J. Jang, *Small*, **2007**, *10*, 1774.

[118] Y. Otsuka, H. Y. Lee, J. Gu, J.-O. Lee, K. H. Yoo, H. Tanaka, H. Tabata, T. Kawai, *Jpn. J. Appl. Phys.*, **2002**, *41*, 891.

[119] J. Jang, J. Ha, S. Kim, *Macromol. Res.*, **2006**, *14*, 401.

[120] X. Li, X. Li, G. Wang, *Appl. Surf. Sci.*, **2005**, *249*, 266.

[121] L. Zhang, M. Wan, Y. Wei, *Macromol. Rapid Commun.*, **2006**, *27*, 366.

[122] J. Qiang, Z. Yu, H. Wu, D. Yun, *Synth. Met.*, **2008**, *158*, 544.

[123] N.-R. Chiou, A. J. Epstein, *Adv. Mater.*, **2005**, *17*, 1679.

[124] J. Stejskal, D. Hlavata, P. Holler, M. Trchov, J. Prokes, I. Sapurina, *Polym. Int.*, **2004**, *53*, 294.

[125] M. G. Han, S. S. Im, *Polymer*, **2000**, *41*, 3253.

[126] J. A. Smith, M. Josowicz, M. Engelhard, D. R. Baer, J. Janata, *Phys. Chem. Chem. Phys.*, **2005**, *7*, 3619.

[127] S. M. Ahmed, *Eur. Polym. J.*, **2002**, *38*, 1151.

[128] R. J. Tseng, C. O. Baker, B. Shedd, J. Huang, R. B. Kaner, J. Ouyang, Y. Yang, *Appl. Phys. Lett.*, **2007**, *90*, 053101.

[129] Z. D. Zujovic, Y. Wang, G. A. Bowmaker, R. B. Kaner, *Macromolecules*, **2011**, *44*, 2735.

[130] G. E. Asturias, A. G. MacDiarmid, *Synth. Met.*, **1989**, *29*, 157.

[131] W. S. Huang, A. G. MacDiarmid, **1993**, *Polymer*, *34*, 1833.

[132] K.-S. Ho, T.-H. Hsieh, C.-W. Kuo, S.-W. Lee, J.-J. Lin, Y.-J. Huang, **2005**, *J. Polym. Sci. A Polym. Chem.*, *43*, 3116.

[133] D. W. Hatchett, M. Josowicz, J. Janata, *J. Phys. Chem. B*, **1999**, *103*, 10992.

[134] Y. Jung, R. J. Kline, D. A. Fischer, E. K. Lin, M. Heeney, I. McCulloch, D. M. DeLongchamp, *Adv. Funct. Mater.*, **2008**, *18*, 742.

[135] D. C. Tiwari, R. Sharma, K. D. Vyas, M. Boopathi, V. V. Singh, P. Pandey, *Sens. and Actuators B*, **2010**, *151*, 256.

[136] J. A-Hernández, J. Skarda, K. P-Kamloth, *Synth. Met*., **1998**, *95*, 197.

[137] L.Bansal, M. El-Sherif, *IEEE Sens. J*, **2005**, *5*, 648.

[138] G. E. Collins, L. J. Buckley, *Synth. Met*., **1996**, *78*, 93.

[139] E. S. Snow, F. K. Perkins, E. J. Houser, S. C. Badescu, T. L. Reinecke, *Science*, **2005**, *307*, 1942.

[140] J. Stejskal, R. G. Gilbert, *Pure Appl. Chem.*, **2002**, *74*, 857.

[141] J. Brandrup, E. H. Immergut, E. A. Grulke, in *Polymer Handbook*, 4th ed., John Wiley, Inc. New York, 1999, p. 2−69.

[142] C. C. Shale, D. G. Simpson, P. S. Lewis, *Chem. Eng. Prog. Symp. Ser.*, **1971**, *67*, 52.

[143] H. S. Lee, T. H. Ha, K. K. Kim, *Mater. Chem. Phys.*, **2005**, *93*, 376.

[144] J. G. Radziszewski, M. R. Nimlos, P. R. Winter, G. B. Ellison, *J. Am. Chem. Soc.*, **1996**, *118*, 7400.

[145] B. Pabin-Szafko, E. Wisniewska, Z. Czech, *Chem. Chemical. Tech.*, **2009**, *3*, 101.

[146] J. Stejskal, I. Sapurina, M. Trchová, J. Prokeš, I. Křivka, E. Tobolková, *Macromolecules*, **1998**, *31*, 2218.

[147] S. A. Curran, D. Zhang, W. Wondmagegn, W. Blau, *Synth. Met.*, **2006**, *156*, 482.

[148] J. Xu, K. Wang, S.-Z. Zu, B.-H. Han, Z. Wei, *ACS Nano*, **2010**, *4*, 5019.

[149] Q. Wu, Y. Xu, Z. Yao, A. Liu, G. Shi, *ACS Nano*, **2010**, *4*, 1963.

[150] D. Benlanger, X. Ben, J. Davey, F. Uribe, S. Gottesfeld, *J. Electrochem. Soc.*, **2000**, *147*, 2923.

[151] M. D. Stoller, R. S. Ruoff, *Energy Environ. Sci.*, **2010**, *3*, 1294.

[152] Y. Gogotsi, P. Simon, *Science*, **2011**, *334*, 917.

[153] L. Li, G. Yan, J. Wu, X. Yu, Q. Guo, Z. Ma, Z. Huang, *J. Polym. Res.*, **2009**, *16*, 421.

[154] L. Kong, X. Lu, E. Jin, S. Jiang, C. Wang, W. Zhang, *Composit. Sci. Tech.*, **2009**, *69*, 561.

[155] D. B. Wolfe, J. C. Love, K. E. Paul, M. L. Chabinyc and G. M. Whitesides, *Appl. Phys. Lett*., **2002**, *80*, 2222.

[156] A. Drelinkiewicz, M. Hasik, M. Choczynski, *Mater. Res. Bull.*, **1993**, *33*, 739.

[157] J.-E. Park, S-G. Park, A. Koukitu, O. Hatozaki, N. Oyama, *Synth. Met.*, **2004**, *141*, 265.

[158] S.-W. Kim, J. Park, Y. Jang, Y. Chung, S. Hwang, T. Hyeon, *Nano. Lett.*, **2003**, *3*, 1289.

[159] R. Lamber, S. Wetjen, N. I. Jaeger, *Phys. Rev. B*, **1995**, *51*, 10968.

[160] S. Maeda, S.P. Armes, *Synth. Met.*, **1995**, *73*, 151.

[161] P. Rannou, M. Nechtschein, *Synth. Met.*, **1997**, *84*, 755.

[162] A. Wolter, P. Rannou, J. P. Travers, *Phys. Rev. B*, **1998**, *58*, 12.

[163] C. A. Muller, M. Maciejewski, R. A. Koeppel, A. Baiker, *J. Catalysis*, **1997**, *166*, 36.

[164] K.-S. Ho, T.-H. Hsieh, C.-W. Kuo, S.-W. Lee, J.-J. Lin, Y.-J. Huang, *J. Polym. Sci., Part A: Polym. Chem.*, **2005**, *43*, 3116.

[165] A. A. Athawale, M. V. Kurkarni, *Sens. and Acts. B*, **2000**, *67*, 173.

[166] Z. Wang, Z. Li, T. Jiang, X. Xu, C. Wang, *ACS Appl. Mater. Interfaces.*, **2013**, *5*, 2013.

[167] C. Liewhiran, N. Tamaekong, A. Wisitsoraat, A. Tuantranont, S. Phanichphant, *Sens. and Acts. B*, **2013**, *176*, 893.

[168] P. A. Pandey, N. R. Wilson, J. A. Covington, *Sens. and Acts. B*, **2013**, *183*, 478.

[169] S. Cho, J. S. Lee, J. Jun, J. Jang, *J. Mater. Chem. A*, **2014**, *2*, 1955.

[170] N. E.Agbor, M. C. Petty, A. P. Monkman, *Sens. and Act. B*, **1995**, *28*, 173.

[171] S. Virji, J. D. Fowler, C. O. Baker, J. Huang, R. B. Kaner, B. H. Weiller, *Small*, **2005**, *1*, 624–627.

[172] S. Bourdo, Z. Li, A. S. Biris, F. Watanabe, T. Viswanathan, I. Pavel, *Adv. Funct. Mater.*, **2008**, *18*, 432.

[173] R. Langner, G. Zundel, *J. Phys. Chem.*, **1995**, *99*, 12214.

[174] S.-I. Na, G. Wang, S.-S. Kim, T.-W. Kim, S.-H. Oh, B.-K. Yu, T. Lee, D.-Y. Kim, *J. Mater. Chem.*, **2009**, *19*, 9045.

[175] H. Wang, Q. Hao, X. Yang, L. Lu, X. Wang, *Nanoscale*, **2010**, *2*, 2164.

[176] H. G. M. Edwards, D. R. Brown, J. A. Dale, S. Plant, *Vib. Spectrosc.* **2000**, *24*, 213.

[177] V. H. Pham, T. V. Cuong, S. H. Hur, E. Oh, E. J. Kim, E. W. Shin, J. S. Chung, *J. Mater. Chem.*, **2011**, *21*, 3371.

[178] F. Gong, X. Xu, G. Zhou, Z.-S. Wang, *Phys. Chem. Chem. Phys.*, **2013**, *15*, 546.

[179] H. Wang, Q. Hao, X. Yang, L. Lu, X. Wang, *Electrochem. Commun.*, **2009**, *11*, 1158.

[180] J. A. Dean, *Lange's Handbook of Chemistry*, 14th ed., McGraw-Hill: New York, 1992.

[181] J. D. Thomas, *J. Am. Chem. Soc.*, **1961**, *83*, 4849.

[182] J. Werber, Y. J. Wang, M. Milligan, X. Li, J. A. Ji, *J. Pharm. Sci.*, **2011**, *100*, 3307.

[183] J. Zhou, G. Lubineau, *ACS Appl. Mater. Interfaces*, **2013**, *5*, 6189.

[184] X. Zhang, D. Chang, J. Liu, Y. Luo, *J. Mater. Chem.*, **2010**, *20*, 5080.

[185] N. Hu, Y. Wang, J. Chai, R. Gao, Z. Yang, E. S.-W. Kong, Y. Zhang, *Sens. and Acts. B*, **2012**, *163*, 107.

[186] M. E. Roberts, M. C. LeMieux, Z. Bao, *ACS Nano*, **2009**, *3*, 3287.

[187] S. K. Arya, S. Krishnan, H. Silva, S. Jeana, S. Bhansali, *Analyst*, **2012**, *137*, 2743.

[188] T. Hübert, L. Boon-Brett, G. Black, U. Banach, *Sens. and Acts. B*, **2011**, *157*, 329.

[189] S. K. Pandey, K.-H. Kim, K.-T. Tang, *Trends Anal. Chem*, **2012**, *32*, 87–99.

[190] L. Deng, J. Wang, G. Zhu, L. Kang, Z. Hao, Z. Lei, Z. Yang, Z.-H. Liu, *J. Power. Sources.*, **2014**, *248*, 407–415.

[191] R. Liu, J. Duay, T. Lane, S. Lee, *Phys. Chem. Chem. Phys.*, **2010**, *12*, 4309–4316.

[192] W. Wang, W. Lei, T. Yao, X. Xia, W. Huang, Q. Hao, X. Wang, *Electrochim. Acta*, **2013**, *108*, 118–126.

[193] Z. Lei, Z. Chen, X. S. Zhao, *J. Phys. Chem. C*, **2010**, *114*, 19867–19874.